ABSTRACT

Title of Dissertation:	MULTISCALE RADIATION-MHD SIMULATIONS OF COMPACT STAR CLUSTERS
	ChongChong He Doctor of Philosophy, 2023
Dissertation Directed by:	Professor Massimo Ricotti Department of Astronomy

Star formation is a crucial process that lies at the center of many important topics in astrophysics: the nature of the first sources of radiation, the formation and evolution of galaxies, the synthesis of elements, and the formation of planets and life. Recent advances in computing technology have brought about unprecedented opportunities to deepen our understanding of this complex process. In this dissertation, I investigate the physics of star formation in galaxies and its role in shaping the galaxies and the Universe through numerical simulations.

My exploration of star formation begins with a large set of simulations of star cluster formation from isolated turbulent Giant Molecular Clouds (GMCs) with stellar feedback using RAMSES-RT, a state-of-the-art radiation-magneto-hydrodynamic (radiation-MHD) code. While resolving the formation of individual stars, I have pushed the parameters (mass and density) of the simulated GMCs well beyond the limit explored in the literature. I establish physically motivated scaling relationships for the timescale and efficiency of star formation regulated by photoionization feedback. I show that this type of stellar feedback is efficient at dispersing dense

molecular clouds before the onset of supernova explosions. I show that star formation in GMCs can be understood as a purely stochastic process, where instantaneous star formation follows a universal mass probability distribution, providing a definitive answer to the open question of the chronological order of low- and high-mass star formation. In a companion project, I publish the first study of the escape of ionizing photons from resolved stars in molecular clouds into the intercloud gas. I conclude that the sources of photons responsible for the epoch of reionization, one of the most important yet poorly understood stages in cosmic evolution, must have been very compact star clusters, or globular cluster progenitors, forming in dense environments different from today's galaxies.

In follow-up work, I use a novel zoom-in adaptive-mesh-refinement method to simulate the formation and fragmentation of prestellar cores and resolve from GMC scales to circumstellar disk scales, achieving an unprecedented dynamic range of 18 orders of magnitude in volume in a set of radiation-MHD simulations. I show that massive stars form from the filamentary collapse of dense cores and grow to several times the core mass due to accretion from larger scales via circumstellar disks. This suggests a competitive accretion scenario of high-mass star formation, a problem that is not well understood. We find that large Keplerian disks can form in magnetically critical cores, suggesting that magnetic braking fails to prevent the formation of rotationally-supported disks, even in cores with mass-to-flux ratios close to critical. This is because the magnetic field is extremely turbulent and incoherent, reducing the effect of magnetic braking by roughly one order of magnitude compared to the perfectly aligned and coherent case, which proposes a solution to the "magnetic braking catastrophe."

MULTISCALE RADIATION-MHD SIMULATIONS OF COMPACT STAR CLUSTERS

by

ChongChong He

Dissertation submitted to the Faculty of the Graduate School of the
University of Maryland, College Park in partial fulfillment
of the requirements for the degree of
Doctor of Philosophy
2023

Advisory Committee:
Professor Massimo Ricotti, Chair/Advisor
Professor Cole Miller
Professor Alberto Bolatto
Professor Carter Hall, Dean's Representative
Professor Susan Kassin, External Examiner

© Copyright by
ChongChong He
2023

Preface

The research presented in Chapters 2-5 and Appendix A of this dissertation has either been published or submitted for publication in the Monthly Notices of the Royal Astronomical Society (MNRAS) or the Astrophysical Journal (ApJ) with minimal modification. Each chapter corresponds to the following papers:

- Chapter 2 – **C.-C. He**, M. Ricotti, and S. Geen, "Simulating star clusters across cosmic time - I. Initial mass function, star formation rates, and efficiencies", *MNRAS* 489, 1880–1898 (2019).

- Chapter 3 – **C.-C. He**, M. Ricotti, and S. Geen, "Simulating star clusters across cosmic time - II. Escape fraction of ionizing photons from molecular clouds", *MNRAS* 492, 4858–4873 (2020).

- Chapter 4 – **C.-C. He** and M. Ricotti, "Massive prestellar cores in radiation-magneto-turbulent simulations of molecular clouds", *MNRAS*, 10.1093/mnras/stad1289 (2023)

- Chapter 5 – **C.-C. He** and M. Ricotti, "Magnetic braking fails to work: formation of large Keplerian disks in magnetically critical giant molecular clouds", *submitted to MNRAS*, (2023).

- Chapter 6 – **C.-C. He**, "A fast and accurate analytic method of calculating galaxy two-point correlation functions", *ApJ* 921, 59, 59 (2021).

The contents of this dissertation form a coherent story. In the first act, I conduct a large set of simulations to explore the laws of star formation. In the second act, I investigate the implications of star cluster formation for the source of radiation during the epoch of reionization. In the third and fourth acts, I delve into smaller scales, focusing on the collapse of prestellar cores and the formation of circumstellar disks. Finally, as an appendix, I present part of my ongoing project on stellar dynamics, which is the subsequent evolution of those simulated star clusters. Throughout, we witness how each of the many characters of star formation drives the behavior of the natal cloud, which ultimately affects star formation itself.

Originally, I researched star formation to study the source of radiation for cosmic reionization but ended up discovering some mysterious and intriguing theories of star formation, which lured me to dive deeper into the subject. In the end, I attempted to uncover its identity and push back its frontier, but it appears what I discovered so far is just the tip of the iceberg.

Dedication

To my parents.

Acknowledgments

I am thrilled to present this dissertation as the culmination of my PhD journey in astrophysics at the University of Maryland. This work would not have been possible without the guidance and support of many people who deserve my sincere gratitude.

First and foremost, I want to thank my advisor, Professor Massimo Ricotti, for his mentorship, encouragement, and inspiration. He has taught me how to be a rigorous and creative researcher, how to communicate my ideas effectively, and how to enjoy the process of discovery. He has always been generous with his time and resources and has given me the freedom and confidence to pursue my own interests. I am honored to have worked with him and learned from him.

I also want to thank my thesis committee members, Cole Miller, Alberto Bolatto, Carter Hall, and Susan Kassin; my collaborator, Sam Geen; and my research group, Benedikt Diemer, Jongwon Park, Calvin Osinga, Katya Leidig, Ronan Hix, and Fred Garcia. They have provided valuable feedback, insights, and suggestions that have improved the quality and clarity of my work. I am also grateful to my first research advisor, Laurens Keek, for introducing me to the field of astrophysics as an exchange student at Georgia Tech. He sparked my curiosity and passion for this subject and encouraged and supported me to pursue a Ph.D. I owe him a debt of gratitude.

I would like to thank all the UMD Astronomy Department Staff – Eric McKenzie, Mary Ann Phillips, Barbara Hansborough, John Cullinan, Olivia Dent, Natalie Rowe, Susan Lehr, Dorinda Kimbrell, Mark Wolfire, Kevin Rauch, and Peter Teuben – for making the administrative end of things so easy for us. They have always been helpful, efficient, and cheerful in dealing with any issues or requests that I had. I also owe a huge debt of gratitude to my wonderful office mates, Sara Frederick, Robyn Smith, and Pradip Gatkine, for their support during my first years in the department. I would also like to thank my classmates, Weizhe, Jialu, Laura, Carrie, and Liz for keeping me company through this journey and helping me adjust to a new country. Finally, I want to thank all of the graduate students – Rebecca, Ginny, Kyle, Amy, Drew, Ramsey, Milena, Charlotte, Guangwei, Harrison, Julian, Vicente, Sergio, Tomas, Rye, Alex, Ben, Erica, Teal, Krista, Dana, Thomas, Mark, Mahmuda, Myra, Zeeve, Vicki, Ell, Joe, Jordan, Arjun, Gokul, and more – and everyone else in the Department of Astronomy. They have been a source of friendship, fun, and support throughout my Ph.D. They have also been friendly and supportive colleagues and created a warm and welcoming atmosphere in the department, which made my research experience enjoyable and rewarding. I could not have asked for a better place or better people to spend the past years with.

It's hard to express how grateful I am for my parents, He Xinyuan and Li Chulan. I would like to extend my heartfelt thanks to them for their unconditional love and support. They have always believed in me and sacrificed a lot for me, giving me everything I needed to become who I am. They have been my biggest fans and cheerleaders. I dedicate this dissertation to them.

This dissertation marks the end of one chapter of my life and the beginning of another. I am excited about what lies ahead, but I will always cherish the memories and lessons from this amazing journey.

Table of Contents

List of Tables

List of Figures

List of Abbreviations

AGN	Active galactic nucleus
ALMA	Atacama Large Millimeter/submillimeter Array
AMR	Adaptive mesh refinement
AU	Astronomical unit
ApJ	Astrophysical Journal
BH	Black hole
CA	Competitive accretion
CMF	Core mass function
CO	Carbon monoxide
CPU	Central processing unit
DD	Data-data
DR	Data-random
EAGLE	Evolution and Assembly of GaLaxies and their Environments
EoR	Epoch of reionization
GC	Globular cluster
GMC	Giant molecular cloud
GPU	Graphical processing unit
H	Hydrogen
H_2	Molecular hydrogen
HM	high-mass
HPC	High Performance Computing
HST	Hubble Space Telescope
He	Helium
He II	Double-ionized helium
IGM	Intergalactic medium
IM	Intermediate-mass
IMBH	Intermediate-mass black hole
IMF	Initial Mass Function
IR	Infrared
ISM	Interstellar medium
JWST	James Webb Space Telescope
KH	Kelvin-Helmholtz
LyC	Lyman-continuum
MC	Molecular cloud

MHD	Magneto-hydrodynamics
MNRAS	Monthly Notices of the Royal Astronomical Society
NSC	Nuclear star cluster
PDF	Probability density function
QSO	Quasi-stellar object
RR	Random-random
RT	Radiation transfer
SFE	Star Formation Efficiency
SFR	Star formation rate
SMBH	Supermassive black hole
SN	Supernova
SPH	Smoothed-particle hydrodynamics
TC	Turbulent Core
TPCFs	Two-point correlation functions
TSFE	Total star formation efficiency
UV	Ultraviolet
YSO	Young stellar objects
H I	Neutral hydrogen
H II	Singly-ionized hydrogen

Simulation names used in Chapter 2:

XXS	Extra-extra-small
XS	Extra-small
S	Small
M	Medium
L	Large
XL	Extra-large
F	Fiducial
C	Compact
VC	Very compact

Chapter 1: Introduction

Stars are the fundamental building blocks of the universe. The problem of how stars form lies at the center of many important topics in astrophysics: the nature of the first sources of radiation, the formation and evolution of galaxies, the synthesis of elements, and the formation of planets and life.

Stars are not born in isolation; they are mostly found in groups called star clusters. These clusters form from molecular clouds, which serve as nurseries for stellar objects. They are sites of intense stellar feedback processes such as UV feedback, jets, winds, and supernovae.

It is difficult to formulate a general theory for star formation due to the wide range of physical processes involved. However, recent advances in computing technology have brought about unprecedented levels of understanding of this complex process. My research has focused on understanding the physics of star formation in galaxies and its role in shaping the galaxies and the universe, using multiscale radiation magneto-hydrodynamics (MHD) simulations of star formation from molecular clouds.

This chapter begins by reviewing two major problems in star formation: the star formation rate and the initial mass function, which provide background for Chapter 2 and Chapter 4. I then review the role of magnetic field in star formation, raising an open question that motivates the work presented in Chapter 5. Next, I provide a brief introduction to the topic of cosmic reionization, which serves as a background for Chapter 3. Then, I present a summary of the techniques used to simulate star formation. Finally, this chapter closes with the thesis outline and a list of software and facilities used in this thesis.

The essence of this thesis and what we hope to convey is that we desperately need more physically-grounded models of star formation to advance our understanding of this fundamental process in the universe. We are in the midst of an exciting period of rapid advancement in computational technology, and future work with the help of large-scale simulations and advanced observations holds the promise of uncovering the full mystery of star formation.

1.1 Star Formation

1.1.1 The star formation rate

One parameter to characterize how fast stars form in a region is the dimensionless star formation rate (SFR) per free-fall time,

$$\epsilon_{\rm ff} = \frac{\dot{m}_*}{m_{gas}} t_{\rm ff}, \tag{1.1}$$

where $t_{\rm ff}$ is the free-fall time of the gas at average density and $\dot{m}_*$ is the SFR. A gas cloud that is not supported against collapse will naturally produce stars at a rate corresponding to $\epsilon_{\rm ff} \approx 1$, since the free-fall time is the natural evolutionary timescale for a self-gravitating system with nothing inhibiting star formation. A direct way to measure $\epsilon_{\rm ff}$ is to estimate the SFR by counting young stellar objects (YSOs) and estimating their masses and the duration of the YSO phase (e.g. Krumholz et al., 2012). A second approach is to match catalogs of star-forming regions identified by tracers such as IR or free-free emission with catalogs of molecular clouds identified by CO or dust emission, and then using the mass, free-fall time, and SFR of the matched clouds and star-forming regions to estimate $\epsilon_{\rm ff}$ (e.g. Lee et al., 2016). A third approach, available for extragalactic systems with extensive molecular gas and star-formation tracer maps, is to pixelate the entire galaxy and estimate masses, densities, and free-fall times in each pixel (e.g. Krumholz et al., 2012).

These methods, applicable to scales from the Milky Way and its satellites to extragalactic systems, provide reasonable consistency in results. In a recent review article, Krumholz et al. (2019) conclude that the preponderance of the current observational evidence favors $\epsilon_{\rm ff} \approx 0.01$ for regions $\gtrsim 1$ pc in size with small dispersion and systematic uncertainty.

The observed value of $\epsilon_{\rm ff}$ is surprisingly low. A number of authors have proposed theoretical models aiming at explaining this low $\epsilon_{\rm ff}$. Earlier models propose magnetic regulation as the reason. Recent measurements of magnetic fields have shown that they are too weak to support the gas (Crutcher, 2012). The unbound cloud models propose that $\epsilon_{\rm ff}$ is low because most of the materials observationally defined as molecular clouds are not actually self-gravitating. However, this hypothesis does not explain the YSO counting studies where the gas is almost certainly bound (Kauffmann et al., 2013). Consequently, attention has been focused on two possibilities: turbulence support and feedback regulation.

There is considerable evidence that GMCs obey the relations discovered by Larson (1981): the 1D velocity dispersion, σ, is supersonic and varies with the size as $\sigma \propto L^p$, where $p \approx 0.5$ in the Milky Way. At a randomly chosen subregion of a cloud, the binding energy per unit mass of a region of mass M scales as $GM/R \propto R^2$, assuming a mean density, while its kinetic energy per unit mass scales as $\sigma^2 \propto R$, therefore the virial ratio obeys $\alpha_{\rm vir} \propto 1/R$. A virial parameter, or virial ratio, is defined as the ratio of the total kinetic energy to the gravitational energy of a dynamical system, $\alpha_{\rm vir} \equiv 2\mathcal{K}/|\mathcal{W}|$, where the numerical coefficient is chosen so that $\alpha_{\rm vir} = 1$ indicates virial equilibrium ($\mathcal{W} = -2\mathcal{K}$), and $\alpha_{\rm vir} > 1$ ($\alpha_{\rm vir} < 1$) means unbound (bound)[1]. Most regions smaller than the size of the cloud are unbound (Krumholz & McKee, 2005). Numerous recent works have focused on modeling the density PDF and the evolution of the self-gravitating parts of a cloud with increasing accuracy (e.g. Hennebelle & Chabrier, 2011). The consensus of these models is that turbulence does substantially reduce $\epsilon_{\rm ff}$ but not to $\epsilon_{\rm ff} \approx 0.01$ as required by observations.

The density PDF of a self-gravitating cloud deviates and develops a prominent power-law tail on its high-density end that causes $\epsilon_{\rm ff}$ to rise with time. This density build-up is likely to be counterbalanced by feedback processes that break up high-density clumps. Recently, Grudić et al. (2018) propose that cloud disruption by stellar feedback is so fast and efficient that a typical cloud never has time to develop power-law tails substantial enough to bring $\epsilon_{\rm ff}$ to large values.

However, the nature and existence of turbulence in molecular clouds are still not well understood. There is considerable debate in the literature between the turbulent theory and the theory of coherent gravitational collapse (Heitsch et al., 2009). Although there is significant evidence from analytic theories (Klessen & Hennebelle, 2010), numerical simulations (e.g. Robertson & Goldreich, 2012), and kinematic measurements with *Gaia* that accretion flows inevitably drive turbulence, the question of the low value of $\epsilon_{\rm ff}$ is still unsettled.

[1]Note that there is another definition commonly used in the literature where $\alpha_{\rm vir} \equiv \mathcal{K}/|\mathcal{W}|$ and $\alpha_{\rm vir} = 0.5$ indicates virial equilibrium.

1.1.2 Initial Mass Function

Zooming in even further from star-forming molecular clouds, we reach the scale of individual stars. One of the properties of stars that is important for determining their observable characteristics and evolutionary path is their mass. The distribution of stellar masses *at birth* is known as the initial mass function (IMF). Almost all inferences of light or physical properties for unresolved stellar populations, as well as most models of galaxy formation, rely on an assumed form of the IMF.

The first attempts to measure the IMF were carried out by Salpeter (1955), using stars in the Solar neighborhood. Observations using the field star, young cluster, and globular cluster methods all appear to produce roughly consistent results. Current evidence suggests that the IMF appears to be quite universal in many locations throughout the Milky Way, with the possible exception of star clusters formed very near the Galactic Center. The IMF has a distinct peak in the mass range $0.1 - 1 \mathrm{M}_\odot$ and falls off as a powerlaw $dN/dm \propto m^{-\alpha}$ at higher masses, with $\alpha \approx 2.35$, the value originally determined by Salpeter (1955). A widely-used functional representation of the IMF is a two-piece powerlaw given by Kroupa (2002):

$$\Phi(m) = \frac{dN}{d\log m} \propto \begin{cases} m^{-(\alpha_1 - 1)} & (m_0 < m < m_1) \\ k\, m^{-(\alpha_2 - 1)} & (m > m_1) \end{cases} \tag{1.2}$$

with $m_0 = 0.08\ \mathrm{M}_\odot$, $m_1 = 0.5\ \mathrm{M}_\odot$, $\alpha_1 = 1.3$, $\alpha_2 = 2.3$, and $k = 0.5$ (to guarantee continuity across the powerlaw break). A large uncertainty is in the brown dwarf regime below $0.08\ \mathrm{M}_\odot$, where there is a clear fall-off from the peak, but its exact functional form is poorly determined.

There may also be an upper cutoff between 100 and 150 $M_\odot$ (Figer, 2005), although whether this is an aspect of star formation or a result of a sharp increase in instability and mass loss is undetermined (Tan et al., 2014).

Various theoretical models have been constructed to explain the universality of the IMF based on gravoturbulent fragmentation of the host cloud (Padoan et al., 1997; Padoan & Nordlund, 2002; Mac Low & Klessen, 2004; Hennebelle & Chabrier, 2008; Hopkins, 2012a). Early pioneering numerical simulations with pure hydrodynamics and gravity based on this model do sometimes return a mass distribution that looks much like the empirical IMF, as illustrated in Figure 1.1. However, this is largely depending on the choice of initial conditions. Simulations that start with more realistic initial conditions, namely with turbulent density structures or with supervirial/subvirial initial state, do not appear to collapse as predicted by the empirical IMF (e.g., Clark et al., 2008). Besides, they were often limited in terms of statistics, resolution, or cloud size.

More recent work, with increasing computing power, provided more reliable statistics and IMF distributions (e.g., Bonnell et al., 2011; Girichidis et al., 2011; Krumholz et al., 2011; Bate, 2012; Ballesteros-Paredes et al., 2015). Furthermore, radiative stellar feedback has been invoked to explain the precise shape of the IMF, using both simulations (e.g., Bate, 2009a; Krumholz et al., 2011; Gavagnin et al., 2017) and analytic models (e.g., Guszejnov & Hopkins, 2016). The core idea is that radiative feedback shuts off fragmentation at a characteristic mass scale that sets the peak of the IMF. Simulations including radiation seem to support the idea that stellar feedback can pick out a characteristic peak mass. However, the limitation of this hypothesis is that it has little to say about the powerlaw tail of the IMF. Indeed, by sacrificing resolution, Gavagnin et al. (2017) captured a large number of massive stars, which emit large quantities of

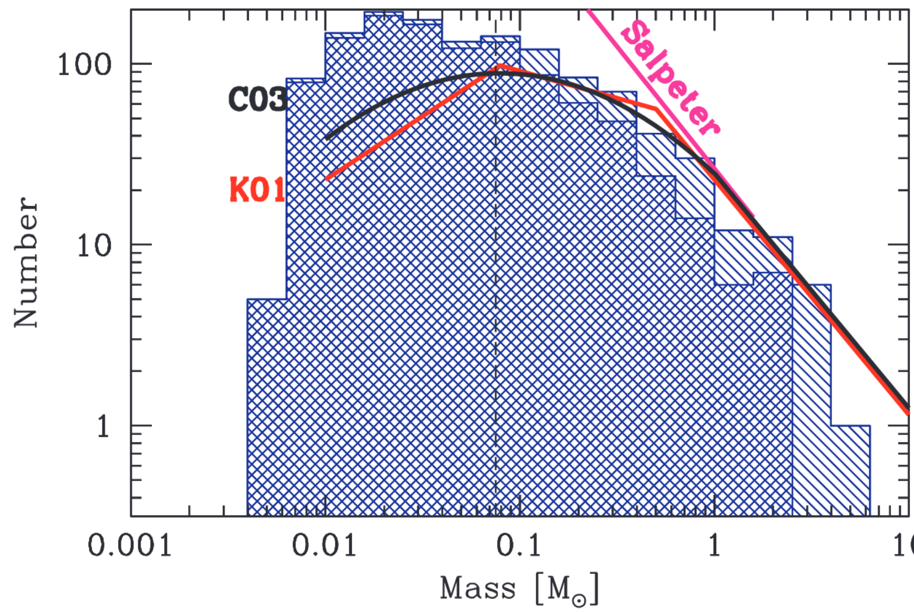

Figure 1.1: The IMF measured in a radiation-hydrodynamic simulation of the collapse of a $500 - M_\odot$ cloud with uniform initial density. The single-hashed region gives all objects, while the double-hashed region gives those that have stopped accreting. Credit: Bate (2009b).

ionizing radiation, and argued that this alters the high mass end of the IMF. So far no radiation-MHD simulation has managed to follow the evolution of a cloud with realistic size and resolve the formation of individual high- and low-mass stars that match the empirical IMF.

1.1.3 Magnetic field and the magnetic braking problem

Molecular clouds are observed to be permeated by magnetic fields (Crutcher, 1999; Lee et al., 2017). Observers use the Zeeman effect to measure magnetic fields in GMCs and find strengths ranging from tens to thousands of μG, with higher-density gas generally showing stronger fields. For a low-density envelope of a GMC with $n \sim 100\ \mathrm{cm}^{-3}$ ($\rho \sim 10^{-22}\mathrm{g\,cm}^{-3}$), the typical dynamic velocity $v \sim$ a few $\mathrm{km\,s}^{-1}$, giving a kinetic energy density

$$e_K = \frac{1}{2}\rho v^2 \sim 10^{-11}\ \mathrm{erg\,cm}^{-3}. \tag{1.3}$$

With a magnetic field strength of 20 μG, typical of molecular clouds on large scales, the energy density is

$$e_B = \frac{B^2}{8\pi} \sim 10^{-11}\,\mathrm{erg\,cm^{-3}}, \tag{1.4}$$

comparable to the kinetic energy density. Therefore, the magnetic field is dynamically significant in the flow of gas.

The strong magnetic field in high-density prestellar cores can in principle strongly affect the evolution of angular momentum during the core collapse. The twisting of the magnetic field lines produced by disk rotation in the flux-freezing regime of ideal magnetohydrodynamics (MHD), can apply a force counter to the rotation velocity, also known as *magnetic braking*, effectively slowing down rotation and increasing radial gas infall. In idealized numerical MHD simulations, the timescale of the braking can become so short that protostellar disks fail to form or are much smaller than the observed sizes, a phenomenon known as the "magnetic braking catastrophe" in the theoretical literature of disk formation (e.g. Allen et al., 2003; Galli et al., 2006; Hennebelle & Fromang, 2008; Li et al., 2014). What is the minimum required magnetic field strength so that magnetic braking significantly affects disk formation?

To answer this question, let us first examine how magnetic fields affect the collapse of a molecular cloud. Magnetic fields support charged gas against gravitational collapse. A common characterization of the relative importance of the gravitational and magnetic forces in a molecular cloud or core is the normalized mass-to-flux ratio,

$$\mu \equiv \frac{M/\Phi_B}{M_\Phi/\Phi_B} = \frac{M}{M_\Phi}, \tag{1.5}$$

where M is the total mass contained within a spherical region of radius R, $\Phi_B = \pi R^2 B$ is the magnetic flux threading the surface of the sphere assuming a uniform magnetic field strength B, and

$$M_\Phi = c_\Phi \frac{\Phi_B}{\sqrt{G}} \tag{1.6}$$

is the magnetic critical mass, the mass at which the magnetic and gravitational forces balance each other. The constant c_Φ is a dimensionless coefficient that depends on the assumed geometry of the system. For a spherical cloud of uniform density, $c_\Phi = \sqrt{10}/(6\pi) = 0.168$. Note that the definition of the normalized mass-to-flux ratio μ is simplified here because the critical value depends on the geometry of the gas and the magnetic fields.

In a sub-critical cloud (defined as a cloud with $\mu < 1$), the magnetic field should prevent the collapse of the cloud core altogether. Analytical predictions (Joos et al., 2012) suggest that there are no centrifugally-supported disks in models with $\mu \leq 10$, although there are disk-like over-densities of gas in which the magnetic fields, rather than the centripetal force, support the gas against collapse in the radial direction. Observations suggest typical values of $\mu \approx 2 - 10$ in molecular cloud cores (e.g. Crutcher, 1999; Bourke et al., 2001), and this value could be even smaller after correcting for projection effects (Li et al., 2013). Theoretically, disk formation should be completely suppressed in the strict ideal MHD limit for the level of core magnetization deduced from observation – analytic study and numerical simulations have shown that the angular momentum of the idealized collapsing core is nearly completely removed by magnetic braking close to the central object (*e.g.*, Mestel & Spitzer, 1956; Mellon & Li, 2008).

However, these results seem to be in contrast to recent high-resolution observations revealing the existence of Keplerian disks around Class 0 protostellar objects (e.g. Tobin et al., 2012;

Codella et al., 2014; Lee et al., 2017; Johnston et al., 2020). How the catastrophe is averted for disk formation is still a question under debate. Recent studies have revealed that the catastrophe can be avoided if the magnetic field and the rotation axis are not aligned (Joos et al., 2012; Gray et al., 2018), the magnetic field is diffused by turbulent velocity field (Santos-Lima et al., 2012; Joos et al., 2013), or the magnetic field is less coherent (Seifried et al., 2013). However, these results largely depend on the choice of artificial initial conditions and fall short on explaining the existence of large (> 1000 AU) disks revealed by recent radio/mm and optical/IR observations (van Kempen et al., 2012; Takahashi et al., 2012; Johnston et al., 2015, 2020). This motivates the work presented in Chapter 5.

1.2 Epoch of Reionization

The epoch of reionization (EoR) is a period in the early universe when the first stars and galaxies formed and began to emit ultraviolet radiation. This radiation ionized the neutral hydrogen atoms that filled the universe, marking the transition from the "Dark Ages" to the "Cosmic Dawn". Cosmic reionization involves the coupling of galaxy formation with the physics of gravity and radiation transfer to produce a global phase transition of ionization, making for a complex problem.

Ionization occurs when photons with energies $E \geq I_H = 13.6$ eV, a.k.a. ionizing photons, or Lyman-continuum (LyC) photons, interact with neutral hydrogen atoms. The radiation from luminous objects will ionize the surrounding IGM once it escapes from its host galaxies. This ionized IGM is known as cosmological H II regions. Recombination occurs when the Coulomb force attracts protons and electrons, which is efficient at temperatures $T \lesssim 10^4$ K. In regions with ionizing radiation, the gas approaches ionization equilibrium when the recombination rate equals the ionization rate. The recombination rate is proportional to the product of the number density of protons and electrons, $n_e n_p$.

The H II regions then evolve. The ionizing photons in a radial direction penetrate until all of them are absorbed by newly recombined atoms inside the H II region and there is no more flux left at the ionization front. The radius of the H II region at this initial stage is determined by the Stromgren radius R_s, by balancing the total number of ionizations and recombinations. At this stage, the H II region is heated to over $10,000$ K and is embraced by the cold ambient medium. The gas expands because it has higher pressure than its surroundings, and it transitions to the second intermediate stage after the time it takes a sound wave to cross the H II region. As the shock wave sweeps up most of the gas in its path and accumulates mass, the H II region expands and diffuses. Eventually, the H II region comes into pressure equilibrium with the ambient medium, and the ionization front stalls out at the final Stromgren radius. Any ionizing radiation that escapes from the galaxy creates a cosmological H II region, which is the building block of cosmic reionization.

What sources are responsible for producing the required ionizing radiation in the EoR? Although quasi-stellar objects (QSOs, or quasars) are some of the brightest objects in the Universe, the latest studies have shown that they only contribute $1-5\%$ of the UV photon budget at $z=6$ due to their low number densities (e.g. Willott et al., 2010). X-rays from compact binaries can penetrate much deeper into the IGM and create large partially ionized regions to a distance of 100 kpc with ionization fraction between 1% and 2% (Xu et al., 2014). However, observations (e.g. the Gunn–Peterson trough or Gunn-Peterson test) have shown that the universe is fully ionized (with a neutral fraction below 10^{-4}) at $z \sim 6$. Therefore, stellar radiation from galaxies must be the dominant source of radiation responsible for cosmic reionization. Two important questions that follow are (1) How abundant are galaxies as a function of luminosity and redshift? (2) What fraction of ionizing photons escaped from theses galaxies into the IGM?

Recent observations have provided valuable constraints on the nature of the first galaxies and their role in the EoR. The Hubble Space Telescope *Ultra Deep Field* (Ellis et al., 2013) and *Frontier Fields* (Coe et al., 2015) projects probe galaxies with stellar masses as small as $10^7\,\mathrm{M}_\odot$ at $z \gtrsim 6$ and galaxies as early as $z \gtrsim 11$. There could be an unseen population of even fainter and more abundant galaxies that may eventually be detected by JWST.

In the calculations of reionization, the key quantity is the ionizing emissivity, ρ_γ (in units of $\mathrm{erg\,s^{-1}\,Hz^{-1}\,Mpc^{-3}}$). The intrinsic ionizing emissivity can be inferred by integrating the product of the luminosity function $\phi(L)$ and star formation rate (SFR), given a relation between total luminosity L and SFR. To get ρ_γ, we need another parameter, namely the fraction of ionizing photons that escape into IGM, f_esc. It is arguably the most uncertain parameter in the models of reionization.

By measuring the hydrogen ionizing photon budget and constraining the best-fit Schechter parameters for the galactic luminosity function, Ouchi et al. (2009) suggests that galaxies at $z = 7$ need large f_esc ($\gtrsim 0.2$) to keep the universe ionized. Khaire et al. (2016) use cosmological radiation simulations and find that the updated QSO emissivity and star formation history have similar implications on the f_esc at $z > 5.5$. This value is too large with respect to what is observed in local galaxies.

A number of attempts have been made to calculate the escape fraction of hydrogen LyC photons from galaxies using analytic models and simulations of galaxy formation (Ricotti & Shull, 2000; Gnedin et al., 2008; Wise et al., 2014; Ma et al., 2015; Xu et al., 2016). However, because of the complexity of the problem and the uncertainty about the properties of the sources of reionization, the results are inconclusive. Furthermore, any realistic theoretical estimate of $f_{\rm esc}$ must take into account the escape fraction of LyC radiation from the molecular clouds in which the stars are born, $\langle f_{\rm esc}^{\rm MC} \rangle$, a sub-grid parameter in galaxy-scale and in cosmological-scale simulations.

Typically $\langle f_{\rm esc}^{\rm MC} \rangle$ is set to unity in these simulations, which could dramatically overpredict the galactic $f_{\rm esc}$ (Ma et al., 2015). Observational constraints of $\langle f_{\rm esc}^{\rm MC} \rangle$ are very limited and suffer from significant uncertainty (Doran et al., 2013). Therefore, a calculation of $\langle f_{\rm esc}^{\rm MC} \rangle$ from simulations of star formation from molecular clouds is essential to the understanding of the EoR, which is the motivation of the work presented in Chapter 3.

1.3 Techniques for Simulating Star Formation

The analytic theory is essential for understanding the big picture for star formation, but only numerical models can capture the nonlinear behaviors of the turbulent collapse of a GMC and take into account the effects of magnetic fields. On this scale, fluid dynamics and gas cooling play a dominant role in structure evolution. The complexity of hydrodynamic processes such as shock heating, atomic radiation cooling, and star formation requires an accurate treatment of the gas and radiation components.

For the sake of completeness, we give a short discussion of the MHD equations. The standard form of the ideal MHD equations is

$$\frac{\partial \rho}{\partial t} + \boldsymbol{\nabla} \cdot (\rho \boldsymbol{v}) = 0, \tag{1.7}$$

$$\rho \left[\frac{\partial \boldsymbol{v}}{\partial t} + (\boldsymbol{v} \cdot \boldsymbol{\nabla}) \boldsymbol{v} \right] = -\boldsymbol{\nabla} P + \frac{(\boldsymbol{\nabla} \times \boldsymbol{B}) \times \boldsymbol{B}}{4\pi}, \tag{1.8}$$

$$\rho \left[\frac{\partial e}{\partial t} + (\boldsymbol{v} \cdot \boldsymbol{\nabla}) e \right] = -P(\boldsymbol{\nabla} \cdot \boldsymbol{v}) - \rho \mathcal{L}, \tag{1.9}$$

$$\frac{\partial \boldsymbol{B}}{\partial t} = \boldsymbol{\nabla} \times (\boldsymbol{v} \times \boldsymbol{B}), \tag{1.10}$$

where ρ is the mass density, $\boldsymbol{v}$ is the fluid velocity, e is the specific total energy, and $\mathcal{L}$ represents the net loss function that describes the radiative heating and cooling of the gas. To close the system of equations, we must complement it with an equation of state. For the ISM, a perfect gas is a good assumption, with $P = (\gamma - 1)\rho\epsilon$, where γ is the adiabatic index and ϵ is the specific energy excluding kinetic energy of the gas.

To get a better physical understanding of the MHD equations and the role of magnetic fields, we write the Lorentz force as

$$\boldsymbol{f}_L = \frac{(\boldsymbol{\nabla} \times \boldsymbol{B}) \times \boldsymbol{B}}{4\pi} = -\boldsymbol{\nabla} \left(\frac{B^2}{8\pi} \right) + \frac{(\boldsymbol{B} \cdot \boldsymbol{\nabla}) \boldsymbol{B}}{4\pi}. \tag{1.11}$$

The first term is the magnetic pressure gradient and the second term is called the magnetic tension.

In computational astrophysics, two main techniques are employed to solve hydrodynamical equations: smoothed-particle hydrodynamics (SPH) and grid-based methods. The fundamental difference is how the fluid is discretized. An SPH solver divides fluid into mass elements (particles), whose evolution is then followed, in line with the Lagrangian approach. Grid methods, however, subdivide the computational domain into volume elements (cells) that are fixed in space, following the Eulerian formulation of hydrodynamics.

The natural outcome of an SPH code is it automatically adapts the numerical resolution in dense regions, with more particles concentrated in those areas, which makes it a valid tool in situations with large density contrasts such as self-gravitating fluids. Grid-based methods can increase their spatial resolution using the adaptive mesh refinement (AMR) technique, introducing new grid elements from the partition of a cell into smaller cells triggered by some specified refinement criteria.

RAMSES (Teyssier, 2002) is a massively parallel grid-based adaptive mesh refinement code, originally developed to study the co-evolution of dark matter and gas in a cosmological context. RAMSES is now a complete tool for simulations of self-gravitating fluid dynamics, equipped with a magneto-hydrodynamic (MHD) solver (Fromang et al., 2006) and several modules which implement AGN feedback, star formation recipes (Bleuler & Teyssier, 2014), interstellar medium cooling functions, and stellar feedback (Rosdahl et al., 2013; Rosdahl & Teyssier, 2015). More physics including stellar evolution, photoionized metal chemistry, and dust dynamics are recently implemented (Geen et al., 2021; Katz, 2022; Moseley et al., 2023).

The AMR structure implemented in RAMSES is tree-based. Every cell can be refined into 2^{dim} child cells called *octs*. Each oct at refinement level l points to all the child cells in the next refinement level $(l+1)$, its parent cell in level $l-1$, and all the sibling cells of the parent cell. A cell can be refined according to several criteria of the user's choice. The refinement criteria used in this thesis work is the Jeans length criteria, stating that the local Jeans length must be resolved by at least N_s cells, where $N_s = 10$.

The formation of stars is modeled with sink particles, following the implementation of Bleuler & Teyssier (2014). When the density is higher than a certain value, the Jeans length criterion (with a smaller N_s) is violated at the highest refinement level and the high-density peak is replaced with a sink particle. Sink particles are allowed to merge and accrete gas according to different merging or accretion schemes (threshold, Bondi, flux). The dynamical interaction between sinks can be computed using direct summation and the force between a sink and gas can be computed using the same technique used for other particles (particle-mesh method).

Rosdahl et al. (2013) have integrated radiation hydrodynamics into RAMSES by enclosing the radiation transfer (RT) equations using the M1 approximation of the Eddington tensor and then solving the differential equations using the first-order Godunov scheme. This moment-based approach has the advantage of being independent of the number of radiative sources and is much more computationally efficient compared to ray-tracing techniques.

Combining all these techniques presented above, RAMSES-RT has become a highly sophisticated and powerful tool in the field of computational astrophysics for cosmological simulations as well as small-scale star formation simulations.

1.4 Thesis Outline

This thesis investigates star formation processes from GMC to protostellar disk scales. In Chapter 2, I explore the physics and laws of star formation from molecular clouds based on a set of radiation-MHD simulations. Next, I postprocess the simulation data and calculate the escape of LyC photons from GMCs into the intercloud medium that takes into account contributions from spatially resolved stars. This part is reported in Chapter 3. In Chapter 4, I investigate the fragmentation of massive prestellar cores and the formation of circumstellar disks using a series of extremely high-resolution simulations of prestellar cores. Then, in Chapter 5, I explore the magnetic braking problem in disk formation and propose a solution to the "magnetic braking catastrophe". As part of an ongoing project on stellar dynamics, I study star clustering by quantifying the clumpiness of the stars using the two-point correlation function $\xi(r)$ in Chapter 6. Finally, in Chapter 7, I summarize the main conclusions and introduce future research directions building on the work presented in this thesis.

1.5 A summary of software and facilities

Computational resources used in this dissertation:

1. The Deepthought2 HPC cluster of the University of Maryland supercomputing resources[2]
2. The Yorp Cluster of the Department of Astronomy, University of Maryland[3]
3. Student workstations of the Department of Astronomy, University of Maryland[4]

Software/codes used:

1. RAMSES-RT (Teyssier, 2002; Bleuler & Teyssier, 2014; Rosdahl et al., 2013)
2. NUMPY (van der Walt et al., 2011), MATPLOTLIB (Hunter, 2007), and YT (Turk et al., 2011)
3. RAMTOOLS[5]
4. HEALPIX[6] (Zonca et al., 2019), HEALPY (Górski et al., 2005)

[2] http://hpcc.umd.edu
[3] https://www.astro.umd.edu/twiki/bin/view/AstroUMD/YorpCluster
[4] https://www.astro.umd.edu/twiki/bin/view/AstroUMD/StudentWorkstations
[5] https://chongchonghe.github.io/ramtools-pages/
[6] http://healpix.sf.net

Chapter 2: Simulating Star Clusters Across Cosmic Time: I. Initial Mass Function, Star Formation Rates and Efficiencies

In this chapter, we present radiation-magneto-hydrodynamic simulations of star formation in self-gravitating, turbulent molecular clouds, modeling the formation of individual massive stars, including their UV radiation feedback. The set of simulations have cloud masses between $m_{\rm gas} = 10^3$ M$_\odot$ to 3×10^5 M$_\odot$ and gas densities typical of clouds in the local universe ($\overline{n}_{\rm gas} \sim 1.8 \times 10^2$ cm^{-3}) and 10$\times$ and 100$\times$ denser, expected to exist in high-redshift galaxies. The main results are: *i*) The observed Salpeter power-law slope and normalisation of the stellar initial mass function at the high-mass end can be reproduced if we assume that each star-forming gas clump (sink particle) fragments into stars producing on average a maximum stellar mass about 40% of the mass of the sink particle, while the remaining 60% is distributed into smaller mass stars. Assuming that the sinks fragment according to a power-law mass function flatter than Salpeter, with log-slope 0.8, satisfies this empirical prescription. *ii*) The star formation law that best describes our set of simulations is $d\rho_*/dt \propto \rho_{gas}^{1.5}$ if $\overline{n}_{gas} < n_{cri} \approx 10^3$ cm^{-3}, and $d\rho_*/dt \propto \rho_{\rm gas}^{2.5}$ otherwise. The duration of the star formation episode is roughly 6 cloud sound crossing times (with $c_s = 10$ km/s). *iii*) The total star formation efficiency in the cloud is $f_* = 2\%(m_{\rm gas}/10^4\ M_\odot)^{0.4}(1+\overline{n}_{\rm gas}/n_{\rm cri})^{0.91}$, for gas at solar metallicity, while for metallicity $Z < 0.1$ Z$_\odot$, based on our limited sample, f_* is reduced by a factor of ~ 5. *iv)* The most compact and massive clouds appear to form globular cluster progenitors, in the sense that star clusters remain gravitationally bound after the gas has been expelled.

2.1 Introduction

Star formation in galaxies is a complex and only partially understood astrophysical phenomenon. It is difficult to formulate a general theory in part because of the wide range of scales and of physical processes involved. From an observational point of view, quantifying star formation efficiency (SFE) in nearby molecular clouds has been the focus of much recent research (e.g., Lada et al., 2010; Heiderman et al., 2010; Gutermuth et al., 2011). A power-law relationship between the gas surface density of galaxies and their star formation rate (SFR) was first proposed by Schmidt (1959) and later tested by large, multi-galaxy data (Kennicutt, 1998). This relationship has been widely used in cosmological simulations of galaxy formation. However, on sub-galactic scales the dispersion of star formation rates for a given gas surface density of H I is large, and other parameters such as gas metallicity (Bolatto et al., 2011; Krumholz, 2013) and stellar surface density (Leroy et al., 2008) appear to become important. As the resolution of surveys improved, numerous studies have shown that star formation on kpc scales is more strongly correlated with H_2 surface density (e.g. Krumholz, 2014) rather than atomic gas. Therefore, modern cosmological simulations of galaxy formation aim at reproducing the molecular phase of the interstellar medium (ISM) and adopt an empirical sub-grid recipe for star formation within partially resolved molecular clouds of the form $\dot{\rho}_* \propto \rho_{H_2}^n$, where typically $n = 1$ or 1.5. The molecular phase of the ISM is treated in simulations using different prescriptions: Robertson & Kravtsov (2008) precomputed a grid of models from a photo-chemistry code, Gnedin et al. (2009) directly solved the formation and dissociation equations for H_2, but with an increased formation rate to model unresolved clumping, and Kuhlen et al. (2012) used an analytic model to estimate the equilibrium H_2 abundance. The sub-grid recipe (with grid maximum resolution typically between few parsecs to few kpc) is calibrated to reproduce observational data in galaxies at $z = 0$.

However, the conditions in the ISM of high-redshift galaxies are likely different to those found in the present day. Krumholz et al. (2012) argue that the SFR is in fact correlated to the local free-fall time set by the gas density, not to the column density. Simulations show that densities and pressures of star-forming regions in high-redshift galaxies are much higher than in today's ISM (e.g., Ricotti, 2002; Wise et al., 2014; Ricotti, 2016). Using Adaptive Mesh Refinement (AMR) simulations of the first stars and galaxies with parsec-resolution, Ricotti et al. (2016) found that compact molecular clouds in primordial galaxies can either form gravitationally bound star clusters that resemble the progenitors of today's globular clusters (GC)[1], or the clusters may disperse and fill up a large fraction of the dark matter halo of primordial dwarf galaxies. In this second case the stars would appear as spheroids 20-200 pc in radius, dark matter dominated and with very low surface brightness. These objects would be identified today as "ultra-faint" dwarf galaxies observed in the Local Group (*e.g.*, Willman et al., 2005; Zucker et al., 2006a,b; Belokurov et al., 2007; Walsh et al., 2007; Majewski et al., 2007; Martin et al., 2009). Star formation in compact star clusters appears to be especially important, even perhaps the dominant mode of star formation at high-redshift. Thus, in order to make progress in understanding the formation of the first dwarf galaxies and the sources of reionisation, it is important to focus on understanding the small-scale physics of this process, which is poorly resolved in cosmological

[1]The compact bound stellar objects found in the simulations are actually not only globular cluster progenitors, but also ultra-compact dwarfs and dwarf-globular transition objects, depending on whether the stellar cluster forms at the center of the halo, in the disk's spiral arms, or even in satellite minihalos.

simulations.

Most numerical work on star formation in molecular clouds focuses on star formation in the local universe, aiming at explaining observed young star forming regions. In this chapter we analyse the results of a large grid of simulations of realistic molecular clouds with initial conditions chosen to reproduce not only local molecular clouds but also clouds that form in higher density and pressure environments, typical of star formation in high redshift galaxies. We vary the masses of the clouds, their compactness (central density), and in few cases explore the effect of changing the gas metallicity and therefore the gas cooling function.

The motivation for this chapter is twofold. The first goal is to deepen our understanding of the physics of star formation in high-pressure environments to justify and inform the sub-grid star formation recipe used in cosmological simulations. A closely related important question in Near Field Cosmology is: how does the formation of self-gravitating bound star-clusters relate to the star formation efficiency, compactness, mass and gas metallicity of molecular clouds found in cosmological simulations? We will only touch on this questions in the present chapter, but more detailed work will be presented in a followup work.

The second goal is to estimate the escape fraction of H I ionising radiation from molecular clouds as a function of cloud compactness and mass. This is the first necessary step for a realistic estimate of the escape fraction from galaxies. Ricotti (2002) have shown that, if a non-negligible fraction of today's GCs formed at $z > 6$ with $\langle f_{\rm esc}^{\rm MC} \rangle \sim 1$, their progenitors would be a dominant source of ionising radiation during reionisation. Katz & Ricotti (2014) presented arguments in support of significant fraction of today's old GCs forming before the epoch of reionisation. However, although it is naively expected, it has not been shown with numerical simulations that $\langle f_{\rm esc}^{\rm MC} \rangle$ from GC progenitors forming in compact molecular clouds is higher than $\langle f_{\rm esc}^{\rm MC} \rangle$ in more diffuse clouds. The answer to this question and the contribution of compact star clusters to reionisation will be presented in the next chapter.

This chapter is organized as follows. In Section 2.1.1 we present a brief review of the current status of numerical simulations of star cluster formation. In Section 2.2 we provide an overview of our numerical methods, including details on the initial conditions of our simulations and the recipes for formation of sink particles and feedback. In Section 2.3 we present some results from the analysis of our large set of simulations with emphasis on the stellar initial mass function (IMF) and the star formation rate (SFR) and efficiency (SFE). A summary and conclusions are presented in Section 2.4.

2.1.1 The IMF and SFE of Molecular Clouds

Simulations of molecular cloud dynamics are valuable tools in understanding the conditions in the ISM. Typically these simulations adopt idealized initial conditions similar to those in observed clouds: a gas cloud $\sim 1-10$ pc in size supported against gravity by a turbulent velocity field such that the initial virial ratio, *i.e.* the ratio of the kinetic energy to the potential energy of the cloud, is $\lesssim 0.5$. One model involves injecting turbulence into a volume of gas in the initial conditions and allowing it to decay over time. This can be done by either using smoothed particle hydrodynamics (SPH, e.g. Klessen, 2001; Bonnell et al., 2006) or grid-based methods (e.g., Gammie et al., 2003). Another model involves adding turbulence continuously over time, simulating the effect of momentum injection from outside flows or energy from massive stars inside the cloud (Vazquez-Semadeni et al., 1997; Ballesteros-Paredes et al., 2006; Padoan et al., 2007). Many of these models adopted an isothermal equation of state, while others have included self-consistent cooling and heating functions (e.g. Koyama & Inutsuka, 2004; Audit & Hennebelle, 2005) and molecular chemistry (e.g. Glover et al., 2010).

The fragmentation of molecular clouds into stars is a long-standing problem. Observational studies (Salpeter, 1955; Kroupa, 2002; Chabrier, 2005) have found that the masses of stars follow a "Initial Mass Function" (IMF) with a power law $\mathrm{d}N/\,\mathrm{d}\log M \propto M^{-\Gamma}$ at the high-mass end (Salpeter 1955 calculate $\Gamma \approx 1.35$). Various theoretical models have been constructed to explain this (Padoan & Nordlund, 2002; Mac Low & Klessen, 2004; Hennebelle & Chabrier, 2008; Hopkins, 2012a) based on gravoturbulent fragmentation of the host cloud. Radiative stellar feedback has been invoked to explain the precise shape of the IMF, using both simulations (e.g., Bate, 2009b) and analytic models (e.g., Guszejnov & Hopkins, 2016). Early pioneering simulations of cluster formation approached the problem of producing a well-defined IMF (e.g., Bate et al., 2003; Bate & Bonnell, 2005; Klessen et al., 2008; Offner et al., 2008), but were often limited in terms of statistics or resolution. More recent work, with increasing computing power, provided more reliable statistics and IMF distributions (e.g., Bonnell et al., 2003; Bate, 2009b; Bonnell et al., 2011; Girichidis et al., 2011; Krumholz et al., 2011; Bate, 2012; Ballesteros-Paredes et al., 2015).

Simulations attempting to capture the stellar IMF require a high dynamic range to resolve both brown dwarfs and OB stars. Most recently, Bate (2019) resolve in detail the mass spectrum of brown dwarfs while only producing stars of up to 3 $\mathrm{M}_{\odot}$, finding that low metallicities do not produce observable differences in the stellar IMF, while increasing fragmentation. Gavagnin et al. (2017) have lower mass resolution but capture more massive stars that emit significant quantities of ionising radiation, arguing that this alters the high mass end of the IMF. In the absence of radiation and cooling, Lee & Hennebelle (2018b) and Lee & Hennebelle (2018a) study the early formation of protostellar Larson cores, and find that the choice of equation of state (eos) has a strong influence on the peak of the IMF. In general, these works are relatively successful at reproducing not only the IMF but also stellar multiplicity and separation.

Previous authors have included ideal MHD in their simulations (Myers et al., 2013; Krumholz et al., 2016; Cunningham et al., 2018). However, since these authors only form stars up to $\sim$20 $\mathrm{M}_{\odot}$, they neglect ionising radiation. Non-ideal MHD effects, while challenging to include in resolving the IMF for reasons of computational cost, appear to affect the dynamics of protostar formation on small scales (Masson et al., 2016; Vaytet et al., 2018). The physics that shapes the IMF is complex, and a full treatment that covers non-ideal MHD, both low and high energy radiation, chemistry and the full mass range of stars remains difficult with modern computational resources.

As well as the stellar IMF, an important consideration is how many stars are formed out of a given mass of gas, or the Star Formation Efficiency (SFE). The efficiency of conversion of gas into stars is typically much lower than 100% since energetic processes from massive stars are able to disperse the cloud in which a star cluster forms before all of the gas collapses into protostars. These processes are widely termed “feedback” (see review by Dale et al., 2015). Recent work favours ionising radiation as the main driver of molecular cloud dispersal (Dale et al., 2005; Gritschneder et al., 2009; Peters et al., 2010; Walch et al., 2012; Dale et al., 2012), as opposed to other effects such as stellar winds (Dale et al., 2014), although Howard et al. (2016) find that UV photoionisation has little effect on the initial evolution of the SFE.

The relationship between gas properties and the SFE is a matter of ongoing study. Lada et al. (2010) and Heiderman et al. (2010) argue for a constant ratio between SFE and cloud mass for gas above a certain surface density, although this is still subject to discussion (Gutermuth et al., 2011; Hony et al., 2015). There is no clear theoretical link between the SFE and projected column density, although Clark & Glover (2014) argue that there may be a link between the observed column density and the local density around the star. Geen et al. (2017) reproduce the SFE observed by Lada et al. (2010), although they find that the result is likely to be dependent on the average density of the neutral gas in the cloud. These simulations produce similar results to the simulations of Colin et al. (2013). Geen et al. (2018) finds that SFE can change by up to a factor of 4 by varying the initial velocity field of the cloud and the stellar IMF, although relationships can be found between the early cloud state and the final SFE. Semi-analytic models by Vázquez-Semadeni et al. (2018) also find considerable scatter in the SFE.

2.2 Numerical Simulations and Methods

We conduct our numerical simulations using the AMR radiative magneto-hydrodynamical code RAMSES (Teyssier, 2002; Bleuler & Teyssier, 2014). Radiative transfer is implemented using a first-order moment method with M1 closure described in Rosdahl et al. (2013). Kim et al. (2017) demonstrates that M1 closure method is inaccurate near sources only in regions where the flux is about an order of magnitude smaller than the mean value (due to shielding), while it agrees with adaptive ray-tracing methods (*e.g.*, Wise et al., 2014; Hartley & Ricotti, 2016) both at larger distances from individual sources and on global scales. M1 closure, however, is significantly more computationally efficient than ray-tracing methods. The ionising photons interact with neutral gas and we track the ionisation state and cooling/heating processed of hydrogen and helium (see Geen et al., 2017, for details). Our simulations include magnetic fields in the initial conditions, but we do not include the chemistry of molecular species (*i.e.*, formation/dissociation). 3-D ‘zoom-in’ simulations of the chemical evolution of molecular clouds suggest that, for gas at solar metallicity, the cloud is almost fully molecular with H_2 fractions around 0.9 in the later stages of transition to dense molecular phase (Seifried et al., 2017).

We simulate a set of isolated and turbulent molecular clouds that collapse due to their own gravity. We explore a grid of simulations varying the initial gas mass and compactness (*i.e.*, the core density) of the clouds. In our simulations, dense proto-stellar cores collapsing below the resolution limit of the simulations produce sink particles. These sinks may represent single stars or multiple stars or even clusters of stars if the resolution is not sufficiently high. However, in all our simulations we aim at reproducing a realistic high-mass end of the stellar IMF and therefore realistic feedback from individual massive stars. To accomplish this goal, sink particles emit hydrogen and helium ionising photons according to their mass as described in § 2.2.3. The gas is ionised and heated by massive stars, producing over-pressurised bubbles that blow out the gas they encounter. In our simulations low mass stars and proto-stellar cores do not produce any feedback. In this work we do not include mechanical feedback from supernova (SN) explosions and from stellar winds and we also neglect the effect of radiation pressure from infrared radiation. However, with the exception of the two most massive clouds in the set of simulations representing today’s molecular clouds (the lowest density set), all the simulations stop forming stars before the explosion of the first SN. Therefore, neglecting SN feedback is well justified in these cases. We find that in all simulations star formation has ceased before $\sim 5 - 6\ t_{\rm ff}$, which is the typical time it takes for feedback to act. We stop simulations no earlier than this point. A few simulations are continued beyond this time. This does not have an effect on the IMF since the mass function of sink particles does not change after star formation has ceased.

For the simulations in the set in which SN explosions should occur while star formation is ongoing, in order to compensate for this missing feedback, we do not shut down UV radiation feedback from massive stars after the time the star should have exploded as SN. In the following sections we provide some more details on the simulations set up.

2.2.1 Initial Conditions

We run a grid of 14 simulations of clouds with a range of central densities and initial gas masses. We also run some additional simulations varying the initial gas metallicity and therefore the gas cooling function. The magnetic field strength in the initial conditions is set such that $v_a = 0.2\ \sigma_{3D}$, where v_a is Alfven wave velocity and σ_{3D} is the turbulence velocity dispersion. This ν_a is ~ 2 times smaller than that measured in a group of molecular clouds by Crutcher (2012) who finds $\nu_a \approx 0.5\sigma_{3D}$.

The clouds have initially a spherically symmetric structure with density profile of a non-singular isothermal sphere with core density $n_{\rm c}$. The cloud extends out to $r_{\rm gas} = 3r_{\rm c}$, where $r_{\rm c}$ is the core radius. Beyond $r_{\rm gas}$ the cloud is embedded in a uniform density envelope that extends to $6r_{\rm c}$ with a density $0.01\ n_{\rm c}$. Outside of the envelope the number density is constant at 1 cm^{-3}. The box length L_{box} is set to $48r_{\rm c}$ in each simulation. The initial value of the (isothermal) sound speed of the cloud is set to $c_{\rm s} = 0.24$ km/s, while the envelope and background densities are in pressure equilibrium.

The initial density profile is perturbed with a turbulent velocity field, analogously to the set up used in Geen et al. (2017). The initial turbulence of the clouds follows a Kolmogorov power spectrum with random phases and has an amplitude such that the cloud is approximately in virial equilibrium. All simulations have the same set of random phases. The initial cloud virial ratio

$$\alpha_{\rm vir} = \frac{5\sigma_{\rm 3D}^2 R}{3GM} \approx 0.4, \tag{2.1}$$

is kept constant in all the simulations. Therefore the ratio $t_{\rm ff}/t_{\rm turb}$, where $t_{\rm turb} \equiv R/\sigma_{\rm 3D}$ is kept constant in all the simulations. However, the sound crossing time $t_{\rm cr} \equiv R/c_s$, where throughout this chapter we assume $c_s = 10$ km/s, is not constant. The virial parameter, $\alpha_{\rm vir}$, is small enough to ensure collapse and fragmentation, but sufficiently large to prevent a rapid radial collapse of the cloud. Before allowing any star formation in the cloud we evolve these idealized initial conditions for $\sim 3t_{\rm ff}$, so that the turbulent velocities develop into density perturbations and the initial conditions relax into a quasi-equilibrium turbulent medium. If we do not allow the initial conditions to relax before forming stars, the stars form mostly near the center of the cloud during the transient relaxation phase.

Table 2.1: Initial conditions of our 16 simulations. (a) Mean number density of the cloud, excluding the envelope. The core density is ~ 5 times higher. (b) The global free-fall time of the cloud ($t_{ff} \equiv 3\sqrt{\frac{3\pi}{32G\rho_c}} \approx 1.3\sqrt{\frac{3\pi}{32G\bar{\rho}}}$). (c) Maximum level of refinement. (d) Initial cloud mass, excluding the envelope. (e) The name of each cloud used throughout the chapter. See Sec. 2.2.1 on how they are defined. (f) Initial cloud radius, excluding the envelope. (g) Maximum spatial resolution. (h) Density threshold for sink formation. (i) Jeans mass at the sink density threshold. (j) Turbulence Mach number. (k) Sound crossing time $r_{\rm gas}/c_s$ for $c_s = 10$ km/s. (l) Metallicity of the gas used in the cooling function, Z = [Fe/H]. (m) This setup has 2 extra simulations with lower metallicities besides one with same metallicity as all other ones. See Sec. 2.3.4. (x) The mean surface density in a square of the size of the cloud radius. (x) Escape velocity at the cloud radius of the initial cloud.

	$m_{\rm gas}(\mathrm{M_\odot})$	1.0×10^3	3.2×10^3	1.0×10^4	3.2×10^4	1.0×10^5	3.2×10^5
	Cloud Name		XS-F	S-F	M-F	L-F	XL-F
$\overline{n}_{\rm gas} = 1.8 \times 10^2\,\mathrm{cm^{-3}}$	$r_{\rm gas}$ (pc)		5.0	7.3	11	16	23
	Σ ($\mathrm{M_\odot\ pc^{-2}}$)		41	61	89	131	193
	v_{esc} (km/s)		2.3	3.4	5.1	7.4	11
	$\Delta x_{\rm min}$ (AU)		500	730	1100	1600	2300
$t_{\rm ff} = 4.4\,\mathrm{Myr}$	$n_{\rm sink}$ ($\mathrm{cm^{-3}}$)		1.2×10^7	5.6×10^6	2.6×10^6	1.2×10^6	5.6×10^5
	$M_{\rm J}$ ($M_\odot$)		0.3	0.4	0.6	0.9	1.3
$l_{\rm max} = 15$	$\mathcal{M}$		4.6	6.8	10	15	22
	$t_{\rm cr}$ (Myr)		0.5	0.7	1.1	1.5	2.3
	$Z/Z_\odot$		1	1	1	1	1
	Cloud Name		XS-C	S-C	M-C	L-C, L-C-lm, L-C-xlm	
$\overline{n}_{\rm gas} = 1.8 \times 10^3\,\mathrm{cm^{-3}}$	$r_{\rm gas}$		2.3	3.4	5.0	7.3	
	Σ		193	283	415	609	
	v_{esc}		3.4	5.1	7.4	11	
	$\Delta x_{\rm min}$		460	680	1000	1500	
$t_{\rm ff} = 1.4\,\mathrm{Myr}$	$n_{\rm sink}$		1.4×10^7	6.5×10^6	3.0×10^6	1.4×10^6	
	$M_{\rm J}$		0.3	0.4	0.6	0.8	
$l_{\rm max} = 14$	$\mathcal{M}$		6.8	10	15	22	
	$t_{\rm cr}$		0.23	0.33	0.5	0.7	
	Z		1	1	1	1, 1/10, 1/40	
	Cloud Name	XXS-VC	XS-VC	S-VC	M-VC	L-VC	
$\overline{n}_{\rm gas} = 1.8 \times 10^4\,\mathrm{cm^{-3}}$	$r_{\rm gas}$	0.7	1.1	1.6	2.3	3.4	
	Σ	609	894	1312	1925	2827	
	v_{esc}	3.4	5.1	7.4	11	16	
	$\Delta x_{\rm min}$	150	220	320	460	680	
$t_{\rm ff} = 0.44\,\mathrm{Myr}$	$n_{\rm sink}$	1.4×10^8	6.5×10^7	3.0×10^7	1.4×10^7	6.5×10^6	
	$M_{\rm J}$	0.08	0.12	0.17	0.26	0.38	
$l_{\rm max} = 14$	$\mathcal{M}$	7	10	15	22	32	
	$t_{\rm cr}$	0.07	0.10	0.15	0.23	0.33	
	Z	1	1	1	1	1	

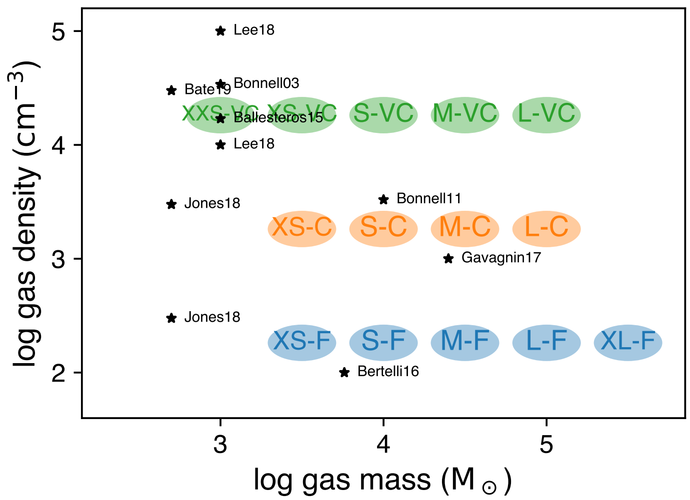

Figure 2.1: Simulation parameters in this work (colored ovals) compared to previous works (stars). The parameter space considered here is mass of the gas cloud (x-axis) versus mean particle number density of the cloud (y-axis). The labels showing the previous work found in the literature include: Bonnell et al. (2003, 2011); Ballesteros-Paredes et al. (2015); Bertelli Motta et al. (2016); Gavagnin et al. (2017); Jones & Bate (2018); Lee & Hennebelle (2018a); Bate (2019).

A detailed list of the parameters in our simulations is shown in Table 2.1. The clouds in Table 2.1 are labelled with letters of two or three parts. The first part is either 'XXS' (extra-extra-small), 'XS' (extra-small), 'S' (small), 'M' (medium), 'L' (large), or 'XL' (extra-large), representing various initial gas masses of 10^3, 3.16×10^3, 10^4, 3.16×10^4, 10^5, and 3.16×10^5 M$_\odot$, respectively. The second part is either 'F' (fiducial, which are the most similar to clouds in the solar neighbourhood), 'C'(compact), or 'VC' (very compact), in order of increasing initial mean gas density. The mean particle number density of the cloud, $\overline{n}_{gas} = \overline{\rho}_{gas}/(\mu m_p)$, where $\mu = 1.4$ is the mean molecular weight of the atomic gas, increases by a factor of ten between each set of simulations from 1.8×10^2 cm^{-3} to 1.8×10^4 cm^{-3}. The 'L-C' setup has two more simulations that have a third part in the name, 'lm' and 'xlm', representing 'low-metallicity' and 'extra-low-metallicity'. A comparison of our setups with the literature is shown in Figure 2.1.

2.2.2 Resolution and Sink Formation

We use a Cartesian grid with an octree structure with cells that we subdivide into 2^3 child cells as the simulation evolves ("adaptive refinement"). Our starting refinement level is $\ell_{\rm min} = 7$ (corresponding to $\Delta x = L_{\rm box}/2^7$) and maximum level of refinement is $\ell_{\rm max} = 15$ for runs with the lowest mean density and $\ell_{\rm max} = 14$ for all the other runs. The resolution is therefore $\Delta x_{\rm min} = L_{\rm box}/2^{15}$ for the "fiducial" runs, which corresponds to resolutions between 500 AU and 2300 AU. The "compact" clouds have resolution between 460 AU and 1500 AU and the "very compact" clouds between 150 AU and 680 AU.

In order to resolve the Jeans length with N grid cells it is required that

$$\lambda_{\rm J} = c_{\rm s}\sqrt{\frac{\pi}{G\rho}} > N_{sink}\Delta x. \tag{2.2}$$

From Equation (2.2), the Jeans length is resolved with at least N_{sink} grid points if $\rho < \rho_J$, where

$$\rho_{\rm J} = \frac{\pi c_{\rm s}^2}{GN^2\Delta x^2}. \tag{2.3}$$

In our simulations we enforce the refinement criterion that the Jeans length is resolved with at least $N_{\rm ref} = 10$ cells. Hence, when the local density goes up and reaches a point where $\lambda_{\rm J}$ becomes smaller than $N_{\rm ref}\Delta x$, each cell is refined individually into eight new child cells. This refinement condition is always true, up to the maximum refinement level (when $\Delta x = \Delta x_{\rm min}$). When the gas density exceeds $\rho_{\rm J}^{\rm max} = \rho_{\rm J}(\Delta x = \Delta x_{\rm min}, N)$ at the maximum refinement level, we cannot continue to resolve the Jeans length with at least $N_{\rm ref}$ cells. We therefore create sink particles to trace material above these densities. We set $\rho_{\rm sink} = \rho_{\rm J}(\Delta x = \Delta x_{\rm min}, N = N_{\rm sink})$ as critical density threshold to form sink particles. Sink particles are created on the fly using a peak detection algorithm (see Bleuler & Teyssier, 2014, for details on sink particle formation in RAMSES). We first detect density clumps above a density threshold $f_{\rm c}\rho_{\rm sink}$, with $f_{\rm c} = 0.1$. Then, the algorithm performs a peak density check, a collapsing check ($\nabla \cdot v = 0$), and virial check before forming a sink particle.

In order to avoid numerical fragmentation it is usually suggested that $N_{\rm sink} \geq 4$ (Truelove et al., 1997). In our simulations we adopt $N_{\rm sink} = 5$ for reasons detailed in Appendix A.1. With an initial sound speed $c_{\rm s} = 0.24$ km/s the Jeans mass at the sink density threshold is

$$M_{\rm J} = \frac{4\pi}{3}\rho_{\rm J}\left(\frac{\lambda_{\rm J}}{2}\right)^3 = 0.55 M_\odot \left(\frac{\Delta x_{\rm min}}{1000\,{\rm AU}}\right), \tag{2.4}$$

which results in $M_{\rm J} \sim 0.08 M_\odot$–$0.8 M_\odot$ for the compact and very compact clouds and $\sim 0.3 M_\odot$–$1.3 M_\odot$ for the fiducial clouds.

The sink particles are then treated like point masses and accrete gas based on the mechanism described as 'threshold accretion' in Bleuler & Teyssier (2014). The dynamics of the sink particles takes into account gravitational force from gas and stars and it is evolved using a leap-frog integration scheme. The effect of gas dynamical friction is not included.

2.2.3 Feedback and Properties of UV source

In our simulations, ionising UV photons are emitted from sink particles from the time they form to the end of the simulation. Massive stars have lifetime of few Myrs, shorter than the duration of some of our simulations, and they may explode as SNe during the simulation. Since we are not implementing SNe feedback, we keep the stars emitting radiation after their death to compensate for the lack of SNe in the attempt of avoiding underestimating feedback effects. While SN explosions produce a significant amount of mechanical energy (typically 10^{51} egs), the energy associated with ionising radiation from massive stars integrated through their main-sequence lifetime is comparable (or larger for more massive stars) and this feedback starts acting earlier than SN feedback. For an O-star, more than half of the radiation is emitted in hydrogen ionising photons. Typically $\sim 10\%$ of a star's hydrogen is burned in the nuclear fusion process, with an energy efficiency of $\sim 0.7\%$. Thus the amount of energy radiated by a massive star during its life time is $\sim 2 \times 10^{-3} M_{*}$, or $\sim 4 \times 10^{52}$ ergs for a 20 $M_{\odot}$ star.

For each simulation we estimate the total hydrogen-ionising photon emission rate at a given time as $S_{\rm cl}(m_{cl}) = 8.96 \times 10^{46}\ {\rm s}^{-1}\ (m_{cl}/M_{\odot})$ (see Geen et al., 2017), where m_{cl} is the total mass of the sink particles. This is calculated by Monte Carlo sampling a stellar population as described in Geen et al. (2016) (See Sec. A.2). The fraction of the total hydrogen ionising photon emission rate attributed to each sink particle is based on the following relation

$$q(m_i) = V(0.3m_i)\left(\frac{S_{\rm cl}(\Sigma_i m_i)}{\Sigma_i V(0.3m_i)}\right), \tag{2.5}$$

where $V(m)$ is the hydrogen-ionising photon emission rate from a star with mass m, using the fits from Vacca et al. (1996).

The factor 0.3 is an empirical factor to account for the scaling between the masses of sink particles and those of massive stars, necessary because we do not fully resolve the fragmentation of sink particles into proto-stars. See Section 2.3.1 for further discussion. The correction factor $X \equiv S_{\rm cl}(\Sigma_i m_i)/\Sigma_i V(0.3m_i)$ is very close to unity in most simulations in which we resolve massive stars and it is introduced only to prevent overproducing ionising radiation in case massive stars are poorly resolved. In all simulations we also impose $X \leq 1$.

For the fiducial clouds we also include He^0 and He^+ ionising photons with total emission rates being $S_{\mathrm{He}^0} = (1.178 \times 10^{46}\,\mathrm{s}^{-1})(M_*/M_\odot)$ and $S_{\mathrm{He}^+} = (2.422 \times 10^{43}\,\mathrm{s}^{-1})(M_*/M_\odot)$. These rates are calculated using the same method as for hydrogen ionising photons described above using a Kroupa IMF (Kroupa, 2002). For the luminosity of individual stars we use Schaerer (2002) fitting for $Q(\mathrm{He}^0)$ and $Q(\mathrm{He}^+)$ with extrapolations above 150 $M_\odot$. This is contrasted by the model of Gavagnin et al. (2017), who assume blackbody spectra for each star. See Appendix A.2 for details.

Various authors have concluded that UV photoionisation is typically the most important process in regulating star formation on a cloud scale. Haworth et al. (2015) find that additional processes beyond hydrogen photoionisation have a correcting factor of 10% at best. Radiation pressure mainly becomes important at very high surface densities, which principally affects smaller scales than the ones studied here - see Crocker et al. (2018) for idealized conditions and Kim et al. (2018) for simulations with self-consistent star formation feedback. Dale et al. (2014) further find that winds have a minimal effect on the star formation efficiency of molecular clouds. We are thus justified in our choice to focus on UV photoionisation feedback in this work, but discuss cases where this may not be sufficient later in the chapter.

2.2.4 Cooling

We use the radiative cooling function described in Geen et al. (2016). The cooling in neutral gas is based on the prescription in Audit & Hennebelle (2005), which includes cooling from carbon, oxygen and dust grains as well as the effect of the ambient UV background in the ISM. For collisionally ionized gas at temperatures $> 10^4$ K we use Sutherland & Dopita (1993) cooling function. The out-of-equilibrium cooling of photoionised hydrogen and helium is treated as described in Rosdahl et al. (2013). Out-of-equilibrium cooling of photoionised metals is treated with a piecewise fit to the cooling curve given in Ferland (2003). We assume a uniform metallicity as listed in Table 2.1. For most simulations, this is solar metallicity, though we perform some simulations at sub-solar metallicity. We do not implement out-of-equilibrium molecular chemistry.

2.3 Results

In this section we present and discuss the results of our simulations. In § 2.3.1, we study the mass function of cores (sink particles) and the IMF. In § 2.3.2 we focus on the star formation efficiency and in § 2.3.3, on the star formation rate.

A representative sample of snapshots from our simulation set is shown in Figures 2.2 and 2.3. These figures show the time evolution of the density-weighted projections of the gas density and temperature as well as the position of the sink particles along line of sight for three simulations with different mean cloud densities (fiducial on the left column, compact, middle column, and very-compact on the right column), and a cloud mass of 3.2×10^4 M$_\odot$.

We observe clearly that the star formation efficiency increases with increasing cloud density, and the stellar cluster that is formed at the end of the simulation remains more compact and self-gravitating for the densest cloud. The effect of radiative feedback from massive stars is also clearly visible in the density and temperature projections. H II regions break out of the dense

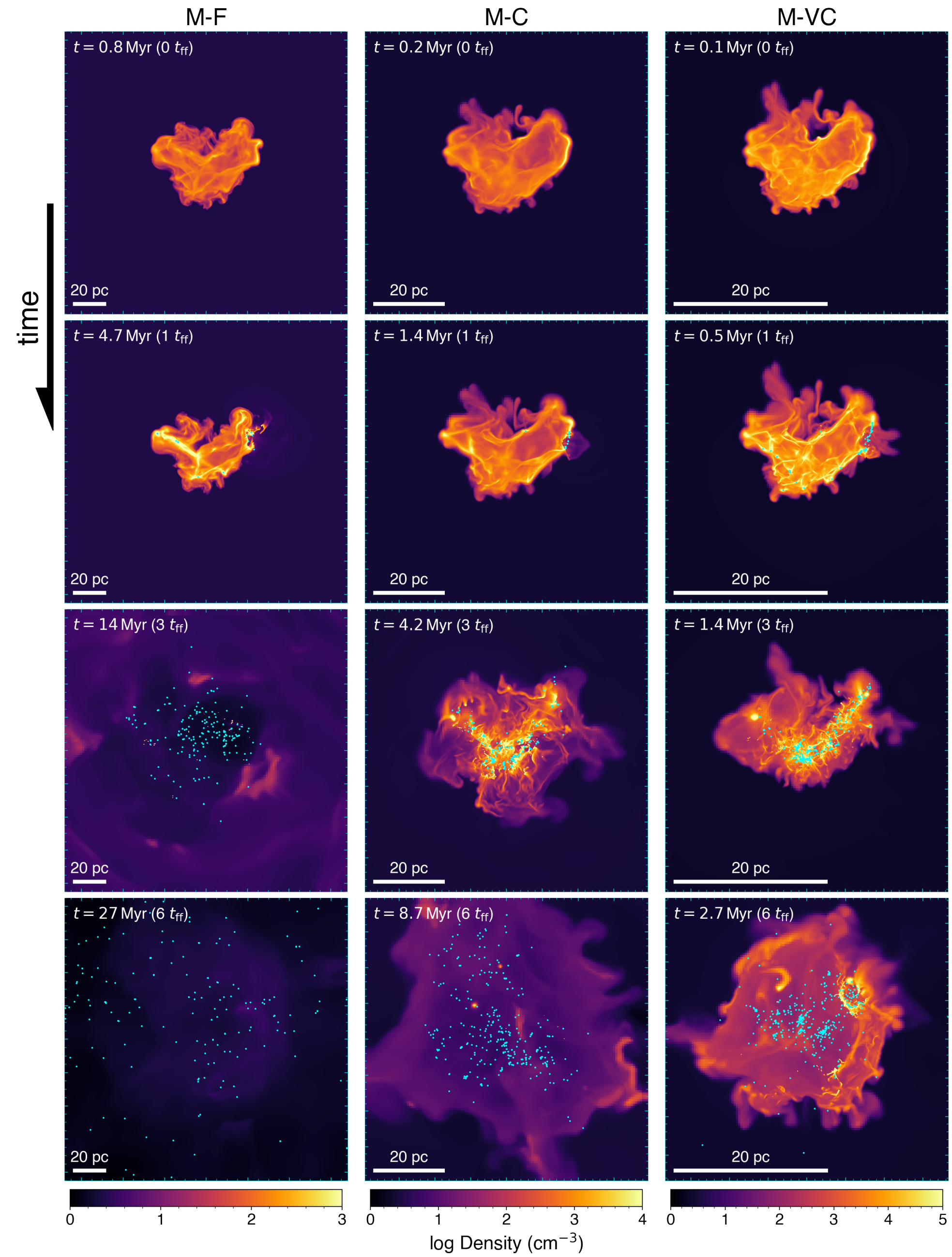

Figure 2.2: Line-of-sight projections of the (density-weighted) gas density for three simulations with cloud mass 3.2×10^4 M$_\odot$. From left to right we show clouds with increasing mean density: $\overline{n}_{\rm gas} \sim 1.8 \times 10^2$ cm^{-3}, representing our fiducial clouds in the local universe, $\overline{n}_{\rm gas} \sim 1.8 \times 10^3$ cm^{-3} and $\overline{n}_{\rm gas} \sim 1.8 \times 10^4$ cm^{-3}, respectively. From top to bottom we show the time evolution of the clouds. Sink particles are displayed as cyan dots. The snapshots shown in the top row represent the initial conditions of the turbulent cloud: no stars have formed at this time because the highest density is below the threshold for star formation, but the cloud idealized initial conditions have been already evolved for $\sim 3\ t_{ff}$ in order to develop a turbulent density field. In the bottom row snapshots, star formation has stopped and most of the gas has been expelled as a result of UV feedback from massive stars.

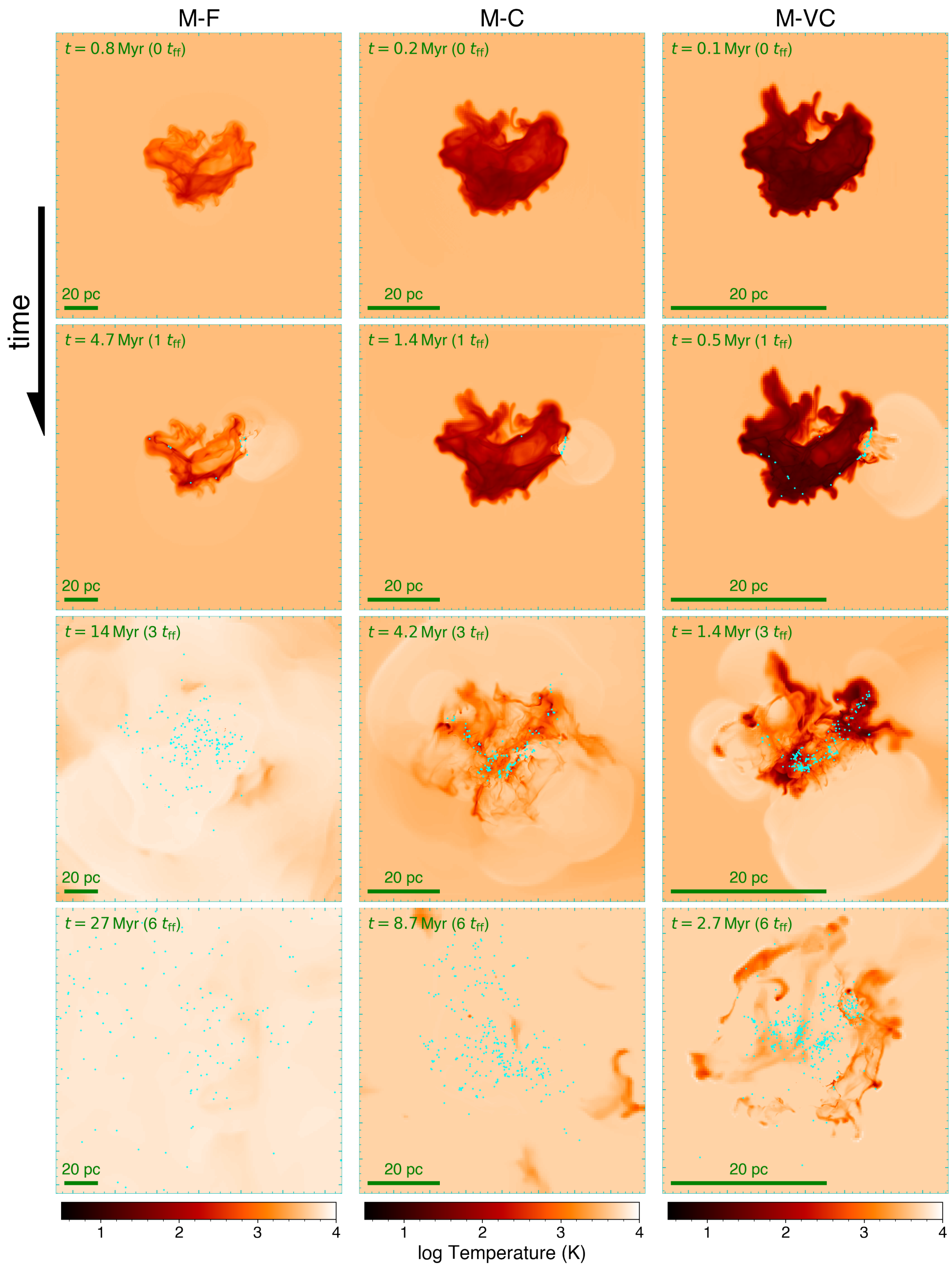

Figure 2.3: Same as Fig. 2.2 but showing the density-weighted projection of the temperature.

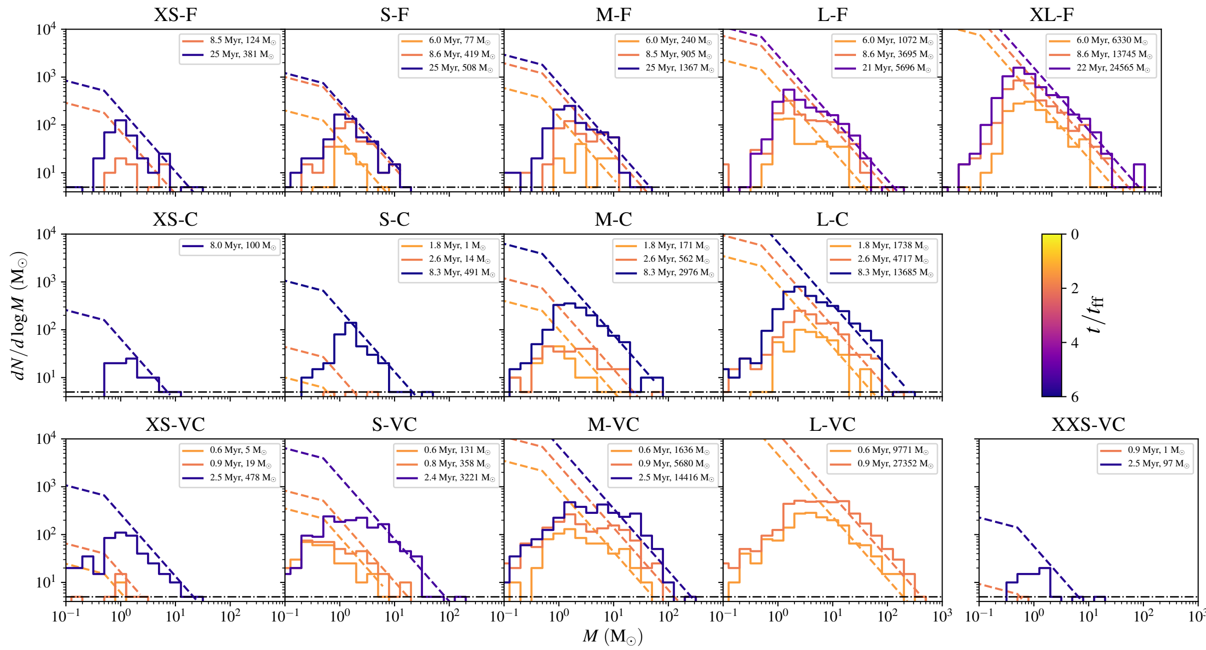

Figure 2.4: Temporal evolution of the mass functions of the stars, obtained by multiplying by 0.4 the masses of the sink particles (see text). The dashed lines are analytic Kroupa IMF for systems normalised to the total mass of the sink particles at the corresponding time. The time and total mass in sink particles are shown in the legend. We see good agreement between the shifted sink particles mass function and the analytic mass-normalised Kroupa IMF at the high-mass end, both in terms of the power-law slope and normalisation.

filaments destroying them and reducing the overall mass in dense gas in which stars are formed.

2.3.1 Stellar Initial Mass Function

2.3.1.1 Cores Fragmentation and Initial Mass Function

Maps in the continuum of cluster regions and larger areas in star-forming systems allow us to construct a core mass function (CMF), that is the mass function of high-density gas concentrations (starless cores) with mass sufficiently large to be identified given the resolution of the observations (e.g., Motte et al., 1998). Observations of a well-resolved CMF in the Pipe nebula show a striking similarity to the stellar IMF, but shifted to higher masses by a factor of a few, which suggests that the IMF is the direct product of the CMF with a roughly constant core-to-star conversion efficiency $\sim 30\%$ (e.g., Matzner & McKee, 2000; Alves et al., 2007)

Previous works on star formation in molecular clouds which adopted sink particles (like in the present chapter) have investigated the mapping between the masses of pre-stellar cores at the time they become self-gravitating and the final masses of the stars that form within them (e.g., Padoan et al., 2001; Smith et al., 2009). For instance, Smith et al. (2009), using SPH simulations, find that at early times the relationship between stellar masses and the parent cores can be reproduced within a modest statistical dispersion with the star being about one-third of the parent core mass.

We find results in agreement with these previous studies. Figure 2.4 (and Figure 2.7) show the stellar mass function for our grid of simulations obtained assuming that the sink particles are about a factor of 2.5 more massive than the corresponding massive stars they produce. This means that the number of stars of a given mass (> 1 $M_{\odot}$) is given by a Kroupa IMF for a star cluster with total mass equal to the total mass of the sinks. In Figure 2.7 the IMF is shown at the end of the simulation when star formation has stopped, while in Figure 2.4 we also show the time evolution of the IMF, together with the Kroupa IMF for a cluster with total mass equal to the total mass in sink particles (dashed lines). This means that we are assuming nearly 100% efficiency of star formation in the cores (*i.e.*, the cores fragment into stars) or a lower efficiency but the gas expelled by feedback is later transformed into low-mass stars. However, we think that this second model is less physically motivated. We can see that the shifted sink mass function (SMF) matches the Kroupa IMF at the high-mass end, both in terms of the slope and normalisation at any time during the formation of the star cluster. The figure suggests that the birth of stars in a cluster follows the same random sampling of the universal mass function throughout the star-formation process. In other words, it appears that there is not a bias toward formation of high mass-stars or low-mass stars during the early times when the cluster is in the formation process.

As discussed above the sink particles can be interpreted as pre-stellar cores, and each sink particle converts $\sim 40\%$ of its mass to a single massive star, with the rest of the mass ending up in low-mass stars, filling up the lower mass end of the IMF. The flattening or cut-off of the IMF at the low-mass end observed in our simulations is likely due to insufficient spatial and mass resolution to capture the formation of low mass cores or the fragmentation of more massive pre-stellar cores. To further clarify, we note that the interpretation that only 40% of the core mass is converted into a star and the remaining 60% is returned to the gas phase, never to participate in star formation, would not produce the correct normalisation of the IMF. This is because in this scenario, although the stellar masses are $\sim 40\%$ of the core masses, the total stellar mass and the star formation efficiency would be reduced by a factor of ~ 2.5, lowering the expected number of massive stars below the value found in the simulations.

So far we have assumed that all the gas in the cores fragments into stars with $\eta = 100\%$ efficiency. In this case we find a conversion factor $\varepsilon = 0.4$ between the CMF and the IMF (such that the normalisation of the IMF agrees with the observed one). However, it is possible to match the observed IMF also in models in which $\eta < 1$. Note that in this case the TSFE shown in all our plots should be re-scaled by a factor η. In models with $\eta < 1$, the conversion factor ε that matches the mass-normalised empirical IMF, is $\varepsilon = 0.4\eta^{1/\Gamma}$. For $\eta = 1, 0.69$ and 0.4, $\varepsilon = 0.4, 0.3$ and 0.2, respectively.

The results of this section justify our assumptions to model radiative feedback in Section 2.2.3 and it further implies that our simulations are self-consistently treating the formation of individual massive stars, their feedback effects, and can be used reliably to estimate of the

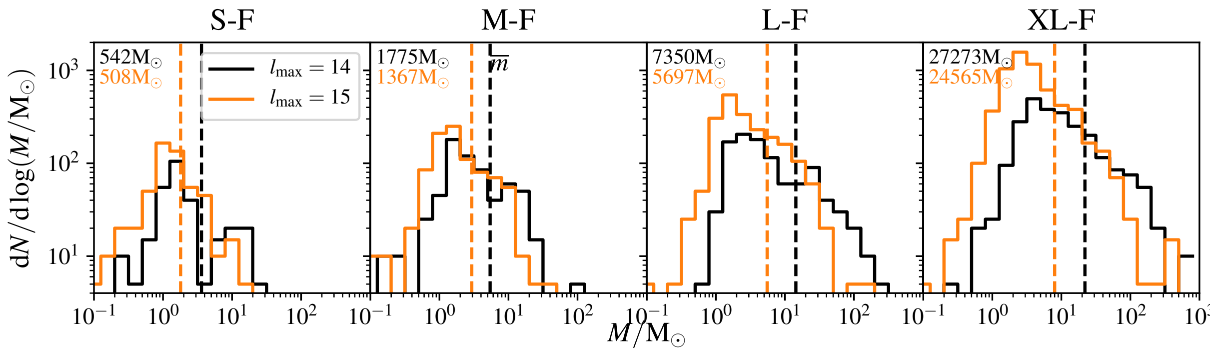

Figure 2.5: Comparing IMFs from simulations with different resolutions. Fewer massive stars and more lower-mass stars form from simulations with higher resolution.

escape fraction of hydrogen and helium ionising photons.

2.3.1.2 Resolution Studies

We conduct four extra runs at lower resolution to evaluate the numerical convergence of our simulations. All other simulations have the highest resolution we could afford computationally, and increasing the resolution is unfeasible for the relatively large cloud masses considered in this study. More massive sink particles and fewer low-mass sink particles form in simulations with lower resolution (see Figure 2.5). The mean mass of the IMF, represented by the vertical dashed line in the figure, increases by a factor $\sim 2-3$ when the spatial resolution halves. As the resolution increases, while there is no significant change in the total mass in sinks, the mean mass of sinks decreases, suggesting that some of the sinks fragment into smaller sub-clumps. A model in which the cores form stars with $\sim 30\%$ efficiency and, as we increase the resolution, additional small mass cores form from unused gas at the low-mass end of the CMF, is instead less consistent with our results for two reasons. i) Allowing more of the diffuse gas to form low mass cores would produce, in some simulations, a total core formation efficiency above unity (in simulations that have $f_* > 0.3-0.4$). ii) Figure 2.5 shows that the core formation efficiency, which is $\sim f_*$,

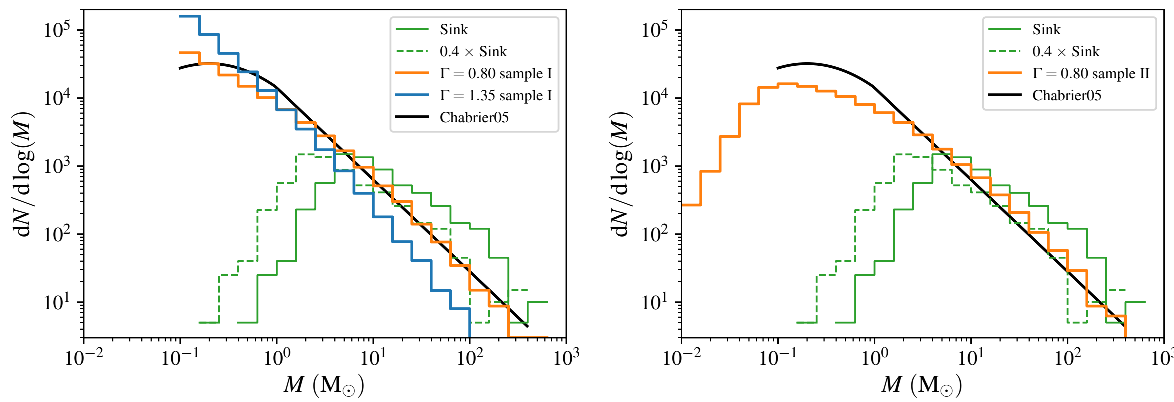

Figure 2.6: Top: Numerical experiments showing the results of fragmenting each sink particle into stars using a power-law PDF with slope Γ for the XL-F simulation. Similar results are obtained for all the other simulations. The green solid and dashed histograms are the sink mass function (SMF) and the "shifted" sink mass function (*i.e.*, sinks masses are multiplied by 0.4), respectively. The blue and orange solid histograms show the mass functions of the stars obtained by fragmenting each sink particle into smaller particles using a power-law probability distribution with a slope Γ in the range of $0.1\ \mathrm{M}_{\odot}$ to m_{sink}, as shown in the legend as 'sample I'. Mass-normalised analytic Chabrier IMF are plotted for comparison. A power-law sampling of the sinks with $\Gamma = 0.8$ produces an IMF in very good agreement with a Chabrier IMF over the whole range of star masses. Bottom: Similar to the Top but the lower limit of the sampled masses is set to max$(0.01\ \mathrm{M}_{\odot}, 0.01 m_{sink})$ (sample II).

is close to being converged. Thus, by increasing the resolution we do not add new cores from the gas, otherwise we would observe an increase of f_*, which instead slightly decreases with increasing resolution. Increasing the resolution simply changes the CMF, but the total mass in cores remains nearly the same. For these reasons, we find that the cores-fragmentation model is the most likely, although we cannot rule out alternative scenarios.

2.3.1.3 Monte-Carlo Numerical Experiments for Fragmentation

To demonstrate more convincingly that our interpretation is robust, we perform a simple numerical experiment. We assume that each pre-stellar core (sink particle) fragments into smaller sub-units with a power-law mass function (MF) with index Γ, and with limits on the fragment masses between $0.1\ \mathrm{M}_{\odot}$ and the sink mass. We draw randomly from this distribution until the total mass of the fragments equals the sink mass. We repeat this procedure for all the sinks. Such sampling is done 20 times and the average of the bins is taken. Figure 2.6 shows the resulting mass function for the XL-F cloud, but we obtain similar results for all the simulations. The mass function we obtain by fragmenting the sinks is shown as the solid histogram (blue for $\Gamma = 1.35$ and orange for $\Gamma = 0.8$). The original SMF is shown by the green solid histogram and the shifted mass function is shown by the dashed histogram. The black solid curves show the Chabrier IMF for a cluster with total mass equal to the total mass in sink particles, which are in very good agreement with the mass function of the fragmented pre-stellar cores assuming $\Gamma = 0.8$.

This sampling method does not produce a modal mass for the IMF. To address this, we tried another sampling method. However, if we assume that the lower mass limit in the sampling is set to max$(0.01\ \mathrm{M}_{\odot}, 0.01 m_{sink})$, instead of $0.1\ \mathrm{M}_{\odot}$, the resulting IMF has a similar shape to the SMF but peaks at a mass 100 times smaller, resulting in a model mass of the IMF $\sim 0.1\ \mathrm{M}_{\odot}$ (see bottom panel in Figure 2.6).

In summary, the fragmentation of the pre-stellar cores into numerous small mass stars, a process which is not captured in our simulations due to limited resolution, explains the deficit of stars with mass below $\sim 1\ \mathrm{M}_{\odot}$ in our simulations with respect to the number expected assuming a Chabrier IMF.

2.3.1.4 High-mass Slope of the IMF

In this section we quantify more rigorously the slope of the IMF. In Figure 2.7 the IMF is shown at the end of the simulations when star formation has stopped. The green lines show the best fit power-law at the high-mass end of the IMF using Bayesian inference as explained

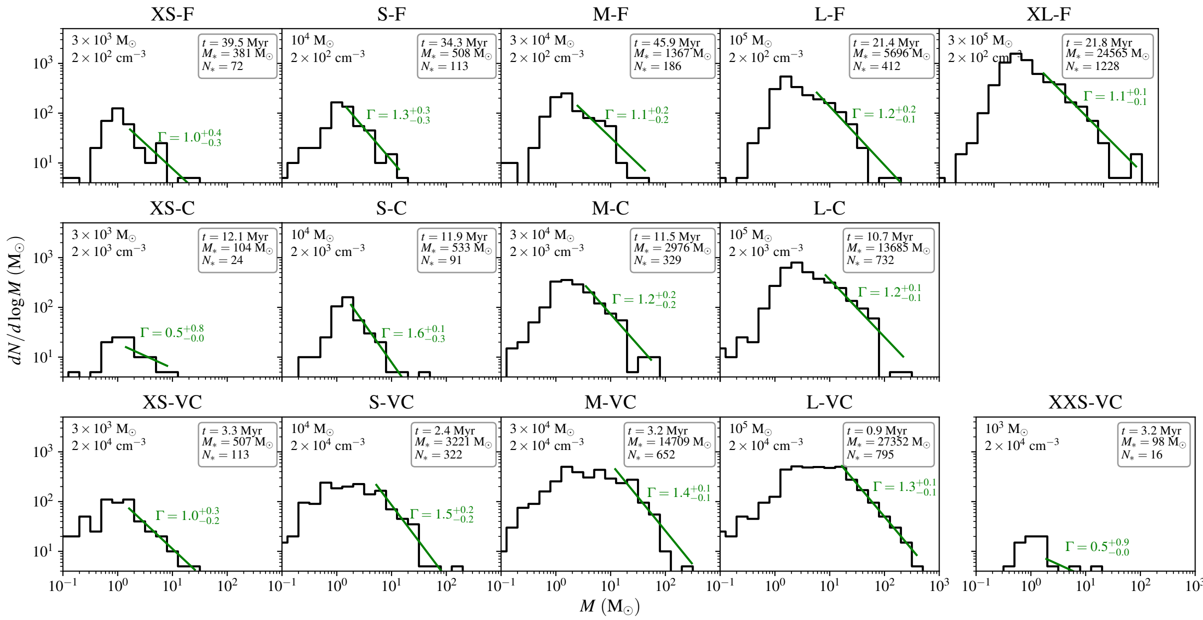

Figure 2.7: Same as Fig. 2.4, but showing the IMF at the end of the simulations along with the best fit power-law (solid green lines). Only sinks above a critical mass are used for the Bayesian fit. Stars more massive than the critical mass account for 70% of the total cluster mass. The mass range of the sinks used in the fit is also shown as the range of the solid green lines. The power-law slopes lie in a range from 1.0 to 1.6 (excluding the simulations that produces less than 50 sink particles), in agreement with the slope of the Salpeter IMF ($\Gamma = 1.35$).

below. We do not notice any significant relationship between the high-mass end slope of the IMF and the mass or compactness of the cloud. We notice, however, a flattening of the IMF at 1-10 M$_\odot$ in very compact clouds of high-mass (M$>$ 10^3 M$_\odot$), which is instead not observed in the fiducial and massive clouds. Since these clouds have the highest star formation efficiency and the strongest radiative feedback, a speculative interpretation would be that we are observing the effect of photo-evaporation of small fragments. When a proto-star is exposed to the ionising flux of a new-born OB star, the disk mass decreases rapidly with time. This may regulate the mass accretion rate through the disk and therefore to the star.

Here are some details of the Bayesian inference of the IMF slope. We assume a power-law slope mass distribution with general form $\mathrm{d}N/\mathrm{d}\log m = Am^{-\Gamma}$ where A is a constant of normalisation and $m_{\min} < m < m_{\max}$. When the total number of stars is N_0, this constant becomes $A = \ln 10\, N_0\ \Gamma/(m_{\min}^{-\Gamma} - m_{\max}^{-\Gamma})$. The likelihood is proportional to the distribution function, $\mathcal{N}(\mu_i|\Gamma) = Am_i^{-\Gamma}$, where $\mu_i \equiv \log(m_i)$. To find the most likely Γ we calculate the value of Γ that maximises the log of the likelihood:

$$
\begin{aligned}
\ln \mathcal{L} &\propto \sum_i \ln \mathcal{N}(\mu_i|\Gamma) \\
&= N_0 \left[\ln \Gamma - \ln(m_{\min}^{-\Gamma} - m_{\max}^{-\Gamma})\right] - \ln 10\, \Gamma \sum_i \mu_i.
\end{aligned}
\tag{2.6}
$$

Model-independent constants are removed from this equation. We do the un-binned fitting only to stars with masses above a critical value. This value is chosen somewhat arbitrarily as the point at which the IMF starts to deviate from the Kroupa IMF. In each panel the best fit line is shown as a segment between the critical mass and the maximum stellar mass along with the slope Γ and 1-σ errors. The errors are calculated as the 16% and the 84% points of the cumulative likelihood for Γ between $\Gamma = 0.5$ to 1.8. The fitted value of Γ has a dependence on the critical minimum mass for the points included in the fit, but we find that the values of Γ agree with a Kroupa IMF within the 1-σ errors in most cases. Here, we adopt a critical mass such that particles above this mass account for 70% of the total mass in stars.

2.3.1.5 Maximum Stellar Mass in the Cluster

Figure 2.8 shows the maximum stellar mass ($M_{\max}$) as a function of the mass of the star cluster. The relationship between $M_{\max}$, obtained by multiplying the maximum sink mass by 0.4,

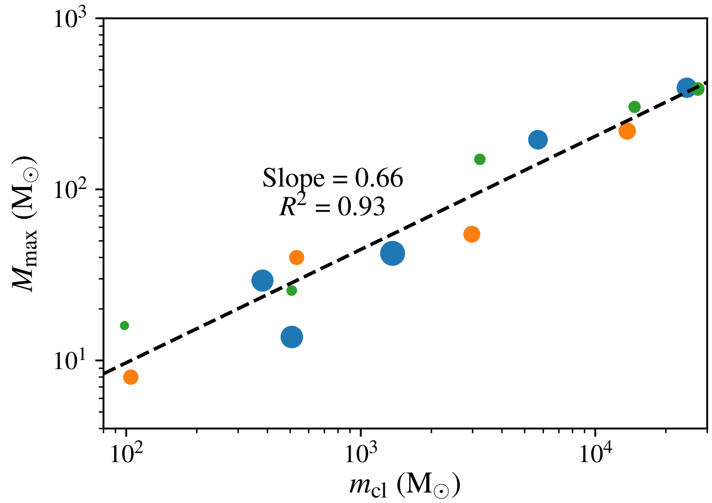

Figure 2.8: Maximum stellar mass in a cluster v.s. the mass of the star cluster. We use a least-square method to fit the data to a power-law with slope 0.66 ± 0.06. The radius of each circle is proportional to the square root of the half-mass effective radius of the cluster and the color represents the compactness of the cloud: orange for fiducial, blue for compact, and green for very compact.

and the stellar cluster mass, m_{cl}, is tight. The best fit power-law is

$$M_{\max}/\mathrm{M}_\odot \approx 205\, m_4^{0.66}, \tag{2.7}$$

where $m_4 = m_{cl}/10^4\ \mathrm{M}_\odot$, valid when $m_{cl} \gtrsim 100\ \mathrm{M}_\odot$. The relationship is well correlated, with a coefficient of determination $\mathrm{R}^2 = 0.93$. A power-law relationship between the maximum stellar mass and the cluster mass is consistent with observations, although the observed power-law slope is 0.45 (Larson, 1969), which is slightly flatter than the value found in our simulations. However, the slope we find is in good agreement with numerical studies of star formation in clusters using SPH codes (Bonnell et al., 2003, 2004). We also neglect smaller-scale feedback from protostellar outflows that can reduce the final mass of stars. In addition, it should be kept in mind that the maximum stellar mass here is defined as 0.4 times the maximum sink mass, therefore it is possible that the fragmentation of the largest sinks may produce stellar masses systematically smaller than

$M_{\max}$.

Given the uncertainty due to Poisson statistical fluctuations, the SMF appears to be consistent with power-law all the way to the mass bin that is expected to have ~ 1 particle in it (the horizontal dashed-dotted lines in Figure 2.7). Hence we do not have strong evidence for a high-mass truncation of the CMF. We conclude that the CMF, as represented by the SMF, does not have a fundamental upper mass limit below $\sim 1000\ \mathrm{M}_{\odot}$ (the maximum sink mass in all simulations). Since our simulations have the same initial turbulence field and we have only one random realisation for each set of parameters (mass, and density of the cloud), we are not able to address the question of whether the maximum stellar mass in a cluster is determined by physical (Kroupa & Weidner, 2003) or statistical effects (*e.g.* Fumagalli et al., 2011). In addition, we use an empirical relationship between sinks mass and massive stars, rather than resolving the fragmentation of sinks into massive stars using a physical model. This also prevents us from drawing robust conclusions about this open question.

2.3.2 Star Formation Efficiency

We define star formation efficiency (SFE, or f_*) in our simulated clouds as the fraction of the initial gas mass that is converted into sink particles. Figure 2.9 shows the SFE as a function of time in units of the free-fall time $t_{\rm ff}$ (shown at the top-right of each panel), for the simulations in Table 2.2. The top panel refers to the fiducial clouds, the middle panel to the compact clouds and the bottom panel to the very compact clouds. Lines in each panel refer to different cloud masses as explained by the simulation IDs in the legend. The vertical lines mark the time of the explosion of the first two SNe in the simulation, where the lifetimes of stars are given by Schaller

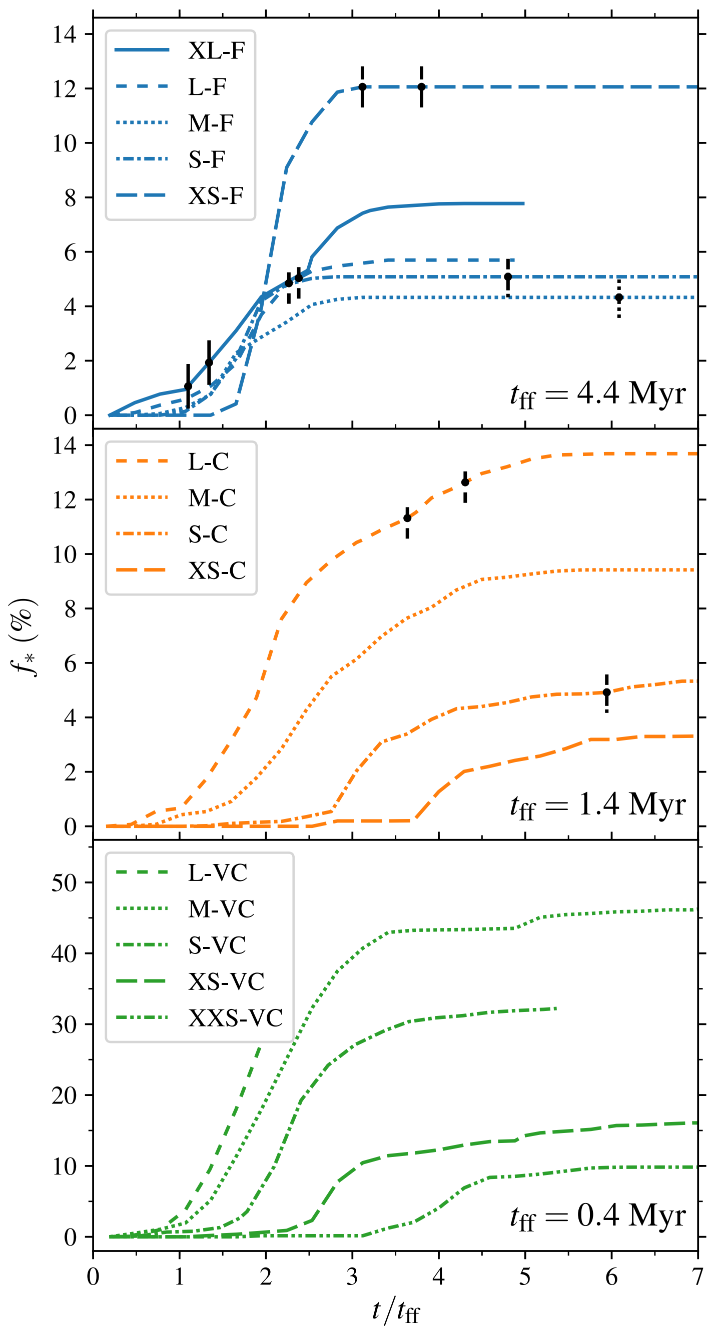

Figure 2.9: Dimensionless star formation efficiency f_* as a function of the dimensionless time $t/t_{\rm ff}$ for all the simulations shown in Table 2.1. The top, middle, and bottom panels show the fiducial, compact, and very compact clouds, respectively. The black vertical lines indicate the time of the first two SN explosions, if they exist, for each simulation, where the lifetimes of stars are given by Schaller et al. (1992) fit. The duration of the star formation episode is roughly proportional to the sound-crossing time of the cloud (see Sec. 2.3.3).

et al. (1992) fitting functions. As discussed before we do not include mechanical feedback from SNe, but star formation has already stopped or it is mostly terminated before the explosion of the first SN in all simulation but XL-F, *i.e.* the fiducial run with mass $m_{gas} = 3.2 \times 10^5$ M$_\odot$.

When time is measured in units of the free-fall time, the shape of the SFE curves are qualitatively similar: the SFE increases rapidly with time and peaks at $t \approx 2 - 3t_{\rm ff}$. Generally the total SFE at the end of the simulations increases with increasing cloud mass and with increasing cloud compactness. This is shown more clearly in Figure 2.10. The top panel in Figure 2.10 shows the stellar mass of the cluster $m_{\rm cl}$ as a function of the cloud gas mass for the 3 set of simulations with different compactness (as shown in the legend). The smaller open circle with the label $Z = 1/40$ Z$_\odot$, shows a compact cloud simulation but with lower gas metallicity (see Section 2.3.4). The dot-dashed line shows SFE= 100%, while the dashed lines are fits to the simulation results with the following function:

$$m_{\rm cl} = 200\ {\rm M}_\odot \cdot \left(\frac{m_{gas}}{10^4\ {\rm M}_\odot}\right)^{1.4} \left(1 + \frac{\overline{n}_{gas}}{n_{\rm cri}}\right)^{0.91} + m_{fl}\,, \tag{2.8}$$

where $n_{\rm cri} \approx 10^3\ {\rm cm}^{-3}$ is the critical density and m_{fl} is the mass floor. The dashed lines show the fit assuming $m_{fl} = 0$, while the dotted line has $m_{fl} = 10$ M$_\odot$. Equation (2.8) is a good fit to the points when excluding the 3 lowest mass simulations for the fiducial run (shown as smaller sized open squares). The motivation for excluding these 3 simulations from the fits is explained below.

The open symbols show star cluster that become dynamically unbound (*i.e.*, open star clusters), while the solid symbols show star cluster that at the end of the simulations, after most of the gas has been used up for star formation or expelled, remain gravitationally bound (*i.e.*, globular

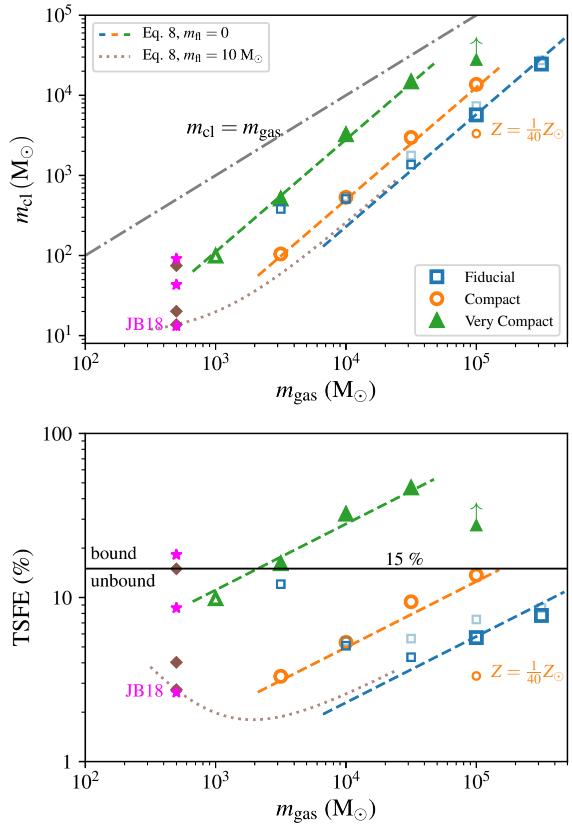

Figure 2.10: (*Top.*) Stellar mass of the cluster m_{cl} as a function of the initial mass of the gas cloud (m_{gas}) for the set of simulations with different initial cloud densities (see legend). The gray dot-dashed line is plotted as a reference for 100% star formation efficiency. Excluding the 3 fiducial cloud simulations with the lower masses, we observe a clear power-law relation between $m_{\rm cl}$ and $m_{\rm gas}$. We speculate that the minimum cluster mass floor observed for the fiducial clouds data points is due to inefficient UV stellar feedback due to lack of realistic implementation of low-mass stars feedback in our simulations. Indeed the simulations by Jones & Bate (2018), shown as magenta stars, are in excellent agreement with the extrapolation of out power-law fits as shown by the brown diamonds, assuming Eq. (2.8) and Eq. (2.9) fits with $m_f = 10{\rm M}_\odot$ (see the brown dashed line for our fit to the smallest density of the three Jones18 data points). (*Bottom.*) Same as the top panel but showing the total star formation efficiency (TSFE), i.e. the SFE once star formation ends and the cloud is dispersed. The solid horizontal line at $f_* = 15\%$ roughly separates clouds that form globular cluster progenitors from open star clusters.

cluster progenitors).

The star symbols show the results of simulations by Jones & Bate (2018) for clouds with mass $m_{gas} = 500$ M$_\odot$ and for mean densities $\overline{n}_{gas} = 3 \times 10^2$, 3×10^3, and 3×10^4 cm^{-3}, from bottom to top, respectively. These densities are slightly different from the mean densities in our fiducial, compact and very compact simulations, thus we show as diamonds the corresponding points obtained using our fitting formula in Equation (2.8) with $m_{fl} = 10$ M$_\odot$. These simulations do not include feedback by massive stars being very small mass clouds in which the most massive star that forms has is < 10 M$_\odot$. However, the resolution of these simulations is higher than our simulations and, contrary to our simulations, feedback by IR radiation is included. In addition, these simulation are run using an SPH code. It is interesting to note that despite the different codes and physics included, the results are consistent with the extrapolation of our fitting formulae to low mass clouds if we assume a minimum mass floor for the star cluster mass of ~ 10 M$_\odot$.

The bottom panel in Figure 2.10 is the same as the top panel but shows the total star formation efficiency $f_{*,tot} \equiv m_{\rm cl}/m_{\rm gas}$ and the best fit:

$$f_{*,tot} = 2.0\% \left(\frac{m_{gas}}{10^4\ M_\odot}\right)^{0.4} \left(1 + \frac{\overline{n}_{gas}}{n_{\rm cri}}\right)^{0.91}. \tag{2.9}$$

The solid horizontal line at TSFE $\sim 15\%$ roughly separates star clusters that become globular cluster progenitors ($f_* > 15\%$) from open star clusters ($f_* < 15\%$). This separation is based on the dynamical state of the cluster at the end of the simulations, but a more detailed analysis of the dynamics of the stellar cluster will be the subject of a followup study.

Let's now address the reason why we excluded the 3 lower mass fiducial simulations from our analysis. We observe that the star cluster mass in these simulations does not obey a simple power-law relationship with the initial gas mass of the molecular cloud. The discrepancy does not appear to be a convergence issue due to insufficient resolution, as confirmed by the lower-resolution simulations (shown as lighter color small squares), but rather lack of the necessary physics for self-regulation feedback. This can be understood inspecting Figure 2.8 which relates the mass of massive stars to the cloud gas mass. The low TSFE of the diffuse clouds in combination with the small cloud gas mass produces stellar masses below 10^2 M$_\odot$, which corresponds to a maximum stellar mass $M_{max} < 10$ M$_\odot$. Such stars do not produce significant quantities of ionising UV radiation, therefore the cloud can continue to form stars. This is due to our neglecting feedback mechanisms from lower mass stars. This requirement for stars that produce ionising radiation to disperse the cloud leads to a minimum cluster mass floor $m_{\rm cl} \sim 300$ M$_\odot$, much larger than the ~ 10 M$_\odot$ floor which is a good fit to the simulations of Jones & Bate (2018).

This large mass floor is not evident in the compact and very compact clouds: if it exists, it must be at masses $m_{\rm cl} < 100$ M$_\odot$. The reason for this apparent inconsistency is not fully understood, but it appears to be related to the smaller ratio of the crossing to free-fall time for the fiducial cloud when compared to the more compact clouds (Sec. 2.3.3). We offer the following hypothesis: Inspecting the middle and bottom panels in Fig. 2.9, we observe a longer delay for onset of star formation in the small mass clouds for the compact and very compact runs, which is not observed in the fiducial runs. This can be understood in terms of the necessary number of crossing times required by the supersonic turbulence to create dense clumps for star formation (with $n > n_{\rm sink}$). In the fiducial cloud this enhancement of the density due to supersonic turbulence is faster when compared to the free-fall timescale, hence the steeper rise of f_* as a function of time. When feedback from massive stars is absent due to random sampling of a small mass stellar cluster, this rapid increase of f_* can lead to significant overshooting of star formation above the threshold expected from self-regulation. This overshooting does not happen, or is milder, for more compact clouds in which f_* increases with t/t_{ff} more slowly. The existence of a minimum cluster mass floor, however, should eventually become evident also in more compact clouds when decreasing further the initial cloud masses.

We observe a power-law relation between the mass of the cloud and the mass of the star cluster. Howard et al. (2018a) find that the stellar mass of the most massive cluster that forms from a molecular cloud has a power-law dependence on the mass of the cloud with an exponent of 0.78. In our work, this relation, taking all sink particles as the cluster, has an exponent of 1.4 (Equation 2.8). By multiplying it with the exponent of the M_{max}-m_{cl} relation, 0.66 (Equation 2.7), we get an exponent of 0.92. Similar to Howard et al. (2018a), our work suggests that young massive star clusters are natural extensions of low-mass cluster formation.

Our results (Figure 2.10, or Table 2.2) are in good agreement with Kim et al. (2018), who find that the TSFE depends primarily on the initial gas surface density, such that the TSFE increases from 4% to 51% as Σ increases from 13 to 1300 $\mathrm{M}_\odot\ \mathrm{pc}^{-2}$.

To summarise, we believe that the increase in TSFE observed for the fiducial simulations with masses $m_{\rm gas} \leq 10^4$ M$_\odot$ is unphysical, meaning that it is due to missing feedback processes in our simulations. When the most massive star has mass $M < 10$ M$_\odot$, IR radiation feedback or proto-stellar jets feedback should be included in the simulation. In all the other simulations UV feedback by massive stars is likely the dominant feedback at play; therefore these simulations incorporate the relevant physics for the formation of realistic star clusters.

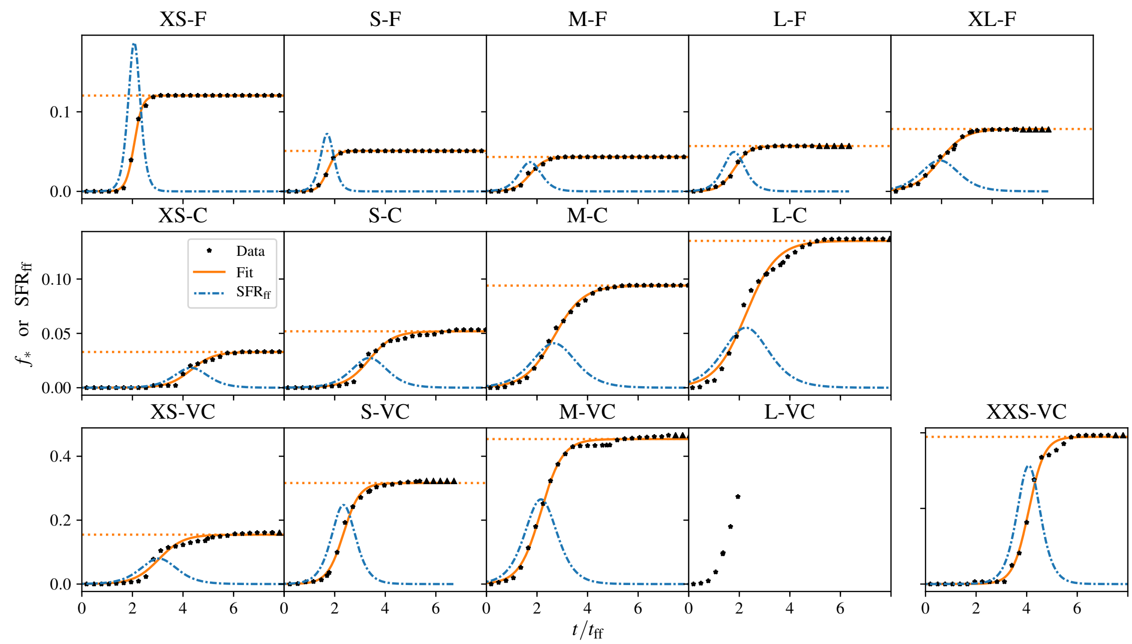

Figure 2.11: Dimensionless star formation efficiency ($f_* = m_*/m_{gas}$) and dimensionless star formation rate per free-fall time (SFR$_{ff} = df_*/d\tau$) as a function of dimensionless time $\tau = t/t_{\rm ff}$ for the simulations in Table 2.1. The points show f_* as a function of time from the simulations, the solid orange line shows a fit to $f_*(\tau)$ using Fermi function (Eq. 2.10), and the solid blue line shows SFR$_{ff}$ using the fit formula. The Fermi function is a good fit to the data, and from it we can calculate the peak star formation rate and star formation time (shown in Fig. 2.12).

2.3.3 Star formation law in molecular clouds

Next, we ask the question of what is the physical interpretation of the empirical relationship we derived for the star formation efficiency as a function of cloud mass and compactness. To answer this question we first fit the SFE $f_*(\tau)$ with an analytic function, where $\tau \equiv t/t_{\rm ff}$, in order to minimise the stochastic noise of the simulations. The $f_*(\tau)$ has a shape that can be fit by an $\arctan$ function or the Fermi function:

$$f_F(\tau) = \frac{f_0}{e^{-(\tau-\tau_0)/\Delta\tau} + 1}. \tag{2.10}$$

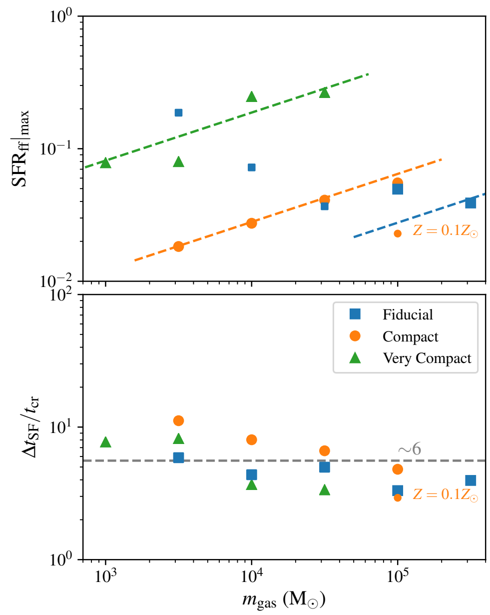

Figure 2.12: *(Top)*: Maximum dimensionless star formation rate per free-fall time, $\mathrm{SFR}_{ff}|_{max} = \mathrm{d}f_*/\mathrm{d}\tau|_{max}$, where $\tau = t/t_{ff}$ v.s. gas mass of the cloud. The dashed lines show a power-law fit to the data (see Eq. 2.11). The smaller squares are data points not used for the fit because of the lack of a realistic feedback loop in these simulations. *(Bottom)*: The ratio of star-formation time $\Delta t_{\rm SF}$ to sound-crossing time $t_{\rm cr} = r_{\rm gas}/c_s$, where $c_s = 10\ \mathrm{km\,s^{-1}}$. This ratio is close to a constant (the gray dashed line). Over-pressured H II regions require approximately 6 crossing times to suppress star formation.

Both fits give similar results for the purpose of interpreting $f_*(\tau)$. In Figure 2.11 we show the fit to $f_*(\tau)$ using the Fermi function f_F (orange solid curves) and its time derivative (blue curves), or the dimensionless SFR per free-fall time, $\mathrm{SFR}_{ff} \equiv \mathrm{d}f_*/\mathrm{d}\tau \approx \mathrm{d}f_F/\mathrm{d}\tau$. The fits are a good approximations to the data points from the simulations (solid points), except for a few clouds where $f_*(\tau)$ has a pit near the end of the star formation process.

The value of the peak of SFR_{ff} has a weak dependence on the cloud mass (see top panel in Figure 2.12) and a stronger dependence on the cloud mean density. We fit the $\mathrm{SFR}_{ff}|_{\rm max}$ with a power-law similar to Eq. (2.9):

$$\mathrm{SFR}_{ff}|_{max} \approx 1.1\% \left(\frac{m_{gas}}{10^4 M_\odot}\right)^{0.36} \left(1 + \frac{\overline{n}_{\rm gas}}{n_{cri}}\right)^{\alpha_f} \tag{2.11}$$

where $\alpha_f \approx 1.0$ and n_{cri} is the same critical density as in Eq. (2.8)[2]. The duration of the star formation burst in units of $t_{\rm ff}$, $\Delta\tau_{SF}$, is proportional to the width of the SFR$_{ff}$ shown as the blue lines in Fig. 2.11. The function $\mathrm{d}f_F/\mathrm{d}\tau$ has a peak value $f_0/4\Delta\tau$ and a full-width half-maximum $3.526\Delta\tau$. We define $\Delta\tau_{SF} \equiv 4\Delta\tau$ so that

$$f_{*,\rm tot} \approx f_0 = \frac{\mathrm{d}f_F}{\mathrm{d}\tau}|_{\rm max} \times \Delta\tau_{SF}. \tag{2.12}$$

Inspecting Fig. 2.11 we see that $\Delta\tau_{SF}$ increases with the cloud mass, and appears to be proportional to the dimensionless sound crossing time of the cloud. Here we define the sound crossing time, $t_{\rm cr}$, as the ratio of the time it takes for a sound wave with $c_s = 10$ km/s to cross the cloud radius. Similarly to the dimensionless $\Delta\tau_{\rm SF}$, we define $\tau_{cr} \equiv t_{\rm cr}/t_{\rm ff}$, where the free-fall time is defined at the cloud's mean density. We find that $\Delta\tau_{\rm SF}/\tau_{\rm cr} = \Delta t_{\rm SF}/t_{\rm cr} \approx 6$ (the horizontal line in the bottom panel of Fig. 2.12). This results makes physical sense because the feedback mechanism stops star formation by creating over-pressured H II regions which require a constant number of crossing times to expel the gas.

Since $t_{\rm cr} \propto r_{\rm gas} \propto (m_{gas}/\overline{n})^{1/3}$, we have $\Delta\tau_{SF} \propto t_{cr}/t_{\rm ff} \propto m_{gas}^{1/3}\overline{n}^{1/6}$. From Equation (2.12) we derive $f_{*,\rm tot} \propto m_{gas}^{0.69}\overline{n}_{gas}^{0.17}(1+\overline{n}_{gas}/n_{\rm cri})^{1.0}$, which is in good agreement with Eq. (2.9) for $\overline{n} > n_{\rm cri}$. The agreement can be improved further by considering a more accurate fit to τ_{SF}/τ_{cr} rather than assuming a constant value ~ 6. Namely, considering the weak dependence of the star formation timescale on the cloud mass and density: $\Delta\tau_{SF}/\tau_{cr} \propto m_{gas}^{-0.3}\overline{n}_{gas}^{-0.2}$.

From the analysis and interpretation of these results we can thus derive a star formation law in molecular clouds that can be used as a more accurate sub-grid recipe in cosmological

[2] The value of α_f is somewhat correlated with $n_{\rm cri}$. We sample a sequence of $n_{\rm cri}$ for which we obtain a good fit and find that for $n_{\rm cri}$ in the range ~ 400 – $1600{\rm cm}^{-3}$, the corresponding $\alpha_{\rm f}$ is in the range $0.85 - 1.1$.

simulations that resolve the molecular cloud phase. Assuming a constant mean volume for the cloud we have $f_* \equiv m_*/m_{\rm gas} \approx \rho_*/\rho_{\rm gas}$. Therefore, assuming $\rho_{\rm gas} = {\rm const}$ (*i.e.*, assuming $f_* \ll 1$) during the episode of star formation, which has a duration Δt_{SF}, we have SFR$_{ff}|_{max} \equiv df_*/d\tau|_{\rm max} \approx d\rho_*/dt|_{\rm max}(t_{\rm ff}/\rho_{\rm gas})$, which implies:

$$\frac{{\rm d}\rho_*}{{\rm d}t} = \epsilon \left(\frac{m_{gas}}{10^4 M_\odot}\right)^{0.36} \left(1 + \frac{\overline{\rho}_{\rm gas}}{\rho_{\rm cri}}\right)^{1.0} \frac{\overline{\rho}_{\rm gas}}{t_{\rm ff}} \propto (\overline{\rho}_{\rm gas})^{2.5}, \qquad \text{if } \overline{n}_{gas} > n_{cri} \approx 10^3 {\rm cm}^{-3} \tag{2.13}$$

with $\epsilon = 1.1\%$ for solar metallicity and $\epsilon = 0.36\%$ for $Z < 0.1\,{\rm Z}_\odot$ (see § 2.3.4). A star formation law $d\rho_*/dt \propto \rho_{\rm gas}^n$ with $n = 1$ or $n = 1.5$ is most often used as a sub-grid star formation recipe in cosmological simulations. Therefore we suggest that a steeper power-law index $n \sim 2.5$ is a better description of the star formation rate at densities typical of molecular clouds in high-redshift galaxies. This theoretical result can, in principle, be tested against observations of young stellar clusters in our galaxy.

Krumholz et al. (2012) suggests a universal star formation law in which the star formation rate is $\sim 1.5\%$ of the molecular gas mass per local free-fall time. Eq. 2.11 results in SFR$_{ff} \approx 1\% - 2\%$ at $\overline{n}_{gas} \lesssim 10^3{\rm cm}^{-3}$, in agreement with this work for local molecular clouds. However, Krumholz et al. (2012) finds this universal value also for high-redshift galaxies but averaged over the whole galaxy. We find that SFR$_{ff}$ can be as large as $\sim 10\%$ for more compact clouds typical of high-redshift galaxies, and/or more massive clouds (see also the top panel of Fig. 12). A direct comparison to Krumholz's results is not trivial for the galaxy as a whole, as it depends on modelling the multi-phase ISM of high-z galaxies.

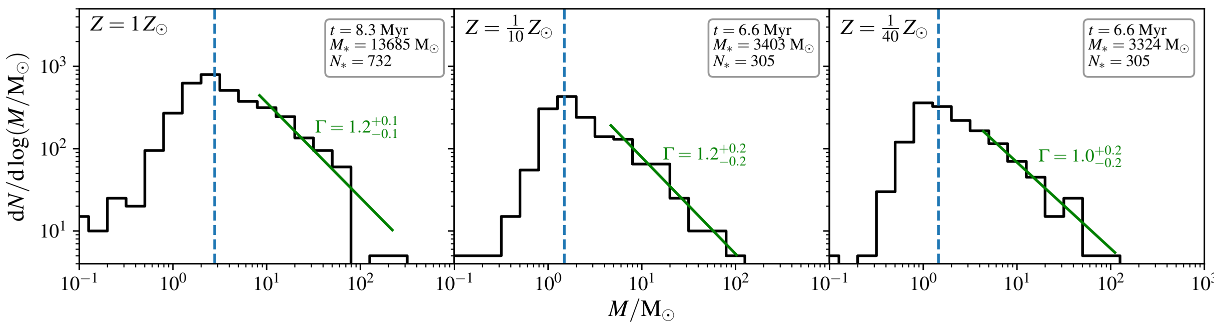

Figure 2.13: Same as Fig. 2.7 but for the L-C cloud with various metallicities. The metallicities are marked at the top-left corner. We see no significant difference on the shape of the IMF for clouds with different metallicities.

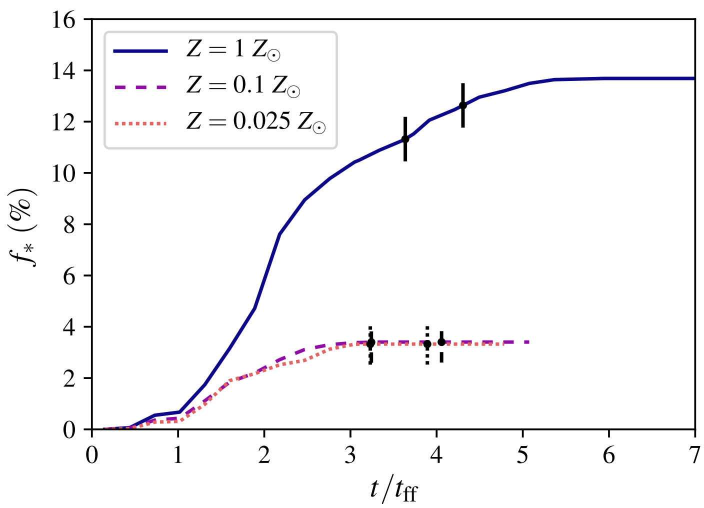

Figure 2.14: Same as Fig. 2.9 but for the L-C cloud with different gas metallicities, as shown in the legend.

2.3.4 Effects of Lowering the Gas Metallicity

The set of compact and very compact molecular clouds we have analysed are meant to represent clouds typical of the ISM in dwarf galaxies forming at high-redshift. However, we also know that the gas metallicity in these dwarf galaxies is less than solar. In order to keep the parameter study consistent we have not changed the gas metallicity in the compact and very compact clouds, but in this section we briefly test the influence of gas metallicity [Fe/H] on the star formation rate and IMF. In our simulations, changing the gas metallicty affects the cooling of the gas (see Section 2.2.4).

Figure 2.13 is the same as Figure 2.7 but for the LC clouds with metallicity $Z = 1\ Z_{\odot}$, $0.1\ Z_{\odot}$, and $0.025\ Z_{\odot}$. The shape of the IMF is not affected by the gas metallicity. Only the normalisation of the IMF is influenced because of the lower SFE in the low-metallicity simulations. This is in agreement result of previous theoretical works (*e.g.* Myers et al., 2011; Bate, 2014).

Lower metallicity translates into lower cooling rates, which should result in lower efficiency of star formation. Figure 2.14 shows f_* as a function of time for the large compact cloud (LC) with intermediate (0.1 $Z_{\odot}$) and low (0.025 $Z_{\odot}$) metallicity. The effect of lowering the metallicity by a factor of ten, from $Z = 1\ Z_{\odot}$ to $Z = 0.1\ Z_{\odot}$ is to lower f_* at the end of the simulation by roughly a factor of 5. But lowering further the metallicity from $Z = 0.1\ Z_{\odot}$ to $Z = 0.025\ Z_{\odot}$ does not change f_*, suggesting that f_* decreases almost linearly with the metallicity from solar to $Z = 0.2\ Z_{\odot}$, but this effect saturates when further lowering the metallicity. The SFE decreases mainly because the peak SFR decreases by roughly a factor of 3 with decreasing metallicity, while the duration of the star formation episode is nearly unchanged (see small circles in Fig. 2.12).

In order to better understand what is causing a decrease of the SFR at lower metallicity, we have analysed the density and temperature structure of these two simulations. We found that lowering the metallicity causes the temperature and the thermal pressure inside H II regions to increase by roughly a factor of 3, as shown in Figure 2.15. This result is in agreement with observations and theoretical models of H II regions. The strength of feedback, due to the increase of thermal pressure inside the H II regions, is therefore stronger at lower metallicity, resulting in a lower star formation efficiency. This result on the effect of the gas metallicity goes in the opposite

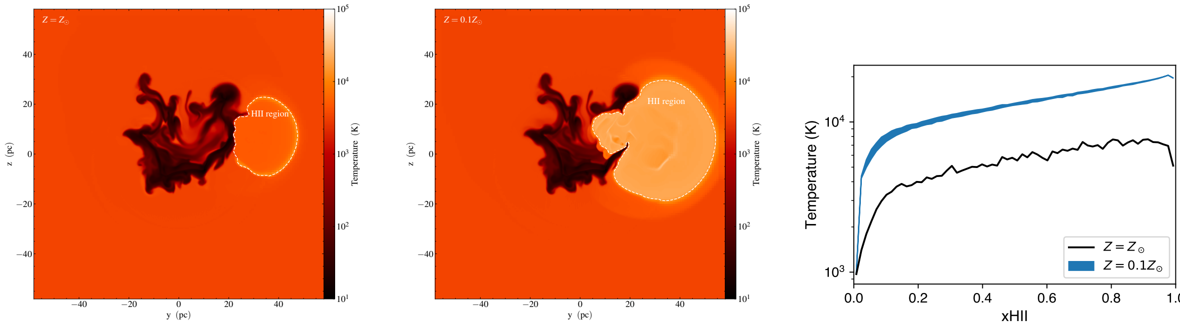

Figure 2.15: *(Left and Middle)*. Slice plots of the gas temperature from simulations with metallicities $Z = 1Z_{\odot}$ (left) and $Z = 0.1Z_{\odot}$ (middle). The snapshots from these two simulations are chosen to be nearly at the same evolutionary stage. We observe a factor a ~ 3 increase in temperature (and thermal pressure) within the H II region as the metallicity of the gas is decreases from solar metallicity to a tenth of it. Right: Phase plot of gas temperature vs hydrogen ionising fraction for the H II regions shown in the left and middle panels. The blue shaded area refers to the $Z = 0.1Z_{\odot}$ simulation for a small range of evolutionary times around the time of the $Z = 1Z_{\odot}$ snapshot (shown as black line).

direction of what was found by Howard et al. (2018a). In their work, lowering the metallicity of the gas cloud reduces the opacity of the gas to radiation and results in higher gas accretion which leads to an increase of the total star formation efficiency. However, this can be understood because in their simulations the dominant feedback mechanism is IR radiation pressure while, contrary to our work, UV feedback does not play a major role. However, their simulations describe more massive clouds and have much lower resolution than the simulations in our work.

2.4 Summary and Conclusions

In this chapter, the first of a series, we present a large set of radiation-magneto-hydrodynamic simulations of star formation in self-gravitating, turbulent molecular clouds. The initial conditions for the clouds are isothermal spheres initially close to virial equilibrium, being supported by turbulent motions.

We model the formation of individual massive stars, replacing self-gravitating clumps that are collapsing below the resolution of the simulations with sink particles, which represent individual massive stars, therefore including their UV radiation feedback self-consistently. We consider a grid of simulations varying the cloud masses between $m_{\rm gas} = 10^3$ M$_\odot$ to 3×10^5 M$_\odot$. Depending on the cloud mass, we resolve scales between 200 AU to 2000 AU. In addition, we consider three compactness for the molecular clouds. The fiducial clouds have gas mean number densities typical of those observed in the local universe ($\overline{n}_{\rm gas} = 1.8 \times 10^2$ cm^{-3}). Compact ($\overline{n}_{\rm gas} = 1.8 \times 10^3$ cm^{-3}) and very compact ($\overline{n}_{\rm gas} = 1.8 \times 10^4$ cm^{-3}) clouds represent clouds expected to exist in high-redshift galaxies. We also partially explore varying the gas metallicity. Our goal is to run a realistic set of simulations of formation of star clusters in molecular clouds to understand the physics of star formation across cosmic time: from conditions typical of present-day ISM to the the higher-pressure environments found in the ISM of higher redshift galaxies.

In this chapter we focus on understanding the IMF, the SFR and SFE as a function of the cloud mass and compactness. We derive a star formation law valid at densities typical of high-redshift molecular clouds that will help to justify and inform the sub-grid star formation recipe used in cosmological simulations.

A summary of simulations results is presented in Table 2.2. The main findings of this chapter are the following:

1. We find that a Chabrier (or Kroupa) stellar IMF with the correct normalization can can be reproduced in all of our simulations if we assume that each star-forming gas clump (sink particle) fragments into stars with a power-law mass function with log-slope $\Gamma \sim 0.8$, flatter than the mass function of the sink particles, which have Kroupa slope $\Gamma \sim 1.3$. With this

Table 2.2: A collection of results. (a) Stellar mass of the cluster formed from the cloud. (b) Total star formation efficiency, equal to $m_{cl}/m_{\rm gas}$. (c) Peak dimensionless star formation rate per free-fall time. (d) Negative IMF power-law slope Γ: $\mathrm{d}N/\mathrm{d}\log m \propto m^{-\Gamma}$. (e) Number of SNe explosions in 7 free-fall time of simulation.

Cloud name	$m_{\rm gas}(\mathrm{M}_\odot)$	$\overline{n}_{\rm gas}(\mathrm{cm}^{-3})$	$\Sigma\,(\mathrm{M}_\odot\ \mathrm{pc}^{-2})$	$Z(Z_\odot)$	$m_{cl}(\mathrm{M}_\odot)$	TSFE (%)	SFR$_{ff}$	IMF slope	$n_{\rm SN}$
XS-F	3.2×10^3	1.8×10^2	41	1	3.8×10^2	12.1	0.18	$1.0^{+0.4}_{-0.3}$	2
S-F	1.0×10^4	1.8×10^2	61	1	5.1×10^2	5.1	0.062	$1.3^{+0.3}_{-0.3}$	2
M-F	3.2×10^4	1.8×10^2	89	1	1.4×10^3	4.3	0.042	$1.1^{+0.2}_{-0.2}$	12
L-F	1.0×10^5	1.8×10^2	131	1	5.7×10^3	5.7	0.053	$1.2^{+0.2}_{-0.1}$	38
XL-F	3.2×10^5	1.8×10^2	193	1	2.5×10^4	7.8	0.043	$1.1^{+0.1}_{-0.1}$	142
XS-C	3.2×10^3	1.8×10^3	193	1	1.0×10^2	3.3	0.033	$0.5^{+0.8}_{-0.0}$	0
S-C	1.0×10^4	1.8×10^3	283	1	5.3×10^2	5.3	0.052	$1.6^{+0.1}_{-0.3}$	1
M-C	3.2×10^4	1.8×10^3	415	1	3.0×10^3	9.4	0.047	$1.2^{+0.2}_{-0.2}$	5
L-C	1.0×10^5	1.8×10^3	609	1	1.4×10^4	13.7	0.099	$1.2^{+0.1}_{-0.1}$	47
L-C-lm	1.0×10^5	1.8×10^3	609	1/10	3.4×10^3	3.4	0.021	$1.2^{+0.2}_{-0.2}$	5
L-C-xlm	1.0×10^5	1.8×10^3	609	1/40	3.3×10^3	3.3	0.025	$1.0^{+0.2}_{-0.2}$	5
XXS-VC	1.0×10^3	1.8×10^4	609	1	9.8×10^1	9.8	0.099	$0.5^{+0.9}_{-0.0}$	0
XS-VC	3.2×10^3	1.8×10^4	894	1	5.1×10^2	16.1	0.2	$1.0^{+0.3}_{-0.2}$	0
S-VC	1.0×10^4	1.8×10^4	1312	1	3.2×10^3	32.2	0.31	$1.5^{+0.2}_{-0.2}$	0
M-VC	3.2×10^4	1.8×10^4	1925	1	1.5×10^4	46.6	0.25	$1.4^{+0.1}_{-0.1}$	0
L-VC	1.0×10^5	1.8×10^4	2827	1	2.7×10^4	27.4		$1.3^{+0.1}_{-0.1}$	0

prescription we find that statistically about 40% of the mass of the sink particle is locked into a single star, while the remaining 60% is distributed into smaller mass stars. This result is in agreement with the observed mass function of dense cores in some molecular clouds. The resolution study shows that increasing the resolution changes the CMF, but the total mass in cores remains nearly the same. For these reasons, we find that the model in which cores fragment with nearly 100% efficiency into stars is the most likely model, although we cannot rule out alternative scenarios.

2. The IMF of stars at any time during the star formation burst is Chabrier-like. Because the total mass in stars is initially small and grows with time, at the beginning of the simula-

tions, statistically, there are fewer high-mass stars. The apparent behaviour is that low and intermediate-mass stars form first, followed by the most massive stars.

3. The star formation law that best describes star formation in molecular clouds found in the local universe (*i.e.*, in fiducial simulations) is $d\rho_*/dt \approx 1.1\%\rho_{gas}/t_{ff}$. In dense molecular clouds with $\overline{n}_{\rm gas} > n_{cri} \approx 10^3$ cm^{-3}, more typically found in high-redshift galaxies, we find $d\rho_*/dt \approx 1.1\%\rho_{gas}^2/(\rho_{cri}t_{ff}) \propto \rho_{\rm gas}^{2.5}$. The duration of the star formation episode in all simulations is roughly 6 sound crossing times of the cloud radius (with $c_s = 10$ km/s).

4. For gas at solar metallicity the total star formation efficiency in the cloud is $f_{*,tot} = 2\%(m_{\rm gas}/10^4\ {\rm M}_\odot)^{0.4}(1+\overline{n}_{\rm gas}/n_{\rm cri})^{0.91}$, where $n_{\rm cri} \approx 10^3$ cm^{-3}, also in agreement with *(iii)*.

5. At metallicity $Z < 0.1$ Z$_\odot$, f_* is reduced by a factor of ~ 5 due to more efficient UV feedback caused by the higher temperature and pressure of H II regions. We do not observe a dependence of the IMF on the metallicity, in agreement with previous studies.

6. We note that the most compact and massive clouds appear to form globular cluster progenitors, in the sense that star clusters remain gravitationally bound after the gas has been mostly expelled. We plan to explore in detail the dynamics of these bound star clusters and possible relationships with the star formation efficiency and the escape fraction of ionising photons in future works.

The second project of this series we will focus on calculating the escape fraction of ionising photons, $\langle f_{\rm esc}^{\rm MC}\rangle$, from molecular clouds. This is the first necessary step for a realistic estimate of the escape fraction from galaxies. Finally, in a third project we will take a closer look at the dynamics of the star clusters and connect with important questions on the role of compact star clusters in creating seed black holes that might grow into supermassive black holes, and questions in Near Field Cosmology on the origin of globular clusters and ultra-faint dwarfs.

Chapter 3: Simulating Star Clusters Across Cosmic Time: II. Escape Fraction of Ionizing Photons from Molecular Clouds

In this chapter, we calculate the hydrogen and helium-ionizing radiation escaping star forming molecular clouds, as a function of the star cluster mass and compactness, using a set of high-resolution radiation-magneto-hydrodynamic simulations of star formation in self-gravitating, turbulent molecular clouds. In these simulations, presented in He, Ricotti and Geen (2019), the formation of individual massive stars is well resolved, and their UV radiation feedback and lifetime on the main sequence are modelled self-consistently. We find that the escape fraction of ionizing radiation from molecular clouds, $\langle f_{\rm esc}^{\rm MC} \rangle$, decreases with increasing mass of the star cluster and with decreasing compactness. Molecular clouds with densities typically found in the local Universe have negligible $\langle f_{\rm esc}^{\rm MC} \rangle$, ranging between 0.5% to 5%. Ten times denser molecular clouds have $\langle f_{\rm esc}^{\rm MC} \rangle \approx 10\% - 20\%$, while $100\times$ denser clouds, which produce globular cluster progenitors, have $\langle f_{\rm esc}^{\rm MC} \rangle \approx 20\% - 60\%$. We find that $\langle f_{\rm esc}^{\rm MC} \rangle$ increases with decreasing gas metallicity, even when ignoring dust extinction, due to stronger radiation feedback. However, the total number of escaping ionizing photons decreases with decreasing metallicity because the star formation efficiency is reduced. We conclude that the sources of reionization at $z > 6$ must have been very compact star clusters forming in molecular clouds about $100\times$ denser than in today's Universe, which lead to a significant production of old globular cluster progenitors.

3.1 Introduction

A large observational effort is underway to understand the epoch of reionization, both by observing the high-redshift sources of radiation with HST and JWST (Ellis et al., 2013; Sharma et al., 2016; Oesch et al., 2016) and detecting the 21cm signal from neutral hydrogen in the intergalactic medium (IGM) (e.g. Bowman et al., 2018). Numerical simulations of galaxy formation are becoming increasingly realistic, but the question of which are the sources that propelled reionization is largely unanswered. To answer this question it is necessary to know the mean value of the escape fraction of ionizing radiation, $\langle f_{\rm esc}^{\rm gal} \rangle$, from dwarf and normal galaxies into the IGM at redshift $z > 6$. This quantity is arguably the most uncertain parameter in models of reionization. It is difficult to measure, and for the cases in which it has been measured in galaxies at $z \approx 1$, upper limits of $f_{esc} \approx 2$ per cent has been typically found (Bridge et al., 2010, *e.g.*,). Using staking techniques in Lyman-break galaxies at $z \sim 3$ some authors claimed higher values of f_{esc} at 5–7 per cent (Vanzella et al., 2012; Nestor et al., 2013). However, according to simulations of reionization a mean value of $\langle f_{\rm esc}^{\rm gal} \rangle \gtrsim 10-20\%$ is required to reionize the IGM by $z \sim 6.2$ (Ouchi et al., 2009; Robertson et al., 2015; Khaire et al., 2016). This value is too large with respect to what observed in local galaxies, unless at high-redshift the value of $\langle f_{\rm esc}^{\rm gal} \rangle$ is significantly larger than in the local Universe.

Recently, a handful of galaxies at high redshifts have been confirmed to have large Lyman continuum (LyC) escape fractions. *Ion2* and *Q1549-C25* are the only two $z \sim 3$ galaxies with a direct spectroscopic detection of uncontaminated LyC emission (Vanzella et al., 2016; Shapley et al., 2016). Escape fractions of $\gtrsim 50\%$ are inferred for both of them. Vanzella et al. (2018) reported the highest redshift individually-confirmed LyC-leaky galaxy, *Ion3*, at $z = 4$. As a proxy for high-z galaxies, Izotov et al. (2018) selected local compact star-forming galaxies in the redshifts range $z = 0.2993 - 0.4317$, using the Cosmic Origins Spectrograph on HST. They found LyC emission with f_{esc} in a range of 2-72 per cent. We should note that $\langle f_{\rm esc}^{\rm gal} \rangle$ in models of reionization is the averaged value over all star forming galaxies, but also a time-average of $f_{esc}(t)$ over the duration of the starburst.

A number of attempts have been made to predict the escape fraction of hydrogen LyC photons from galaxies using analytic models and simulations of galaxy formation (Ricotti & Shull, 2000; Gnedin et al., 2008; Wise & Cen, 2009; Razoumov & Sommer-Larsen, 2010; Yajima et al., 2011; Wise et al., 2014; Ma et al., 2015; Xu et al., 2016), but because of the complexity of the problem and the uncertainty about the properties of the sources of reionization, the results are inconclusive. In addition, any realistic theoretical estimate of $\langle f_{\rm esc}^{\rm gal} \rangle$ must take into account the escape fraction of ionizing radiation from the molecular clouds in which the stars are born, $\langle f_{\rm esc}^{\rm MC} \rangle$, a sub-grid parameter in galaxy-scale and in cosmological-scale simulations. Typically $\langle f_{\rm esc}^{\rm MC} \rangle$ is set to unity in cosmological simulations of reionization, which could dramatically overpredict $\langle f_{\rm esc}^{\rm gal} \rangle$ (*e.g.*, Ma et al., 2015). More recent simulations which do not make a priori assumptions about subgrid escape fractions (*e.g.*, Rosdahl et al., 2018) remain very sensitive to small-scale effects. In addition, they require that outflows from star-forming regions clear channels in the galaxies while ionising radiation is still being emitted in large enough quantities, for example by invoking binary stellar evolution models.

A small body of work exists that estimates $\langle f_{\rm esc}^{\rm MC} \rangle$ in star-forming molecular clouds (Dale et al., 2014; Howard et al., 2017, 2018b; Kimm et al., 2019), although systematic studies remain limited in number. Dale et al. (2014) finds that $\langle f_{\rm esc}^{\rm MC} \rangle \propto 1/L_{\rm cl}$, or that the escaping ionizing radiation rate from star clusters of different masses is roughly constant at a few $\times 10^{49}$ s^{-1}. However, in this work the calculation of $\langle f_{\rm esc}^{\rm MC} \rangle$ assumes that all the radiation is emitted from a point source located at the center of the cloud. Also, in this work the clouds have the same initial density, similar to today's molecular clouds associated with young star forming regions. Howard et al. (2018b) find the overall escape fraction is not a monotonic function of the cloud mass, $m_{\rm gas}$, varying from 31% for $m_{\rm gas} = 10^4 {\rm M}_\odot$, to 100% for $m_{\rm gas} = 10^5 {\rm M}_\odot$, and 9% for from $m_{\rm gas} = 10^6 {\rm M}_\odot$. They also use a rather crude estimation of $\langle f_{\rm esc}^{\rm MC} \rangle$ in their simulations by assuming that all the radiation is emitted from a point source located at the center of the star cluster. Observationally, escape fractions from molecular clouds remain uncertain. Doran et al. (2013) find an escape fraction of ionising photons of 6% from 30 Doradus in the Large Magellanic Cloud, but their error bars give a maximum possible escape fraction of 71%.

In this chapter, the second of a series, we estimate $\langle f_{\rm esc}^{\rm MC} \rangle$ using a large set of realistic simulations of star cluster formation in molecular clouds. These are radiation-magneto-hydrodynamic simulations of star formation in self-gravitating, turbulent molecular clouds, presented in He, Ricotti & Geen (2019) (hereafter, Chapter 2). We model self-consistently the formation of individual massive stars, including their UV radiation feedback and their lifetime. We consider a grid of simulations varying the molecular cloud masses between $m_{gas} = 10^3$ M$_\odot$ to 3×10^5 M$_\odot$, and resolving scales between 200 AU to 2000 AU. We also varied the compactness of the molecular clouds, with mean gas number densities typical of those observed in the local Universe ($\overline{n}_{gas} \sim 1.8 \times 10^2$ cm^{-3}) and denser molecular clouds ($\overline{n}_{gas} \sim 1.8 \times 10^3$ cm^{-3} and 1.8×10^4 cm^{-3}) expected to exist, according to cosmological simulations (Ricotti, 2016), in high-redshift galaxies. We also partially explored the effects of varying the gas metallicity.

Previous works have suggested that the progenitors of today's old globular clusters, and more generally compact star cluster formation, may have been the dominant mode of star formation before the epoch of reionization, and that GC progenitors may have dominated the reionization process (Ricotti, 2002; Katz & Ricotti, 2013, 2014; Schaerer & Charbonnel, 2011; Boylan-Kolchin, 2018). Ricotti (2002) have shown that if a non-negligible fraction of today's GCs formed at $z > 6$ and had $\langle f_{\rm esc}^{\rm MC} \rangle \sim 1$, they would be a dominant source of ionizing radiation during reionization. Katz & Ricotti (2013) presented arguments in support of significant fraction of today's old GCs forming before the epoch of reionization. However, although it seems intuitive, it has not been shown that $\langle f_{\rm esc}^{\rm MC} \rangle$ from proto-GCs forming in compact molecular clouds is higher than $\langle f_{\rm esc}^{\rm MC} \rangle$ in more diffuse clouds. Answering this question, and quantifying the contribution of compact star clusters to reionization is a strong motivation for this work.

In a scenario in which the progenitors of today's GCs dominate the reionization process, we expect a short effective duty cycle in the rest-frame UV bands, leading to a large fraction of halos of any given mass being nearly dark in between short-lived bursts of star formation. In addition, large volumes of the universe would be only partially ionized inside relic H II regions produced by bursting star formation. Hartley & Ricotti (2016) have shown that the number of recombinations and therefore the number of ionizing photons necessary to reionize the IGM by $z = 6.2$ is lower in this class of models with short bursts of star formation with respect to models in which star formation is continuous (producing fully ionized H II bubbles). In summary, for the reasons discussed above, compact star clusters are a very favorable candidate to propel reionization: i) deep field surveys of sources at $z > 6$ suggest that the sources of reionization are a numerous but faint population. Compact star clusters would fit this requirement, also due to their short duty cycle. ii) The value of $\langle f_{\rm esc}^{\rm MC} \rangle$ necessary for reionization is reduced if star formation is bursty. iii) We naively expect that compact star clusters have higher star formation efficiency (SFE) and $\langle f_{\rm esc}^{\rm MC} \rangle$ than less compact star clusters. This last point is the focus of this chapter.

This chapter is organised as follows. In Section 3.2 we present the simulations and the analysis methods. Section 3.3 presents all the results from the numerical simulations regarding $\langle f_{\rm esc}^{\rm MC} \rangle$, while in Section 3.4 we discuss the physical interpretation of the results and their analytical modelling. We also discuss the implications for reionization assuming a simple power-law distribution of the cluster masses, similar to what is observed in the local universe. A summary of the results and conclusions are in Section 3.5.

3.2 Numerical Simulations and Methods

3.2.1 Simulations

The results presented in this chapter are based on a grid of 14 simulations of star formation in molecular clouds with a range of initial gas densities and masses, and 2 simulations varying the initial gas metallicity. For details about the simulations and main results regarding the IMF, star formation efficiency and star formation rate, we refer to Chatper 2. Here, for the sake of completeness, we briefly describe the main characteristic of the code we used, and the simulations set up.

We run the simulations using an Adaptive Mesh Refinement radiative magneto-hydrodynamical code RAMSES (Teyssier, 2002; Bleuler & Teyssier, 2014). Radiative transfer is implemented using a first-order moment method described in Rosdahl et al. (2013). The ionising photons interact with neutral gas and we track the ionization state and cooling/heating processes of hydrogen and helium. We include magnetic fields in the initial conditions. We do not track the chemistry of molecular species.

We simulate a set of isolated and turbulent molecular clouds that collapse due to their own

Table 3.1: A table of parameters in all simulations.

Compactness	Cloud Name	m_{gas} ($M_\odot$) [a]	$\overline{n}_{gas}$ (cm^{-3}) [b]	Σ ($M_\odot$ pc^{-2}) [c]	Z ($Z_\odot$) [d]	Photon bins	t_{ff} (Myr) [e]	t_{cr} (Myr) [f]
Fiducial	XS-F	3.2×10^3	1.8×10^2	41	1	H, He, He^+	4.4	0.5
Fiducial	S-F	1.0×10^4	1.8×10^2	61	1	H, He, He^+	4.4	0.7
Fiducial	M-F	3.2×10^4	1.8×10^2	89	1	H, He, He^+	4.4	1.1
Fiducial	L-F	1.0×10^5	1.8×10^2	131	1	H, He, He^+	4.4	1.5
Fiducial	XL-F	3.2×10^5	1.8×10^2	193	1	H, He, He^+	4.4	2.3
Compact	XS-C	3.2×10^3	1.8×10^3	193	1	H, He, He^+	1.4	0.23
Compact	S-C	1.0×10^4	1.8×10^3	283	1	H	1.4	0.33
Compact	M-C	3.2×10^4	1.8×10^3	415	1	H	1.4	0.5
Compact	L-C	1.0×10^5	1.8×10^3	609	1	H	1.4	0.7
Compact	L-C-lm	1.0×10^5	1.8×10^3	609	1/10	H	1.4	0.7
Compact	L-C-xlm	1.0×10^5	1.8×10^3	609	1/40	H	1.4	0.7
Very Compact	XXS-VC	1.0×10^3	1.8×10^4	609	1	H, He, He^+	0.44	0.07
Very Compact	XS-VC	3.2×10^3	1.8×10^4	894	1	H	0.44	0.1
Very Compact	S-VC	1.0×10^4	1.8×10^4	1312	1	H	0.44	0.15
Very Compact	M-VC	3.2×10^4	1.8×10^4	1925	1	H	0.44	0.23
Very Compact	L-VC	1.0×10^5	1.8×10^4	2827	1	H	0.44	0.33

(a) Initial cloud mass, excluding the envelope. (b) Mean number density of the cloud, excluding the envelope. The core density is ~ 5 times higher. (c) The mean surface density in a square of the size of the cloud radius. (d) Metallicity of the gas used in the cooling function, Z = [Fe/H]. (e) The global free-fall time of the cloud ($t_{ff} \equiv 3\sqrt{\frac{3\pi}{32G\rho_c}} \approx 1.3\sqrt{\frac{3\pi}{32G\overline{\rho}}}$). (f) Sound crossing time $r_{\rm gas}/c_s$ with $c_s = 10$ km/s.

gravity. The clouds have initially a spherically symmetric structure with density profile of a non-singular isothermal sphere with core density ρ_c. The initial density profile is perturbed with a Kolmogorov turbulent velocity field with an amplitude such that the cloud is approximately in virial equilibrium. A summary of the parameters of the simulations is presented in Table 3.1.

Proto-stellar cores collapsing below the resolution limit of the simulations produce sink particles. These sinks represent molecular cloud cores in which we empirically assume that fragmentation leads to formation of a single star with a mass roughly 40% of the mass of the sink particle, and the remaining 60% of the mass fragments into smaller mass stars. With this prescription we reproduce the slope and normalization of the IMF at the high-mass end. Stars emit hydrogen and helium ionising photons according to their mass using Vacca et al. (1996) emission rates with a slight modification. We extend the high-mass-end power-law slope down to about $1\,\mathrm{M}_{\odot}$, therefore increasing the feedback of stars with masses between 1 and $30\,\mathrm{M}_{\odot}$[1]. The gas is ionized and heated by massive stars, producing over-pressurised bubbles that blow out the gas they encounter. In our simulations low mass stars and proto-stellar cores do not produce any feedback. We do not include mechanical feedback from supernova (SN) explosions and from stellar winds and we also neglect the effect of radiation pressure from infrared radiation. However, with the exception of a sub-set of simulations representing today's molecular clouds (the two most massive clouds in lowest density set), all the simulations stop forming stars before the explosion of the first SN. Therefore, neglecting SN feedback is well justified in these cases.

[1]This modification was an unintended result of a coding error, but further investigations have shown that it is important in producing the correct slope of the IMF.

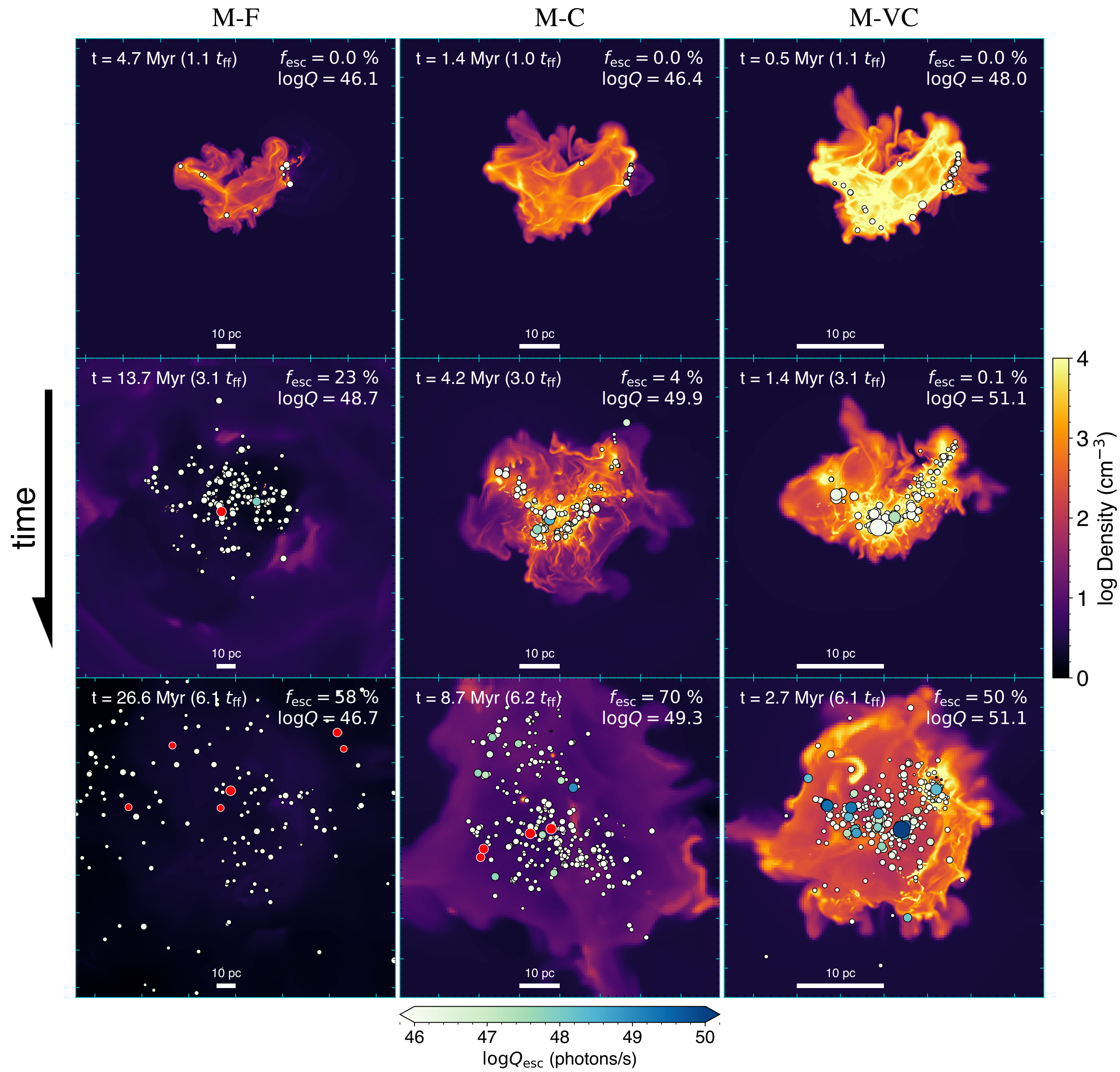

Figure 3.1: Time sequence plot of line-of-sight projections of density-weighted gas density from the Medium mass-Fiducial (M-F), Compact (M-C), and Very Compact (M-VC) clouds. These clouds have initial mass of $3 \times 10^4 \mathrm{M}_\odot$ and initial mean density of 2×10^2, 2×10^3, and 2×10^4 cm^{-3}. Sink particles are plotted as filled circles on top of the density map. These circles have radii related to the mass. The circles are filled with colors according to their escaped ionizing luminosity with the colorbar shown at the bottom. Sink particles with greater mass are plotted on top of those with lower mass to make the former ones more prominent. The time marked at the top-left corner is counted from the end of relaxation. Red circles represent stars that are dead and radiation has been shut off. The very compact cloud does not have SNe explosion during the duration of the simulation ($\sim 7t_{\mathrm{ff}} \approx 3$ Myr), as all stars live longer than 3 Myr. For the other two less compact clouds, SNe explosions occur when most of the gas is already expelled by radiation. Thus, SNe have little effect on the overall $\langle f_{\mathrm{esc}}^{\mathrm{MC}} \rangle$. For these compact clouds, most of the ionising photons are emitted during middle stage ($3 - 5t_{\mathrm{ff}}$).

3.2.2 Calculation of the Ionizing Escape Fraction

We trace rays from each sink particle and calculate the column density and the optical depth as a function of angular direction. We extract a sphere with radius of the size of the box around each sink particle and pick $12 \times 16^2 = 3072$ directions evenly distributed in the sky using the Mollweide equal-area projection. In each direction we implement a Monte Carlo integration method to calculate the neutral hydrogen column density by doing random sampling of ~ 4000 points in each ray, achieving an accuracy on the escape fraction within 1%. The column density is then converted to the escape fraction of ionizing photons in that direction (see Section 3.2.2.1). The escape fraction from each sink particle is calculated in all directions, then the escape fractions are averaged over all stars, weighting by their ionizing photon luminosity, to get the escape fraction as a function of direction and time, $f_{\rm esc}(\boldsymbol{\theta}, t)$, from the whole cluster (see Figure 3.2). We can also define a mean mean escape fraction (averaged over the whole solid angle) from individual sink particles, which is then multiplied by the hydrogen LyC emission rate, Q, to get the LyC escaping rate, $Q_{\rm esc}$, as shown in Figure 3.1.

In the calculation of the ionizing escape fraction, the emission from sink particles is shut down after the stellar lifetime, which depends on the mass of the star. We use the equation from Schaller et al. (1992) as an estimate of the lifetime of a star as a function of its mass, where M is in units of $\mathrm{M}_{\odot}$:

$$t_{MS}(M) = \frac{2.5 \times 10^3 + 6.7 \times 10^2 M^{2.5} + M^{4.5}}{3.3 \times 10^{-2} M^{1.5} + 3.5 \times 10^{-1} M^{4.5}}\ \mathrm{Myr}, \tag{3.1}$$

Note that due to the short lifetime of the clouds after the first star is formed, we do not expect the end of the star's main sequence to significantly affect the dynamical evolution of the simulations (see Section 3.2.1).

For a subset of simulations we also implement radiative transfer of helium ionizing radiation and helium chemistry (simulations that include this have He escape fractions listed in Table 3.2). The calculation of the helium ionizing escape fraction is implemented analogously to hydrogen as explained above. We use fits from Vacca et al. (1996) for the H-ionizing photon emission rate from individual stars, Q^{H} (or Q for simplicity), and fits from Schaerer (2002) for Q^{He} and Q^{He^+}.

3.2.2.1 Conversion from column density to escape fraction

The neutral hydrogen ionization cross section as a function of frequency is well approximated by a power-law (e.g. Draine, 2011):

$$\sigma(\nu) \approx \sigma_0 \left(\frac{h\nu}{I_{\mathrm{H}}}\right)^{-3} \text{ for } I_{\mathrm{H}} < h\nu \lesssim 100 I_{\mathrm{H}},$$

where $\sigma_0 = 6.304 \times 10^{-18}\,\mathrm{cm}^2$ and $I_H = 13.6$ eV. The escape fraction of photons at a frequency ν and direction $\boldsymbol{\theta}$ from a given star is

$$f_{esc,*}(\nu, \boldsymbol{\theta}) = \mathrm{e}^{-\tau(\nu,\boldsymbol{\theta})} = \mathrm{e}^{-\sigma(\nu) N_{HI}(\boldsymbol{\theta})}, \tag{3.2}$$

where $N_{HI}(\boldsymbol{\theta})$ is the neutral hydrogen column density from the surface of a star to direction $\boldsymbol{\theta}$. If we assume that the stars radiate as perfect black bodies at temperature T, then the frequency-averaged escape fraction of hydrogen-ionizing photons is

$$f_{\mathrm{esc},*}(\boldsymbol{\theta};T)=\frac{\displaystyle\int_{I_{\mathrm{H}}}^{\infty}\frac{B_\nu(\nu,T)}{h\nu}f_{esc,*}(\nu,\boldsymbol{\theta})\,\mathrm{d}(h\nu)}{\displaystyle\int_{I_{\mathrm{H}}}^{\infty}\frac{B_\nu(\nu,T)}{h\nu}\,\mathrm{d}(h\nu)}, \tag{3.3}$$

where $B_\nu(\nu,T)$ is the Planck function. The details on how $f_{\mathrm{esc},*}(\boldsymbol{\theta};T)$ behaves for stars with different masses and therefore black-body temperatures is discussed in Appendix B.1.

3.3 Results

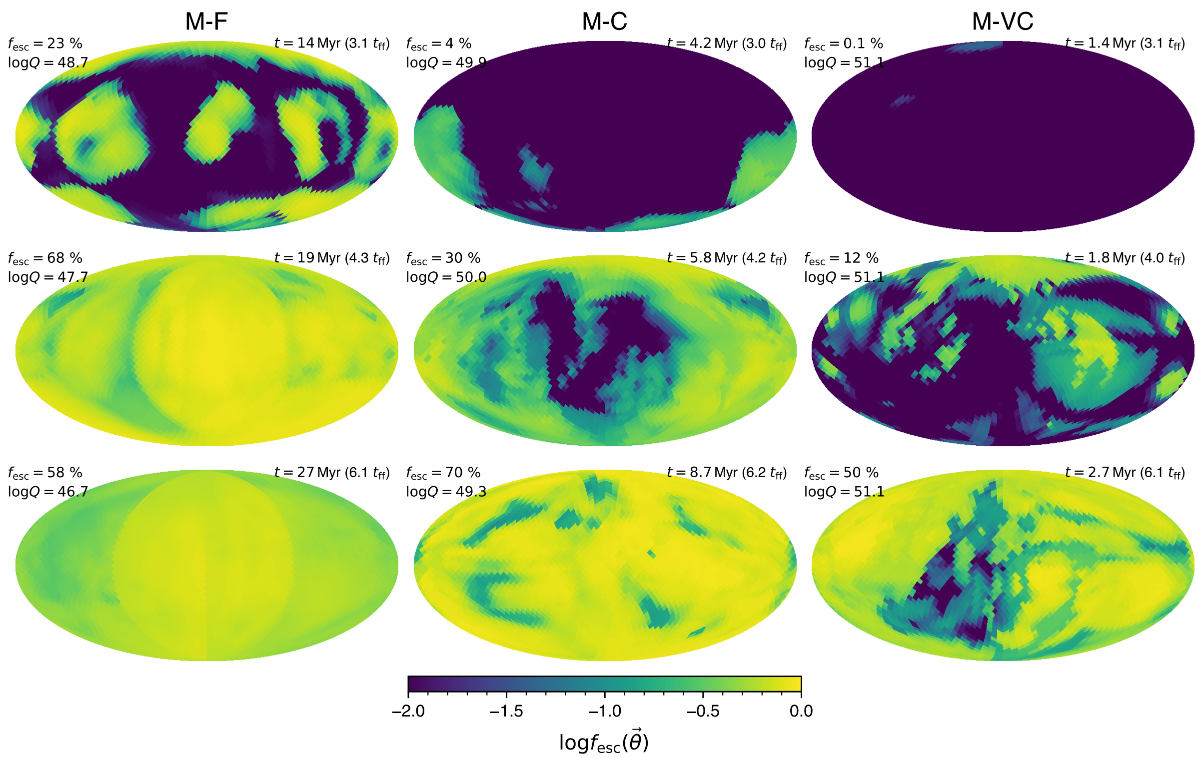

Figure 3.2: Equal-area projection of angular distribution of escape fraction of ionizing photons at three different times (top to bottom) from the Medium mass-Fiducial (M-F), Compact (M-C), and Very Compact (M-VC) clouds, left to right, respectively. The time labelled is the time since relaxation. The escape fraction $f_{esc}(\theta)$, is calculated as a ionizing luminosity weighted average over all stars. The f_{esc} shown in the legend at the top-left corner of each panel, is the average over the whole sky. Escaped radiation from star-forming molecular clouds is anisotropic when the cloud is partially ionized. Ionizing chimneys form on part of the sky and expand to the whole sky. See the text for how escaped photon emission rate is calculated for individual stars. The hemispherical feature appearing in the bottom-left panel is a numerical artifact that is evident only when $\langle f_{\rm esc}^{\rm MC} \rangle \sim 1$ and is due to the finite size of the simulation box and the boundary condition.

Table 3.2: A summary of results from the analysis of the simulations in Table 3.1. The columns show the number of hydrogen and helium ionizing photons emitted by the star clusters, S, and the fraction escaping the clouds, $\langle f_{\rm esc}^{\rm MC} \rangle$. [a] The gray data in this table are from the 'XS-F', 'S-F', and 'XS-C' clouds where the simulation results are less reliable because the SFE is likely overestimated due to missing feedback processes in low-mass stars (see Chatper 2).

Compactness	Cloud name	$m_{\rm gas}/{\rm M}_\odot$	$m_{cl}/{\rm M}_\odot$	LyC Emission ($\log S$/photons)			$\langle f_{\rm esc}^{\rm MC} \rangle$ / %			
				H	He	He^+	H LyC	H Ly edge	He Ly edge	He^+ Ly edge
Fiducial	XS-F	3.2×10^3	3.8×10^2	62.9 [a]	61.6	58.3	53	44	53	0.2
Fiducial	S-F	1.0×10^4	5.1×10^2	61.7	59.3	57.1	60	53	58	8.2
Fiducial	M-F	3.2×10^4	1.4×10^3	63.5	62.4	59.1	8	5.2	3.7	0.063
Fiducial	L-F	1.0×10^5	5.7×10^3	64.6	63.7	61.0	2.3	1.3	0.85	1.7e-09
Fiducial	XL-F	3.2×10^5	2.5×10^4	65.3	64.4	61.7	1.4	0.45	0.58	9.5e-18
Compact	XS-C	3.2×10^3	1.0×10^2	60.5	-inf	-inf	92	92	-	-
Compact	S-C	1.0×10^4	5.3×10^2	63.3	62.2	59.0	31	24	-	-
Compact	M-C	3.2×10^4	3.0×10^3	64.1	63.1	59.9	23	16	-	-
Compact	L-C	1.0×10^5	1.4×10^4	65.0	64.1	61.4	21	14	-	-
Compact	L-C-lm	1.0×10^5	3.4×10^3	64.4	63.5	60.7	44	35	-	-
Compact	L-C-xlm	1.0×10^5	3.3×10^3	64.4	63.5	60.7	49	43	-	-
Very Compact	XXS-VC	1.0×10^3	9.8×10^1	61.9	59.9	57.2	83	79	85	15
Very Compact	XS-VC	3.2×10^3	5.1×10^2	62.8	61.4	58.2	71	63	71	0.2
Very Compact	S-VC	1.0×10^4	3.2×10^3	64.4	63.5	60.8	48	40	-	-
Very Compact	M-VC	3.2×10^4	1.5×10^4	65.1	64.2	61.4	35	27	-	-
Very Compact	L-VC	1.0×10^5	¿2.7×10^4	-	-	-	-	-	-	-

Figure 3.1 shows snapshots at times $t \approx 1, 3, 6\ t_{\rm ff}$ (top to bottom) for three medium-mass ($3 \times 10^4 \rm M_\odot$) cloud simulations with initial mean densities $\overline{n}_{\rm gas} = 2 \times 10^2$, 2×10^3, and $2 \times 10^4\ \rm cm^{-3}$, from left to right, respectively. The free-fall time t_{ff} for these clouds are 4.4, 1.4, and 0.44 Myr, respectively. Each panel shows the density-weighted projection plots of the density (see colorbar on the right of the figure), while the circles show the stars with radii proportional to the cube root of their masses (see Chapter 2 for results on the mass function of the stars) and colors representing the number of ionizing photons escaping the cloud per unit time, $Q_{\rm esc}$ (photons/sec), as indicated by the colorbar at the bottom of the figure (see Section 3.2.2 for details on how $Q_{\rm esc}$ is calculated). Red circles represent stars that are dead so that their radiation has been shut off. Inspecting the figure, it is clear that the radiation from massive stars that form in the cloud is initially heavily absorbed by the cloud, while at later times, when radiative feedback has blown bubbles and chimneys through which radiation can escape, the radiation from stars can partially escape the cloud. Massive stars are born deeply embedded in dense clumps, thus their ionising radiation is initially absorbed by the gas and their overall contribution to the total LyC photons is reduced. A summary of quantitative results for all 16 simulations in Table 3.1 is shown in Table 3.2. The meaning of the different quantities in the table is explained in the remainder of this section.

3.3.1 Sky maps of the Escaping Ionizing Radiation

Initially, when the radiation starts escaping the cloud (*i.e.*, when the mean value of the escape fraction is small), it does so only in certain directions as illustrated in Figure 3.2 for compact clouds of different masses. The panels are analogous to Figure 3.1 (except that the time

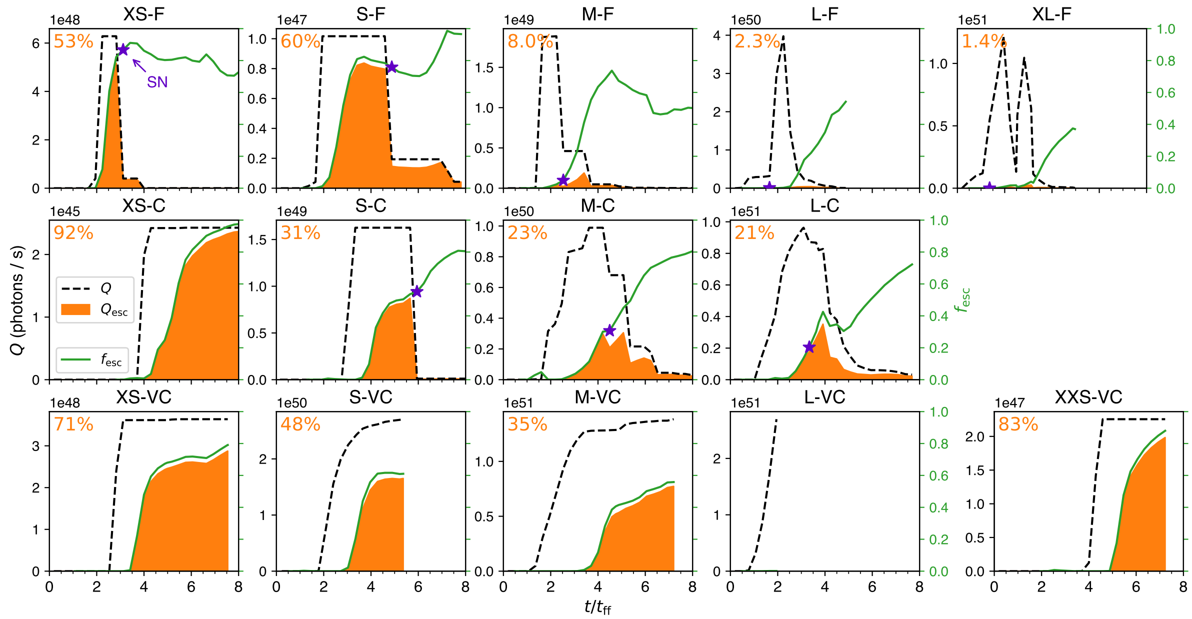

Figure 3.3: Time evolution of the LyC emission rate (Q), escaping rate ($Q_{\rm esc}$), and escaping fraction ($f_{\rm esc} \equiv Q_{\rm esc}/Q$) for our grid of simulations with varying masses (columns) and compactness (rows). We notice that in most clouds $f_{\rm esc}(t)$ becomes significant at $3-5t_{\rm ff}$, when most of the volume in the simulation box is ionized. At this time, the Fiducial clouds have a much lower emission rate of ionizing photons ($Q(t)$) with respect to the peak value because the most massive stars in cluster have died, resulting in a low $\langle f_{\rm esc}^{\rm MC}\rangle$. The very compact clouds, on the other hand, have a high Q after $3t_{\rm ff}$, resulting in relatively high $\langle f_{\rm esc}^{\rm MC}\rangle$. The free-fall times for the clouds in the top (Fiducial), middle (Compact), and bottom panels (Very Compact) are 4.4, 1.4, and 0.44 Myr, respectively. The purple stars mark the time when the first SN explosion occurs. Except for the two most massive Fiducial clouds, the first SN explosion happens when $f_{\rm esc}$ is already close to unity and/or when Q has dropped by over an order of magnitude from the maximum, hence in most simulations SN explosions would have little effect on the escape of LyC photons from the cloud.

sequence is chosen differently). Each column shows, for different cloud compactness (density), a time-sequence of sky maps of the leakage of ionizing photons in different directions across the sky using Mollweide projection maps. Columns, from left to right, refer to simulations: M-F, M-C, and M-VC, respectively. Each row refers to a different time: t = 3, 4, and 6 times $t_{\rm ff}$. The clouds start fully neutral and as the first stars form and produce feedback, they start to carve chimneys of ionized gas from where ionizing photons escape. These chimneys then expand and overlap covering larger portions of the sky and finally totally ionizing the whole solid angle. At this time most of the cloud's volume is ionized and $f_{\rm esc}(t)$ is above 10%. The neutral fraction in most of the volume is tiny, but due to the large hydrogen column density, the optical depth to LyC photons is typically ~ 1, preventing $f_{\rm esc}(t)$ from reaching unity.

However, for the small and medium mass clouds, by the time most of the radiation escapes isotropically, the emission rate of ionizing photons is small because all massive stars have died. In addition, if we consider that these molecular clouds are embedded into galactic disks, the high $f_{esc}(\boldsymbol{\theta})$ channels will be randomly oriented with respect to the disk plane, further reducing $\langle f_{\rm esc}^{\rm MC} \rangle$ and increasing the anisotropic leaking of ionizing radiation.

The escape fraction is anisotropic at early times when most of the radiation from massive stars is emitted. Later, when the leakage of ionising radiation become more isotropic, massive stars, which dominate the ionizing radiation emission, start to die. In the next section we will average the rates of ionizing radiation emitted, Q, and escaping $Q_{\rm esc}$, over the whole solid angle and analyse in detail the time evolution of these quantities and calculate the instantaneous escape fraction defined as $f_{\rm esc}(t) \equiv Q_{\rm esc}(t)/Q(t)$. We will see that unless $\langle f_{\rm esc}^{\rm MC} \rangle \gtrsim 50\%$ (averaged over the whole sky and over time), the radiation escaping a star cluster is highly anisotropic.

3.3.2 Time Evolution of the Sky-Averaged Escape Fraction

Figure 3.3 shows the emission rate of hydrogen-ionizing photon, Q (dashed lines), the portion that escapes from the cloud, $Q_{\rm esc}$ (shaded regions), and the instantaneous escape fraction, $f_{\rm esc}(t) \equiv Q_{\rm esc}/Q$ (solid lines) as a function of time for all our simulations with solar metallicity.

The stellar lifetime is calculated as the main-sequence lifetime Schaller et al. (1992) of a star with mass 40% of the sink mass (see Chapter 2). Radiation from a star is turned off after the

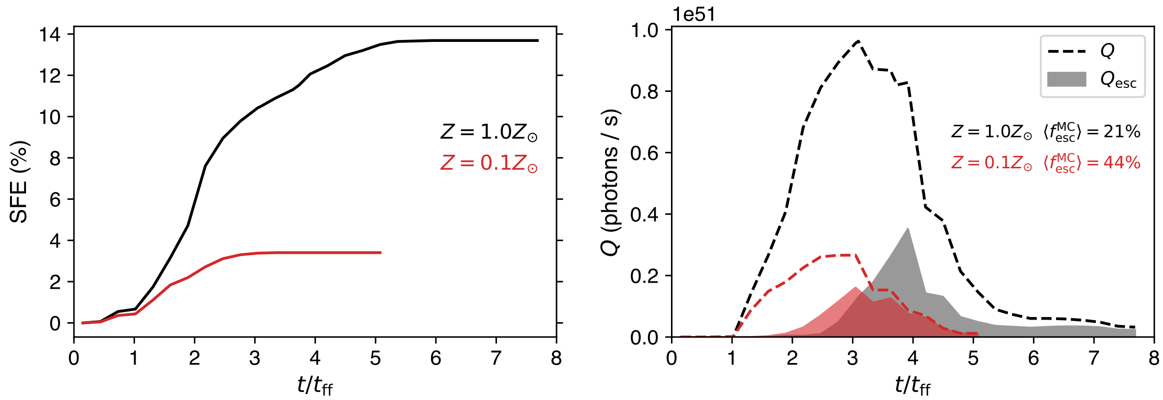

Figure 3.4: *(Left).* Time evolution of the SFE for the large Compact (L-C) run with solar metallicity (black line) and $Z = 1/10\ \mathrm{Z}_\odot$ (red line). *(Right).* Hydrogen ionizing-photon emission rate (dashed lines) and escaping rate (shaded area) for the same simulations as in the left panel. The lower-metallicity run (red lines) has ~ 3 times lower photon emission rate Q due to the lower SFE. The stronger stellar feedback in the lower-metallicity cloud clears out the gas in less than $3t_{\rm ff}$, when star formation is quenched and the escape fraction approaches unity as indicated by the convergence of the $Q_{\rm esc}$ and Q curves, resulting in higher $\langle f_{\rm esc}^{\rm MC}\rangle$ but substantially lower number of total escaped ionizing photons.

star is dead. As a result, there is a sharp drop of $Q(t)$, thus $Q_{\rm esc}(t)$, after about 3-5 Myr from the beginning of star formation due to the death of the most massive stars in the cluster. Some of our simulations have not been run sufficiently long for all massive stars to die, as we stop the simulations after roughly $6t_{\rm ff}$, when feedback has shut down star formation in the cloud. In all our simulations, except for the 'L-VC' run, the SFE reaches its maximum long before the end of the simulation, therefore we are able to extrapolate $Q(t)$ beyond the end of the simulation. We calculate the total number of ionizing photons emitted by the star cluster $S = \int_0^{t_{end}} Q(t')\,dt'$, and the total number of ionising photons that escape the molecular cloud, $S_{\rm esc} = \int_0^{t_{end}} Q_{\rm esc}(t')\,dt'$, where t_{end} is chosen to be the end of the simulation or a sufficiently long time after the end of the simulation such that all massive stars in the simulation have died. We define a time-averaged total escape fraction of ionizing photons as $\langle f_{\rm esc}^{\rm MC}\rangle \equiv S_{\rm esc}/S$, which is shown in the top-left corner of each panel in Figure 3.3. The figure shows that $f_{\rm esc}(t)$ is practically zero at the time star formation begins when massive stars start emitting ionising radiation. After a time delay $f_{\rm esc}(t)$ increases almost linearly with time and in several simulations it reaches a roughly constant value as a function of time after $t \sim 5t_{\rm ff}$. This is the time when the bulk of the gas is blown away by radiation feedback and the remaining gas is mostly ionized (see Chapter 2). For the simulations in which we do not have a sufficiently long time evolution to measure $f_{\rm esc}$(t) until the time all massive stars have left the main sequence, we assume that $f_{\rm esc}(t)$ maintains the same value found at the end of the simulation and we calculate $Q_{\rm esc}(t)$ from $Q(t)$ and $f_{\rm esc}(t)$ up to the time when all massive stars are dead. We will further discuss the results for the integrated ionising photon emission in Section 3.3.3.

Mechanical energy and metal enrichment from SN explosions is not included in our simulations. We compensate for the missing feedback by not shutting down UV radiation after the star dies (see Chapter 2). Note, however, that in the calculation of $\langle f_{\rm esc}^{\rm MC} \rangle$ we consider realistic lifetimes of massive stars. As shown in Figure 3.3 (star symbols), SNe explosions happen typically either when Q is already small and $\langle f_{\rm esc}^{\rm MC} \rangle \sim 1$, or after the end of the simulation. The only exception is the two most massive fiducial clouds. For the Compact and Very Compact clouds as well as the less massive fiducial clouds, both the star formation time scale and feedback time scale (related to the sound crossing time) are shorter than the first SN explosion time (~ 3 Myr). Therefore, we may have underestimated $\langle f_{\rm esc}^{\rm MC} \rangle$ in the two most massive fiducial clouds, although enrichment from SN may also reduce $\langle f_{\rm esc}^{\rm MC} \rangle$ if dust is produced on sufficiently short time scale.

3.3.2.1 Effects of Gas Metallicity

Figure 3.4 compares two simulations of the L-C cloud, with the only difference being the gas metallicity which affects the cooling of the gas. For a given cloud mass and density, lowering the gas metallicity increases $\langle f_{\rm esc}^{\rm MC} \rangle$, even though here we do not consider dust opacity. In Chapter 2 we found that for gas metallicity $Z < 0.1$ Z$_\odot$, the SFE is reduced by a factor of ~ 5 due to more efficient UV feedback caused by the higher temperature and pressure inside H II regions, but we do not observe a dependence of the IMF on the metallicity. From Figure 3.4 we can see that the peak value of $Q(t)$ for the lower metallicity simulation is reduced with respect to the solar metallicity case by a factor of 4 due to the lower SFE. However, the timescale over which f_{esc} increases from 0 to some value of order unity is shorter with decreasing metallicity, suggesting a faster destruction of the cloud due to a more efficient feedback, in agreement with what we found in Chapter 2. We will investigate quantitatively the dependence of $\langle f_{\rm esc}^{\rm MC} \rangle$ on feedback time scale in Section 3.4.1 with an analytic model.

3.3.3 Time-Averaged Escape Fraction $\langle f_{\rm esc}^{\rm MC} \rangle$

Figure 3.5 summarizes the final result for the escape fraction for all our simulations, showing $\langle f_{\rm esc}^{\rm MC} \rangle \equiv S_{esc}/S$ as a function of the mass of the star cluster, $m_{\rm cl}$, for different molecular cloud compactness (as shown in the legend). The two least massive fiducial clouds are removed from the analysis because we believe that the SFE of these simulations is overestimated due to missing physics (*i.e.*, IR feedback, that is not included in these simulations, becomes significant in this regime. See Chapter 2 for more explanation). We find that $\langle f_{\rm esc}^{\rm MC} \rangle$ increases with decreasing mass of the cluster and with increasing compactness. We also find a strong dependence of $\langle f_{\rm esc}^{\rm MC} \rangle$ on

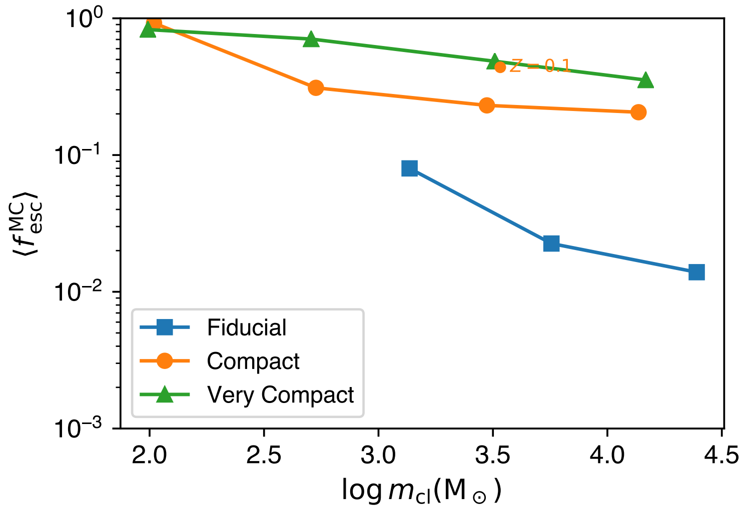

Figure 3.5: The total escape fraction of ionizing photons $\langle f_{\rm esc}^{\rm MC} \rangle = S_{\rm esc}/S$. The blue, orange, and green lines in both panels connect clouds with same density to guide our eyes. The low-mass clouds have high $\langle f_{\rm esc}^{\rm MC} \rangle$ due to lower mass stars dominating UV radiation (and lower mass stars live longer)

the gas metallicity.

As we decrease the gas metallicity, the typical pressure inside H II regions increases. Therefore the feedback becomes stronger, leading to an increases of $\langle f_{\rm esc}^{\rm MC} \rangle$, but also a reduction of the SFE. Therefore, the total number of escaped LyC photons decreases with decreasing metallicity, because of the reduced SFE.

Figure 3.6 shows $\langle f_{\rm esc}^{\rm MC} \rangle$ as a function of the SFE for 12 out of our 16 simulations. For comparison, results from Kimm et al. (2019) are plotted as purple squares. The methodology in the simulations by Kimm et al. (2019) is rather different from ours, because star formation is not modelled self-consistently but rather a fixed SFE (of 1% or 10%) is assumed and stars placed at the center of the cloud inject energy and radiation according to a pre-computed stellar population. They assume gas clouds of fixed density, similar to our fiducial case, and explore masses of 10^5 $\rm M_\odot$ and 10^6 $\rm M_\odot$ and metallicities of 0.1 solar and solar metallicity.

In Chapter 2 we have shown that there is a tight positive correlation between the SFE and

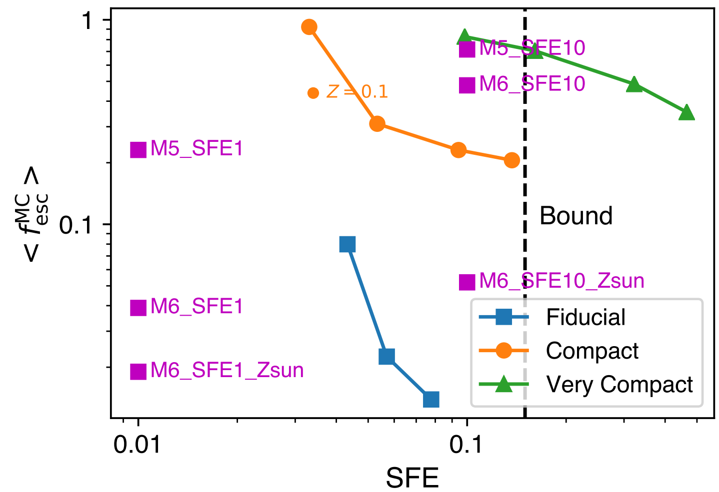

Figure 3.6: $\langle f_{\rm esc}^{\rm MC} \rangle$ plotted against SFE for 11 out of our 16 simulations. Magenta squares are data from Kimm et al. (2019). In the labels the number after 'M' refers to $\log_{10}(m_{\rm MC}/{\rm M}_{\odot})$, and the number after 'SFE' is the SFE in per cent. The metallicity is $0.1\,Z_{\odot}$ unless otherwise specified.

$m_{\rm cl}$. Therefore in our simulations $\langle f_{\rm esc}^{\rm MC} \rangle$ decreases with increasing cloud mass and therefore with increasing SFE. The results for gas at solar metallicity and the dependence of $\langle f_{\rm esc}^{\rm MC} \rangle$ on the cloud mass are in qualitative agreement with Kimm et al. (2019), as well as the significant increase of $\langle f_{\rm esc}^{\rm MC} \rangle$ as the gas metallcity is reduced with respect to the solar value.

For the fiducial clouds, with densities typical of star forming regions in the local Universe, $\langle f_{\rm esc}^{\rm MC} \rangle$ is extremely small: going from $\langle f_{\rm esc}^{\rm MC} \rangle \sim 8\%$ for star clusters of 10^3 ${\rm M}_{\odot}$, to 1.4% for clusters of 3×10^4 ${\rm M}_{\odot}$. Clearly if high-redshift star clusters had the same properties as today's ones, their $\langle f_{\rm esc}^{\rm MC} \rangle$ would be too low to contribute significantly to the reionization process. However, for our compact and very compact clouds, we find higher values of $\langle f_{\rm esc}^{\rm MC} \rangle$: ranging from $\langle f_{\rm esc}^{\rm MC} \rangle > 50\%$ for clusters of mass < 500 ${\rm M}_{\odot}$, to 20% (compact) and 35% (very compact) for star clusters with masses $\sim 2 \times 10^4$ ${\rm M}_{\odot}$.

We emphasize that $\langle f_{\rm esc}^{\rm MC} \rangle$ we are reporting in this work is an upper limit for $\langle f_{\rm esc}^{\rm gal} \rangle$ from galaxies. Here we are simulating the escape fraction just from the molecular clouds, without

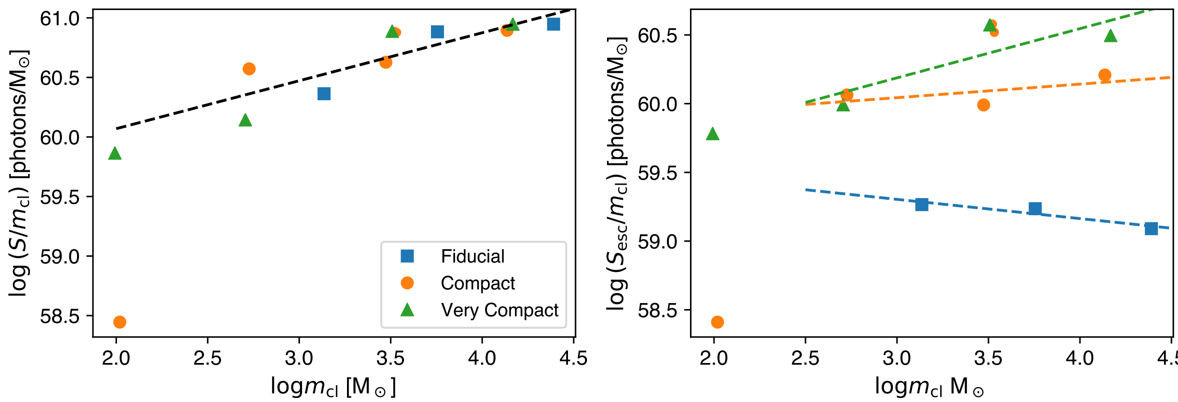

Figure 3.7: Time-integrated number of hydrogen-ionizing photons per unit star cluster mass emitted (top) and escaping the cloud (bottom) as a function of the star cluster mass and for gas cloud densities as in the legend. The relation between S/m_{cl} and m_{cl} is a tight power-law function with a slope ~ 0.4, independent of the density of the initial cloud, as expected. For clusters forming in molecular clouds with same initial density, the relationship between S_{esc}/m_{cl} and m_{cl} is also well approximated by a power-law with negative slope for the fiducial clouds (local Universe clouds) and increasing positive slope with increasing cloud compactness.

including a likely further reduction of $\langle f_{\rm esc}^{\rm gal} \rangle$ due to absorption of ionising radiation by the ISM in the galaxy. We also do not include the effect of dust. Therefore, even for compact clouds, $\langle f_{\rm esc}^{\rm MC} \rangle$ is already quite close to the average value required for reionization, which is an interesting result in order to understand the nature of the sources of reionization.

A complementary way to characterise the ionising radiation escaping molecular clouds is in term of S_{esc} or Q_{esc}. Since more massive star clusters emit more ionizing radiation per unit mass, these quantities show more directly the relative importance of clusters with different mass to the total ionising photons escaping a galaxy. The top panel in Figure 3.7 shows the total number of ionizing photons emitted by the cluster per unit mass, S/m_{cl}, over its lifetime as a function of the mass of the star cluster for all the simulations in Table 3.1. The dashed line shows a power-law fit to S/m_{cl} as a function of m_{cl}, excluding the two data points with $m_{cl} \lesssim 300$ M$_\odot$:

$$\frac{S}{m_{cl}} = 1.2 \times 10^{60} \left(\frac{m_{cl}}{100 \mathrm{M}_\odot} \right)^{0.4} . \tag{3.4}$$

We exclude from the fit star clusters with mass below $300\mathrm{M}_{\odot}$ because for small mass clusters the scatter of S becomes very large due to sparse sampling of massive stars in small clouds (see Figure 7 in Chapter 2). We can roughly understand the 0.4 slope of the power-law fit by assuming that the most massive star in a cluster dominates the emission of ionising radiation. In Chapter 2 we found that the most massive star in the cluster has a mass $M_{max} \propto m_{cl}^{0.66}$, and for stellar masses $M \gtrsim 30\mathrm{M}_{\odot}$, $Q(M) \propto M^{1.9}$ with a lifetime on the main sequence $t_{MS}(M)$ nearly constant as a function of mass. Thus, we get $S \propto Q(M_{\mathrm{max}}) \propto m_{cl}^{1.3}$ and $S/m_{\mathrm{cl}} \propto m_{cl}^{0.3}$, which is close to the exponent in Eq. (3.4). We will show later that the most massive star in the cluster typically contributes a fraction 25% to 95% of all the emitted ionising photons.

The bottom panel in Figure 3.7 shows the total number of ionising photons escaping the cloud per unit mass, S_{esc}/m_{cl}, as a function of the cluster mass for the same simulations as in the top panel. The dashed lines show power-law fits

$$\frac{S_{esc}}{m_{cl}} = E\left(\frac{m_{cl}}{100\ M_{\odot}}\right)^{\alpha}, \tag{3.5}$$

where $E = 2.8 \times 10^{59}$, 8.8×10^{59}, and $6.8 \times 10^{59}\mathrm{M}_{\odot}^{-1}$ and $\alpha = -0.1, 0.1, 0.4$ for the fiducial, compact and very compact clouds, respectively. The figure shows that for clouds in the local Universe (fiducial clouds) and for compact clouds, the number of escaping ionising photons per unit mass (S_{esc}/m_{cl}) is nearly constant with increasing cluster mass, while for very compact clouds S_{esc}/m_{cl} increases with increasing cluster mass. We will see in Section 3.4.2 that this trend is reflected in the total number of escaping ionising photons integrated over the observed (in the local Universe) star cluster mass function.

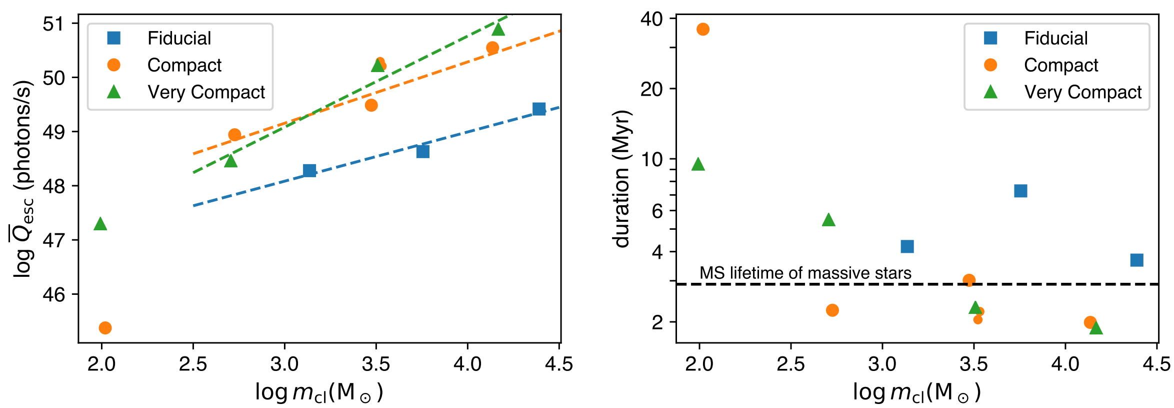

Figure 3.8: Top: Mean escaped ionizing-photon emission rate Q_{esc} as a function of cluster mass m_{cl}. Power-law fits to each group of data is shown as dashed lines with corresponding colors. The slopes are 1.7, 2.2, and 0.4 for the VC, C, and F clouds, respectively. Bottom: Duration of ionizing-photon escaping.

Combining Eqs. (3.4) and (3.5), the power-law fitting function for the escape fraction is

$$\langle f_{esc} \rangle = F \left(\frac{m_{cl}}{100\ M_\odot} \right)^{\beta}, \tag{3.6}$$

where the power-law slopes are $\beta = \alpha - 0.4 = -0.5, -0.3, 0.0$ and normalizations $F = 0.23, 0.73, 0.57$ for the fiducial, compact and very compact clouds, respectively.

In cosmological simulations and analytic models, the sources of ionising radiation are typically modelled as sub-grid physics in terms of the mean ionising photon escape rate $\overline{Q}_{esc}$ during the UV burst, and the duration of the ionising burst t_{esc}. The duration of the burst and the anisotropy of the radiation escaping galaxies actually plays an important role in determining the photon-budged for completing IGM reionization and the topology of reionization (Hartley & Ricotti, 2016). These quantities for star forming molecular clouds are shown in Figure 3.8 as a function of the stellar cluster mass m_{cl}, where we approximate $\overline{Q}_{esc}$ as the peak value of $Q_{esc}(t)$ and define $t_{esc} \equiv S_{esc}/\overline{Q}_{esc}$.

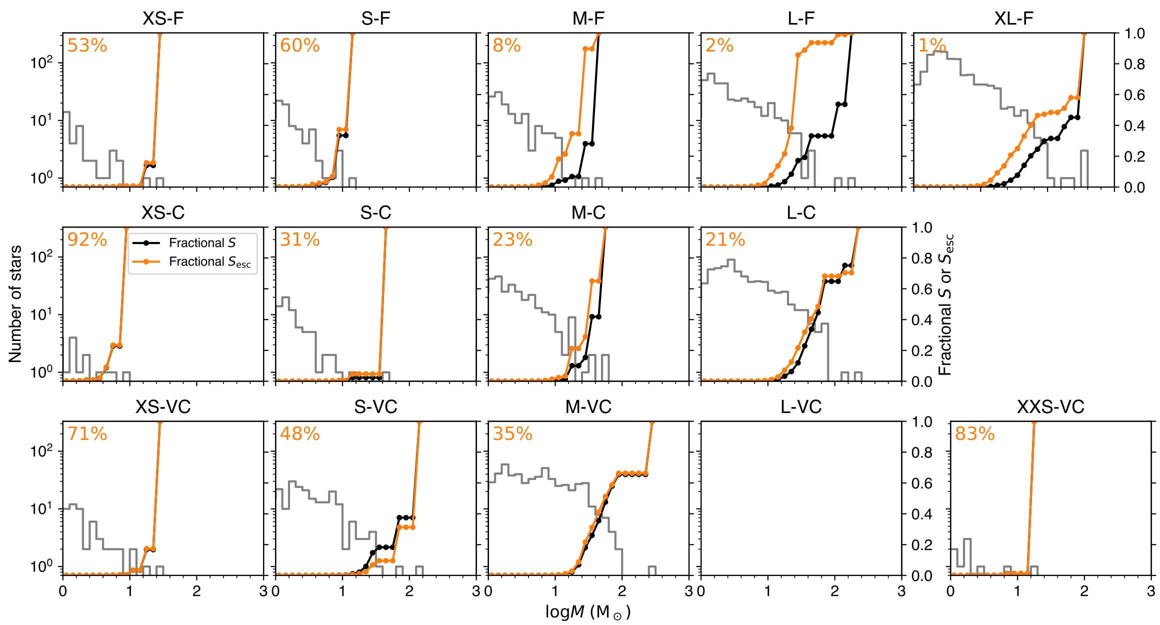

Figure 3.9: Fractional cumulative radiation emission (black) and escaping (orange) as a function of the mass of the star. The gray histogram shows the numbers of stars per log bin. The black lines show that, although there are on average only a few massive stars in clusters, they dominate the emission of ionizing radiation. Inspecting the orange lines, we see that, except for the two most massive fiducial runs (L-F and XL-F), the same is true for the total escaped radiation from the cluster. In the massive fiducial clouds, very massive stars live shorter than a free-fall time (~ 4 Myr) and die before the gas is ionized and radiation can escape. This also results in lower ($\lesssim 5\%$) $\langle f_{\rm esc}^{\rm MC} \rangle$ (the numbers on the top-left corner of each panel.)

The dashed lines are power-law fits to the data. We find

$$\overline{Q}_{esc} = Q_0 \left(\frac{m_{cl}}{100\ M_\odot} \right)^\gamma \tag{3.7}$$

where $\gamma = 0.9, 1.1, 1.7$ and $Q_0 = 1.5 \times 10^{47}$, 1.1×10^{48}, 2.5×10^{47} s^{-1}, for the fiducial, compact and very compact clouds, respectively. For the local Universe clouds (fiducial case), $\overline{Q}_{esc} \sim 10^{48} - 3 \times 10^{49}$ s^{-1} in the range $m_{cl} \sim 10^3 - 3 \times 10^4$ M$_\odot$, increasing nearly linearly with increasing cluster mass. We have also noticed that, if we consider $\overline{Q}_{esc}$ of radiation at the hydrogen ionization edge (13.6 eV) rather than the weighted mean over the stellar spectrum (see Appendix B.1), we find that $\overline{Q}_{esc}$ is nearly constant as a function of the cluster mass, in good agreement with Dale et al. (2014). For very compact star clusters, however, the dependence on the mass is quite strong: $\overline{Q}_{esc} \sim 5 \times 10^{48}$ s^{-1} for $m_{cl} \sim 500$ M$_\odot$, but increases to 10^{51} s^{-1} for $m_{cl} \sim 20,000$ M$_\odot$. For the very compact and, to some extent, for the compact clouds, the duration of the burst of ionising radiation escaping the molecular cloud reflects the duration of the emitted radiation, that is roughly the lifetime of the most massive star formed in the cluster (*i.e.*, $t_{burst} \sim t_{uv} \approx t_{MS}(M_{max})$), although the emitted radiation is partially absorbed by the gas cloud. Hence, for small mass clusters the duration of the burst is longer: increasing from 2 Myr for $m_{cl} \sim 10^4$ M$_\odot$ to 10 Myr for $m_{cl} \sim 100$ M$_\odot$. However, this trend with the cluster mass is not observed for the two most massive fiducial clouds, for which $t_{burst} \sim 7$ Myr, about twice as large as the duration of the emitted burst of ionising radiation $t_{uv} \sim t_{MS}(M_{max})$. The reason for why the effective timescales of the emitted and escaping radiation differ from each other, can be found inspecting Figure 3.9 for those two clusters. For massive clusters, especially when $\langle f_{\rm esc}^{\rm MC} \rangle$ is very small, not only the most massive star, but also stars with $M \sim 10 - 20$ M$_\odot$ contribute to

Q_{esc}. Hence, the effective timescale for the escaping radiation can be longer than the effective timescale when most of the ionising radiation is emitted.

3.3.4 Escape Fraction of Helium Ionising Photons

Having discussed the emission rate of hydrogen-ionising photons, we explore another group of photons that ionize He and He^{+}. We enable the emission of these photons from sink particles in a subset of our simulations (the fiducial simulations plus the least massive compact and very compact runs). Massive stars with non-zero metallicity do not emit He II ionising photons with energy > 54 eV, hence we will not consider this energy bin[2].

We find that in all the simulations in which we include photon bins that ionize He, the escape fraction of HeI-ionising photons is nearly identical to that of HI-ionizing photons, with the only exceptions of the three most massive fiducial clouds where the $\langle f_{\rm esc}^{\rm MC} \rangle$ for HeI is lower by a factor of 2 – 3.

We interpret this result arguing that the sizes of H II and He^{+} ionization fronts are comparable around the sources that dominate the emission of ionising radiation. The radius of the ionization front can be estimated using the Strömgren radius equation:

$$R_{S0}^{i} \equiv \left(\frac{3Q^{i}}{4\pi {n_i}^{2} \alpha_{B}^{i}} \right)^{1/3}, \tag{3.8}$$

with i being H or He^{+}. At 10^{4} K, the case-B recombination rate, $\alpha_{B}^{\rm He^{+}}$, is about 1.9 times higher than that of hydrogen. With a He abundance ratio $n_{He}/n_{H} = (\mu - 1)/(4 - \mu) \approx 0.154$, where $\mu = 1.4$ is the mean atomic weight of the gas in our simulations, the He II front is larger or equals

[2]Wolf-Rayet stars actually emit some He II ionising radiation, but so far we have not included these type of stars in our simulations.

the radius of the H II I-front when the hardness of the spectrum, $Q^{\rm He}/Q^{\rm H}$, is greater than 0.29. Hot O stars have spectrum hardness close to or above this critical value, therefore around massive stars, which dominate the ionizing radiation, the He I-front is slightly larger than the H ionization front. Therefore, we expect that $\langle f_{\rm esc}^{\rm MC}\rangle$ for He-ionizing photons is close to or slightly larger than that of H-ionizing photons. This expectation is supported by the analysis of all our simulations that include radiation transfer in the He-ionizing frequency bins (see Table 3.2 as well as left panel of Figure 3.10).

3.3.5 Absorption by Dust

It is well known that dust may contribute significantly to the absorption of ionizing radiation (*e.g.*, Weingartner & Draine, 2001). In this section we estimate the effect of dust absorption on the escape fraction of LyC photons by adopting the dust extinction parameterization for the Small Magellanic Clouds (SMC) in Gnedin et al. (2008), which is based on Pei (1992) and Weingartner & Draine (2001). When dust absorption is included, the escape fraction in each direction is

$$f_{\rm esc}(\nu,\boldsymbol{\theta}) = f_{\rm esc,gas}{\rm e}^{-\tau_d(\nu,\boldsymbol{\theta})} = {\rm e}^{-(\tau_{\rm gas}+\tau_d)}. \tag{3.9}$$

If we assume that dust is completely sublimated inside H II regions, we find that the ratio of the dust extinction optical depth to the gas optical depth, τ_d/τ_{gas}, is below 8×10^{-4} along any line of sight. This is estimated by taking the peak value of the fitting formula for $\tau_d(\nu)$, that is $\tau_d \approx 5\, N_H/(10^{21}\ {\rm cm}^{-2})$. In this scenario the effect of dust is always negligible in our simulations. Estimates based on observations and numerical simulations (Inoue, 2002; Ishiki et al., 2018), have shown that radiation pressure creates a dust cavity inside H II regions, with a typical size of

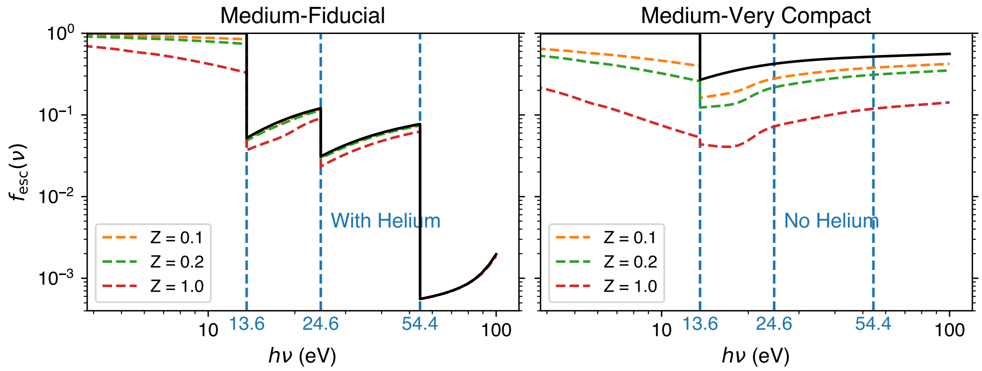

Figure 3.10: Escape fraction of photons as a function of $h\nu$ from two of the clouds: Medium-Fiducial (left) and Medium-Very Compact (right). From the simulation with He and He^+ ionizing photons enabled, we observe that the escape fraction of He ionizing photons is nearly identical to the escape fraction of H ionizing photons. Stars generally do not emit enough high energy photons to ionize He^+, hence $f_{\rm esc}(\nu)$ at the He^+-ionizing edge is close to zero.

$\sim 30\%$ of Strömgren radius. It has also been shown that the grain size distribution is less affected by the radiation from a star cluster than by a single O or B star.

In this section, we estimate the effects of dust extinction on $\langle f_{\rm esc}^{\rm MC} \rangle$ by assuming no sublimation, therefore setting an upper limit on the effect of dust. In this case, the dust column density is directly proportional to the total hydrogen column density:

$$\tau_{\rm d}(\nu) = N_{\rm H} \left(\frac{Z}{Z_0} \right) \sigma_{\rm d,eff}(\nu), \tag{3.10}$$

where $Z_0 = 0.2 Z_\odot$ is the gas-phase metallicity of the SMC and we use the fitting formula from Gnedin et al. (2008) for the effective cross section $\sigma_{\rm d,eff}(\nu)$.

In Figure 3.10, we plot the escape fraction, $\langle f_{esc}(\nu) \rangle$, as a function of photon energy. Here $\langle f_{esc}(\nu) \rangle$ is averaged over the whole sky, weighted by the ionising luminosity of stars in the correspondent bin, and averaged over time. The luminosity per frequency below the hydrogen ionization edge is approximated as a constant fraction of Q_H, i.e. $L/(\text{ergs s}^{-1}) = c_1 Q_H/(\text{s}^{-1})$,

Table 3.3: Escape fraction (percentages) at the Lyman edge with and without dust extinction. We consider four models in the calculation of photon optical depth: pure hydrogen and helium gas and gas plus dust with metallicities $Z = 0.1$, 0.2, and 1.0. The numbers highlighted in bold face mark the metallicity at which including dust extinction causes a relative decrease $> 20\%$ with respect to $\langle f_{\rm esc}^{\rm MC} \rangle$ without dust. [a] The gray data in this table is from the 'XS-F', 'S-F', and 'XS-C' clouds where the simulation results are less reliable because the SFE is overestimated due to missing feedback processes in low-mass stars (see Chapter 2).

Compactness	Job Names	$\langle f_{\rm esc}^{\rm MC} \rangle$	$\langle f_{\rm esc}^{\rm MC} \rangle^{+\rm dust}_{Z=0.1}$	$\langle f_{\rm esc}^{\rm MC} \rangle^{+\rm dust}_{Z=0.2}$	$\langle f_{\rm esc}^{\rm MC} \rangle^{+\rm dust}_{Z=1.0}$
Fiducial	XS-F	43.7 [a]	43.0	42.3	37.1
Fiducial	S-F	53.3	52.3	51.4	44.7
Fiducial	M-F	5.2	5.0	4.9	**3.7**
Fiducial	L-F	1.3	1.2	1.1	**0.6**
Fiducial	XL-F	0.5	**0.4**	**0.3**	**0.1**
Compact	XS-C	91.6	91.3	91.0	88.7
Compact	S-C	23.5	22.5	21.5	**15.1**
Compact	M-C	15.8	14.5	13.3	**7.4**
Compact	L-C	13.7	11.8	**10.3**	**3.9**
Compact	L-C-lm	35.2	31.8	28.9	**15.5**
Very Compact	XXS-VC	78.6	77.6	76.5	68.9
Very Compact	XS-VC	63.2	59.9	56.8	**37.9**
Very Compact	S-VC	39.7	35.5	**31.8**	**14.5**
Very Compact	M-VC	26.9	**16.2**	**12.3**	**4.4**

where c_1 is constant as a function of stellar mass. As shown in Table 3.3, we find that dust extinction becomes increasingly dominant with increasing cloud mass and cloud compactness, especially for clouds with $Z = 1.0\ \mathrm{Z}_\odot$. More compact clouds have higher total hydrogen column density, thus higher dust column density, even though $\langle f_{\rm esc}^{\rm MC} \rangle$ due to dust free gas is large because the neutral hydrogen column density becomes low. The most compact and most massive cloud in the table have 80% reduction of $\langle f_{\rm esc}^{\rm MC} \rangle$ for gas with solar metallicity, while the reduction is between 3% to 50% for less massive and less compact clouds. The effect of dust on $\langle f_{\rm esc}^{\rm MC} \rangle$, however, becomes small or negligible for a gas with metallicity below $1/10$ solar.

3.4 Discussion

3.4.1 Analytic Modelling and Interpretation of $\langle f_{\rm esc}^{\rm MC} \rangle$

In this section we investigate the trends observed in the simulation for $\langle f_{\rm esc}^{\rm MC} \rangle$, using a simple analytic model to better understand the dominant physical processes which determine $\langle f_{\rm esc}^{\rm MC} \rangle$, and make informed guesses on the extrapolation of the results to a broader parameter space. In this model we ignore dust extinction.

The qualitative trends for $\langle f_{\rm esc}^{\rm MC} \rangle$ as a function of compactness and cloud mass can be explained rather simply in terms of two timescale: t_{uv} that is the time interval during which the bulk of ionizing radiation is emitted, and t_{esc} that is the typical timescale over which f_{esc} increases from being negligible to unity, that is related to the timescale of the duration of the star formation episode, t_{SF}, because UV feedback is responsible for stopping star formation and clearing our the gas in the star cluster. When $t_{esc} \gg t_{uv}$, most of the ionising radiation is absorbed in the cloud and $\langle f_{\rm esc}^{\rm MC} \rangle$ is very small. In Chapter 2 we found that $t_{SF} \approx 6\, t_{cr}$, where

$$t_{cr} = 0.40 \text{ Myr} \left(\frac{m_{gas}}{10^4\, M_\odot} \right)^{1/3} \left(\frac{\overline{n}_{gas}}{10^3\, cm^{-3}} \right)^{-1/3}, \tag{3.11}$$

is the sound crossing time (assuming $c_s = 10$ km/s), which increases with the mass of the cloud and decreases with increasing compactness of the cloud.

In other words, $\langle f_{\rm esc}^{\rm MC} \rangle$ in the two most massive fiducial clouds is very small because massive stars are short lived with respect to the star formation timescale of the cloud, therefore they spend most of their life on the main sequence deeply embedded inside the gas rich molecular cloud and their radiation is mostly absorbed. Vice versa, the very compact clouds form all their stars and expel/consume their gas on a timescale shorter than $t_{uv} \sim 3$ Myr, therefore $\langle f_{\rm esc}^{\rm MC} \rangle$ is closer to unity.

Next we describe the quantitative details of our analytic model for $\langle f_{\rm esc}^{\rm MC} \rangle$, that we will show can reproduce quite accurately the simulation results. Informed by the results of the simulations, we assume that $f_{esc}(t)$ grows linearly with time from a value of zero at time $t \leq t_{in}$ to a maximum value $f_{esc}^{\rm max}$ at time t_{esc}:

$$f_{esc}(t) = \begin{cases} 0 & \text{if } t < t_{in}, \\ \frac{t - t_{in}}{t_{esc}} & \text{if } t_{in} \leq t < t_{in} + t_{esc}, \\ 1 & \text{if } t \geq t_{in} + t_{esc}. \end{cases} \tag{3.12}$$

For the sake of simplicity, we model the UV burst as a simple top-hat function with origin at $t = 0$ and width t_{uv}. This assumption appears to be a good approximation for most of the simulations (see Figure 3.3) because the dominant fraction of the ionising radiation is emitted by the most massive stars in the star cluster that have a rather constant main-sequence lifetime as a function of their mass, $t_{MS} \sim 3$ Myr, for masses above $\sim 30 \rm M_\odot$. The mass of the most massive star in the cluster, $M_{*,max}$, correlates with the mass of the star cluster, m_{cl}, according to the relationship (see Chapter 2):

$$M_{max} \approx 205\, M_\odot \left(\frac{m_{cl}}{10^4 \rm M_\odot} \right)^{0.66}. \tag{3.13}$$

Note that Eq. (3.13) is a numerical fit to the simulation data, and it seems to overestimate $\rm M_{max}$ in massive clouds, likely due to our finite resolution and the inability to fully resolve sink fragmentation. We then convert this mass to the main-sequence lifetime using Eq. (3.1) and set $t_{uv} = t_{MS}(M_{max})$.

Our assumption may fail for the cases in which $\langle f_{\rm esc}^{\rm MC} \rangle$ is very small (the most massive fiducial clouds), because $f_{esc}(t)$ remains negligibly small for nearly the duration of the life on the main sequence of massive stars (*i.e.*, $t_{uv} \lesssim t_{in}$), and only slightly less massive stars are able to stay on the main sequence long enough when $f_{esc}(t)$ starts to rise to larger values.

In order to test this assumption we compare t_{MS} calculated as explained above, with the values of t_{uv} measured in the simulations as the full-width half maximum of the $Q_{esc}(t)$ curve. Figure 3.11 shows that indeed $t_{MS}(M_{max})/t_{uv}$ is close to unity with small scatter, even for the fiducial clouds, demonstrating the goodness of our assumption.

With these two simple assumptions on the shape of $f_{esc}(t)$ and $Q(t)$, we find that the time-averaged $\langle f_{\rm esc}^{\rm MC} \rangle$ is:

$$\langle f_{\rm esc}^{\rm MC} \rangle = \begin{cases} \frac{t_{uv}-t_{in}}{t_{uv}} - \frac{1}{2}\frac{t_{esc}}{t_{uv}} & \text{if } t_{esc} < (t_{uv} - t_{in}), \\ \frac{1}{2}\frac{(t_{uv}-t_{in})^2}{t_{uv}t_{esc}} & \text{if } t_{esc} \geq (t_{uv} - t_{in}). \end{cases} \tag{3.14}$$

Guided by a physically motivated prior for t_{esc} and t_{in}, we found that they are both proportional to $t_{SF} \propto t_{cr}$, being the timescale over which feedback is able to destroy the molecular cloud and stop star formation.

Assuming $t_{uv} = t_{MS}(M_{max})$, we fit Eq. (3.14) to the data, using t_{in}/t_{cr} and t_{esc}/t_{cr} as free parameters. In Figure 3.12 we show the best fits compared to the data for two models: in the top panel we fit the data with a one-parameter model by setting $t_{in} = 0$ (hence $\langle f_{\rm esc}^{\rm MC} \rangle$ $= 1 - 0.5t_{esc}/t_{uv}$ when $t_{esc} < t_{uv}$ and $0.5t_{uv}/t_{esc}$ otherwise). The best fit parameter in this model is $t_{esc} = 21t_{cr} \approx 3.5t_{SF}$, where we have used $t_{SF} = 6t_{cr}$, found for simulations with gas at solar

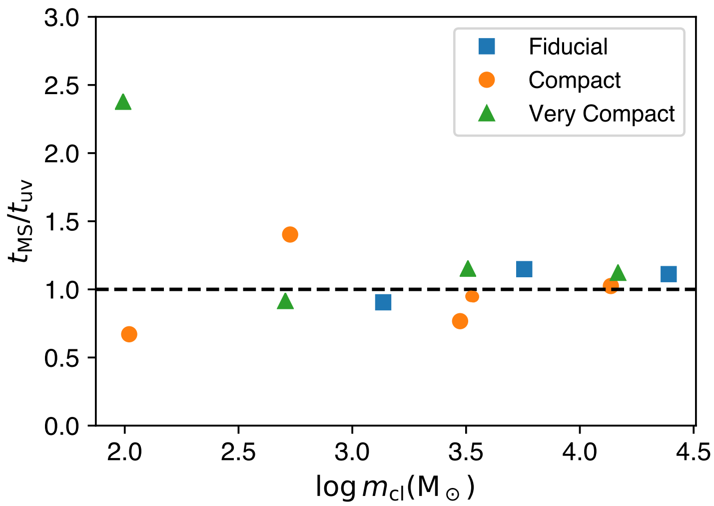

Figure 3.11: Ratio of $t_{MS}(M_{max})$ to the measured t_{uv}. The t_{uv} is measured as the Full-Width Half-Maximum of the $Q(t)$ curve.

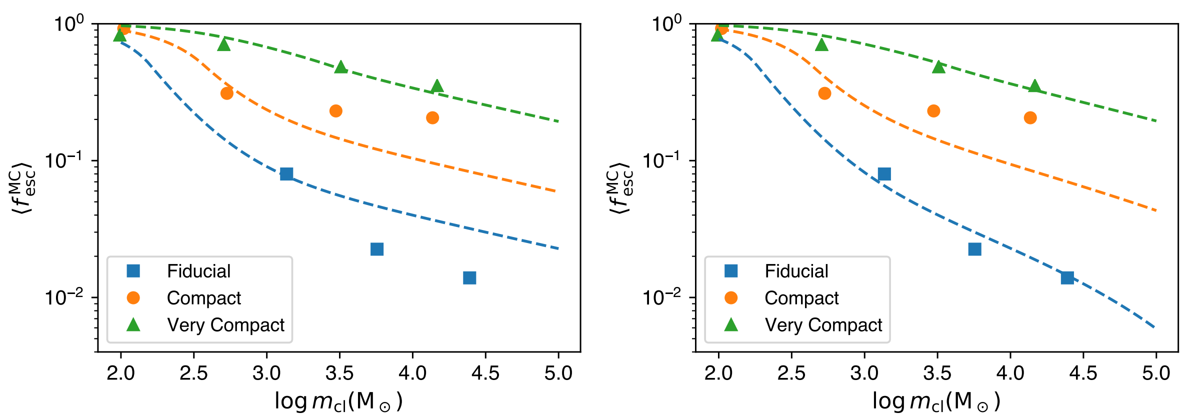

Figure 3.12: Comparing model $\langle f_{\rm esc}^{\rm MC} \rangle$ (dashed lines) with $\langle f_{\rm esc}^{\rm MC} \rangle$ from simulations (shapes). The models have t_{esc} (top) or t_{in} and t_{esc} (bottom) as parameters. Both models work equally well on the Compact and Very Compact clouds while only the latter model works well on the Fiducial clouds. Bottom: The modeled $\langle f_{\rm esc}^{\rm MC} \rangle$ using pure cloud parameters. Eq. (3.14) and (3.18) are used.

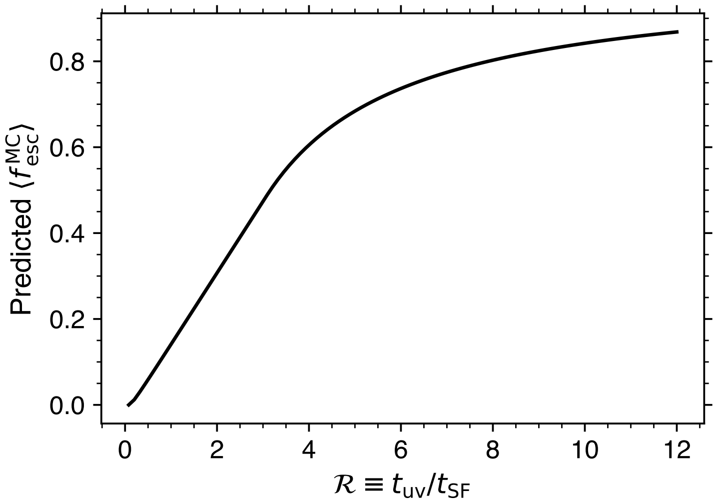

Figure 3.13: Conversion from the $\mathcal{R}$ parameter to $\langle f_{\rm esc}^{\rm MC} \rangle$, following Eq. (3.15).

metallicity (see Chapter 2). This model works well for the Very Compact clouds and slightly underestimates $\langle f_{\rm esc}^{\rm MC} \rangle$ for massive Compact clouds by a factor of $\lesssim 2$. It also overestimates $\langle f_{\rm esc}^{\rm MC} \rangle$ for the Fiducial clouds where the lifetime of the most massive star ($\sim$ 3 Myr) is shorter than several free-fall times and UV radiation is shut down before the gas is expelled, resulting in $\langle f_{\rm esc}^{\rm MC} \rangle$ below 10%.

The bottom panel of Figure 3.12 shows the two-parameter model in Eq. (3.14). This model resolves the discrepancy between the model-predicted $\langle f_{\rm esc}^{\rm MC} \rangle$ and the simulation results from the massive fiducial clouds. This model, similar to the one-parameter model, slightly underestimates $\langle f_{\rm esc}^{\rm MC} \rangle$ from the massive Compact clouds. We believe that part of the discrepancy is due to second order effects from weighting $\langle f_{\rm esc}^{\rm MC} \rangle$ over the stellar spectra of different mass stars. As shown in Table 3.2, $\langle f_{\rm esc}^{\rm MC} \rangle$ at the Lyman edge from these clouds, being significantly smaller, is closer to the model predictions. For this model the best fit parameters are $t_{in} = 0.5 t_{cr} \approx 0.08 t_{SF}$ and $t_{esc} = 18 t_{cr} \approx 3 t_{SF}$. In both models we find that at the end of the star formation episode (at $t = t_{SF}$) the value of the escape fraction is $f_{esc}(t = t_{SF}) \sim 30\%$ (see Eq. (3.12)), and this value keeps increasing approximately linearly as a function of time after that.

Hence, if we define $\mathcal{R} \equiv t_{uv}/t_{SF}$, using the best fit parameters for the two-parameters model, we can rewrite Eq. (3.14) as

$$\langle f_{\rm esc}^{\rm MC} \rangle = \begin{cases} 1 - \frac{1.58}{\mathcal{R}} & \text{if } \mathcal{R} > 3.1, \\ 0.167\,\frac{(\mathcal{R}-0.08)^2}{\mathcal{R}} & \text{if } 0.08 \leq \mathcal{R} \leq 3.1. \end{cases} \tag{3.15}$$

Eq. (3.15) is shown in Figure 3.13. Due to the non-linear term $(\mathcal{R} - 0.08)^2/\mathcal{R}$, when $\mathcal{R} \lesssim 1$, $\langle f_{\rm esc}^{\rm MC} \rangle$ becomes very small and approaches zero as $\mathcal{R} \to 0.08$. This is the limit when $t_{uv} = t_{in}$ and all massive stars have died by the time $f_{esc}(t) > 0$. In this limit our model assumption fails and we need to consider longer lived (less massive) stars. But for these cases we expect $\langle f_{\rm esc}^{\rm MC} \rangle \ll 1\%$. When $\mathcal{R} \lesssim 3$ (or $\langle f_{\rm esc}^{\rm MC} \rangle < 50\%$), $\langle f_{\rm esc}^{\rm MC} \rangle$ is roughly proportional to $\mathcal{R}$: $\langle f_{\rm esc}^{\rm MC} \rangle \sim 0.17\mathcal{R}$.

This equation can help us interpret the results on $\langle f_{\rm esc}^{\rm MC} \rangle$ for simulations with gas at sub-solar metallicity. In Chapter 2 we found that for gas metallicitities $< 1/10$ $Z_\odot$, the duration of the star formation in the cloud was reduced by roughly 1/2 (*i.e.*, $t_{SF} = 3t_{cr}$). Hence, for a given molecular cloud mass and compactness, we expect that $\mathcal{R}$ is roughly twice the value found for solar metallicity, and $\langle f_{\rm esc}^{\rm MC} \rangle$ is also roughly twice as large if $\langle f_{\rm esc}^{\rm MC} \rangle < 50\%$. We also note that lowering the metallicity reduces the SFE of the cloud, hence for a given molecular cloud mass, the mass of the star cluster is reduced and $\langle f_{\rm esc}^{\rm MC} \rangle$ increases with respect to the solar metallicity case. The overall effect is a strong sensitivity of $\langle f_{\rm esc}^{\rm MC} \rangle$ on the gas metallicity for two clusters of equal stellar mass.

Using the results in Chapter 2 for a cloud at solar metallicity we can write $\mathcal{R}$ as a function of the cloud's parameters. For star masses $M > 10$ $M_\odot$ we can approximate $t_{uv} = t_{MS} =$

$2.86 + 1.9 \times 10^3 (M/\mathrm{M}_\odot)^{-2}$ Myr and using Eq. (3.13) we have

$$t_{uv} = 2.86 + 0.045 m_{cl,4}^{-1.32} \text{ Myr} \tag{3.16}$$

where $m_{cl,4} \equiv m_{cl}/10^4\ M_\odot$, For clouds with solar metallicity, we can also write t_{cr} in Eq. (3.11) as a function of m_{cl} and the cloud compactness, by expressing m_{gas} as a function of the cluster mass using the following relationship found in Chapter 2 (valid for clouds at solar metallicity):

$$m_{\mathrm{cl}} = 200\ \mathrm{M}_\odot \cdot \left(\frac{m_{gas}}{10^4 \mathrm{M}_\odot}\right)^{1.4} \left(1 + \frac{\overline{n}_{gas}}{n_{\mathrm{cri}}}\right)^{0.91} + m_{fl}\,, \tag{3.17}$$

where $n_{\mathrm{cri}} \approx 10^3\ \mathrm{cm}^{-3}$ is the critical density and $m_{fl} = 10\ \mathrm{M}_\odot$ is the mass floor. Therefore, neglecting the mass floor (*i.e.*, $m_{fl} = 0$), since $t_{SF} = 6 t_{cr}$, we find:

$$\mathcal{R} = (0.473 + 0.008 m_{cl,4}^{-1.32})\, m_{cl,4}^{-0.24} \left(\frac{\overline{n}_{gas}}{n_{cri}}\right)^{0.33} \left(1 + \frac{\overline{n}_{gas}}{n_{cri}}\right)^{0.22}. \tag{3.18}$$

3.4.2 Ionising Photons from OB Associations

In our Galaxy and nearby dwarf and spiral galaxies, the mass function of young massive star clusters (or OB associations) is a power-law with slope $\xi \simeq -2 \pm 0.5$ (Rosolowsky, 2005; Hopkins, 2012b):

$$\frac{dN}{dm_{\mathrm{cl}}} = A m_{\mathrm{cl}}^{\xi},$$

where, assuming $\xi = -2$ (Hopkins, 2012b), we find $A = M_{*,gal}/\Lambda$, with $\Lambda = \ln\left(m_{cl}^{\max}/m_{cl}^{\min}\right)$. Assuming $m_{cl}^{\max} = 10^6\ \mathrm{M}_\odot$ and $m_{cl}^{\min} = 100\ \mathrm{M}_\odot$, we estimate $\Lambda \approx 9.2$. Therefore, assuming an escape fraction $f_{\mathrm{esc}}^{\mathrm{ISM}}$ from the atomic phase of the ISM in the galaxy (defined excluding the absorption due to the molecular cloud) that is constant as a function of the cluster mass, we find:

$$
\begin{aligned}
S_{esc}^{\rm gal} &= f_{\rm esc}^{\rm ISM} \int_{m_{cl}^{\rm min}}^{m_{cl}^{\rm max}} \frac{{\rm d}N}{{\rm d}m_{cl}} S_{esc}(m_{cl})\, {\rm d}m_{cl} \\
&= f_{\rm esc}^{\rm ISM} \frac{M_{*,\rm gal}}{\Lambda} \int_{m_{cl}^{\rm min}}^{m_{cl}^{\rm max}} m_{cl}^{-1} \frac{S_{esc}}{m_{cl}}\, {\rm d}m_{cl} \\
&\approx f_{\rm esc}^{\rm ISM} \left(\frac{M_{*,gal}}{1{\rm M}_\odot}\right) \cdot \begin{cases} \frac{7.4\times10^{60}}{\Lambda/9.2} \left(\frac{m_{cl}^{\rm max}}{10^6\ M_\odot}\right)^{0.4} & \text{(very compact)}, \\ 1.4\times10^{60} & \text{(compact))}, \\ 1.8\times10^{59} & \text{(fiducial)}. \end{cases}
\end{aligned}
\tag{3.19}
$$

Therefore, as anticipated before in Section 3.3.3, in the local Universe (fiducial clouds) the escaping ionising radiation from a galaxy is produced by roughly equal contribution from small and large mass star clusters, and the number of escaping photons is $\sim 10^{59}$ per unit solar mass in stars. Therefore, the total escaping radiation is quite insensitive to the upper and lower mass limits of the mass distribution of OB associations. Compact star clusters are similar but with ~ 10 times more ionizing photons per mass in stars. For very compact clouds (100 times denser than the fiducial clouds) the escaping ionising radiation is dominated by the few most massive star clusters in the galaxy, and the number of escaping photons per units star mass is about 40 times higher than for the fiducial clouds.

Also, if we make the simple assumption that the mass of the most massive star cluster is related to the total stellar mass $M_{*,gal}$ of the galaxy, by setting $\int_{m_{cl}^{\rm max}}^{+\infty} dN/d\ln m_{cl} = 1$, we find $m_{cl}^{\rm max} \sim M_{*,gal}/\Lambda$. Hence, if star clusters in high-redshift galaxies form in very compact molecular clouds, massive galaxies would be more efficient contributor to propel reionization than dwarf galaxies. Of course the discussion above is only valid if $f_{\rm esc}^{\rm ISM}$is constant not only as a function of the star cluster mass but also as a function of the mass of the galaxy.

Similarly to $S_{esc,tot}$, we can estimate the total emitted ionising radiation by OB association:

$$S_{tot} = \int \frac{dN}{dm_{cl}} S(m_{cl})\, dm_{cl} \tag{3.20}$$

$$\approx \frac{1.2 \times 10^{62}}{\Lambda} \left(\frac{M_{*,gal}}{1\ M_\odot}\right) \left(\frac{m_{cl}^{\max}}{10^6\ M_\odot}\right)^{0.4}, \tag{3.21}$$

and the mean escape fraction from a galaxy by taking the ratio $S_{esc}^{\rm gal}/S_{tot}$:

$$\langle f_{\rm esc}^{\rm gal} \rangle \approx f_{\rm esc}^{\rm ISM} \cdot \begin{cases} 56.7\% & \text{(Very Compact)}, \\ 10.7\% \left(\frac{\Lambda}{9.2}\right) \left(\frac{m_{cl}^{\max}}{10^6\ M_\odot}\right)^{-0.4} & \text{(Compact)}, \\ 1.4\% \left(\frac{\Lambda}{9.2}\right) \left(\frac{m_{cl}^{\max}}{10^6\ M_\odot}\right)^{-0.4} & \text{(Fiducial)}. \end{cases} \tag{3.22}$$

This last equation confirms that $\langle f_{\rm esc}^{\rm gal} \rangle$ from galaxies in the local Universe (fiducial clouds) is extremely small $\langle f_{\rm esc}^{\rm gal} \rangle \approx f_{\rm esc}^{\rm ISM} \times 1.4\%$, and only assuming that molecular clouds at redshift $z > 6$ were $100\times$ denser than in the local Universe is possible to propel reionization with UV radiation from massive stars in galaxies.

3.5 Summary and Conclusions

In this chapter, the second of a series, we calculate the hydrogen and helium ionizing radiation escaping realistic young star cluster forming in turbulent molecular clouds. To the best of our knowledge this is the first work in which $\langle f_{\rm esc}^{\rm MC} \rangle$ is calculated by self-consistently simulating the formation, UV radiation feedback, and contribution to the escaping ionising radiation from individual massive stars producing the observed IMF slope and normalization. We used a set of high-resolution radiation-magneto-hydrodynamic simulations of star formation in self-gravitating, turbulent molecular clouds presented in He, Ricotti and Geen (2019), in which we vary the mass of the star forming molecular clouds between $m_{\rm gas} = 10^3$ M$_\odot$ to 3×10^5 M$_\odot$ and adopt gas densities typical of clouds in the local universe ($\overline{n}_{\rm gas} \sim 1.8 \times 10^2$ cm^{-3}), and 10× and 100× denser, expected to exist in high-redshift galaxies.

We find that $\langle f_{\rm esc}^{\rm MC} \rangle$ decreases with increasing mass of the star cluster and with decreasing initial gas density. Molecular clouds with densities typically found in the local Universe have negligible $\langle f_{\rm esc}^{\rm MC} \rangle$, ranging between 8% to 1.4% for clouds with masses ranging from 3×10^4 to $3 \times 10^5 {\rm M}_\odot$. Ten times denser molecular clouds have $\langle f_{\rm esc}^{\rm MC} \rangle \approx 20\% - 30\%$, while $100\times$ denser clouds, which produce globular cluster progenitors, have $\langle f_{\rm esc}^{\rm MC} \rangle \approx 30\% - 50\%$. Star clusters with mass $\lesssim 500$ M$_\odot$ have $\langle f_{\rm esc}^{\rm MC} \rangle > 50\%$ independently of their compactness but assuming the observed OB association luminosity function, $dN/dm_{cl} \propto m_{cl}^{-2}$, fall short in providing the required ionising photons for reionization.

We reproduce the simulation results for $\langle f_{\rm esc}^{\rm MC} \rangle$ using a simple analytic model, in which the observed trends with cloud mass and density are understood in terms of the parameter $\mathcal{R}$, the ratio of the lifetime of the most massive star in the cluster to the star formation timescale, that, for clouds with solar metallicity is about 6 times the sound crossing time of the cloud. We find that it takes about 20 times the sound-crossing time ($t_{\rm cr} = r_{\rm gas}/10$ km/s), or 3.5× the star-formation time, for the stars to ionize the cloud and for $f_{\rm esc}(t)$ to become of order of unity. Since $r_{\rm gas}$, therefore $t_{\rm cr}$, increases with increasing cloud mass and decreasing density and the lifetime of the dominating LyC sources is constant at ~ 3 Myr, our model quantitatively reproduce the increase of $\langle f_{\rm esc}^{\rm MC} \rangle$ with decreasing cloud mass and increasing cloud density, observed in the simulations.

We find that $\langle f_{\rm esc}^{\rm MC}\rangle$ increases with decreasing gas metallicity, even when ignoring dust extinction, due to stronger LyC radiation feedback and faster ionization of the cloud. However, as the metallicity decreases, the SFE declines, therefore the total number of escaped LyC photons decreases. For the L-C cloud which we use to investigate this effect, the value of $Q_{\rm esc}$ decreases by a factor of 2 as we decrease the metallicity from $Z_\odot$ to $0.1Z_\odot$, although the value of $\langle f_{\rm esc}^{\rm MC}\rangle$ doubles.

We find that in all our simulations the values of $\langle f_{\rm esc}^{\rm MC}\rangle$ for He LyC photons are nearly identical to $\langle f_{\rm esc}^{\rm MC}\rangle$ for H LyC photons. We explain this result by noting that the ionization fronts of H II and He II are comparable around the dominant sources of ionization, namely hot O stars.

When dust extinction is considered, assuming no sublimation inside H II region, $\langle f_{\rm esc}^{\rm MC}\rangle$ is nearly unaffected compared to dust-free estimates for values of the metallicity < 0.1 solar (see Table 3.3). Assuming solar metallicity, while $\langle f_{\rm esc}^{\rm MC}\rangle$ for the least massive and least compact clouds is nearly unchanged, $\langle f_{\rm esc}^{\rm MC}\rangle$ for the more massive and more compact clouds is reduced significantly, by up to 80%. SN explosions have little effect on the time-averaged $\langle f_{\rm esc}^{\rm MC}\rangle$ for nearly all the star clusters considered in this work, unless we consider fiducial clouds (local Universe) with mass $\gtrsim 10^5{\rm M}_\odot$. In these simulations SN explosions occur before $f_{\rm esc}(t)$ becomes significantly larger than zero, hence mechanical feedback may increase $\langle f_{\rm esc}^{\rm MC}\rangle$.

In conclusion, we find an upper limit on $\langle f_{\rm esc}^{\rm gal}\rangle < 3\% - 10\%$ for star clusters forming in molecular clouds similar in compactness to today's clouds (see discussion in § 3.4 and Eq. (3.22)). Therefore, since large scale simulations show that cosmic re-ionization requires $\langle f_{\rm esc}^{\rm gal}\rangle \gtrsim 10\% - 20\%$, we conclude that the stellar component of the sources of reionization at $z > 6$ must have been very compact star clusters forming in molecular clouds about 10 to $100\times$ denser than in today's Universe. This result indirectly suggests a significant formation of old globular cluster progenitors at redshifts $z > 6$.

Chapter 4: Massive Prestellar Cores in Radiation-magneto-turbulent Simulations of Molecular Clouds

In this chapter, we present simulations of the formation and collapse of prestellar cores at few-AU resolution in a set of radiation-magneto-hydrodynamic simulations of giant molecular clouds (GMCs) using the grid-based code RAMSES-RT. We adopt, for the first time to our best knowledge, realistic initial/boundary conditions by zooming in onto individual massive prestellar cores within the GMC. We identify two distinct modes of fragmentation: "quasi-spherical" and "filamentary". In both modes, the fragments eventually become embedded in a quasi-steady accretion disk or toroid with radii $\sim 500 - 5000$ AU and opening angles $H/R \sim 0.5 - 1$. The disks/toroids are Toomre stable but the accreted pre-existing fragments are found orbiting the outer disk, appearing as disk fragmentation. Each core converts nearly 100 per cent of the gas mass into a few massive stars forming near the disk centre. Large and massive disks around high-mass stars are supported by magnetic pressure in the outer disk, at radii $> 200 - 1000$ AU, and turbulent pressure in the inner disk. The most massive core accretes several times more mass than its initial mass, forming a cluster of 8 massive (proto)stars enshrouded by a toroid, suggesting a competitive accretion scenario for the formation of stars above $\sim 30\ \mathrm{M}_{\odot}$. We also find that the H II regions produced by a single massive star remain trapped in the dense circumstellar disks for a few hundred kiloyears, while the dynamic motions of massive stars in wide binaries or multiple systems displace the stars from the densest parts of the disk, allowing UV radiation to escape producing steady or pulsating bipolar H II regions.

4.1 Introduction

Whether high-mass (HM) stars form from the monolithic collapse of massive prestellar cores – supported by turbulence, and/or magnetic fields rather than thermal pressure – known as the Turbulent Core (TC) scenario (McKee & Tan, 2003; Tan et al., 2014), or via accretion inflows from larger scales, known as the Competitive Accretion (CA) scenario (Bonnell et al., 2001; Padoan et al., 2020), still remains an open question. Observations (Fuller et al., 2005; van der Tak et al., 2019) of accreting HM young stellar objects (YSOs) suggest that HM stars form similar to their low-mass counterparts via infall from a surrounding envelope and from anisotropic accretion flow from an accretion disk. However, the physical processes involved are not well understood partially due to the lack of high-resolution observations of structures below ~ 1000 AU owing to the large distances of the sources, high dust extinction, high multiplicity, and complexity of the environment typical of high-mass star formation. The shorter timescale of formation and rarity of the objects result in a low probability of finding a O-type massive (proto)star or massive starless core.

The CA model postulates that low-mass protostellar seeds accrete unbound gas within the clump from large scales in a hierarchical structure. To test the idea of the CA scenario from a theoretical perspective, we need to simulate the formation of prestellar cores from the collapse of turbulent giant molecular clouds (GMCs), which is the site of star formation. Several numerical studies have investigated the formation of star clusters from GMCs (Jones & Bate, 2018; Lee &

Hennebelle, 2018a; Kim et al., 2018; Bate, 2019; Fukushima et al., 2020; Grudić et al., 2021; Kim et al., 2021). In He, Ricotti & Geen (2019); He, Ricotti & Geen (2020) we have conducted a series of simulations of the collapse of isolated turbulent GMCs using RAMSES-RT. In these works we have run a large grid of GMC simulations and pushed the parameters of the GMC mass and density to include very massive ($\sim 10^5$ M$_\odot$) and extremely dense ($\sim 10^4$ cm^{-3}) clouds, resolving the formation of individual stars with masses $M \gtrsim 1 M_\odot$, significantly improving the resolution with respect to previous works (see a summary in Table 2 of Lee & Hennebelle 2018a). The initial mass functions (IMFs) of the stars forming in these simulations have not only characteristic power-law slopes very close to Kroupa (2002) at the high-mass end, but also the correct normalization to a mass-normalized Kroupa IMF if we assume that each sink particle converts $\sim 40\%$ of its mass to a single star and the remaining mass forms several smaller mass stars. This scaling is also inferred from the mapping between the observed core mass function (CMF) and stellar IMF that preserves the slope and normalization of the IMF. Hence, we hypothesize that the unresolved sinks in the simulation form stars with high efficiency but fragment into lower-mass stars.

Motivated by these previous results, in this work we aim at testing our assumption on the fragmentation of sink particles in order to understand the mass function, star multiplicity, and kinematics which is important to eventually understand the long-term evolution of the star cluster and a possible role of high-z compact star clusters in forming and growing intermediate-mass black holes (IMBHs) seeds. The methodology we use is to perform higher-resolution "zoom" simulations of the fragmenting protostellar cores, while simultaneously following the collapse of the GMC in which the cores are located.

There is growing evidence from ALMA observations that accretion disks around massive proto-stars undergo fragmentation and produce companion stars (*e.g.*, Johnston et al., 2015; Guzmán et al., 2020; Williams et al., 2022; Olguin et al., 2022). Ilee et al. (2018) reported the observation of a fragmented Keplerian disk around an O-type protostar, with a fragment in the outskirts of the disk at ~ 2000 AU from the primary. Johnston et al. (2020) observed spiral arms and instability in a disk of radius ~ 1000 AU around an O-type star.

Disks are observed to not only possess substructures in the (r, θ) plane, but also show clear signs of substructures in the vertical (z) direction (Muzerolle et al., 2009; Espaillat et al., 2011). Warped geometries or misalignment ("broken" disks) have been inferred kinematically with resolved spectral line data (Rosenfeld et al., 2012; Casassus et al., 2015) and scatter light shadows at larger r (Marino et al., 2015).

A considerable amount of research has studied disks around nearby solar-type stars. However, the number of disks studied around more distant, massive stars (type A and earlier) is comparatively small. This is because massive protostellar cores that may form massive stars, multiple systems or even a mini-cluster of stars are fewer and short-lived, and hence are less likely to be found nearby.

Recent advances in radio/mm and optical/IR interferometers have enabled important progress in the field of disks around intermediate-mass (IM) and HM YSOs. These observations of embedded IM protostars (A to late-B spectral type) (Zapata et al., 2007; Sánchez-Monge et al., 2010; van Kempen et al., 2012; Takahashi et al., 2012) have revealed circumstellar disks with typical radii of a few hundred of AU. These disks are geometrically thick with a scale height that is more than 20-30 per cent of their radius. The disks have masses of a few solar masses and could be in Keplerian rotation. Evidence for circumstellar disks has been reported (Cesaroni et al., 2005; Patel et al., 2005; Kraus et al., 2010; de Wit et al., 2011; Ginsburg et al., 2018; Law et al., 2022) for HM (proto)stars (early-B to late-O type) that correspond to zero-age main sequence stars of about 25-30 $\mathrm{M}_{\odot}$ with typical radii of a few thousands of AU, although radii smaller than 1000 AU have been estimated in some samples. These geometrically thick structures have scale heights of $> 30 - 40$ per cent of their radii and masses that range from a few $\mathrm{M}_{\odot}$ to a few tens of $\mathrm{M}_{\odot}$. They are gravitationally stable as suggested by Toomre's stability parameter $Q > 1$. In short, the basic properties of the disks around HM (proto)stars appear as a scaled-up version of those found for disks around low-mass and intermediate-mass protostars (see Beltrán & de Wit, 2016, for a review).

For stars of extremely high mass ($> 30\mathrm{M}_{\odot}$), the existence of a circumstellar disk has been elusive in observations. Simulations have shown that radiation pressure does not prevent disk accretion to form stars up to $140\mathrm{M}_{\odot}$ (Krumholz et al., 2009; Kuiper et al., 2010). However, no models of protostars allow the formation of a hydrostatic object beyond this limit. Large, dense ($n \gtrsim 10^{7}$ cm^{-3}) and massive (a few $\times 100$ $\mathrm{M}_{\odot}$) rotating cores have been detected around early-O-type protostars. These are likely non-equilibrium structures that favour the formation of young stellar mini-clusters instead of individual massive stars (Cesaroni et al., 2007; Beltrán et al., 2011).

In this work, we study the collapse of prestellar cores and the structure of protostellar disks around massive stars in realistic simulations of turbulent GMCs. These disks span a large range in sizes and masses. In this chapter, we emphasize the dominant role of turbulence and magnetic field in determining the formation and support against the gravity of massive disks within prestellar cores. In a companion work, we will address in more detail the structure and evolution of the magnetic field and the problem of magnetic braking.

The rest of this article is organized as follows. We describe our simulation method in

Table 4.1: (17) disk aspect ratio.

Core	$M_{\rm core}$ ($M_\odot$)	$M_{*,\rm base}$ ($M_\odot$)	$n_{\rm sink,base}$ (cm^{-3})	$\alpha_{\rm vir}$	$\beta_{\rm rot}$	μ	$l_{\rm max}$	$n_{\rm sink}$ (cm^{-3})	$\Delta x_{\rm min}$ (AU)	$M_{*,\rm tot}$ ($M_\odot$)	$M_{*,\rm max}$ ($M_\odot$)	$N_{\rm stars}$	mode	$R_{\rm disk}$ (AU)	$H_{\rm disk}$ (AU)	$H_{\rm disk}/R_{\rm disk}$
*Ahr**	27.7	12.0	1.4×10^7	0.270	0.095	3.146	20	5.7×10^{10}	7.2	12.6	4.9	12	spherical	600	100-200	0.17-0.33
*B**	119	309	3.0×10^6	0.489	0.071	2.351	18	7.7×10^8	60	¿601	75.1	9	filamentary	6000	3000	0.5-1.3
C	50.8	32.6	1.4×10^7	0.348	0.058	2.114	18	3.6×10^9	29	43.1	42.7	4	spherical	200	100	0.5
D	63.3	8.4	6.5×10^6	0.182	0.060	1.826	18	1.7×10^9	42	14.7	14.7	1	filamentary	600	200	0.33

Section 4.2. We present the basic results in Section 4.3, where we discuss the formation of turbulent massive disks. In Section 4.4, we discuss the properties of the core fragments. We provide discussions and the summary in Section 4.5.

4.2 Methods and Simulations

We conduct "zoom-in" radiation-MHD simulations of collapsing molecular clouds resolving individual prestellar cores. We focus on the fragmentation of the cores and the formation of protostellar disks. We have conducted a set of 6 simulations on a large range of sink masses selected from several parental GMCs. We summarize the key parameters and results in Table 4.1.

We perform simulations using the grid-based adaptive mesh refinement (AMR) MHD code RAMSES-RT (Teyssier, 2002; Fromang et al., 2006). Radiation transfer is modelled using a moment-based method with the M1 closure relation for the Eddington tensor (Rosdahl et al., 2013). The ionizing photons emitted from stars interact with neutral gas and we keep track of the ionization chemistry of hydrogen and helium, but we do not include the chemical evolution of the molecular phase. Heating from photoionization and cooling from hydrogen, helium, metals, and dust grains are implemented (see Geen et al. 2017 for details). Cooling below 10 K is shut down to keep the temperature floor at 10 K. We carry out simulations starting from a subset of simulations presented in He et al. (2019) and zooming into prestellar cores to resolve their fragmentation and disk formation. We refer to the original paper for details of the method and key results of these baseline simulations. Here we briefly summarize the AMR technique and sink particle recipe before getting into the zoom-in method.

The baseline simulations (He et al., 2019) are started from idealized spherical isothermal clouds in hydrostatic equilibrium surrounded by a low-density shell, in which gravity is nearly balanced by turbulent motions ($\alpha_{\rm vir} \equiv \mathcal{K}/|\mathcal{W}| = 0.4$). We let the GMC evolve for three free-fall times with gravity reduced by 1/2, to allow the turbulence to develop. Then, gravity is fully turned on and the cloud undergoes filamentary collapse and fragments to form sink particles in dense regions that represent singular stars or small clusters of stars, as described in Bleuler & Teyssier (2014). Adaptive mesh refinement is applied to the whole domain to make sure at any time and any location the local Jeans length, $L_J = c_s\sqrt{\pi/(G\rho)}$, is resolved by at least 10 grid points. The maximum refinement level $l_{\rm max}$ is set to 14, reaching a minimum grid size $\Delta x_{\rm min}$ that is $1/2^{14}$ of the box size, or around 200 - 1600 AU. When the density reaches the critical density, $n_{\rm sink}$, defined such that the corresponding Jeans length equals 5$\times$ the grid size at the maximum refinement level $l_{\rm max}$, a sink particle is placed to prevent the increase of the gas density beyond $n_{\rm sink}$ at which a local Jeans length is not fully resolved. The critical density for sink formation is set to $n_{\rm sink} = 2.16 \times 10^{10}$ cm$^{-3}(\Delta x_{\rm min}/10$ AU$)^{-2}$, motivated by the criterion that a Jeans length must be resolved by no less than 5 grid cells. The corresponding Jeans mass is 0.0055 M$_\odot(\Delta x_{\rm min}/10$ AU$)$. In the baseline simulations in He et al. (2019) used as initial conditions, $n_{\rm sink}$ ranges from 10^6 cm^{-3} to 6×10^7 cm^{-3}, while in the zoom-in simulations presented here, we reach densities three orders of magnitude higher: $n_{\rm sink}$ ranges from 10^9 cm^{-3} to 5×10^{10} cm^{-3}. Accretion onto the sink particles is modelled using a threshold method such that 75% of the mass above $n_{\rm sink}$ is transferred to the sink particle in each time step (Bleuler & Teyssier, 2014). Ionizing photons are emitted from the sink particles to ionize and heat the gas,

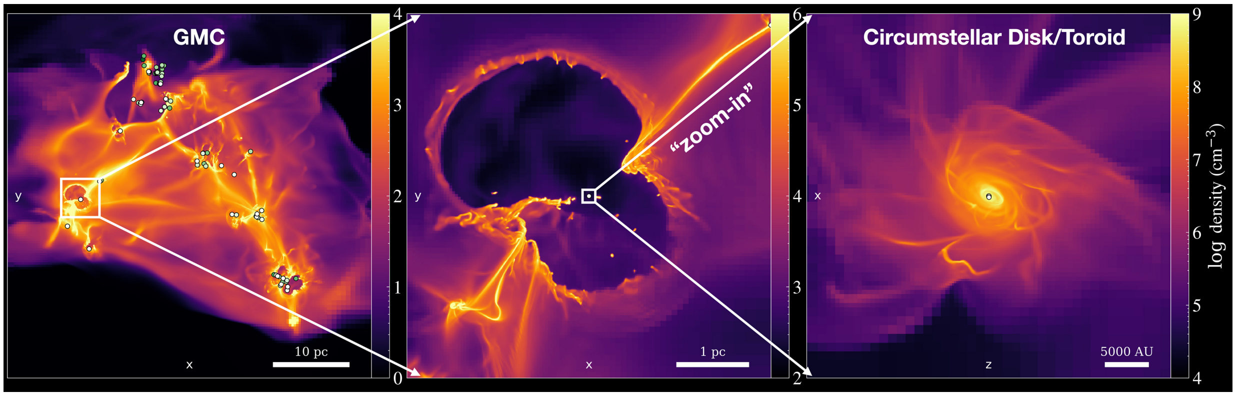

Figure 4.1: Outline of the simulation method. We pick a zoom region which is a box at the formation location of a sink particle. Inside the box, we allow a high level of refinement to reach high density before star formation. The whole simulation spans a dynamic range up to $2^{20} \approx 10^6$ in linear scale, or a volumetric dynamic range of 18 orders of magnitude.

dispersing the cloud and quenching star formation. These sink particles in the baseline simulations are shown to resemble prestellar cores observed in local star-forming regions.

In the "zoom-in" simulations presented in this chapter, we start a simulation from a snapshot of a baseline AMR simulation right before the formation of a sink particle (Figure 4.1). We define a "zoom" region, about 0.5 to 1 pc in size, where the sink particle is about to form and allow a higher $l_{\rm max}$ only within this region. To reach the best possible resolution, we use a nested refinement structure where $l_{\rm max}$ increases as it gets closer to the domain centre. In the simulation with the best resolution (Core *A-hr*, as we will introduce later), $l_{\rm max}$ at the centre of the "zoom-in" region is set to 20, reaching a dynamic range of $2^{20} \approx 10^6$, or 18 orders of magnitude in volume. The corresponding critical density of sink formation $\rho_{\rm sink}$ is 1.4×10^{-13} g cm^{-3}, approaching the density at which the core transitions from isothermal to adiabatic (Masunaga et al., 1998; Masunaga & Inutsuka, 2000). The corresponding spatial resolution and other parameters for all simulations are listed in Table 4.1. This "zoom-in" AMR method has been applied to MHD simulations of low-mass star formation without radiation feedback (Kuffmeier et al., 2017, 2019).

In this work we report the first application of this method in radiation-MHD simulations of star formation.

Hydrogen and helium-ionizing photons are emitted from sinks and heat the gas. The hydrogen-ionizing luminosity of a sink particle with mass $M_{\rm sink}$ is given by:

$$S = 9.63 \times 10^{48}\ \mathrm{s}^{-1} \left(\frac{0.4\ M_{\rm sink}}{27.28\ M_{\odot}} \right)^{1.86}. \tag{4.1}$$

This is the same as the fits given in Vacca et al. (1996) for high-mass stars ($\gtrsim 30$ M$_{\odot}$). However, Vacca et al. (1996) fits are described by a broken power law and have a steeper slope for masses < 10 M$_{\odot}$. Hence, we are overestimating the ionizing radiation emitted by stars with masses smaller than ~ 10 M$_{\odot}$. The excess of ionizing photons from low/intermediate-mass stars is used to compensate for the lack of protostellar outflows or jets in our simulations. This recipe proved to be effective in reproducing the canonical IMF in our previous simulations (He et al., 2019).[1] However, we acknowledge that the lack of protostellar outflows and radiative heating (e.g. Krumholz et al., 2007) in our feedback recipe may cause the gas temperature during the protostellar phase to be underestimated and the efficiency of conversion of core gas mass into stars to be overestimated. We also neglect radiation pressure from stars that could be important in high-mass star formation (e.g. Krumholz & Matzner, 2009; Kuiper et al., 2010; Rosen et al., 2016). Further simulations with more realistic feedback mechanisms are left for future work.

We set a magnetic field with moderate strength in the x-direction threading the isothermal cloud in the initial conditions. The GMC starts from an idealized sphere with an isothermal core

[1]In He et al. (2019) we adopted a broken power-law as in Vacca et al. (1996), but due to a bug in the code, the change in power-law slope at the low-mass end did happen at much lower masses. When we found and fixed the bug, we observed that the IMF at the high-mass end was not reproduced as well as before. We interpreted this result as the need for stronger feedback from the low-mass end, perhaps produced by protostellar outflows.

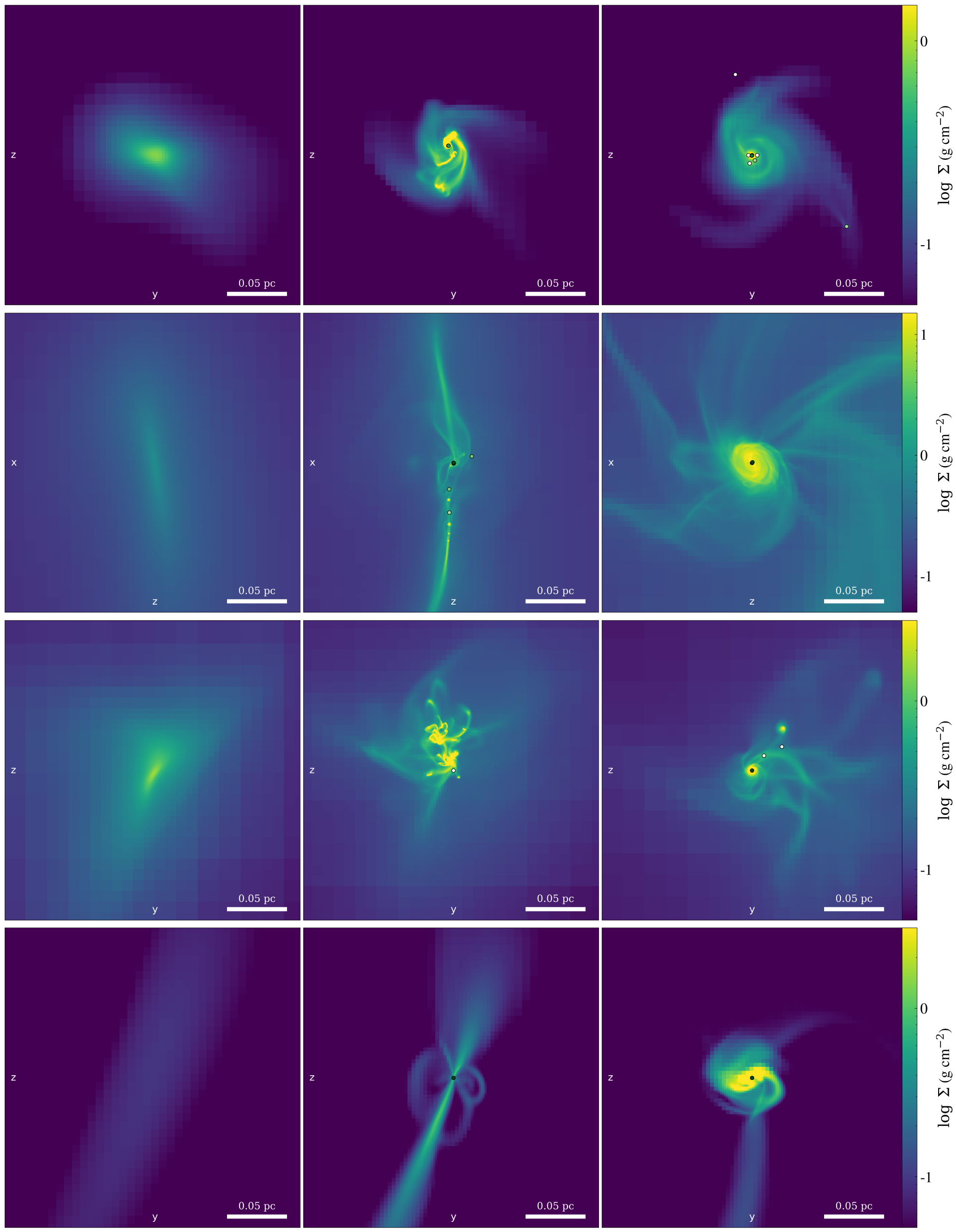

Figure 4.2: Gallery of the collapsing prestellar cores *A-hr*, *B*, *C*, and *D*, from top to bottom, respectively. The colours are the column density of the gas in a direction aligned with the box but nearly parallel to the angular momentum direction of the gas. The first snapshot for each core shows its initial morphology and the second snapshot shows how the core collapses. The third snapshot is at a time when the disk reaches a quiescent, nearly steady-state phase. Sink particles representing single stars are plotted on top as coloured circles, with darker shades indicating higher masses. The cores display two distinct kinds of morphology. Cores *A-hr* and *C* are examples of a spherical mode of collapse, while Cores *B* and *D* are examples of the filamentary collapse mode. Note that the colourmap in the second row has a higher upper limit.

surrounded by a low-density shell that extends twice the radius. The magnetic intensity is about $10 - 25\mu$G at a density of 10^3 cm^{-3} and the mass-to-flux ratio is $\mu \approx 5$ averaged over the whole GMC. The value of μ in the isothermal core of the GMC is higher (≈ 8) due to the fact that the mass is more concentrated in the core but the magnetic field is more evenly distributed. After a period of relaxation to let the turbulence develop, the initial mean density decreases slightly and μ settles at 3 – 4, averaged over the whole molecular cloud. Instead of the traditional definition of the mass-to-flux ratio, $\mu \equiv M/M_\Phi$, where M_Φ is the magnetic critical mass, we adopt a definition that takes into account the non-homogeneity of the density and magnetic field, $\mu = \sqrt{|\mathcal{W}|/\mathcal{B}}$, where $\mathcal{W}$ is the gravitational binding energy and $\mathcal{B}$ is the magnetic energy. The two definitions are equivalent for a uniform spherical cloud with uniform magnetic field. We will explain further the derivation and significance of the μ parameter in § 4.3.

The motion of the sink particles is determined by combining direct N-body integration (using the leapfrog method) between the sinks and between the sinks and the gas based on the particle mesh method. A softening length of $2\Delta x_{\rm min}$ is set to avoid singularities.

4.3 Results. I. Turbulent massive disks

The main result of this study is the formation of rotationally supported thick disks, characterized by supersonic turbulence and a moderately strong magnetic field. Figure 4.2 shows snapshots for a grid of simulations illustrating the evolution of the prestellar cores inside turbulent GMCs. In all four simulated prestellar cores with various initial masses and morphologies, quasi-Keplerian disks form around the central proto-star/binary. The morphologies of the disks are very similar to those found in many previous studies (Bate et al., 2003; Goodwin et al., 2004a;

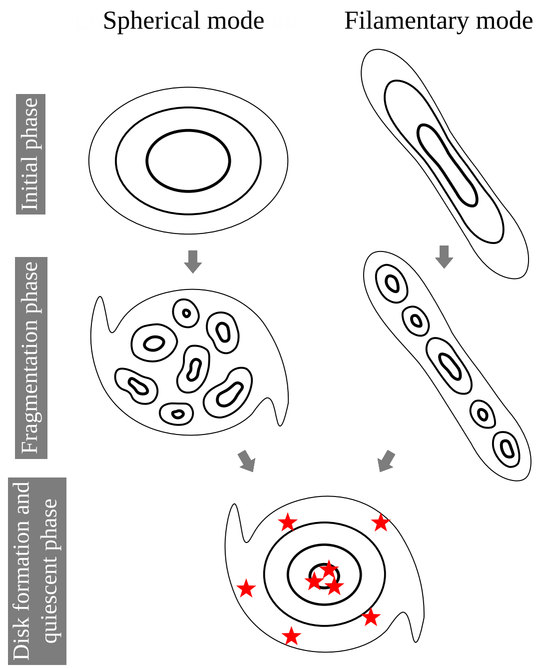

Figure 4.3: Schematic of the two modes of prestellar core fragmentation and disk formation. In the spherical mode, the core begins with a spherical/oblate shape and fragmentation occurs in arms, bars or mini-filaments inside the core. In the filamentary mode, or mode B, the core starts from a long, thin tube and instabilities occur on the arms of the filament. In both scenarios, a centrifugal disk forms at the core centre a few hundred kiloyears after the initial phase. The disks have sizes up to several thousand AU. The central star/binary and secondary stars that form from the core fragments orbit around the disk centre, entering a quiescent phase.

Hennebelle & Fromang, 2008): spiral arms that could potentially transport angular momentum are prominent features. We summarize the key properties of the disks in Table 4.1.

In the classical picture, the gravitational collapse of a magnetized prestellar core occurs from an initially spherical structure that tends to flatten along magnetic field lines, leading to the formation of an oblate pseudo-disk (Galli & Shu, 1993). These pseudo disks are disk-like but are not supported by centrifugal force and may transition into centrifugally supported disks (Galli & Shu, 1993; Joos et al., 2012). The collapse of turbulent cores in our simulations spans a wide variety of morphologies (Figure 4.2) that are far different from idealized spherical collapse.

Examples of spherical collapse geometry are cores *A-hr* and *C* in Figure 4.2. In the second geometry, the core collapses into a thin elongated filament, which breaks into aligned quasi-spherical fragments. This fragmentation mode is represented by cores *B* and *D*. In the filamentary fragmentation the prestellar cores form from a larger-scale filament structure, hence they are aligned in one direction before reaching the centre of mass and become randomized. This is in contrast to the spherical collapse in which the core initial positions are already randomized during the fragmentation phase. Even in the spherical collapse geometry small filaments are visible but not aligned on large scales: the fragments form in hierarchical arms or bars probably due to the higher angular momentum of the gas in this mode of collapse. Regardless of the different modes of collapse, the outcome is a geometrically thick massive disc, in which the pre-existing fragments are collected (see Figure 4.3). The orbiting fragments may lead to the formation of low-mass stars that are either ejected or spiral toward the centre.

The 5th, 6th, and 7th columns in Table 4.1 report the initial (when the core density reaches $10^6 - 10^7\ \mathrm{cm}^{-3}$) kinetic, rotational, and magnetic energy compared to the gravitational potential energy of each core. We do not find any strong correlation between these initial properties of the cores and their subsequent collapsing mode. For instance, in the case of Core *B*, the core has initially large kinetic energy (high α_{vir}) and weak rotation (low β_{rot}), consistent with a strong radial infall along the arms, hence filamentary collapse. However, this interpretation fails to apply to Core *C* which similarly has large kinetic energy and weak rotational support but collapses in the spherical mode. We, therefore, do not find a strong connection between the aforementioned initial properties of the cores and their collapsing mode other than their initial geometry, as shown in Figure 4.2. With only 4 cores reported in this work, we do not have enough statistics to comment on the probability of one mode over the other. At this time we simply conclude that different modes are primarily determined by the initial degree of elongation of the cores.

As the gas collapses and the density becomes higher than $\sim 10^6 - 10^7$ cm^{-3}, almost inevitably conservation of angular momentum produces quasi-Keplerian protostellar disks. Almost all the gas with density above 10^7 cm^{-3} is in disks rather than turbulent quasi-spherical cores (see Figure 4.2). This is in contrast to the hierarchical structure of the molecular cloud at larger scales and lower densities, better described as clumps composed of more compact mini-clumps (see, He et al., 2019). The cores in our zoom-in simulations have masses between ~ 27 M$_\odot$ and ~ 120 M$_\odot$, and the protostellar disks forming from their collapse are thick and supported in the vertical direction by magnetic pressure and turbulent pressure rather than thermal pressure. This is contrary to what is observed in simulations of standard lower mass protostellar disks around solar mass protostars, in which the disk scale height is determined by thermal pressure (*e.g.*, André Oliva & Kuiper, 2020). We will discuss this result in detail in § 4.3.3.

Apart from a central star/binary that eventually grows to have a large fraction of the total mass of the core, multiple secondary stars form at the outskirt of the pseudo-disk. These stars form from pre-existing fragments formed uniformly inside a quasi-spherical turbulent core or from the fragmentation of a collapsing filament. Shortly after their formation, some of these fragments spiral into the centre of the disk owning to either dynamical friction or torques exerted by accretion or gravity from the asymmetric core, and some are ejected from the system. In the last phase of the evolution, between 1 to 12 stars form in the core. This is consistent with previous numerical studies (Bate & Burkert, 1997; Goodwin et al., 2004a,b). Nonetheless, these small N-body systems are unlikely to be observed because they evaporate into the field on timescales shorter than the lifetime of the disks. It remains to be understood whether the stars produced by the dissolution of this small hierarchical N-body system retain their original binary fraction.

In the rest of this section, we closely examine the properties of the centrifugal disks in cores *A-hr* and *B*, demonstrating that the disk's scale-height is primarily determined by magnetic support and turbulent motions.

Let us first introduce some definitions useful to describe the stability of the cloud to fragmentation and the importance of the magnetic field.

The dynamical importance of the magnetic field in a cloud of mass M is often parameterized in terms of the dimensionless ratio $\mu \equiv M/M_\Phi$, where M_Φ is the magnetic critical mass: the mass at which the pressure from the magnetic energy, $\mathcal{B}$, balances the gravitational binding energy, $\mathcal{W}$, of the cloud. For a spherical cloud of uniform density and uniform magnetic intensity, $\mathcal{W} = -3GM^2/(5R)$ and $\mathcal{B} = B^2R^3/6 = \Phi_B^2/(6\pi^2 R)$, where $\Phi_B \equiv \int B_\perp dS = \pi R^2 B$ is the magnetic flux. By setting $|\mathcal{W}| = \mathcal{B}$, we get the magnetic critical mass

$$M_\Phi = \sqrt{\frac{5}{2}}\frac{\Phi_B}{3\pi G^{1/2}}. \tag{4.2}$$

Then,

$$\frac{|\mathcal{W}|}{\mathcal{B}} = \frac{18\pi^2}{5}\frac{GM^2}{\Phi_B^2} = \frac{M^2}{M_\Phi^2} = \mu^2. \tag{4.3}$$

In our analysis, we adopt the equivalent definition $\mu = \sqrt{|\mathcal{W}|/\mathcal{B}}$ to calculate the mass-to-flux ratio in our simulations. The advantage is that it accounts for the inhomogeneity of the density and magnetic field distribution as well as the binding energy between the central stars and the disk. For a cloud or a core that is centrally concentrated, μ calculated using this definition is slightly higher than the classical definition because the binding energy is increased by the mass concentration in the centre.

Simulations (Joos et al., 2012) have shown that if $\mu \lesssim 1$, the cloud does not collapse due to the support of the magnetic field. If $1 \lesssim \mu \lesssim 5$ the cloud collapses but magnetic braking prevents the formation of a disk and the gas collapses quasi-spherically. If $\mu \gtrsim 5$ a quasi-Keplerian disk can form. We will show that in our simulations pre-stellar cores have $\mu \sim 1 - 5$, however, we nevertheless observe the formation of quasi-Keplerian disks.

Neglecting the effect of the magnetic forces, we define the Toomre Q parameter

$$Q = \frac{\Omega\,\sigma(v_z)}{\pi G \Sigma}, \tag{4.4}$$

where we have replaced c_s with the vertical turbulent velocity $\sigma(v_z)$ since, as we will show later, the support of the disk against gravity in the vertical direction is dominated by turbulent motions rather than thermal pressure.

4.3.1 Evolution of a 27 solar mass core (Core *A-hr*)

In this subsection, we describe the properties of one of the smaller cores in our set of simulations: core *A-hr*. The general properties of this core are shown in Table 4.1, also showing that the resolution of this simulation is ~ 7 AU, the highest in our set. This core forms in the quasi-spherical geometry of fragmentation. Each panel in the top two rows of Figure 4.4 shows the gas density on a slice through the centre of the core/disk and the smaller insert shows the projected gas density in a view parallel to the angular momentum of the gas (face-on, first row) and a view perpendicular to it (edge-on, second row). From left to right, each panel shows the time evolution of the core as indicated by the labels.

When the core starts collapsing it has a spheroidal shape; we define time $t = 0$ when the central density of the core reaches $\sim 10^6$ cm^{-3}. In Figure 4.4, the snapshots are shown at times

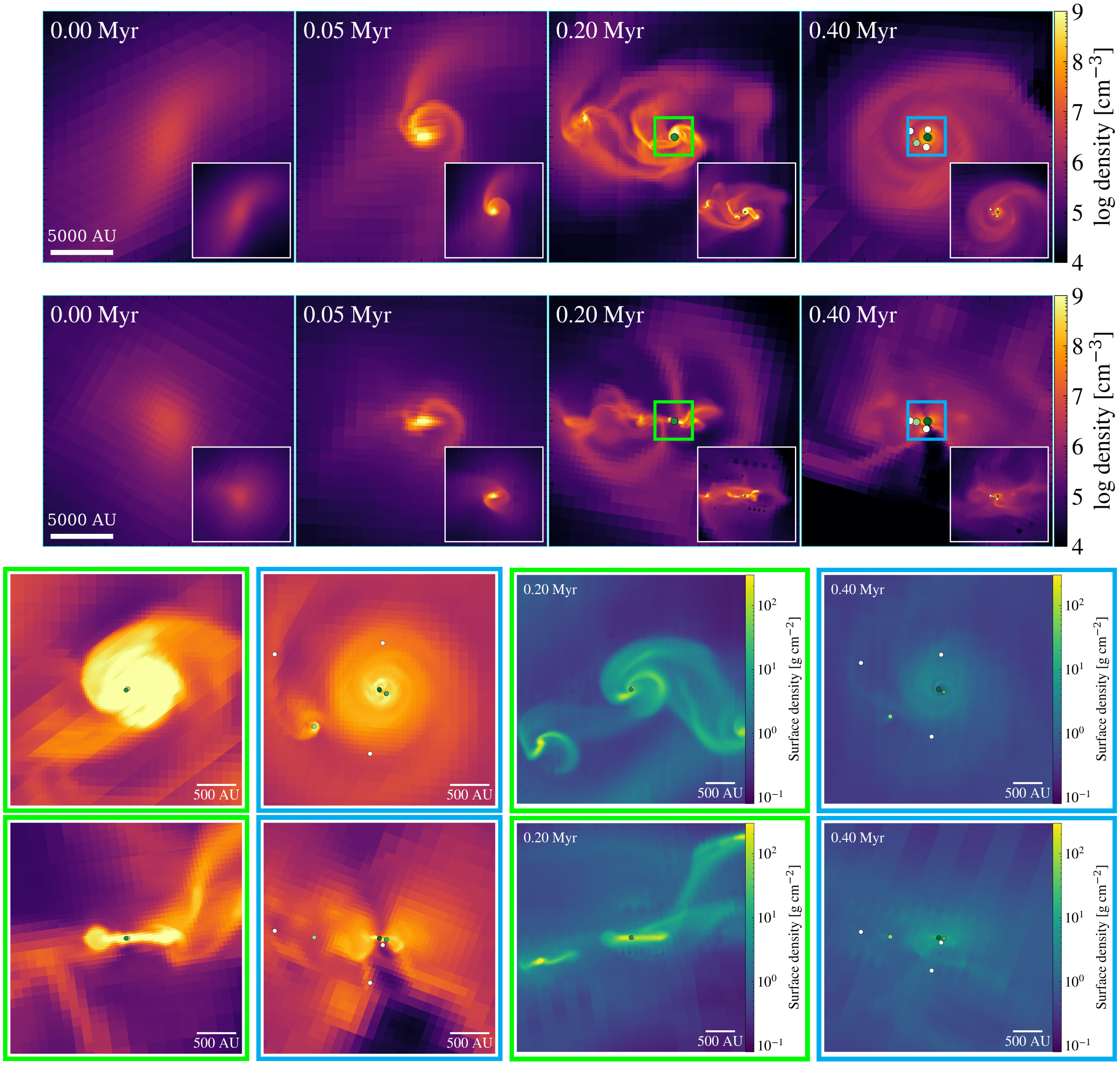

Figure 4.4: Density slices of the $\sim$ 27 M$_\odot$ core (Core *A-hr*) at the mid-plane (first row) or cross-section (second row) at various ages. The images measure 2×10^4 AU ($\sim$ 0.1 pc) on a side, and the circles mark the positions of the star particles with darker shades indicating higher mass. Density-weighted projections of the gas density are inserted at the bottom right corners of each panel to better demonstrate the core structure. The first snapshot is chosen at the initial isothermal phase when the central density reaches 10^6 cm^{-3}. The second snapshot is picked when the instability occurs in the centre. The third snapshot is picked when the first stars form at the centre. The fourth snapshot is picked when the disk comes to a quiescent phase. The last two rows display a zoomed view of the disk which is characterized by volume density above 10^{8-9} cm^{-3}, or surface density above $\sim$ 10 g cm^{-2}. The core spherically collapses from the initial sphere into a disk whose spiral arms could potentially transport angular momentum outward. A mini-cluster of stars orbits around the disk centre.

$t = 0, 50, 200$ kyr and 400 kyr, from left to right. The last three snapshots correspond to times when: i) a disk forms and becomes Toomre unstable at its centre; ii) when the first star forms; and iii) when a quasi-steady (quiescent) disk forms.

Due to the conservation of angular momentum, the spherically symmetric collapse transitions into a rotation-dominated but turbulent fragmentation. As the central density increases and the disk becomes more gravitationally (Toomre) unstable, a spiral arm forms at the centre of the core. The subsequent evolution of the core is crucially dependent on supersonic turbulence. Eddies of eddies emerge and dense sub-cores at their centres spiral inward. This is a well-known mechanism that allows rapid gas accretion and transport of angular momentum in an unstable disk. These dense blobs are the locations where later on a single-star or a multiple-star system will form. When the first star forms at the centre of the system, accretion of gas into the central star clearly appear as a protostellar disk with prominent spiral arms, similar to those seen in many previous studies (Bate et al., 2003; Goodwin et al., 2004a; Hennebelle & Fromang, 2008). A zoom-in view of this smaller disk at times 200 kyr and 400 kyr is shown in the last two rows of Figure 4.4. The first two columns show the gas density in a slice through the disk face-on (third row) and edge-on (fourth row) to emphasize the typical flared shape of the disk in the edge-on view. The last two columns show the gas surface density, emphasizing the presence of spiral arms and the presence of other smaller disks forming from the contraction of other nearby smaller fragments, in good agreement with recent observations discussed above.

In Figure 4.5 we show a detailed quantitative characterization of the time evolution and properties of the collapsing core leading to the formation of the disk. We consider either spherically averaged profiles, most appropriate to describe the initial phases of the evolution and the outer parts of the core that maintain quasi-spherical geometry, or cylindrical coordinates, most

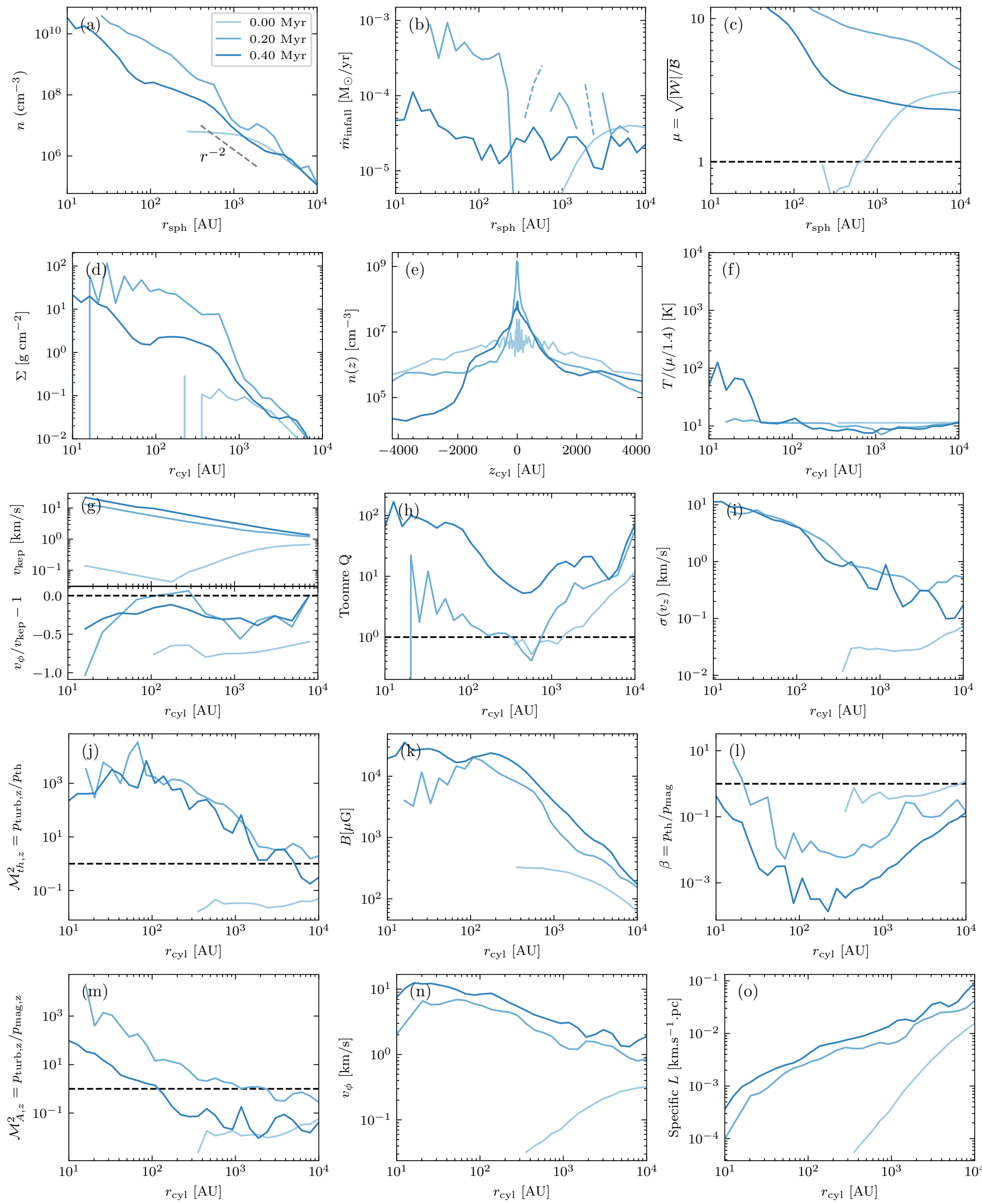

Figure 4.5: Radial and vertical profiles of the 27 M$_\odot$ core *A-hr*. The x axis represents the radius in a spherical coordinate $r_{\rm sph}$, i.e. the distance to the centre, or the radial distance in a cylindrical coordinate $r_{\rm cyl}$, or the longitudinal position $z_{\rm cyl}$. The curves are averaged values of the following physical quantitates: (a) Number density at spherical radius $r_{\rm sph}$. (b) Mass infall rate at $r_{\rm sph}$. The dashed curve indicates a negative infall rate. (c) Mass-to-flux ratio at $r_{\rm sph}$, defined as the square root of the ratio of gravitational binding energy to magnetic energy, $\beta = \sqrt{\mathcal{W}/\mathcal{B}}$, enclosed within $r_{\rm sph}$. This is equivalent to the common mass-to-critical mass definition. (d) Column density at cylindrical radius $r_{\rm cyl}$ in a depth of 5000 AU. (e) Number density of a cylinder with radius 6000 AU at cylindrical height $z_{\rm cyl}$. (f) Temperature at $r_{\rm cyl}$. (g) Non-Keplerianity on the disk plane defined as $(v_\phi - v_{\rm kep})/v_{\rm kep}$. (h) Toomre Q at $r_{\rm cyl}$. (i) Vertical-component velocity dispersion at $r_{\rm cyl}$. (j) Square of z-component thermal Mach number, $\mathcal{M}^2_{\rm th} = p_{\rm turb,z}/p_{\rm th}$ at $r_{\rm cyl}$. (k) Magnetic field strength at $r_{\rm cyl}$. (l) Plasma beta, $\beta = p_{\rm th}/p_{\rm mag}$, at $r_{\rm cyl}$. (m) Square of the z-component Alfven Mach number, $\mathcal{M}^2_A = p_{\rm turb,z}/p_{\rm mag}$, at $r_{\rm cyl}$. (n) Disk's azimuthal velocity as a function of $r_{\rm cyl}$. (o) Disk's specific angular momentum as a function of $r_{\rm cyl}$.

appropriate to describe the disk structure. The origin of the coordinate system is set at the centre of the disk or core. For the cylindrical coordinate system, the z-axis is set along the direction of the angular momentum of the gas. The different lines show the profiles at times corresponding to the three times shown in the legend, which also corresponds to the 1st, 3rd, and 4th columns in the top two rows of Figure 4.4, with an increasing shade of darkness indicating later times in the evolution.

1) Evolution and structure of the collapsing core and the disk. Panel (a) shows the density profile of the gas in spherical coordinates, $n(r_{\rm sph})$. At the time $t = 0$ the core can be approximated by an isothermal cloud in hydrostatic equilibrium, showing a Bonnor-Ebert density profile with a central density $6 \times 10^6\ {\rm cm}^{-3}$ and core radius ~ 900 AU. The envelope of the isothermal sphere extends up to 0.25 parsec (5×10^4 AU), despite being beyond the range of the x axis and not visible in the figure. The collapsing core has an enclosed mass of $\sim 27\ {\rm M}_\odot$ within 0.25 parsec, or above a density of $3000\ {\rm cm}^{-3}$. The density of the isothermal core increases self-similarly as the core collapses and reaches a density of $5 \times 10^9\ {\rm cm}^{-3}$ before a protostar (sink particle) forms at the centre. The density profile has a power-law slope of about -2 in the outskirt of the core, consistent with an isothermal sphere in hydrostatic equilibrium. The net mass infall rate (panel b) is between 10^{-5} and $10^{-4}\ {\rm M}_\odot/{\rm yr}$ and the total accreted mass into the centre is about 17 ${\rm M}_\odot$ by the end of the simulation at $t = 0.4$ Myr.

At the time $t = 0$ the core is marginally magnetically supercritical as shown in panel (c): μ ranges from 0.6 to 3 from the inner region to the outer region. Over time, as the mass accumulates into the central stars in a compact region, the gravitational binding energy increases dramatically while the magnetic energy does not increase as rapidly, due to the decoupling of the magnetic fields from gas as a result of star formation. We will discuss the properties of the magnetic fields and the disk formation in follow-up work.

The remaining panels show the properties of the pseudo-disk in cylindrical coordinates. Panel (d) shows the face-on surface density profile of the disk, which increases from $1\ \mathrm{g\,cm^{-2}}$ at $r_{cyl} = 10^4$ AU to $10 - 100\ \mathrm{g\,cm^{-2}}$ at the centre. This surface density is comparable to what is observed in Class II disks around young stellar objects in Ophiuchus (*e.g.* Andrews et al., 2009).

The density profile of the disk in the vertical (z-axis) direction $n(|z|)$ (the average of z and $-z$) is shown in panel (e). The disk thickness is 400 - 500 AU at a threshold density of $10^7\ \mathrm{cm^{-3}}$ at times $t > 200$ kyr. At the same mean density cutoff, the radius of the disk is roughly 1000-2000 AU, therefore the disk is rather thick with an aspect ratio $H/R \sim 1/2 - 1/4$.

The average gas temperature in the disk (panel f) remains near 10 Kelvin throughout the simulation. In the centre of the disk after the formation of the first star, the gas temperature increases to $\sim$ 100 K as a result of photoionization heating from massive stars. As will be discussed in § 4.5.2, the ionizing UV radiation from the stars at these early times is trapped in the thick dense disk and the disk remains cold at radii > 100 AU in most simulations.

2) Keplerianity and stability of the disk. The disk has a quasi-Keplerian rotation, with a deviation from Keplerianity $\beta_{\mathrm{kep}} \equiv (v_\phi - v_{\mathrm{kep}})/v_{\mathrm{kep}}$ of the order 50% (see bottom of panel g). The deviation is mainly due to the relatively large accretion rate of gas: as shown in panel (b), where and when the mass accretion rate is higher, corresponds to a larger deviation from Keplerianity. In addition, both the radial infall rate and the deviation from Keplerianity are larger when the disk is more strongly gravitationally unstable as illustrated in panel (h) showing the profile of the Toomre Q parameter. The pseudo-disk starts more strongly gravitationally unstable ($Q < 1$) and transitions into a stable disk after about 0.3 Myr from $t = 0$.

3) Turbulent, thermal and magnetic support of the disk. The disk is very turbulent: the turbulent velocity in the vertical direction, $\sigma(v_z)^2 = \langle v_z^2 \rangle - \langle v_z \rangle^2$, is between 1 km/s and 10 km/s (panel i) and the turbulence is highly supersonic as shown by the square of the thermal Mach number in the vertical direction (or the ratio of the turbulence pressure over the thermal pressure in the z-direction) shown in panel (j). The core starts with negligible turbulence, supported by thermal pressure. The pseudo-disk phase is instead dominated by turbulence motions, with rms velocity in the z-direction of about a third of the Keplerian velocity and significantly higher than the sound speed of the gas ($c_s \sim 0.3$ km/s), reaching Mach numbers of 10-30. Hence, we expect a geometrically thick disk supported by supersonic turbulent motions, as discussed in more detail in § 4.3.3.

The core is magnetized with an initial magnetic strength of about 50 – 300 μB (panel k). The magnetic field is amplified by the accretion of gas and increase of the surface density of the gas, which can be partially explained owning to magnetic flux freezing, *i.e.*, $\mu \propto M/\Phi_B = \Sigma/B \sim \mathrm{const}$. The turbulence also grows dramatically due to non-axisymmetric collapse, despite the existence of relatively strong magnetic fields. During this process, the core transitions from a thermal and magnetic pressure-dominated phase into a turbulent pressure-dominated phase (panels j and l), with a plasma β as low as 10^{-2} at a few 100 AU and thermal Mach number as high as $10 - 10^2$ in the inner region ($<$ 100 AU). Finally, in the quasi-steady phase of the disk, the turbulent pressure in the inner parts of the disk still dominates over the magnetic pressure but this is reversed at radii $r_{\rm cyl} \gtrsim 100$ AU (see panel m).

4) Analysis of velocity gradients in comparison to observations. In this part, we analyze this simulation with the objective of comparing it to observations in terms of the velocity gradients and specific angular momentum and discuss whether or not our simulations successfully reproduce some features of the observations.

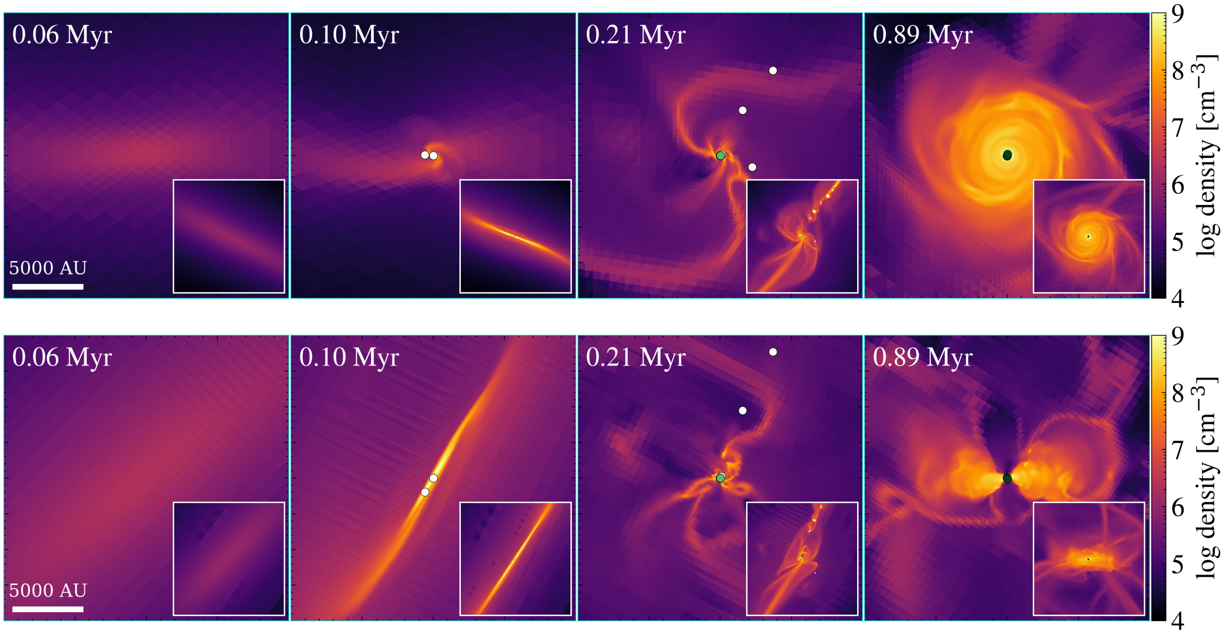

Figure 4.6: Same as Figure 4.4 but for the very massive core (Core *B*). Starting from a thin tube, the core undergoes fragmentation at the centre as well as along the arms of the cylinder. With large feeding of gas along the filament, the central stars grow in mass rapidly, ending in a total mass of over 600 $\mathrm{M}_{\odot}$. The gas keeps feeding the central stars via a large, thick disk, tens of solar masses in mass.

In an axis-symmetric model with initial rotation, the angular momentum measured at various scales is perfectly aligned.

We analyze the magnitude of the angular momentum in our simulated disk and its alignment at various scales. We consider a cylinder of height $h = 500$ AU centred by the disk and aligned with the spin axis of the disk. The average specific angular momentum is measured to be 4×10^{-3} km s^{-1} pc and 1.5×10^{-2} km s^{-1} pc, measured within $R = 800$ AU, the radius of the disk, and $R = 5000$ AU, enclosing the envelope, respectively. These values are consistent with observations of the protostellar regime from the CALYPSO dataset ($j \sim 10^{-3}$ km s^{-1}, see Belloche 2013; Gaudel et al. 2020 and the citations therein). The specific angular momentum as a function of distance to the centre (panel o of Figure 4.5) also follows the power-law relation $j \propto r^{1.6-1.7}$, highly consistent with observations of Class 0 envelopes (Goodman et al., 1993;

Caselli et al., 2002). The relative angle between the angular momentum measured at two scales is 12°. This misalignment is largely due to the turbulence of the initial core. This is in agreement with Verliat et al. (2020), who find that the formation of a disk can be a result of small perturbations of the initial density field in the core in the absence of large-scale rotation.

Panel (n) in Figure 4.5 displays the azimuthal velocity at various distances. We see a transition from the inward velocity gradient in the initial core to the outward velocity gradient of the disk and envelope, which indicates an evolution from a slowly rotating rigid body (*i.e.*, nearly constant angular velocity) to a differentially rotating Keplerian disk. The amplitude profile of the velocity gradient, or the angular velocity with respect to the disk centre, roughly follows a power law $\Omega \sim r^{-1.4}$, close to that of a Keplerian disk with all the mass concentrated at the centre, which gives $r^{-1.5}$. These features can be tested with observations of molecular lines in nearby star-forming regions which can measure velocity gradients in the cores (at large scales) and in the disks (at smaller scales) with a precision of about $1\ \mathrm{km\ s^{-1}\ pc^{-1}}$ (*e.g.* Cheng et al., 2022), which is sufficient to detect the slow rotation (at subsonic/sonic speeds) of cores out to 10,000 AU scales.

4.3.2 Evolution of a 130 solar mass core

The properties of core *B*, a very massive core that grows from 130 $\mathrm{M}_{\odot}$ to a mass of over 600 $\mathrm{M}_{\odot}$, are qualitatively similar to core *A-hr* once we account for the fact that it is much more massive. In this section, we will emphasize the differences between this core and the less massive core *A-hr* discussed above. Figure 4.6 shows the projected density distributions of the core from face-on (top) and edge-on (bottom) views, as in Figure 4.4.

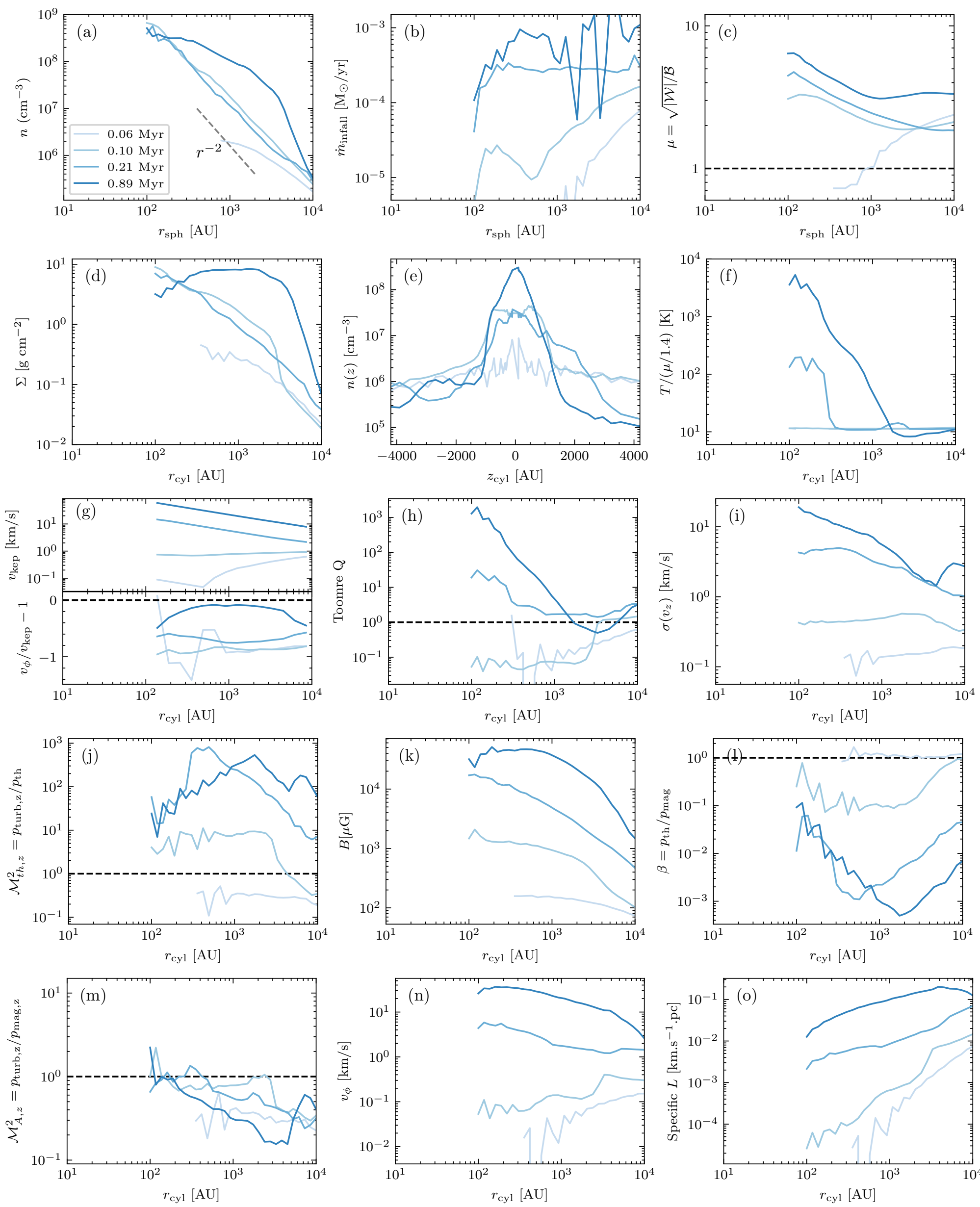

Figure 4.7: Same as Figure 4.5 but for the $\sim 130\ \mathrm{M}_\odot$ core *B*. Refer to the texts for the implications and interpretations.

Unlike core *A-hr* which collapses spherically, core *B* starts from the collapse of a filamentary structure and fragments along the length of the filament. This filamentary collapse of a massive core is observed in recent ALMA continuum maps at mm wavelength of a highly magnetized clump (Fontani et al., 2016). However, the final outcome of the collapse is a disk similar to the case of core *A-hr*, although much more massive. At the time $t = 0$ the initial density structure is better described by a cylindrical geometry than a spherical core (see the first and second frames in Figure 4.6). The fragmentation of the core starts at the centre of the frame where the density is highest. As the density reaches $10^9\ \mathrm{cm}^{-3}$, the Jeans length drops to a few hundred AU and the local free-fall time is a few kyr. The filament undergoes fragmentation along the length of the cylinder and breaks into blobs that become eddies (the third frame). Finally, these eddies migrate into the centre of the system in about one dynamic time. Conservation of angular momentum turns the filamentary collapse into rotational collapse, forming a large, thick disk (the last frame).

We plot the properties of this filament/disk as a function of time in Figure 4.7, with timestamps corresponding to the four snapshots in Figure 4.6.

Even though the geometry of the core at $t = 0$ is not spherical but filamentary, the spherically averaged density profile is well described by a Bonnor-Ebert density profile with a central density $2 \times 10^6\ \mathrm{cm}^{-3}$ and core radius ~ 2000 AU (panel a). Between 0.1 Myr and 0.4 Myr, the radial distribution of density displays a power-law profile with an exponent close to -1.5, which is flatter than an isothermal sphere, likely because the geometry is clearly filamentary at these times. After ~ 0.4 Myr, the core exhibits a nearly constant density profile with $n \sim 10^7\ \mathrm{cm}^{-3}$ within 4000 AU, indicative of a disk with nearly constant density and constant surface density as shown in panel (d). This disk is about 4 times larger than disk *A-hr* at the same density threshold, but disk *A-hr* has an increasing density and surface density toward the centre. By $t = 0.9$ Myr (the dark blue curve), a large, thick, near-Keplerian disk forms with a surface density of $\sim 10\,\mathrm{g\,cm^{-2}}$. The radius of the disk is about 4000 AU at a cutoff density $10^7\ \mathrm{cm^{-3}}$, equivalent to a column density of $3\ \mathrm{g\ cm^{-2}}$ (panel d). Within this radius, the disk is near Keplerian (panel g) and at late times is Toomre-stable ($Q > 1$, see panel h): even though in the outer parts $Q \sim 1$ we do not observe late time fragmentation probably due to the stabilizing effect of magnetic fields. The thickness of the disk is about 2000 AU at the same cutoff density of $10^7\ \mathrm{cm^{-3}}$ (panel e).

Unlike disk *A-hr* where the radial component is extremely turbulent and the mass inflow is discontinuous, disk *B* has a steady inflow at a constant velocity of $2 - 3$ km/s, which is close to the escape velocity at the edge of the disk at 5000 AU from the centre. With a $\rho \sim r^{-2}$ relation, the inflow of mass has a constant rate $3 \times 10^{-4}\mathrm{M_\odot/yr}$ (panel b). This inflow rate results in an accreted mass of $> 400\ \mathrm{M_\odot}$ in the accretion period of 0.5 Myr.

Due to the large central mass, the Keplerian velocity of the disk is high, reaching $7{-}20$ km/s at 1000 AU. The turbulent velocity is also very high, between 3 and 6 km/s in the z component (panel i).

Due of magnetic flux freezing, the large mass in the disk results in large magnetic strength, reaching between 10^3 to 5×10^4 μG (panel k). Despite of the strong magnetic field, the mass-to-flux ratio μ stays high between 3 and 7 (panel c) due to the large gravitational binding energy from the large mass of the cluster at the centre. Although the inner part of the disk is heated by UV radiation to 100 - 3000 K (panel f), the disk is supported primarily by magnetic pressure and secondarily by turbulence in the axial direction (see panels j, l, and m). We will discuss the support of the disk in more detail in the next section.

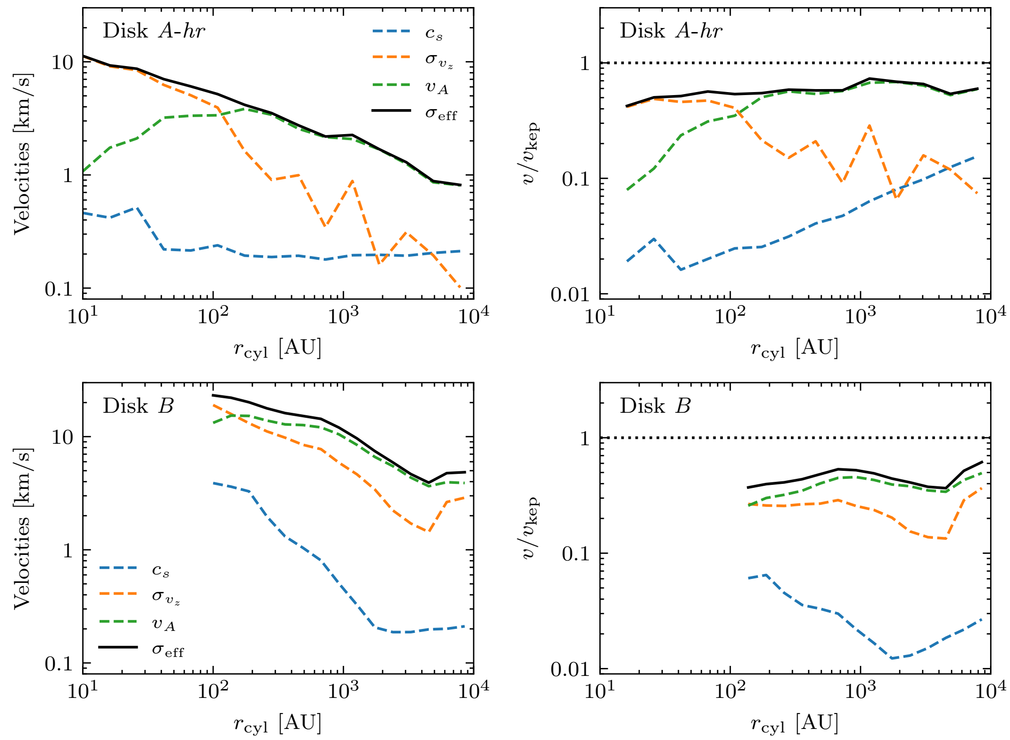

Figure 4.8: (*Top*) Left panel: radial profiles of the sound speed (dot-dashed line), the Alfven speed (dashed line), and the z-component turbulent velocity (rms velocity in the z-direction, solid line) for our lower-mass disk (Disk *A-hr*). Right panel: the same quantities normalized to the Keplerian velocity $v_{\rm kep}$. This ratio reliably predicts the scale height H/r of a gas disk in hydrostatic equilibrium, where the vertical component of gravity is balanced by the pressure ρv^2 gradient. The panels illustrate that the vertical support of the disk is dominated by turbulence and by the magnetic field, while thermal pressure support is negligible. The right panel also shows that $\sigma_{\rm eff}/v_{\rm kep} \sim 0.5$, and hence the disk is geometrically thick, *i.e.*, the disk has an aspect ratio of about 0.5. (*Bottom*). The same as the top panels but for our most massive disk (Disk *B*). We note that in both disks the turbulent support dominates from the centre to 200 AU and the magnetic support from $r_{\rm cyl}\sim$ 200 AU to $\sim 10^4$ AU.

4.3.3 The disk thickness is determined by magnetic support and supersonic turbulent motions

The disks in the six simulated cores measure from 200 AU to 6000 AU in radius, with Disk *B* being the largest and most massive one. They are generally very thick as well, mostly with an aspect ratio (thickness to diameter ratio) of 0.2 to 0.5. Here we explore the physics behind the existence of these large disks.

For a disk of gas around a massive central object that is in hydrostatic equilibrium with the z component of gravity from the centre,

$$\frac{dP}{dz} = -\frac{GM\rho z}{(r^2+z^2)^{3/2}} \approx -\frac{GM\rho z}{r^3}. \tag{4.5}$$

where r is the radial cylindrical coordinate for the distance from the centre and z is the altitude cylindrical coordinate for the distance from the disk midplane. Assume the pressure P can be expressed as $P = \rho\langle v^2\rangle$, then

$$\langle v^2\rangle \frac{d\rho}{dz} = -\frac{GMz}{r^3}\rho, \tag{4.6}$$

therefore

$$\rho = \rho_0 \exp\left(-\frac{v_\phi^2 z^2}{2\langle v^2\rangle r^2}\right) = \rho_0 \exp\left(-\frac{z^2}{H^2}\right), \tag{4.7}$$

where $v_\phi = \sqrt{GM/r}$ is the Keplerian velocity and H is the disk scale height,

$$H/r \approx \frac{\sqrt{2}\,\langle v^2\rangle^{1/2}}{v_\phi}. \tag{4.8}$$

The rms velocity $\sigma_{\rm eff} \equiv \langle v^2\rangle^{1/2}$ should account for all the possible pressure supports: thermal, turbulent or magnetic. These three components can be identified as the sound speed c_s, the dispersion (rms) of the z-component velocity σ_{v_z}, or the Alfven speed v_A, respectively. We compare these three velocities and $\sigma_{\rm eff} = (\sigma_{v_z}^2 + v_A^2 + c_s^2)^{1/2}$ as a function of r in Figure 4.8. It is clear that turbulent pressure dominates the vertical support of the disk in the inner disk and magnetic pressure dominates in the outer disk, while thermal pressure support is negligible everywhere. For the two disks shown in Figure 4.8, the transition from turbulent support to magnetic support occurs at ~ 200 AU. However, in another disk, we observed the transition radius to be closer to 1000 AU. We will further investigate the dependence of the critical radius on the physical parameters of the core in future work.

We notice that σ_{v_z} decreases with the distance to the centre with an empirical relation $\sigma_{v_z} \sim r^{-0.6}$, while v_A peaks at $r_{\rm cyl} = 200$ AU and decreases slowly outward. The effective rms velocity $\sigma_{\rm eff}$ scales with radius as $\sigma_{\rm eff} \sim r^{-0.5}$. Assuming a roughly Keplerian azimuthal velocity profile $v_{\rm kep} \sim r^{-0.5}$, we have $\sigma_{\rm eff}/v_{\rm kep} \sim r^0$. The predicted disk aspect ratio H/r according to Equation 4.8 is nearly constant as a function of radius and of the order of unity, as shown in the right panels of Figure 4.8. Assuming an isothermal density profile $\rho \propto r^{-2}$ as for disk *A-hr*, the disk surface density is $\Sigma \propto r^{-1}$, while disk *B* has $\rho \propto r^{-1}$ and a nearly constant surface density profile, $\Sigma \sim \mathrm{const}(r)$. Indeed the disks have nearly constant opening angles and the surface density profiles we derived above are consistent with the actually geometrical properties of the disks shown in the fourth column of Figures 4.4 and 4.6.

The magnetic field plays a more significant role in determining the structure of the outer disk. At large radii ($\gtrsim 200$ AU in both disk *A-hr* and disk *B*) the magnetic pressure dominates over turbulent pressure. Even though the initial strength of the magnetic field ($10 - 25\ \mu$G) of the cloud at density $10^3\ \mathrm{cm}^{-3}$ is in the typical range of what is observed in present-day molecular clouds and the initial velocity dispersion is 5 times higher than v_A, the strengths inside both disks are above 1000 μG and even stronger at the very centre. The Alfven velocity is between 1 and 4 km/s in Disk *A-hr* and between 4 km/s and 15 km/s in Disk *B*, many times higher than the thermal sound speed. Therefore, we expect that the magnetic field could become dominant dynamically over turbulence even in the inner parts of the disk in simulations with mildly stronger initial values of the magnetic field. We will explore this possibility in a follow-up work.

In our simulations, the gas temperature is underestimated near sources of radiation due to neglecting heating processes important at high densities (*i.e.*, gas heating from stellar radiation absorbed by dust grains). With a more complete description of stellar feedback, the gas temperature could reach a value between 20 and 100 K at $n \sim 10^8\ \mathrm{cm}^{-3}$ (Krumholz et al., 2007; Krumholz et al., 2011), corresponding to a sound speed of up to 0.9 km/s. Nevertheless, even assuming these higher temperatures, the thermal pressure is still small when compared to the turbulent and magnetic pressures found at these densities in our simulations. Thus, we speculate that even though we have neglected gas heating from dust grains, the enhanced thermal pressure support that this process provides should not play an important role in determining the structure of the disk and the protostars, at least for the massive cores studied in this work.

4.4 Results. II. Low-mass stars form from the fragmentation of massive prestellar cores

4.4.1 Fragmentation into low-mass stars before the formation of a steady disk structure

In the classical picture of prestellar disk formation, an unstable disk undergoes fragmentation and stars likely form from the disk fragments (Agertz et al., 2007; Kratter & Lodato, 2016). Recent simulations of Pop III star formation (Machida et al., 2008; Stacy et al., 2010; Sugimura & Ricotti, 2020; Park et al., 2021a,b, 2022) clearly show that high-mass stars in a metal-free gas disk, although they form near the centre of the disk, which is most gravitationally unstable, nearly

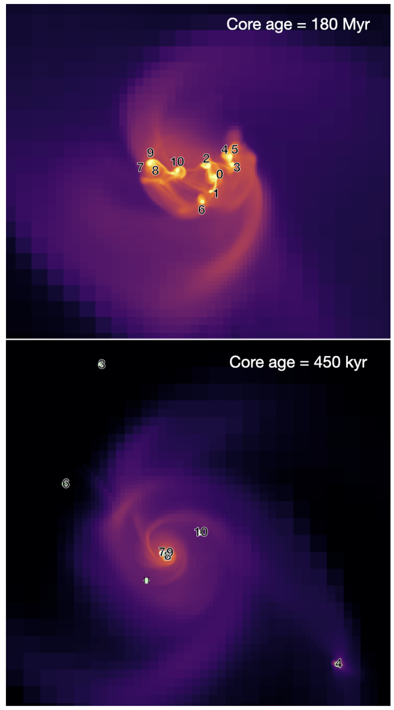

Figure 4.9: Snapshots of projected density of core *A-hr* after 180 kyr (*top*) and 450 kyr (*bottom*) from the isothermal core formation (defined as when the core density reaches 10^6 cm^{-3}). In the top panel, we identify the positions of the prestellar cores where sink particles form at later times, and show the IDs of the sink particles that form in them. In the bottom panel, the circles and numbers indicate the locations and IDs of the sink particles existing at the time shown in the snapshot. The figure shows that most sinks form from the fragmentation of a turbulent disk at an early time, but the sinks form with a time delay, and they either spiral in toward the centre of the disk or are ejected (or in the process of being ejected). The image measures 2×10^4 AU on a side.

all of them migrate outward due to accretion of gas with higher specific angular momentum from the disk (but see also Chon & Hosokawa (2019), reporting exceptions to this behaviour for small mass fragments).

However, although we recognize a few low-mass disk fragments in our simulations, we find that steady quasi-Keplerian disks form only after the initial collapse and fragmentation phase of the cores: when clear disk morphologies can be identified these disks are relatively Toomre-stable.

André Oliva & Kuiper (2020) characterize the temporal evolution of protostellar disks start-

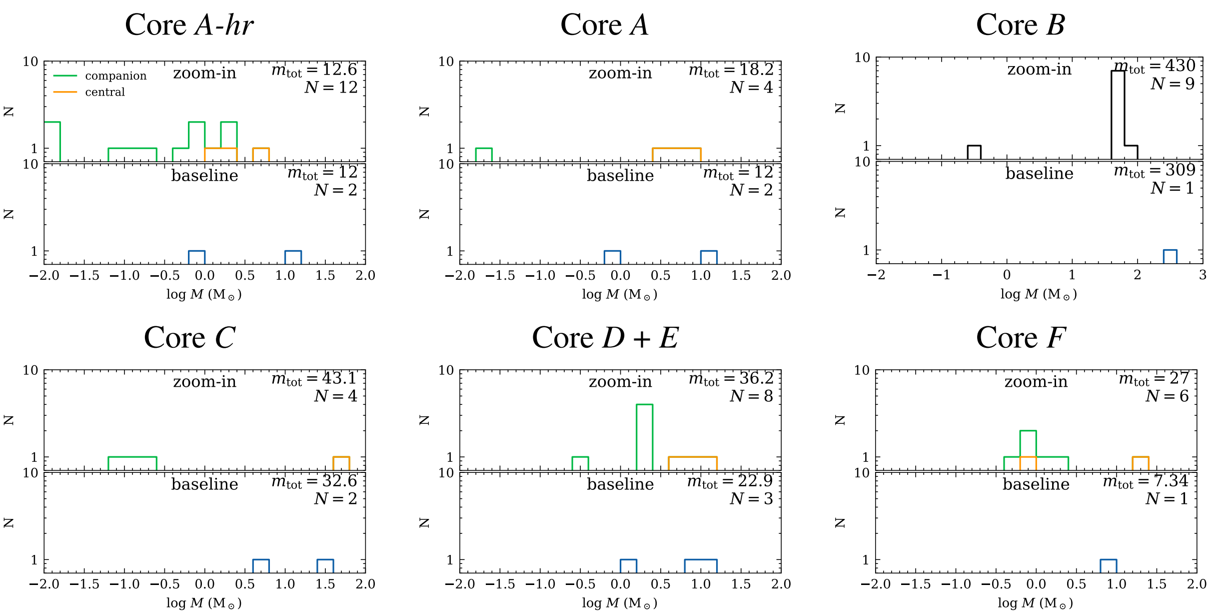

Figure 4.10: The mass distribution of the stars forming in each core in our 'zoom-in' simulations, labelled 'zoom-in', compared to the stars that form from the same core in the baseline run, labelled 'baseline'. The mass functions of the stars in the 'zoom-in' simulations are plotted in two colours to distinguish the central stars (orange) and companion stars (green), or in black when these two groups of stars are indistinguishable. In the case of cores D and E, because they are in close proximity to each other, their central stars, as well as their companion stars, are grouped together. Overall, the number of stars that form from the fragments of a core ranges from 1 to 12.

ing from idealized initial conditions into four epochs: the initial setup, the disk formation epoch, the fragmentation epoch, and the quiescent epoch. In our simulations, we also identify four phases of the core evolution: the quasi-hydrostatic phase, the core fragmentation phase, the disk formation phase, and the steady-state (quiescent) phase.

In core A-hr, almost all of the self-gravitating fragments in which a star or a multiple stellar system forms, originate from high-density perturbations that appear and grow during the quasi-spherical collapse phase of the core, well before the formation of the pseudo-disk, as shown in Figure 4.9. Keeping in mind the caveat that our disks are generally more massive than those in André Oliva & Kuiper (2020), the main qualitative difference between these two sets of simulations is that in the present work the fragmentation epoch precedes the disk formation phase. In other words, the formation of low-mass (disk) stars is initiated during the fragmentation of the core and before the disk formation phase. These phases are discussed in § 4.3, and illustrated in Figure 4.3.

A more realistic model of star formation from core fragmentation should take into account accurate modelling of stellar evolution. In our simulations, the formation time of protostar particles is instantaneous when a clump centre exceeds a given density threshold (see § 4.3 for details on the sink formation criteria in RAMSES-RT (Bleuler & Teyssier, 2014)). More realistically, the formation of protostars follows a thermal timescale, or the Kelvin-Helmholtz (KH) timescale. This time is extremely short for massive stars. For a low-mass star, say a solar-mass star, even though the KH timescale is about 30 Myr long, the protostar shrinks to 100 solar radii, or about 0.5 AU, by 1/100 of the KH time, or 0.3 Myr, assuming a constant rate of radiating thermal energy. This means that in a very short time after sink particle formation, a star becomes a subgrid particle in the simulation, well-tracked by a point-source sink particle.

The N-body integrator in the code uses a softening length of $2\Delta x_{\rm min}$, which is 14 AU for Core *A-hr* and 120 AU for Core *B*. As a consequence, the formation of hard binaries is not captured and their dynamical evolution is not accurately resolved. We leave a robust treatment of the dynamics of these multiple systems for future work.

4.4.2 Star formation efficiency in cores and multiplicity

The observed core mass function (CMF) closely resembles the stellar IMF but is shifted to the higher-mass end by a factor of ~ 3 (e.g. Alves et al., 2007). This similarity seems to suggest the idea that the efficiency of star formation in dense cores ($n > 10^4\ {\rm cm}^{-3}$) is of the order of

30 per cent. Previous studies tend to explain this offset invoking feedback, namely, protostellar outflows acting on core scales, entraining and expelling a large fraction of the core (Hansen et al., 2012; Kuiper et al., 2016). Numerical simulations (Kuiper et al., 2010; Offner & Chaban, 2017) of isolated core collapse suggest outflows have a mass-loading factor of ~ 3. In He et al. (2019) we instead argue that cores have close to 100 per cent star formation efficiency (SFE) but the cores fragment into several smaller mass stars with a relatively flat IMF. We show that such a model can reproduce both the shape and normalization of the IMF in our MC scale simulations, which we refer to here as "baseline" simulations. One of the main motivations of this present work is to test this hypothesis by zooming on a few selected cores with high resolution.

Figure 4.10 shows the mass function of the stars forming in each core in our simulations. The mass functions are plotted in two colours to distinguish the central stars (orange) from the companion stars (green). Black histograms are used when these two groups of stars are indistinguishable. We can see that each core fragments into a mini cluster consisting of 1 to 12 stars, as found in previous numerical studies (Bate & Burkert, 1997; Goodwin et al., 2004a). In each panel, we compare the stellar masses in our zoom simulations to the sink masses of the "baseline" lower-resolution simulation of the same core, shown in the lower half of each panel. In the zoom-in simulations the spatial resolution increases by a factor ~ 20 (~ 60 for core *A-hr*), reaching densities 3 orders of magnitude larger with respect to the baseline.

The labels in each panel of Figure 4.10 compare the total stellar masses in the zoom-in simulations to the corresponding sink mass (representing a prestellar core) in baseline simulations. We find that the total masses of stars in the zoom-in simulations are either equal to or higher than the sink mass in the baseline, indicating that star formation efficiencies in cores are close to 100 per cent, independent of the core mass. In addition, we find that the cores in the zoom-in simulations have nearly 100 per cent efficiency of conversion of gas into stars: *i.e.*, the final mass in stars is between 50 to 100 per cent the initial core mass, and for core *B* the mass in stars is higher than the initial core mass. However, the core forms multiple stars with the masses of the highest mass stars reduced by approximately $1/3$. Hence, we argue that the CMF/IMF scaling parameter is due to the fragmentation of the core into multiple smaller mass stars rather than the inefficient conversion of gas into stars due to feedback effects. However, most of the mass in stars is locked in a few (2 to 3) relatively massive stars at the center of the disk, while low mass stars – that can be numerous, *e.g.*, core *A-hr* forms a total of 12 stars – account for a minority of the total mass of the core. Regardless of the mass of the fragments, the central stars accrete gas rapidly and grow in mass, contrary to disk star that instead remain of small mass, especially if they are ejected from the disk. Note that after sink particles are formed, they are not allowed to merge. Due to the small-number statistics, we cannot infer a shape for the mass function of stars in cores, but it appears to be flat. Additionally, the lack of proper treatment of protostellar outflow could result in an overestimation of the SFE in cores. A more rigorous study of feedback mechanisms in zoom-in simulations is necessary to better understand the SFE at these scales.

Recent studies have painted a picture of star formation as a highly dynamic process, replacing the idea that cores evolve slowly via ambipolar diffusion with one in which cores form in converging flow within a highly turbulent molecular cloud (Elmegreen, 2000; Elmegreen & Scalo, 2004). Goodwin et al. (2004a) suggests that low levels of turbulence (i.e. $\alpha_{\rm vir} \sim 0.025$) are enough to cause a core to fragment and form more than one star, with the average number of stars growing as the level of turbulence is increased (Fontani et al., 2018). This trend is reflected in our simulations; as demonstrated in Table 4.1, the number of fragments increases from 1 to 4 to 9 as the turbulent Mach number grows from 0.18 to 0.35 to 0.49.

In most of our zoom-in simulations where the resolution is lower and the peak density is below 10^9 cm^{-3}, the total number of stars is ≤ 9, the total mass in stars exceeds by roughly 30 per cent the sink mass in the corresponding baseline simulation and the most massive star have sometimes a higher mass than $1/3$ of the sink mass. We partially attribute this non-convergent result to the limited resolution. Indeed in core *A-hr*, that is our highest resolution zoom-in simulation, where the sink formation density reaches $\sim 10^{10}$ cm^{-3} (close to the density where the gas becomes adiabatic), 12 stars are formed, we reproduce very closely the stellar mass of the sink in the baseline simulation, our highest mass star is $< 1/3$ of the baseline sink mass and we resolve low mass stars down to 0.01 M$_\odot$.

It has been argued that the formation of low-mass stars from the fragmentation of massive cores contradicts the observations of a high binary fraction of low-mass stars (Goodwin et al., 2007). However, if the low-mass stars form in a hierarchical system as in our simulations, when they are ejected from the systems they can retain their binary companion. Indeed in core *A-hr* we observe binaries in disk stars and ejected binary systems, even though the limited resolution prevents us from resolving close binaries with separations < 14 AU. We will study stellar dynamics in more detail in future work.

It remains to be seen if this type of fragmentation is realistic in small ($<$ a few M$_\odot$) cores, given the observed levels of non-thermal motion therein which rules out any significant highly supersonic turbulence found in high-mass cores.

4.5 Discussion

4.5.1 Formation of ultra-high-mass stars – a competitive accretion scenario

Recent advancement of radio/mm and optical/IR interferometers has enabled important progress in the field of disks around high-mass (early-B to late-O type) YSOs (see Davies et al., 2011; Mottram et al., 2011). The current unambiguous evidence for circumstellar disks around high-mass young stars is limited to objects with masses up to 30 $\mathrm{M_\odot}$ (late-O type) (Beltrán & de Wit, 2016). Stars with these spectral types or brighter have strong UV emissions that can heat and disperse the gas. Typical disk radii of these sources are a few thousand AU with rare exceptions of radii as small as 300-400 AU. Most of the protostars in our simulations (Cores *A-hr*, *D*, *E*, *F*) fall in the range of high-mass stars, with Cores *B* and *C* forming stars that are over 40 $\mathrm{M_\odot}$. The range of the radii of the simulated disks in this work (see Table 4.1) agrees well with the observations.

In the observations mentioned above, the circumstellar disks have typical gas masses ranging from 4 to a few $\times 10\ \mathrm{M_\odot}$. In our simulations the masses of disks, defined as disk gas above a density threshold of $\sim 10^5\ \mathrm{cm^{-3}}$, ranges between 3 $\mathrm{M_\odot}$ to 50 $\mathrm{M_\odot}$, in agreement with the observed range. The disk mass remains relatively low ($\sim$ 40 $\mathrm{M_\odot}$) even in the very massive core *B* where the central star cluster mass is above 600 $\mathrm{M_\odot}$. This is due to the surface density being roughly constant at 8 g/cm^2 up to a disk radius of $\sim$ 6000 AU, where the azimuthal velocity becomes comparable to the gas velocity dispersion, typically 1 to 3 km/s. Higher mass (up to 200 $\mathrm{M_\odot}$) disks are only reported in a few cases where the angular resolution is not enough to properly separate the envelope from the disk (Beltrán et al., 2004).

At the lower bound of the high-mass range where there are enough nearby sources, observers are able to estimate the hydrostatic scale height of these structures from (sub)millimetre observations of the line width. The typical line width is found to be $\sim 2\ \mathrm{km\ s^{-1}}$ and the estimated scale height is in most cases $> 30 - 40$ per cent of the disk radius, indicating that the disks of embedded protostars are likely geometrically thick (e.g., Beltrán et al., 2006).

Both the velocity field probed via molecular lines at high angular resolution ($\leq 0.5''$) and the CO bandhead profile suggest that the rotation of the majority of the disks is consistent with Keplerian or quasi-Keplerian rotation (e.g. Wang et al., 2012; Cesaroni et al., 2014; Beltrán et al., 2014). For some sources, observations reveal both sub-Keplerian (e.g. Cesaroni et al., 2005; Wang et al., 2012; Beltrán et al., 2014) and super-Keplerian (Beuther et al., 2008). Wang et al. (2012) argues that sub-Keplerian motions suggest a role for magnetic fields that could slow down the rotation below pure Keplerian by, i.e., magnetic braking. In our simulations, the disks are generally sub-Keplerian, with the non-Keplerianity parameter β_{kep} being in the range of -0.5 to -0.1. The low values of β_{kep} indicate a relatively large accretion rate from the large-scale envelope.

Another feature of protostellar disks of high-mass stars is the presence of asymmetries and inhomogeneities (e.g. Cesaroni et al., 2014). The authors claim that these asymmetries could be caused by the presence of spiral arms or infalling filaments accreting material onto the disk or by interacting with companions nearby. Disks that have been observed with an extremely high angular resolution where a clear disk structure could be resolved, appear to be slightly elongated and oriented perpendicular to molecular outflows (Wang et al., 2012; Beltrán et al., 2014). This structure is similar to the early phase of collapse of our simulated Case *B* core.

During the initial phase of collapse, our simulated core *B* has a spherical shape with a radius of ~ 0.5 parsec within a density threshold of $3000\ \mathrm{cm^{-3}}$, enclosing a total mass of $131\ \mathrm{M_{\odot}}$. The

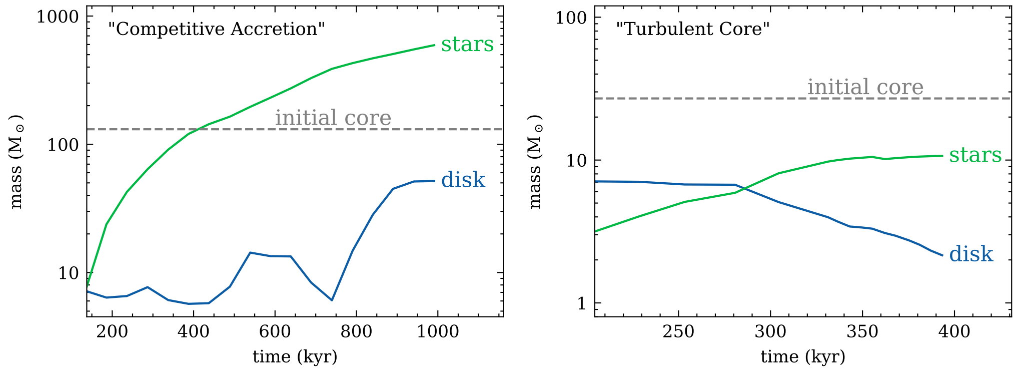

Figure 4.11: *Top*: The growth of Core *B* from a 130 $\mathrm{M}_\odot$ core into a mini-cluster of stars with a total mass of $\sim$ 600 $\mathrm{M}_\odot$ and average mass of 70 $\mathrm{M}_\odot$ via filamentary accretion from the background, demonstrating a competitive accretion scenario for ultra-high-mass star formation. *Bottom:* The collapse of 27 $\mathrm{M}_\odot$ Core *A-hr* into a central binary of $\sim$ 10 $\mathrm{M}_\odot$ plus low-mass companions, demonstrating a "turbulent core" scenario for intemediate- to high-mass star formation. The colour curves show the evolution over time of the total mass in stars, labelled as 'stars', or the mass of the disk, labelled as 'disk'.

core has a density profile that is shallower than that of a Bonnor-Ebert sphere, with both magnetic and turbulent pressure in the envelope being 10 times stronger than thermal pressure (Figure 4.5). However, the mass accreted in the central (proto)star cluster is > 600 $\mathrm{M}_\odot$ over a timescale of about 0.9 Myr, more than four times the initial gas reservoir in the core (Figure 4.11). This is due to the sustained high accretion rate (10^{-4}–10^{-3} $\mathrm{M}_\odot/\mathrm{yr}$) over 0.9 Myr at a inflow velocity of 1 to 3 km/s. We, therefore, argue that the large masses (50 – 100 $\mathrm{M}_\odot$) of the YSOs in core *B* can be described, at least partially, in the context of the competitive accretion scenario, in which the gas is collected over time from scales beyond the initial core radius. This agrees with Gong & Ostriker (2015) who, through a set of simulations of turbulent, unmagnetized GMCs, find that sink particles accrete at a nearly constant rate even after the initial mass reservoir is depleted. However, this kind of "competitive accretion" is only seen in the most massive ($> 50\mathrm{M}_\odot$) core in our simulations.

Observational evidence of circumstellar structures in the most massive protostars, *i.e.*, early-O type, is very limited. Huge, dense, massive, rotating cores have been detected around early-O-type protostars in studies performed at moderate spatial resolutions. These objects are in all likelihood non-equilibrium structures surrounding clusters of young protostars and not merely individual massive stars (see Beltrán et al., 2011, and references therein). These structures are characterized by a much higher mass and larger size than the rotationally supported disks around lower-mass protostars discussed above. Beltrán et al. (2005) referred to these massive structures as "toroids" to make a distinction. The reported toroids have radii of a few $\times 1000$ AU to up to 10^4 AU (e.g. Zapata et al., 2008). The hydrostatic scale height of these toroids, estimated by assuming hydrostatic equilibrium, is $> 50\%$ of the radius – these structures are extremely thick.

We find that the most massive stars in our star cluster formation simulations form as clusters inside large and dynamically stable toroids with significant mass infall. Our simulated Core *B* matches the properties of the toroids discussed above. The structure that enshrouds the central protostar cluster forms a toroid that is both large (4000–8000 AU in radius) and thick (3000–8000 AU in thickness) and is largely sub-Keplerian. The high infall rate, of the order of $10^{-3}\ \mathrm{M}_\odot/\mathrm{yr}$, could be high enough to quench the formation of an H II region or to slow down its expansion (Yorke 1986, see also § 4.5.2). In the next section, we will show that core *B* produces a bipolar H II region and an outflow. However, in general, the question of whether or not the launching of outflows could be quenched initially by the massive envelope requires further studies that take into account jet-driven outflow and perhaps stellar winds.

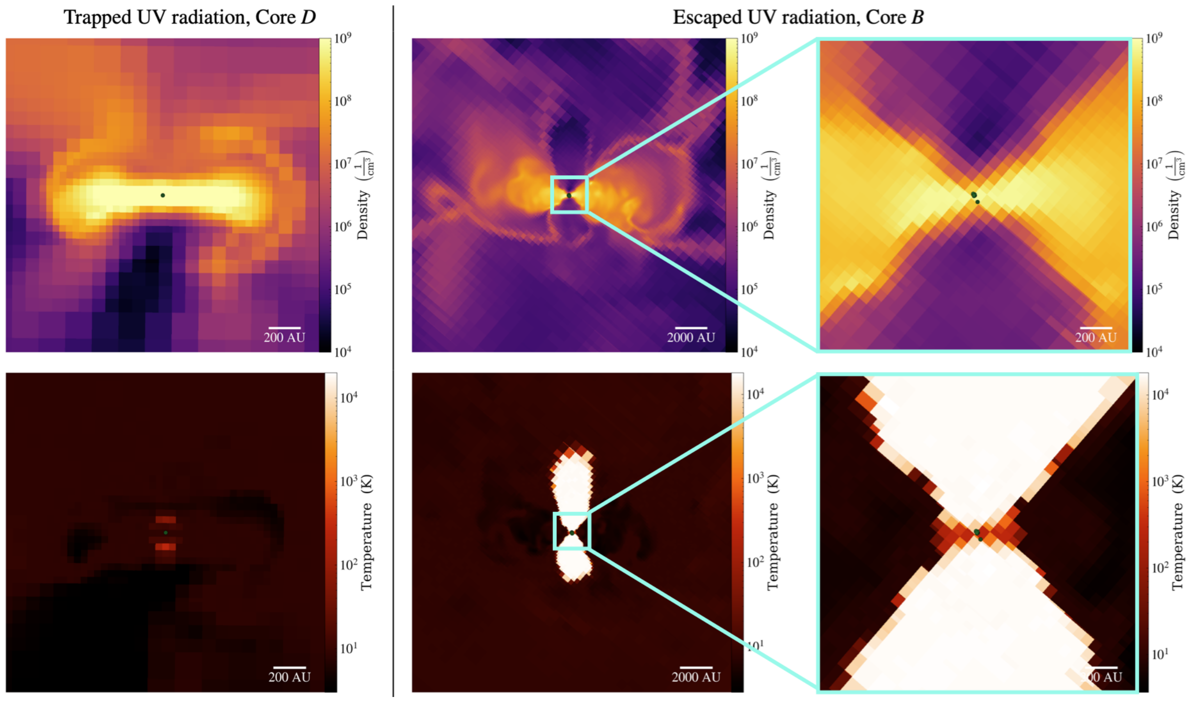

Figure 4.12: The trapping (left) and escaping (right) of H II regions. *Left*: Density (top) and temperature (bottom) slices of core *D* showing the UV radiation from a $\sim 10\mathrm{M}_{\odot}$ star is trapped inside an ultra-compact region at the centre of a disk. *Right*: Similar to *Left* but for the Core *B* showing the escaping of an ultracompact H II region. The dynamical motions of the multi-star system create a channel for radiation to escape.

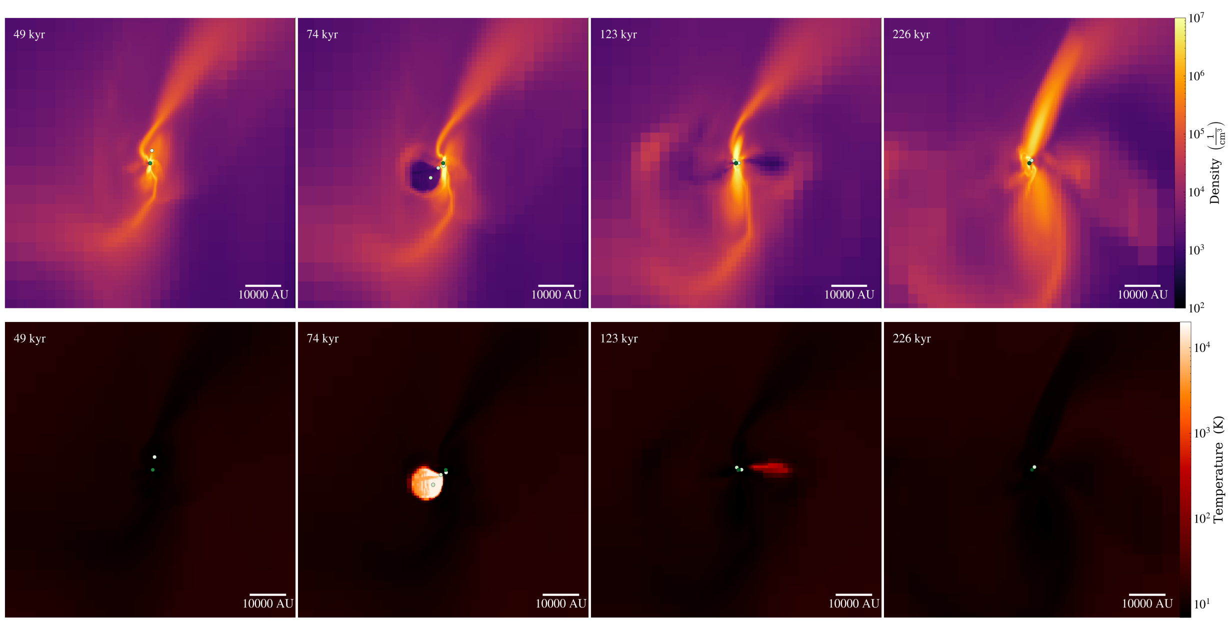

Figure 4.13: The escaping of UV radiation from a dense filament due to dynamical motion. From left to right, it shows a time sequence of the density (top) and temperature (bottom) slices. The dancing of the stars creates a channel for UV photons to escape from the dense region when

4.5.2 UV radiation trapping

High-mass stars are often observed to be deeply embedded in dense gas and their H II regions in the gas above a density of $\sim 10^4 \mathrm{cm}^{-3}$ can remain trapped forming ultracompact H II regions (Jaura et al., 2022; Churchwell, 2002). In our simulated prestellar cores, we notice two main distinct scenarios: A) when a single massive star is deeply embedded in a thick disk, where the density reaches $\sim 10^8\ \mathrm{cm}^{-3}$, the H II regions remain trapped at least during the first 0.5 Myr while the disk is still relatively massive. B) Often massive stars orbit a common centre of mass in binary or multiple star systems: in these cases the stellar orbit may displace the massive star from the densest regions in the disk or in a filament, allowing the H II regions to break out the dense disk or filament. Case A) can be observed in the left panels of Figure 4.12), showing core *D*, where a single massive star forms from the collapse of the small core. The UV radiation of the protostar is trapped inside the dense neutral gas The H II region remains trapped for a few hundred kiloyears. Note that the consumption rate of ionizing photons, emitted uniformly within the sink particles, is equal to the recombination rate in the ionized gas calculated in each cell, even inside the sink particles. However, here we do not adopt any sub-sink recipe to account for the radiation transfer inside the poorly resolved density structure within the sinks, as done in other studies (Jaura et al., 2022; Park et al., 2022). In Core *A-hr*, however, multiple stars form at or migrate into the disk centre (see right panels of Figure 4.12). The dynamics of the few-body star system displaces the stars by about the virial radius of the star system, which is tens of AU, close to or higher than the disk thickness. In this case, radiation can escape when one of the massive stars approaches the edges of the disk. Once a channel of lower-density ionized gas is created a long-lasting bipolar H II region and outflow are created.

Finally Figure 4.13) shows another interesting mechanism that allows UV ionizing radiation to break out of a dense filament. The figure shows the density (top panels) and the temperature (bottom panels) in a set of snapshots showing a disk embedded in a filament in which a multiple system, including a massive star, forms. The stars are shown as circles colour-coded according to their masses from white (1 $\mathrm{M}_\odot$) to dark green (10 $\mathrm{M}_\odot$). From the time sequence, it is clear that H II regions are created intermittently on either side of the filament when the massive star in its orbit is further from the densest part of the filament, allowing the H II region to break out of the filament. This is more evident in the animation that we make available in the electronic version of this paper.

4.5.3 Influence of metallicity on disk stability

Our simulations are conducted at solar metallicity and the cooling from hydrogen, helium, carbon, oxygen, and dust grains. Lower metallicity could make a big difference in how the disk fragments. Recent study (Matsukoba et al., 2022) of the metallicity dependence of protostellar-disk fragmentation has shown that fragmentation of spiral arms is more common in lower metallicities where dust cooling is effective. At high metallicity, the disk is stabilized by stellar irradiation. We find that despite being cold (close to 10 K) due to the lack of effective heating from the stars, the disks are stable and do not undergo fragmentation, as discussed in § 4.4.1.

4.6 Summary

We have simulated the formation and collapse of prestellar cores in a set of grid-based radiation-MHD simulations, resolving from GMC scales, tens of parsec in size, down to disk scales, with resolutions up to 7 astronomical units in our highest resolution simulation.

We studied a set of 4 massive ($\sim$ 10 $M_{\odot}$) or very massive ($\sim$ 100 $M_{\odot}$) cores in two GMCs, following their collapse, fragmentation, and the formation of (proto)stars embedded in circumstellar disks with sizes ranging from 200 AU to 6000 AU. The properties of the simulated cores, and the (proto)stars and disks that form therein are listed in Table 4.1.

The following is a list of the main results:

1. The disks are generally large ($R = 200 - 6000$ AU), thick (aspect ratio $H/R = 0.2 - 1.3$), and massive with masses spanning from a few to 40 $\mathrm{M}_{\odot}$ (Table 4.1 and Figure 4.2). These disks or toroids sit in the range of observed disk properties around high-mass YSOs.

2. Each core undergoes fragmentation in the early collapsing phase with geometries that can be separated into two main distinct modes: “quasi-spherical” collapse and “filamentary” collapse (see Figure 4.3). However, in both modes of collapse, the fragments eventually become embedded in a quasi-steady accretion disk or toroid.

3. We observe the formation of multiple massive stars at the centre of the disk, but also lower-mass stars apparently forming in outer parts of the disk. However, the disk is on average Toomre-stable. We find that “disk stars” form from pre-existing self-gravitating fragments created before the formation of the gravitationally stable disks and are accreted into the disk as mentioned in the point above (see Figures 4.3 and 4.9). We, therefore, conclude that in order to realistically

simulate the formation and evolution of massive stars and their circumstellar disks it is crucial to capture the environment and initial conditions of the protostellar core. Idealized initial conditions starting from smooth disk structures, often used to model circumstellar disks around solar-mass stars, will likely not capture the full picture of fragmentation of the disk for the high-mass case.

4. Large and massive disks around high-mass stars are supported by both magnetic and turbulent pressure. This is in contrast to the case of disks around lower-mass stars, supported instead by thermal pressure. Regardless of the core mass/size, the magnetic pressure dominates in the envelope as well as the outer disk at radii $\gtrsim 200 - 1000$ AU, while turbulent pressure dominates in the inner disk at $< 200 - 1000$ AU (see Figure 4.8). The turbulent velocity of the disk is close to the virial velocity of the core, including the central protostars (~ 1 km/s), which suggests that the source of the turbulence is the non-axisymmetric gravitational collapse of the gas.

5. The final number of (proto)stars that form in a core is between 1 and 12 (Figure 4.10). Most of the accreted mass is distributed among 1 to 3 stars of similar mass (up to a mini cluster of 8 stars for our most massive core) that form near the centre of the disk/toroid. The disk stars account for a small or negligible fraction of the mass of stars.

6. In our highest resolution simulation ($\Delta x_{\rm min} = 7$ AU) where the sink formation density is above 10^{10} $\rm cm^{-3}$, close to the density where the gas becomes adiabatic, the total mass in stars (12.6 $\rm M_{\odot}$) is approximately equal to the mass of the sink particle in the baseline run, which is believed to represent a prestellar core. This suggests a nearly 100 per cent SFE in high-mass cores.

7. In the most massive core we simulated, the core evolves from a spherical shape with a radius

of 0.5 parsec and a mass of 131 $\mathrm{M}_{\odot}$ into a (proto)star cluster that is over 600 $\mathrm{M}_{\odot}$ enshrouded by a massive toroid over a timescale of about 0.9 Myr (Figure 4.11). We explain the large masses in these ultra-high-mass (proto)stars in the context of the competitive accretion scenario, in which gas is continuously supplied from larger scales beyond the mass reservoir of the core.

8. O/B stars that form as a single star typically produce an ultracompact H II region that remains trapped in the dense and thick circumstellar disk for an extended period of time ($\sim$ 500 kyrs). However, when high-mass stars form as wide binaries or in multiple systems, the dynamic motion of the system displaces the stars periodically from the densest parts in the disk plane or filament where the density is lower allowing UV radiation to escape and creating a long-lasting or periodic bipolar H II regions (see Figures 4.12-4.13).

In Chapter 5, we will further study the properties and growth of the magnetic field in magnetically critical and sub-critical cores, where we will also address the origin of the density-B relationship and the magnetic braking problem.

Chapter 5: Magnetic Braking Fails to Work: Formation of Large Keplerian Disks in Magnetically Critical Giant Molecular Clouds

The formation of circumstellar disks is a critical step in the formation of stars and planets. However, magnetic fields can strongly affect the evolution of angular momentum during prestellar core collapse, potentially leading to the failure of protostellar disk formation. This phenomenon, known as the magnetic braking catastrophe, has been observed in idealized MHD simulations. In this chapter, we present a numerical study of circumstellar disk formation from realistic initial conditions of strongly magnetized massive cores resolved by zooming into Giant Molecular Clouds (GMC) with initial mass-to-magnetic flux ratios $0.6 \leq \mu_0 \leq 3$. Due to the large turbulence caused by the non-axisymmetric gravitational collapse of the gas, the dominant vertical support of disks is turbulent motions, while magnetic and turbulent pressures contribute equally in outer toroid. The magnetic field topology is extremely turbulent and incoherent, reducing the effect of magnetic braking by roughly one order of magnitude and leading to the formation of large Keplerian disks even in magnetically critical cores (with $\mu \approx 1$) that form in magnetically critical/supercritical GMCs. Only cores in GMCs with $\mu_0 = 0.6$ fail to form disks. Instead, they collapse into a sheet-like structure and produce a large number of low-mass stars. We also discuss the geometry of the B field in cores and the emergence of a universal $B - \rho$ relation valid over a large range of scales from the GMC to massive cores, independently of the GMC magnetization.

This study provides insights into the initial conditions of prestellar core collapse and their role in determining disk formation.

5.1 Introduction

The formation of protostellar disks is ubiquitous during the collapse of prestellar cores. As a molecular core collapses under its own self-gravity, the angular momentum of the gas will slow down its collapse at small scales promoting the formation of a protostellar disk. This simple argument of conservation of angular momentum is corroborated by observations, also suggesting that protostellar disk formation is a natural byproduct of the star formation process (O'dell & Wen, 1992; Tobin et al., 2012; Murillo et al., 2013; Codella et al., 2014; Lee et al., 2017).

However, molecular clouds are observed to be permeated by magnetic fields (Crutcher, 1999; Lee et al., 2017), which can in principle strongly affect the evolution of angular momentum during the core collapse. The twisting of the magnetic field lines produced by the disk rotation in the flux-freezing regime of ideal magnetohydrodynamics (MHD), can apply a force counter to the rotation velocity, also known as magnetic braking, effectively slowing down rotation and increasing radial gas infall. In idealized numerical MHD simulations, the timescale of the braking can become so short that protostellar disks fail to form or are much smaller than the observed sizes, a phenomenon known as "the magnetic braking catastrophe" (e.g. Allen et al., 2003; Galli et al., 2006; Hennebelle & Fromang, 2008; Li et al., 2014). Indeed, disk formation should be completely suppressed in the strict ideal MHD limit for the level of core magnetization deduced from observation – the angular momentum of the idealized collapsing core is nearly completely removed by magnetic braking close to the central object (*e.g.*, Mestel & Spitzer, 1956; Mellon

& Li, 2008). These results seem to be in contrast to the observed existence of Keplerian disks around Class 0 protostellar objects.

Magnetic fields support charged gas against gravitational collapse. A common characterization of the relative importance of the gravitational and magnetic forces in a molecular cloud or core is the normalized mass-to-flux ratio,

$$\mu \equiv \frac{M/\Phi_B}{M_\Phi/\Phi_B} = \frac{M}{M_\Phi}, \tag{5.1}$$

where M is the total mass contained within a spherical region of radius R, $\Phi_B = \pi R^2 B$ is the magnetic flux threading the surface of the sphere assuming a uniform magnetic field strength B, and

$$M_\Phi = c_\Phi \frac{\Phi_B}{\sqrt{G}}, \tag{5.2}$$

is the magnetic critical mass, the mass at which the magnetic and gravitational forces balance each other. The constant c_Φ is a dimensionless coefficient that depends on the assumed geometry of the system. For a spherical cloud of uniform density, $c_\Phi = \sqrt{10}/(6\pi) = 0.168$. However, the mass-to-flux ratio μ should be used with caution, since the definition of the critical value dependents on the geometry of the gas and the magnetic fields.

In a sub-critical cloud (defined as a cloud with $\mu < 1$), the magnetic field should prevent the collapse of the cloud core altogether. Observations suggest typical values of $\mu \approx 2 - 10$ in molecular cloud cores (e.g. Crutcher, 1999; Bourke et al., 2001), and this value could be even smaller after correcting for projection effects (Li et al., 2013). Moreover, analytical predictions (Joos et al., 2012) suggest that there are no centrifugally-supported disks in models with $\mu \leq 10$, although there are pseudo-disks which are disk-like over-densities of gas in which the magnetic fields, rather than the centripetal force, support the gas against collapse in the radial direction.

More recent studies have explored how magnetic configurations, *i.e.*, misalignment, may reduce the power of magnetic braking. Joos et al. (2012) and Gray et al. (2018) explored the misalignment between the magnetic field and the rotation axis of the gas. However, in models of Joos et al. (2012) with $\mu = 2$, disks never form, independent of the misalignment angle. Thus, the effect of misalignment on disk formation is inconclusive. Several studies have investigated the effects of turbulent initial magnetic fields on disk formation (e.g. Santos-Lima et al., 2012; Joos et al., 2013; Li et al., 2014; Fielding et al., 2015; Gray et al., 2018; Lewis & Bate, 2018). However, these simulations reach contradicting results, with some suggesting increased turbulence promotes disk formation while others suggest it hinders disk formation. Seifried et al. (2013) argued that the turbulent velocity field diffuses the magnetic field and makes the structure of the magnetic field less coherent, producing disks 50 – 150 AU in size in strongly magnetized cores. These works have shown that misalignment and turbulence can promote disk formation. However, none of these previous studies predicts the formation of large disks ($>$ 500 AU) in strongly magnetized cores, even in cores that are massive (*e.g.*, $> 100\ \mathrm{M}_\odot$). However, the existence of massive disks is revealed by recent radio/mm and optical/IR observations (Zapata et al., 2007; Sánchez-Monge et al., 2010; van Kempen et al., 2012; Takahashi et al., 2012; Johnston et al., 2015, 2020). For example, Johnston et al. (2015) and Johnston et al. (2020) observed disks of radii $\gtrsim 1000$ AU around an O-type star. The initial conditions of prestellar core collapse will likely play an important role in determining disk formation.

Motivated by the above discussion, we present this study of circumstellar disk formation from realistic initial conditions of strongly magnetized cores resolved in simulations of $\sim 10^4\ \mathrm{M}_\odot$

GMC/core name	μ_0	$\mathcal{M}$	B (μG)	$\mathcal{M}_A$	β	$\Delta x_{\rm min}$ (AU)
μ3Ma15	3	15	10	5	0.1	60
μ3Ma15-large*	3	15	10	5	0.1	60
μ1Ma15	1	15	30	1.7	0.01	60
μ0.6Ma15	0.6	15	50	1	0.004	60
μ3Ma7	3	7	5	5	0.5	29
μ3Ma7-hires	3	7	5	5	0.5	7
μ1Ma7	1	7	15	1.7	0.06	29
μ0.6Ma7	0.6	7	25	1	0.02	29

Table 5.1: List of zoom-in simulations presented in this chapter. All the cores are chosen as the first star-forming core in the corresponding GMC, except for the one with a *, which is chosen from the later stage of the GMC evolution and is a very massive core with over 100 $\mathrm{M}_\odot$.

GMCs, along with realistic boundary conditions from the co-evolving GMC. This is an extension of the work presented in He & Ricotti (2022) (hereafter Paper I), in which we studied the formation and fragmentation of high-mass prestellar cores and the formation of large circumstellar disks. In this work, we focus on the magnetic phenomenon and the influence of varying magnetic intensity.

The rest of this chapter is organized as follows. We describe the methods in our simulations in § 5.2. We present the results in § 5.3, where we provide a solution to the magnetic braking catastrophe. We summarize our conclusions in § 5.4.

5.2 Method

In Paper I we have conducted a set of "zoom-in" radiation-MHD simulations of prestellar core formation and evolution within collapsing GMCs. In this work we extend the set of simulations to explore the effects of stronger magnetic fields. We present a suite of six "zoom-in" simulations of prestellar cores in molecular clouds with varying magnetization and turbulence. We summarize the key parameters of the simulated GMCs and cores in Table 5.1. Two GMCs,

μ3Ma15 and μ3Ma7 are fiducial runs with the same initial magnetization ($\mu_0 = 3.0$) as those presented in Paper I and in He et al. (2019), in which we present the results for the larger scale GMCs evolution. The two clouds have initial turbulent Mach numbers $\mathcal{M} = 15$ and $\mathcal{M} = 7$ and masses of 3×10^4 $\mathrm{M}_\odot$ and 3×10^3 $\mathrm{M}_\odot$, respectively. These two GMCs are the XS-C and M-C clouds in He et al. (2019), respectively. They both have an initial average number density of $1000\ \mathrm{cm}^{-3}$. The other four GMCs on which we zoom in (μ1Ma15, μ1Ma7, μ0.6Ma15, and μ0.6Ma7) have the same properties as the two fiducial clouds but increased magnetic field intensities with $\mu_0 = 1.0$ and $\mu_0 = 0.6$, as shown by the name of the run. We also list the Alfven Mach number $\mathcal{M}_A$ and the Plasma beta β of the initial GMC, as well as the spatial resolution Δx_{min} of the zoom-in simulations.

For all the six zoom-in simulations mentioned above, we zoom into the first cores forming in each GMC, and study their subsequent collapse. In this work we also include two extra cores selected from Paper I: 1) μ3Ma7-hires – which corresponds to Core *A-hr* in Paper I – is a higher-resolution zoom-in version of μ3Ma7; 2) μ3Ma15-large corresponds to Core *B* in Paper I, which is a very massive core that forms in the later stage of star formation in the fiducial GMC μ3Ma15.

The sink particle (star formation) and stellar feedback recipes and "zoom-in" method used in this work are described in Paper I. Here, we provide only a brief summary. We perform simulations of star formation using the grid-based adaptive mesh refinement (AMR) MHD code RAMSES-RT (Teyssier, 2002; Fromang et al., 2006). Radiation transfer is modelled using a moment-based method with the M1 closure relationship for the Eddington tensor (Rosdahl et al., 2013). The ionizing photons emitted from stars interact with neutral gas and we keep track of the time-dependent ionization chemistry of atomic hydrogen and helium, but we do not include the

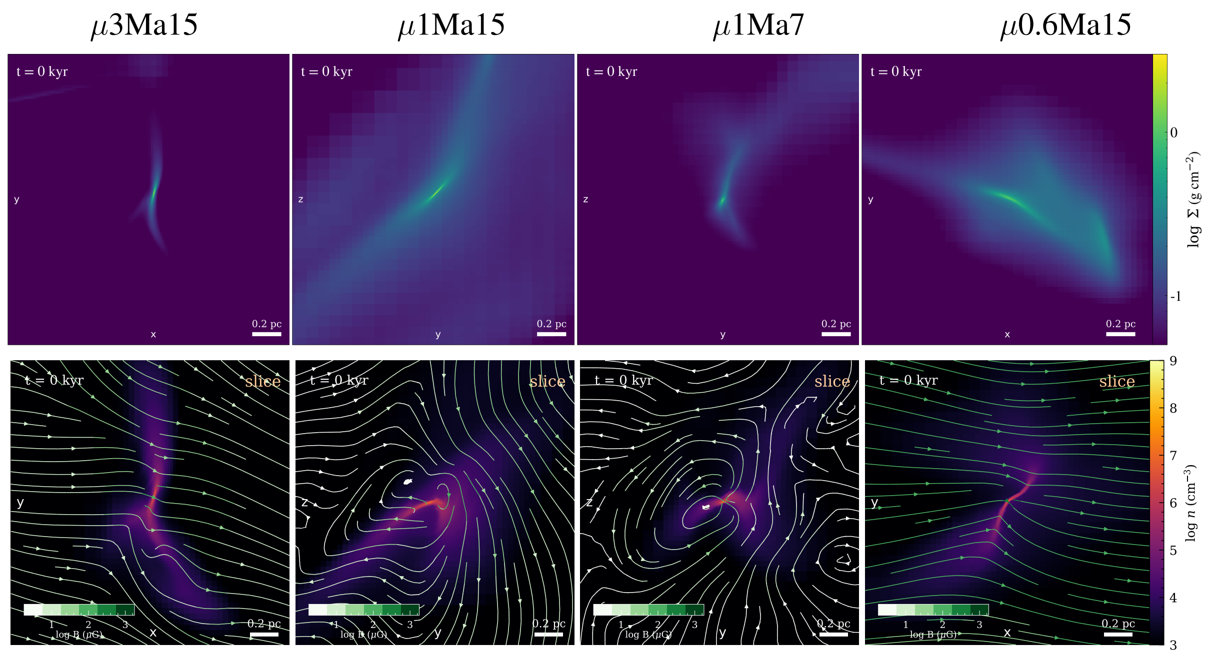

Figure 5.1: (*Top*) Surface density of the cores μ`3Ma15`, μ`1Ma15`, μ`1Ma7`, and μ`0.6Ma15`, showing their morphology at $t = 0$, shortly before the formation of stars. (*Bottom*) Density slices of the corresponding cores centred at the peak density overplotted with magnetic field streamlines. The field of view and viewing angle orientation are the same as in the top panels. The magnetic field streamlines are colour-coded according to their magnitudes and a colorbar is shown at the bottom-left corner. Note how the surface density of the core μ`0.6Ma15` does not intuitively reflect the actual geometry of its sheet-like shape.

chemical evolution of the molecular phase and metal chemistry, used only for cooling/heating rates, is treated assuming equilibrium abundances. Heating from photoionization and cooling from hydrogen and helium, metals, and dust grains are implemented. Cooling below 10 K is shut down to keep the temperature floor at 10 K. The photoionization feedback from stars heats the gas, dispersing the cloud and quenching star formation.

The baseline simulations of GMCs are started from idealized spherical isothermal clouds in hydrostatic equilibrium surrounded by a low-density shell, in which gravity is nearly balanced by turbulent motions ($\alpha \equiv K/|W| = 0.4$). The clouds measure 3×10^3 M$_\odot$ (3×10^4 M$_\odot$) in mass and 4.6 pc (10 pc) in radius for the `Ma7` (`Ma15`) runs. The simulation box is 4 times larger than the diameter of the cloud to follow the expansion and dissolution of the cloud. We let the cloud relax for three free-fall times to allow the turbulence to develop before turning on full gravity and sink particle formation (*i.e.*, star formation). Adaptive mesh refinement is applied to the whole domain to make sure at any time and any location the local Jeans length, $L_J = c_s\sqrt{\pi/(G\rho)}$, is resolved by at least 10 grid points. The maximum refinement level $l_{\max}$ is set to 14 in the whole domain.

In the zoom-in simulations presented in this work, we rerun each GMC simulation starting right before the first sink particle (prestellar core) forms in the baseline run. We define a "zoom" region, about 2 pc in size, at the location where the first core forms and set a higher refinement level of $l_{\max} = 18$ inside this region. To reach the best possible resolution with manageable computational power, we use a nested refinement structure where $l_{\max}$ increases as it gets closer to the domain centre. The critical density for sink formation is $n_{\rm sink} = 3.6 \times 10^9~{\rm cm}^{-3}$ and $7.7 \times 10^8~{\rm cm}^{-3}$ for the `Ma7` and `Ma15` clouds, respectively.

In order to measure the cloud magnetization we use an alternative formulation of the dimensionless mass-to-flux μ given by Equation (5.1), which is more reliable for systems that depart from uniform density and physical symmetry. The following definition remains accurate for general inhomogeneous mass distribution and/or asymmetric geometry:

$$\mu^2 \equiv \frac{|W|}{\mathcal{B}} = \frac{18\pi^2}{5}\frac{GM^2}{\Phi_B^2} = \frac{M^2}{M_\Phi^2}. \tag{5.3}$$

Here, W is the gravitational potential energy and $\mathcal{B} \equiv VB^2/(8\pi)$ is the magnetic energy. The last equal sign holds for the uniform spherical geometry, in which case the μ defined in Equation (5.3) is equivalent to the mass-to-flux ratio definition. For a more centrally concentrated geometry, *e.g.*, a non-singular isothermal sphere, the equivalent geometrical factor c_Φ is up to 70% higher and μ is 40% lower than the uniform density case (see Appendix C.1).

5.3 Results

In this section we present results focusing on the core morphologies and evolution in § 5.3.1, the magnetic field-gas density relationship in § 5.3.2, the pressure support of the disks in § 5.3.2, and a solution to the magnetic braking problem in § 5.3.4.

5.3.1 Morphology of Gas Density and Magnetic Field in Cores

For the same GMC simulation and sink particle we zoom into, the strength of the background magnetic field has an effect on the early phase of collapse and the initial morphologies of the collapsing cores. The top row of Figure 5.1 shows the surface density of the gas for a representative set of 4 simulations while to bottom row shows the density in a slice through the same filament and the magnetic field lines. In the weaker magnetic field cases (μ`3Ma15`, μ`1Ma15`, and μ`1Ma7`), the core collapses starting from a gas filament oriented perpendicular to the magnetic field lines. This nearly one-dimensional structure is denser near its centre of mass and the density decreases in the outer parts of the filament. Both the projection plots and the slice plots show similar morphology and orientation of the filament geometry, which is also confirmed by an inspection of the 3D rendering of the gas density. In the stronger magnetic field case (μ`0.6Ma15`), the gas also collapses along the field lines but into a two-dimensional sheet-like structure. The gas surface density of the sheet is also not uniform and the peak density defines a one-dimensional curve, or filament, that is not necessarily oriented perpendicular to the B-field lines. This can be

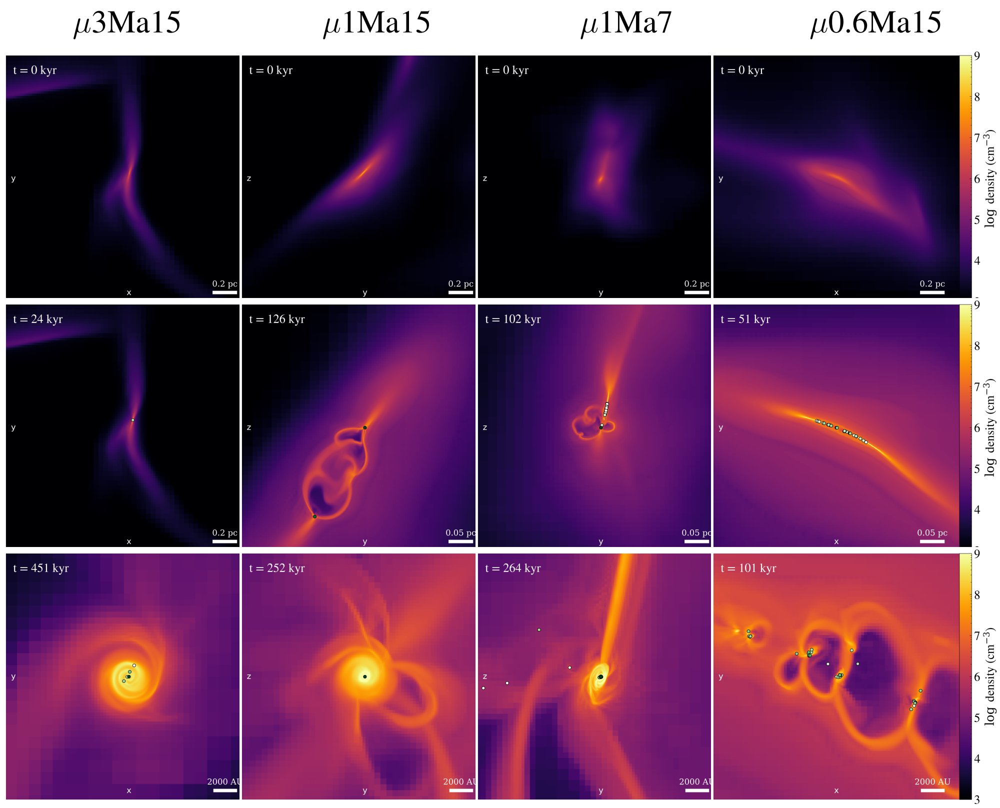

Figure 5.2: Density projections of the four cores (from left to right) inspected in Figure 5.1, showing their time evolution (from top to bottom) and the formation of stars. The circles mark the positions of the sink particles which represent individual stars. The colors of the circles, from white to dark green, correspond to their masses from 0.1 $\mathrm{M}_\odot$ to 10 $\mathrm{M}_\odot$ in log scale. A large Keplerian disk forms in all cores in GMCs with $\mu_0 \gtrsim 1$. In the case where $\mu_0 < 1$ (μ0.6Ma15), the core collapses into a sheet-like shape with negligible angular momentum with respect to the center of mass, preventing disk formation.

observed in the projection plot for run μ0.6Ma15 in Figure 5.1, showing a filament structure apparently oriented along the B-field lines. However, the slice plot indeed shows the magnetic field lines threading through the sheet are perpendicular to its surface. To summarize, since the surface density is the quantity more readily observable, in the weak B-field case the surface density maps reflect the actual filamentary shape of the gas leading to core formation. In the strongly magnetized cloud, however, the surface density map may lead observers to mistakenly think that the structure is a filamentary or disk-like structure rather than a two-dimensional sheet structure.

During the next stage of collapse, the gas fragments along the filament or along the central

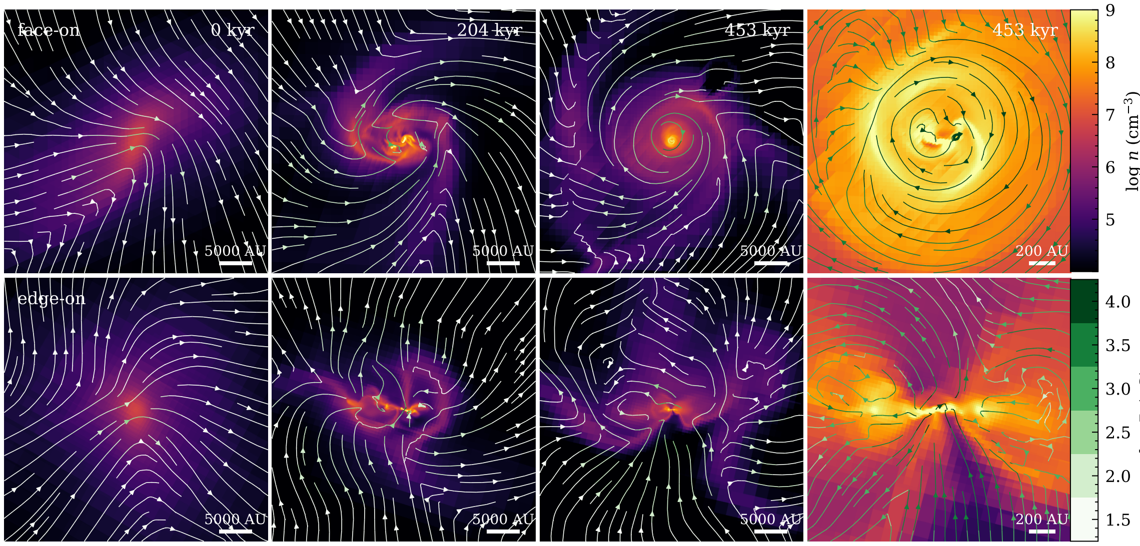

Figure 5.3: Temporal evolution (from left to right) of the magnetic field morphology of core μ3Ma15-hires in a face-on view (top row) and edge-on view (bottom row). Each panel shows a slice of the gas density centred at the peak density overplotted with magnetic field streamlines. The color of the streamlines shows the magnetic strength as indicated by the colorbar at bottom right. Note that the last column shows a zoomed view of the center of the disk for the same time snapshot shown in the third column panels. These figures show how the magnetic field lines are wound up as the disk forms and that the magnetic field is extremely turbulent especially near the disk centre.

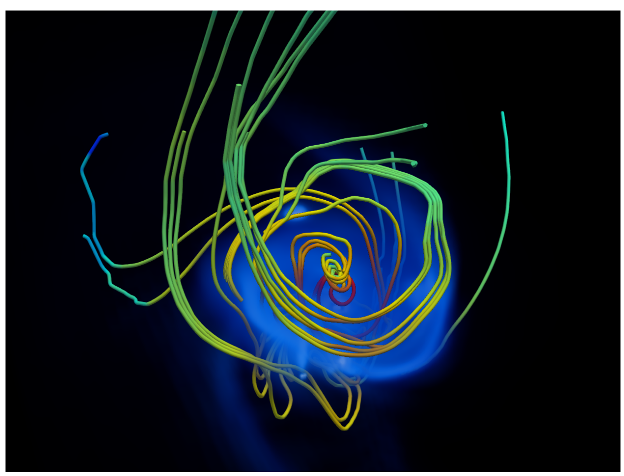

Figure 5.4: 3D view of the magnetic field lines on top of the volume rendering of the disk μ3Ma15-hires. The rendering in blue shows the gas at densities above $10^6\ \mathrm{cm}^{-3}$. The tubes indicate the direction of the field lines and their colours indicate the strength of the magnetic field with red to blue meaning strong to weak. The disk measures 10,000 AU in diameter.

high-density line of the sheet (Figure 5.2). In the supercritical/critical ($\mu_0 \geq 1$) cases, the core fragments into multiple stars along the filament. Due to the conservation of angular momentum, the filament spirals inward and forms a Keplerian disk. The fragments are ultimately embedded in the Keplerian disk, as already shown in our previous work (Paper I). In the cases where $\mu_0 < 1$, the sheet-like structure collapses toward the central high-density line. When the central density reaches the local Jeans density, the gas collapses to form numerous stars that are clustered into clumps. Due to magnetic braking, as will be discussed in § 5.3.4, the angular momentum of the gas is transferred outward and the gas flows directly into the centre of local clump without forming a disk.

To take a peek at how the magnetic field morphology evolves over time, we plot the magnetic field lines of core μ3Ma7-hires at four snapshots in Figure 5.3. As the cores collapse, the magnetic field is bent by the rotation of the gas through the dynamo effect. The field lines are twisted and the magnetic strength is enhanced at the disk centre, which is also demonstrated by the 3D volume rendering of the magnetic field lines in Figure 5.4. The field is dominated by the toroidal component in the inner region and by the poloidal component in the outer region, which has implications on the strength of magnetic braking as will be discussed in § 5.3.4.

5.3.2 $B - \rho$ Relationship

Understanding the relationship between density and magnetic field, as well as their physical origin, is crucial for both observations and theoretical models. According to simple models (*e.g.*, Crutcher, 1999), the magnetic field and gas density of a collapsing molecular cloud follow a power-law scaling relationship, $B \sim \rho^{\kappa}$. Assuming flux-freezing in ideal MHD, in the scenario

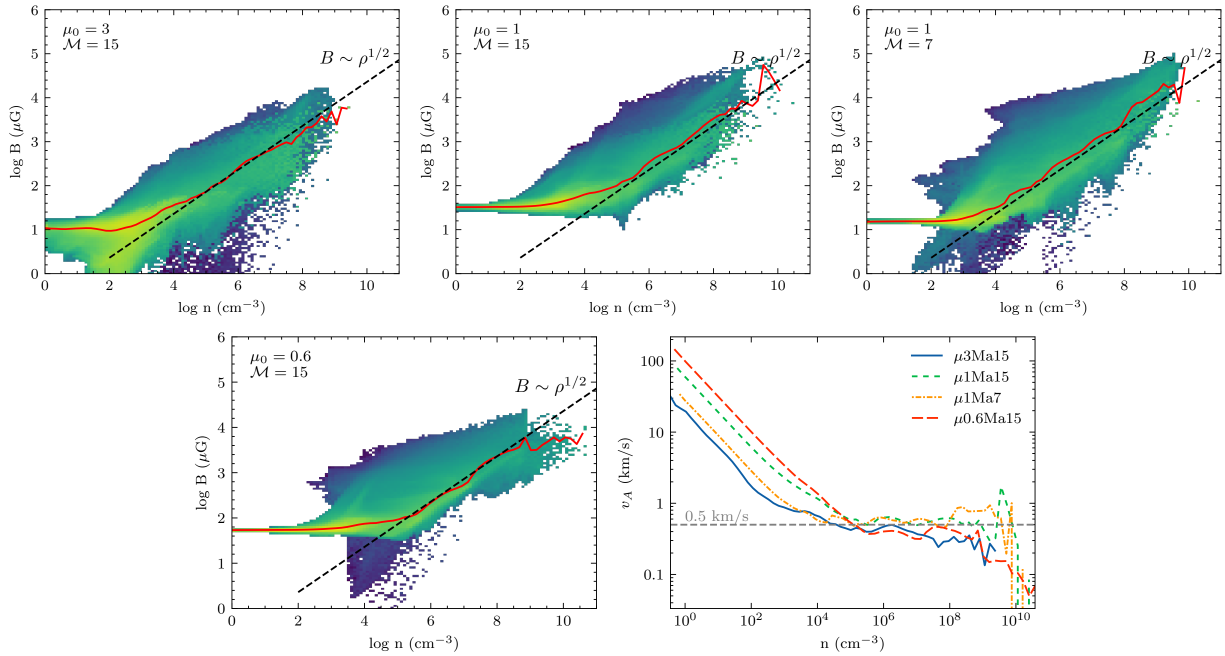

Figure 5.5: The global $B - \rho$ relationship at GMC scales for the μ`3Ma15`, μ`1Ma15`, μ`1Ma7`, and μ`0.6Ma15` runs. At low density ($\lesssim 10^3$ cm^{-3}), the magnetic field intensity is independent on the density and the global value is determined by the initial magnetization. At high density up to $\sim 10^9$ cm^{-3}, we find a universal $B - \rho$ relation: $B \approx 86$ μB $(n/10^5 \text{ cm}^{-3})^{1/2}$, corresponding to a constant Alfven velocity of ~ 0.5 km/s. The first four panels show the 2-D phase diagram of magnetic intensity B vs gas number density n of the four clouds, respectively, and the colors representing the log of the gas mass with increasing mass from dark to bright. The red curves are the mass-weighted 1-D relationship. The last panel plots the Alfven velocity v_A as a function of n, converted from the 1-D $B - n$ relationship for all four clouds.

of the isotropic collapse of a spherical cloud threaded by uniform parallel magnetic field lines, the relationships $B \propto R^{-2}$ and $\rho \propto R^{-3}$, imply $B \propto \rho^{2/3}$. In the scenario of the anisotropic collapse of a flattened structure or disk, the evolution of the gas collapse consists of two stages: during the first stage the cloud collapses along the field lines to form a disk. The gravitational acceleration at the disk surface, according to Gauss's law, is approximately $g \approx -2\pi G \Sigma$, where $\Sigma = \rho H = M/(\pi R^2)$ is the gas surface density, and H, R and M are the disk thickness, radius and mass, respectively. In the second stage, assuming flux-freezing, the mass-to-flux ratio $M/\Phi_B = \Sigma/B$ is conserved, therefore $B \approx \Sigma \Phi_B / M$. Assuming $g \approx \sigma^2/H$, *i.e.*, the disk is

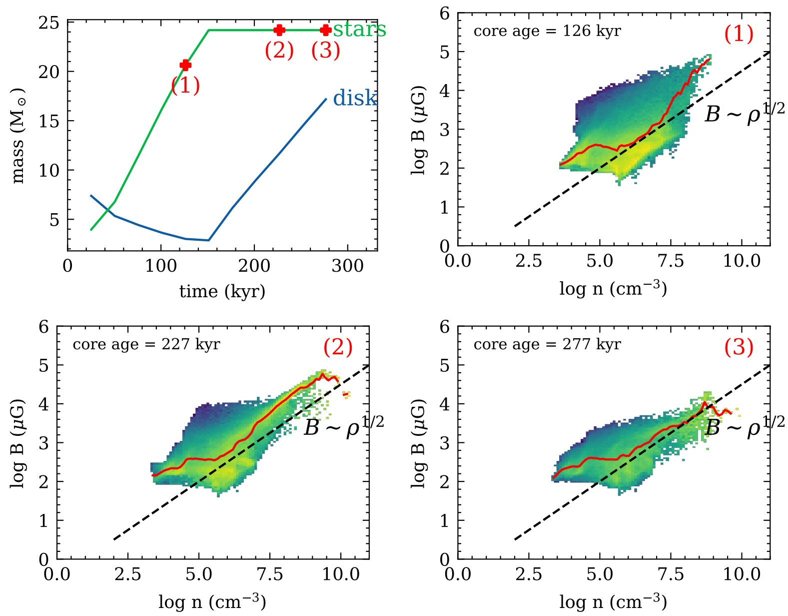

Figure 5.6: Enhancement of the magnetic intensity at high density inside the core μ1Ma15. The first panel shows the temporal evolution of the mass in stars and in disk. The rest of the panels show 2-D phase diagram of $B - n$, similar to Figure 5.5, inside the core at various times as marked in the first panel. We show that as the gas is accreted by sink particles while the magnetic field is retained outside, the magnetic intensity is boosted by nearly an order of magnitude at a density above $10^7\ \mathrm{cm}^{-3}$. As the accretion stops, the strong magnetic field disperses itself due to magnetic pressure/tension.

supported by turbulent pressure in the vertical direction, we find $\sigma^2 \approx 2\pi G \rho H^2 \sim 2\pi G \Sigma^2/\rho$.

Therefore,

$$B \approx \frac{\sigma}{\sqrt{2\pi}\ c_\Phi \mu} \rho^{1/2}, \tag{5.4}$$

or expressed in terms of the Alfven velocity

$$v_A = \frac{B}{\sqrt{4\pi\rho}} \approx \frac{\sigma}{2\sqrt{2}\pi c_\Phi \mu}. \tag{5.5}$$

An even simpler interpretation of this relation is the equipartition between magnetic and kinetic energy, $B^2/(4\pi) \propto \rho\sigma^2$, noting that

$$\frac{v_A^2}{\sigma^2} = \frac{1}{8\pi^2 c_\Phi^2 \mu^2} = \frac{0.45}{\mu^2}. \tag{5.6}$$

In flattened cores where μ is marginally greater than 1, this relationship predicts that magnetic pressure is slightly weaker than turbulent pressure.

5.3.2.1 $B - \rho$ Relationship in GMCs

It is well established (Troland & Heiles, 1986; Crutcher et al., 2010) that at low densities ($\lesssim 10^3$ cm^{-3}), the intensity of the magnetic field does not depend on gas density. This phenomenon is clearly seen in our simulations (Figure 5.5), and the intensity is determined by the strength in the initial condition. At higher densities, up to $\sim 10^9$ cm^{-3}, the magnetic field scales with density as $B \propto \rho^{1/2}$, resulting in a universal value of the Alfven velocity of $v_A \sim 0.5 \pm 0.1$ km/s. This exponent suggests that the collapse is anisotropic in all clouds, regardless of whether the turbulent energy is stronger ($\mathcal{M}_A = 5$) or equal to the magnetic energy ($\mathcal{M}_A = 1$). This result differs from a previous study (Mocz et al., 2017), which suggests that the collapse is isotropic ($B \propto \rho^{2/3}$) when turbulence dominates over the magnetic field and transitions into anisotropic when magnetic energy dominates. In Figure 5.5 we show phase plots of B vs gas number density n for GMCs with a range of μ_0 from 3 to 0.6 and for turbulent Mach numbers $\mathcal{M} = 7$ and 15. The red line, showing the median value of B at a given n, suggests that the Alfven velocity derived from this median relationship is nearly constant independently of μ_0 and $\mathcal{M}$. It is important to note, however, that the Alfven velocity is only approximately constant above the critical density, and the exact value may also depend on other properties of the cloud. In Section 5.3.2.3, we will explore the physical mechanisms that govern the scaling of the magnetic field with density in more detail. The critical density at which there is a transition from $B = B_0 = \mathrm{const.}$ to $v_A = \mathrm{const.}$ is:

$$n_{\mathrm{cr}} \equiv \frac{1}{4\pi m_{\mathrm{H}} \mu_{\mathrm{H}}} \left(\frac{B_0}{v_A} \right)^2 \approx 2.2 \times 10^4 \ \mathrm{cm}^{-3} \left(\frac{B_0}{30 \ \mu G} \right)^2 . \tag{5.7}$$

This critical density is roughly consistent with the observed density of cores in GMCs, suggesting that cores form when the magnetic field is no longer strong enough to support the cloud against gravitational collapse.

5.3.2.2 $B - \rho$ Relationship in Cores

In Figure 5.6, we show the $B - \rho$ relationship at smaller scales in the zoom-in simulations (for gas in the cores). Also in the cores, the $B - \rho$ relationship follows the same universal relationship $B \propto \rho^{1/2}$ with the same normalization as at GMC scales (Figure 5.5). However, at densities $> 10^7 \ \mathrm{cm}^{-3}$we notice that the magnetic field intensity at a given density is enhanced with respect to the universal value when the sink particle accretes gas. Probably this phenomenon is a result of the release of magnetic field during sink accretion, as the sink particles accrete gas but not magnetic field, hence the conservation of mass-to-flux ratio, valid in ideal MHD, is broken within the sink particles. This recipe for sink accretion is particularly motivated by the magnetic flux problem in star formation: the mass-to-flux ratio in a star is 10^{5-8} times higher than that at the cores' scale. The boost in the B field at a given ρ persists as long as the sink particle is accreting gas. Shortly after the accretion stops, the magnetic field strength reduces back to the average value following the global $B - \rho$ relationship. Evidently, the accumulation of B-field lines in the sink produces a temporarily stronger magnetic pressure diffusing the magnetic field lines outward.

5.3.2.3 Interpretation of the Universal B-ρ Relationship

In all the phase plots we observe two regimes: (A) a low-density regime where the mean of the magnetic field is constant as a function of ρ, even though the spread around the mean can be large, especially for weaker values of the initial B-field (large μ cases); (B) a high-density regime, where $B \propto \rho^{1/2}$, or $v_A = \mathrm{const}(\rho)$. These two regimes are observed for the GMC as a whole (in this case the constant B value is the one set in initial conditions), and for individual cores: in this second case the constant B value regime is the one at the boundary of the core where the density is lowest.

The regime (A) is the case when the density of the gas can increase or decrease while leaving B constant: this happens when the motion of the gas is along the magnetic field line. For instance, the initial turbulent motions of the gas can compress or de-compress the gas: when the gas is compressed (de-compressed) in the direction of the magnetic field lines, B remains the same but the density increases (decreases). If the motion is perpendicular to B, the value of B can increase or decrease for compression/decompression. However, this will just produce a constant scatter in the $B - \rho$ relationship around the mean if there is no preferred direction for the turbulence (isotropic turbulence). We expect the scatter around the mean to be small for smaller μ, as the stronger magnetic tension/pressure suppresses compression/de-compression perpendicular to the B-filed direction. This is indeed observed in Figure 5.5.

This regime no longer exists at cores scales (high densities) when the gas motion is no longer isotropic, rather it is mostly compression due to the self-gravity of the cores. Assuming that cores can be initially approximated as isothermal spheres embedded in a uniform magnetic field supported by thermal and turbulent pressure in the direction of the magnetic field lines, one can apply the derivation in § 5.3.2 and Eq. (5.6). After the initial phase of compression in the z-direction at constant Σ and B, any further density increase is produced by compression perpendicular to the B-field lines, producing $B \propto \rho^{1/2}$ or $v_A = \mathrm{const}(\rho)$. But what sets the constant value of $v_A \sim 0.5$ km s^{-1} observed across different scales and densities?

The value of σ and μ in Eq. (5.6) are not the initial values for the GMC, but rather the initial values for self-gravitating cores. If the cores are in quasi-hydrostatic equilibrium supported by turbulence and magnetic pressure, $W \sim (\mathcal{B} + K_{\rm turb})$. If the initial value of the magnetic pressure is comparable to or dominates over turbulence we expect $\mu \equiv \sqrt{|W/\mathcal{B}|} \sim 1$. Assuming that the core is marginally Jeans unstable and partially supported by turbulent pressure, the equivalent Jeans mass is given by

$$M_J = \frac{\pi^{5/2}}{6} \frac{\sigma^3}{(G^3\rho)^{1/2}}, \tag{5.8}$$

where σ is the rms of the turbulent velocity. In GMC simulations by He et al. (2019) the typical masses of prestellar cores (the most numerous cores in the core mass function) is $M \approx 1-5$ M$_\odot$, and $n = 10^7$ cm^{-3} is their typical gas number density. Using these values in Eq. (5.8) we get $\sigma \approx 0.6$ km/s. Finally, using Eq. (5.6) with $\mu \sim 1$ we have $v_A \approx 0.67\sigma \approx 0.4$ km/s, in agreement with the mean value for the whole GMC and for individual cores. Because σ is weakly dependent on M_J and the core mass function in the GMC is dominated by small-mass cores with $M \sim 1-5$ M$_\odot$, most of the dense gas in the GMC is in cores with $\sigma \sim 0.6$ km/s.

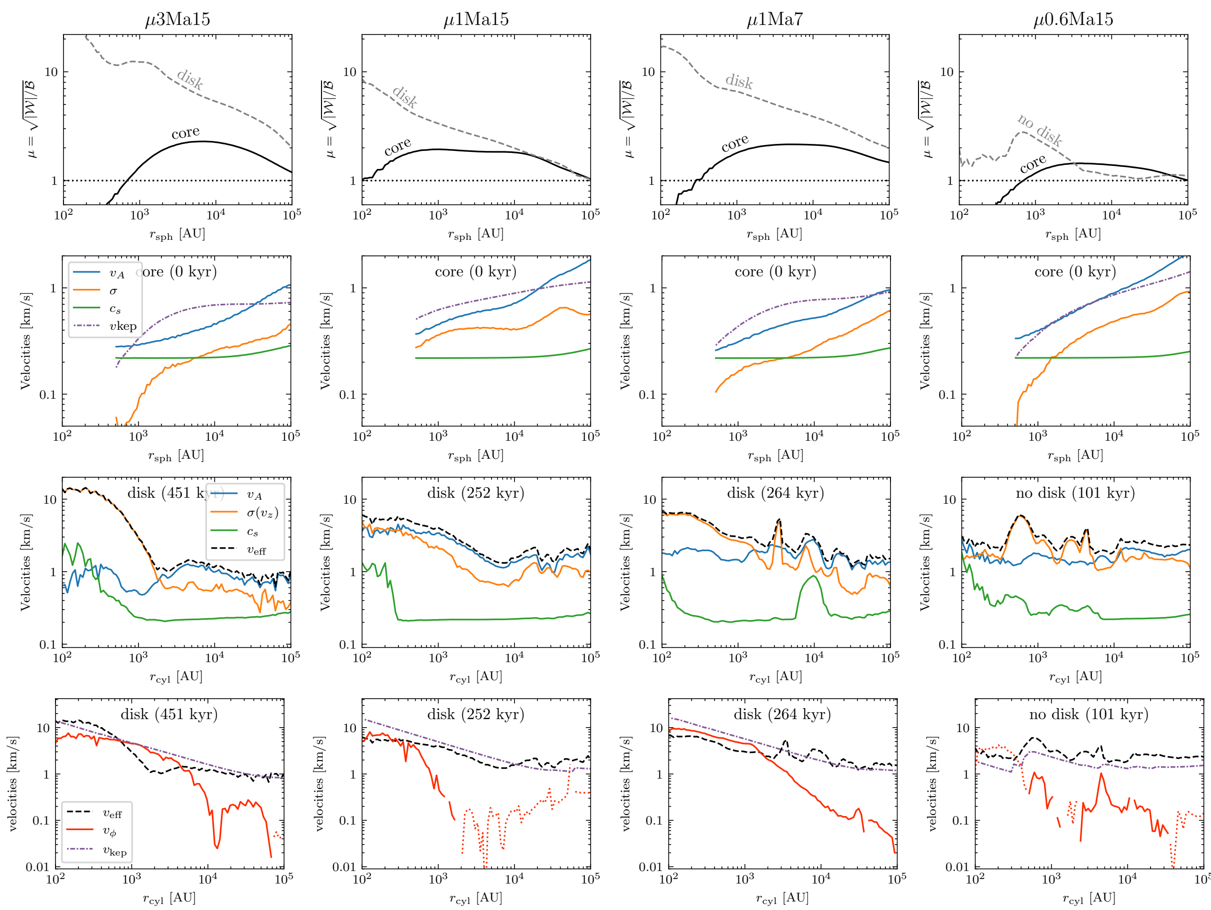

Figure 5.7: The magnetic, turbulent, and thermal support of the cores and disks. From left to right are the cores μ3Ma15, μ1Ma15, μ1Ma7, and μ0.6Ma15. Row 1: the mass-to-flux ratio radial profile of the gas at the core phase (initial time $t = 0$) and disk phase (later stage) as a function of radius. Row 2: radial profiles of the Alfven velocity, turbulence velocity, sound speed, and Keplerian velocity at the core phase as a function of the radius. Row 3: radial profiles of the Alfven velocity, z-component turbulent velocity, sound speed, and the effective velocity of support $v_{\rm eff} = (v_A^2 + \sigma(v_z)^2 + c_s^2)^{1/2}$ during the disk phase as a function of the radius in cylindrical coordinates. Row 4: radial profiles of the effective velocity, the azimuthal velocity, and the Keplerian velocity during the disk phase as a function of the radius in cylindrical coordinates. Quasi-Keplerian disks with $v_\phi \approx v_{\rm kep}$ extending to radii $r_{\rm cyl} \sim 500 - 5000$ AU form in all runs but μ0.6Ma15. The cores are initially supported by magnetic pressure, while thermal and turbulent pressures are sub-dominant. The toroids that form in the cores are supported by both turbulent and magnetic pressure, with the former slightly dominating in the quasi-Keplerian disks found in the inner part of the cores ($\lesssim$ 1000 AU) and the latter slightly dominating in the outer part (toroid). Thermal support is negligible in all the massive cores in this study.

Therefore, in the high-density regime $v_A \approx 0.4$ km/s when averaged over the whole cloud. Note, however, that our most massive cores have $M \sim 130\mathrm{M}_\odot$. Indeed, the B-$\rho$ phase diagram for the most massive core in our set (μ`3Ma15-large`) shows higher values of v_A, consistent with our interpretation.

5.3.3 Magnetic and Turbulent Support in the Cores and Disks

The cores initially have nearly critical magnetic field strengths, with values of the mass-to-flux ratio radial profiles, $\mu(r)$, ranging from 0.5 to 2 from the inner to the outer part of the core (see the top row in Figure 5.7). The μ radial profiles in cores that form from GMCs with different initial magnetic field strengths are virtually indistinguishable from each other: the mass-to-flux ratio in the μ`0.6Ma15` core is only slightly lower than that in the μ`3Ma15` core. This is likely due to a selection effect because magnetically sub-critical "clumps" would fail to collapse and form a sink particle. During the quasi-spherical initial collapse of the cores, the magnetic pressure dominates over the turbulent and thermal pressure, and the core is nearly in hydrostatic equilibrium with the magnetic pressure supporting the core against gravitational collapse as shown by $v_{kep} \sim v_A$ in the panels in the second row of Figure 5.7.

The bottom two rows in Figure 5.7 show that, as the core collapses, the turbulence is amplified especially in the inner parts of the disk/core. In the outer disk, turbulent kinetic energy and magnetic energy are nearly in equipartition. In the disk, the Alfven velocity (v_A) remains around 1 km/s, occasionally increasing to 5 km/s in the inner part. The effective velocity, $v_{\mathrm{eff}}^2 = v_A^2 + \sigma^2 + c_s^2$, always approaches the Keplerian velocity within the disk radius, while it drops significantly below v_{kep} outside of the disk radius. The disk remains quasi-Keplerian ($v_\phi \approx v_{\mathrm{kep}}$)

up to a characteristic radius of about 1000 ± 500 AU in all the cores but the sub-critical one with $\mu = 0.6$: in this run $v_\phi << v_{\rm kep}$ at all radii and a Keplerian disk fails to form (see Figure 5.2).

The grey dashed lines in the top row of Figure 5.7 show the μ profiles of the disks at late times. The disks have $\mu(r) \sim 10$ in the inner parts where turbulent support is dominant, but $\mu(r)$ decreases to ~ 2 in the outer envelope. This decrease of $\mu(r)$ in the outer parts of cores has already been observed: Yen et al. (2022) has shown that the mass-to-flux ratio increases from 1-4 to 9-32 from 0.1 pc to 600 AU scales, which suggests that the magnetic field is partially decoupled from the neutral matter from large to small scales. The authors suggest non-ideal MHD (*e.g.*, ambipolar diffusion) as the cause of this μ radial profile that allows the formation of a Keplerian disk. In our simulations, modelling of non-ideal MHD processes is not included in our equations, other than indirectly in our recipe for sink accretion: sinks accrete mass, momentum and angular momentum but not magnetic field. Hence, a deviation from flux-freezing is caused by the accumulation and subsequent diffusion of the magnetic field within sink particles described before. The increase of μ in the inner part is mainly produced by the increase of the gravitational potential energy $|W|$ from the mass increase of the sink particle which, however, does not accumulate magnetic energy.

5.3.4 Magnetic Braking Problem

As discussed before, the formation of a toroid or a disk can be suppressed or its radius reduced by magnetic braking. The spinning of the gas twists up the magnetic fields, creating a tension force that opposes rotation. The magnetic field exerts a Lorentz force per unit volume on

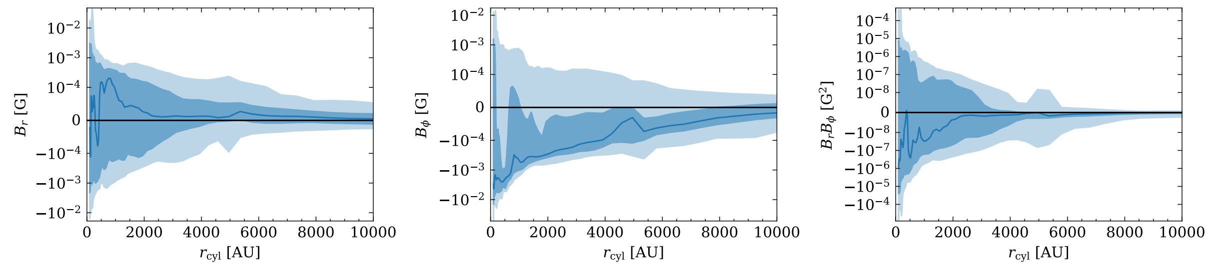

Figure 5.8: Explanation of the weak overall magnetic braking in disk μ3Ma7-hires. From left to right are the distributions of the radial component of the magnetic field, the azimuthal component of the magnetic field, and their product, which is proportional to of $t_{\rm br}^{-1}$, as a function of disk radius in cylindrical coordination. The thick curve displays the median values and the shaded area displays the 1-σ and 3-σ contours for the probability distribution function. Positive and negative values of $B_r B_\phi$ (therefore $t_{\rm br}$) cancel each other, resulting in a small overall magnetic braking effect.

the fluid element which, at a given radius r, can be written as

$$\mathbf{f} = \frac{1}{4\pi}\left[(\nabla \times \mathbf{B}) \times \mathbf{B}\right] \tag{5.9}$$

$$= \frac{1}{4\pi r}\left[\mathbf{B}_p \cdot \nabla_p (r B_\phi)\right]\hat{\phi} \tag{5.10}$$

$$= \frac{1}{4\pi}\left(B_r B_\phi + r B_r \frac{\partial}{\partial r} B_\phi + r B_z \frac{\partial}{\partial z} B_\phi\right)\hat{\phi} \tag{5.11}$$

$$\approx \frac{B_r B_\phi}{4\pi}\hat{\phi}, \tag{5.12}$$

where we have only considered the ϕ component of the torque and assumed that the gradient of B_ϕ with respect to the z-direction vanishes due to symmetry. The second term in the parenthesis of Equation (5.11) is negligible compared to the first term for a B-field with azimuthal component that is nearly constant as a function or radius (*i.e.*, $d \ln B_\phi / d \ln r < 1$). Therefore, we have

$$\frac{d}{dt}(\rho v_\phi) = -\frac{|\mathbf{f}|}{r} \approx -\frac{B_r B_\phi}{4\pi r}. \tag{5.13}$$

The magnetic braking time is defined as the characteristic timescale for the magnetic torque to remove completely the gas angular momentum:

$$t_{\rm br} = \frac{\rho v_\phi}{-\frac{d}{dt}(\rho v_\phi)} \approx \frac{4\pi \rho v_\phi r}{B_r B_\phi}. \tag{5.14}$$

To compare $t_{\rm br}$ with the dynamic timescale, we assume $B_r B_\phi \approx B^2$ and get

$$t_{\rm br} \approx \frac{4\pi \rho v_\phi r}{B^2} = \left(\frac{v_\phi}{v_A}\right)^2 \frac{r}{v_\phi} = \left(\frac{v_\phi}{v_A}\right)^2 t_{\rm cr}. \tag{5.15}$$

This means that if a cloud has a magnetic field nearly in equipartition with gravitational potential energy and if the field is marginally wound up such that the poloidal and toroidal components become comparable, we expect $t_{\rm br} \sim t_{\rm cr}$, *i.e.*, the field is capable of stopping Keplerian rotation in a timescale of the order of the disk rotation period. For instance, at r = 500 AU in the disk of core μ`3Ma15`, $v_\phi \approx 6$ km/s, $v_A \approx 1$ km/s, and $t_{\rm cr} = 0.4$ kyr. From Eq. (5.15) we have $t_{\rm br} \approx 36 t_{\rm cr} \approx 14$ kyr that is significantly shorter of the disk lifetime $\gtrsim 300$ kyr. A timescale $t_{\rm br}$ a factor of two times longer is obtained if we assume $B_r B_\phi \approx B^2/2$.

However, (near-)Keplerian disks can exist in strongly magnetized cores, as demonstrated by both our simulations and numerous observations. As shown in Figure 5.7, within the typical radius of disks ($\sim$ 2000 AU) the azimuthal velocity is nearly Keplerian velocity ($v_\phi \sim v_{\rm kep}$). Previous numerical studies have also shown that, when turbulence was taken into account, the build-up of early-type Keplerian disks was reported even for strong magnetic fields (Santos-Lima et al., 2012; Seifried et al., 2013). In general, these results are based on idealized initial conditions, not extracted from turbulent GMCs. The particular choice of the initial conditions, namely the inclusion of supersonic or near-supersonic turbulence determines the disk formation for a given strength of the magnetic field. However, no large Keplerian disks with radii > 100 AU were found in those simulations, even in very massive cores. Using realistic initial conditions extracted from larger scales in GMCs with different initial magnetization, we also find that the controversy surrounding the timescale for magnetic braking and the critical μ value suppressing disk formation can be attributed to the turbulent and incoherent nature of magnetic fields in turbulent cores/toroids. In Figure 5.8, we plot the distribution of the toroidal and poloidal components of the magnetic field, B_ϕ and B_r, as a function of the distance to the disk centre for core μ3Ma7hires. We can see that while the azimuthal component of the magnetic field is mostly directional, the radial component, on the other hand, evenly scatters around zero. The radial component B_r is extremely turbulent and the turbulent velocity rms is roughly of equal strength with respect to the median velocity and the velocity rms of the azimuthal component (Figure 5.9). Consequently, the magnetic torque, proportional to $B_r B_\phi$, also scatters around zero. This results in the torque exerted on the gas cancelling itself out, greatly weakening the magnetic braking effect. This reduction of roughly a factor of ten of the torque increases the braking timescale $t_{\rm bf}$ by the same factor, ultimately influencing the longevity and stability of the disks.

As demonstrated by Figure 5.9, showing the radial profile of the mean and rms of B_ϕ, $B_{\rm r}$ and $B_{\rm r} B_\phi$ for three cores in Table 5.1, this incoherent character of the magnetic field does not depend on the initial turbulence of the GMC, which ranges from $\mathcal{M} = 7$ to 15, nor on the magnetic strength, which ranges from marginally-supercritical to critical ($1 < \mu < 3$). Disk μ1Ma15 has the strongest magnetic strength (lowest μ) in the disk and also the smallest degree of turbulence-induced weakening of the magnetic braking effect among the three disks inspected. We have also performed a resolution study, presented in Appendix C.2, to rule out resolution

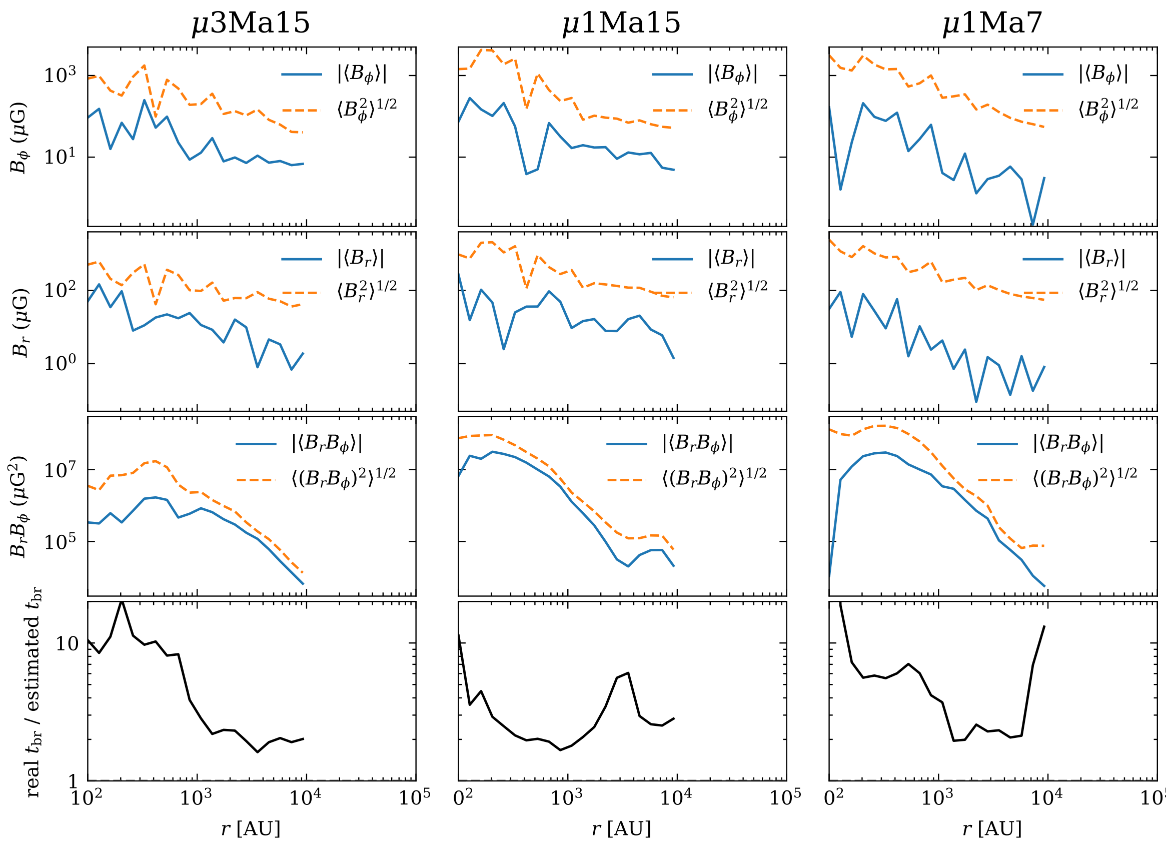

Figure 5.9: The extremely turbulent and incoherent magnetic field on the circumstellar disks as a solution to the magnetic braking problem. The columns from left to right are disks μ3Ma15, μ1Ma15, and μ1Ma7, respectively. Top row: the mean and standard deviation of the azimuthal component of the B field as a function of the cylindrical radius. Second row: the mean and standard deviation of the radial component of the B field. Third row: the mean and standard deviation of the products of the azimuthal and radial components of the B field. Bottom row: The ratio of the magnetic braking time, $t_{\rm br} \propto |\langle B_r B_\phi\rangle|^{-1}$, to the naive estimation, proportional to $\langle (B_r B_\phi)^2\rangle^{-1/2} \approx \langle B^2\rangle^{-1}$.

effects as cause for the formation of large disks.

5.3.5 Evidence for Magnetically-Driven Winds

Protostellar outflows, which are streams of gas emitted from young, low-mass protostars, have been the subject of many studies in recent years (Arce & Shepherd, 2007; Bally, 2016). The outflows are of great interest to astrophysicists because they are believed to play a significant role in star formation, shaping the structure and composition of the interstellar medium.

Our simulations have revealed the ejection of neutral gas from one of the poles of the circumstellar disk, as shown in Figure 5.10. We believe that this outflow is caused by strong magnetic tension or pressure gradients, which are captured by our MHD simulations even though we do not include a sub-grid model for protostellar outflows. Magnetically-driven outflows with velocities of a few km/s specifically occur at the low-density poles of the disk where the plasma beta is extremely low, indicating that the magnetic pressure is much stronger than the thermal pressure. This provides strong evidence for the existence of magnetically-driven winds around young protostars, which are thought to be driven by the conversion of gravitational energy into magnetic and kinetic energy (Bontemps et al., 1996). This process contributes to driving the outflow through magnetic pressure or magneto-centrifugal forces around the circumstellar disk.

Overall, our simulations provide valuable insights into the formation and evolution of young protostars and the role of magnetic fields in these processes. Further research and observations will be needed to fully understand the complex interplay between magnetic fields, gravitational energy, and the evolution of young protostars.

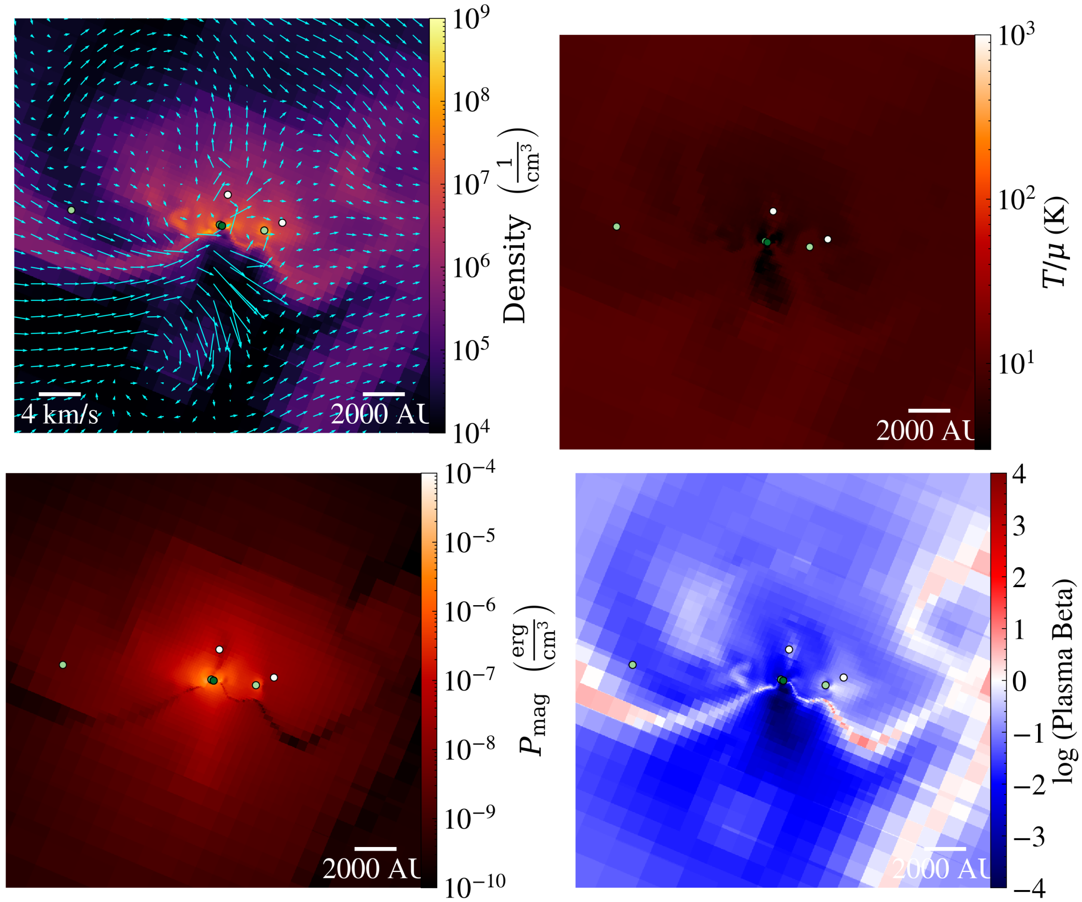

Figure 5.10: Demonstration of magnetically driven outflow from the disk μ3Ma7-hires, also shown in Figure 5.3. (Top left): a density slice extracted from an edge-on view of the disk through its center, with overplotted velocity field. The vectors show the direction of gas velocity, and their length indicates the magnitude with a scale bar shown at bottom left of the panel. The circles mark the positions of stars. The colors of the circles, from white to dark green, correspond to their masses from 0.1 $\mathrm{M}_\odot$ to 10 $\mathrm{M}_\odot$ in log scale. (Top right): gas temperature divided by mean molecular weight T/μ. (Bottom left): magnetic pressure. (Bottom right): plasma beta $\beta = p_{\mathrm{th}}/p_{\mathrm{mag}}$. The outflow is driven by the magnetic force at the poles where the density, temperature and thermal pressures are low, while the plasma beta is extremely small indicating dominance of magnetic pressure over thermal pressure by 3 to 4 orders of magnitude.

5.4 Summary

We have studied the collapse of strongly magnetized prestellar cores from a set of zoom-in radiation-MHD simulations of star formation in GMCs. The study includes a suite of six simulations of prestellar cores in molecular clouds with varying magnetization ($\mu_0 = 3, 1, 0.6$) and turbulence ($\mathcal{M} = 15, 7$). We come to the following main conclusions:

1. We find a universal B-ρ relationship, $B \approx 86\ \mu\mathrm{G}(n/10^5\ \mathrm{cm}^{-3})^{\frac{1}{2}}$, for number density in the range between $10^5\ \mathrm{cm}^{-3}$ and $10^9\ \mathrm{cm}^{-3}$ in the evolution of magnetically critical or marginally super-critical GMCs, regardless of the initial magnetic intensity or cloud size (see Figure 5.5).

2. Magnetic fields at a given density are enhanced by up to 10 times in the highest density gas near the protostar when the protostar forms and accretes gas from the environment (see Figure 5.6).

3. Keplerian circumstellar disks can form in critical and supercritical cores. Subcritical cores, however, fragment into numerous low-mass clumps that undergo direct collapse without any accretion, causing the absence of circumstellar disks (Figure 5.2).

4. Large disks can form in magnetically (near-)critical cores because the magnetic field is extremely turbulent and incoherent, which reduces the effect of magnetic braking by roughly one order of magnitude (see Figure 5.9).

5. The cores at the initial phase are near critical with μ ranging between 0.6 and 2 (Figure 5.7). The cores are initially supported by magnetic pressure, while thermal and turbulent pressures are sub-dominant. The disks that form in the cores are supported by both turbulent and magnetic

pressure, with the former slightly dominating in the inner part ($\lesssim 1000$ AU) and the latter slightly dominating in the outer part. Thermal support is negligible.

6. Although our model does not have a sub-grid recipe for protostellar outflow, our simulations have revealed magnetically-driven outflow of neutral gas from the poles of the circumstellar disk (Figure 5.10) where the plasma beta is extremely low.

Despite the success of our model in reproducing some key features of circumstellar disk formation, we acknowledge that it has known limitations. For instance, we do not account for the effects of protostellar outflow/jet feedback, radiation pressure, and radiative heating by low-energy photons on disk evolution. These feedback mechanisms could significantly alter the disk structure and dynamics. In future work, we plan to incorporate more realistic stellar feedback prescriptions in our code to overcome these limitations and improve the accuracy of our circumstellar disk models.

Chapter 6: A Fast and Accurate Analytic Method of Calculating Galaxy Two-point Correlation Functions

In this chapter, we present a new analytic method to calculate the galaxy two-point correlation functions (TPCFs) accurately and efficiently, applicable to surveys with finite, regular, and mask-free geometries. We have derived simple, accurate formulas of the normalized random-random pair counts RR as functions of the survey area dimensions. We have also suggested algorithms to compute the normalized data-random pair counts DR analytically. With all edge corrections fully accounted for analytically, our method computes RR and DR with perfect accuracy and zero variance in $O(1)$ and $O(N_{\mathrm{g}})$ time, respectively. We test our method on a galaxy catalogue from the EAGLE simulation. Our method calculates $RR+DR$ at a speed 3 to 6 orders of magnitude faster than the brute-force Monte Carlo method and 2.5 orders of magnitude faster than tree-based algorithms. For a galaxy catalogue with 10 million data points in a cube, this reduces the computation time to under 1 minute on a laptop. Our analytic method is favored over the traditional Monte Carlo method whenever applicable. Some applications in the study of correlation functions and power spectra in cosmological simulations and galaxy surveys are discussed. However, we recognize that its applicability is very limited for realistic surveys with masks, irregular shapes, and/or weighted patterns.

6.1 Introduction

The two-point correlation function (TPCF) $\xi(r)$ has been the primary tool for quantifying large-scale cosmic structures (Peebles, 1980). $\xi(r)$ is defined as the fractional increase relative to a random Poisson distribution in the probability δP of finding objects in two volume elements δV_1 and δV_2 separated by distance r:

$$\delta P = [1 + \xi(r)]n^2 dV_1 dV_2, \tag{6.1}$$

where n is the mean number density of objects (galaxies or dark matter halos).

The Fourier transform of $\xi(r)$ is the galaxy power spectrum, which is often used to describe the structure of the Universe (Peebles, 1980). Starting from Eisenstein et al. (2005), $\xi(r)$ has become a popular tool for the detection of the galaxy clustering signal at 150 Mpc known as the baryon acoustic oscillations. It is a signature of the density difference that arose from the first million years of the Universe.

Given a survey or simulation containing the 3D coordinates of all galaxies, the most straightforward way to estimate $\xi(r)$ is to take the ratio of the number of data-data pairs, DD, to that expected from a random distribution in the same area, the random-random pair counts RR, properly normalized, minus one:

$$\xi_0(r) = \frac{\widehat{DD}}{\widehat{RR}} - 1. \tag{6.2}$$

This is known as the natural estimator. Other estimators involving cross-pair separation count DR between the data set and random set have been proposed to reduce the estimation variance, notably induced by edge effects. The Landy-Szalay estimator (Landy & Szalay, 1993),

$$\xi_{\text{LS}}(r) = \frac{\widehat{DD} - 2\,\widehat{DR} + \widehat{RR}}{\widehat{RR}}, \tag{6.3}$$

is the most commonly used estimator because it has minimal variance and converges to the direct estimate the fastest (Kerscher et al., 2000).

For surveys with non-periodical boundary conditions, it is a common practice to measure the average available bin using Monte Carlo integration, by generating a comparison random distribution of a large number of points over the same survey area. To reduce statistical fluctuations, it is standard to use densely populated random fields, usually 50 times denser than the survey population. Because the number of computations needed to measure the separations between N objects scales as N^2, the random-random pair counts RR dominates the computing time. For a large survey or simulation, especially, the computation of RR can be extremely time-consuming.

Tree-based algorithms and codes exist that are much faster than the brute-force method (Moore et al., 2001; Jarvis et al., 2004; Zhang & Pen, 2005). TreeCorr, for instance, is a widely used tree-based code that computes TPCFs in $O(N \log N)$ time (Jarvis et al., 2004). This improvement in speed, however, comes with a sacrifice in accuracy. As pointed out in Siewert et al. (2020), TreeCorr shows noticeable errors in the computation of angular correlation function under any setting that has a significant advantage in speed. Computationally efficient approaches to calculating TPCFs have also been proposed (Demina et al., 2018; Keihänen et al., 2019). However, they reply on a populated random catalogue and their efficiency and accuracy are limited.

The random-random pair counts $\widehat{RR}\ (r)$ is a purely geometrical quantity that depends only on the geometry of the galaxy catalogue and the radial selection function in the case of cosmological survey. The data-random pair counts $\widehat{DR}(r)$ is also a well-defined quantity given a galaxy population in a given geometry. However, analytic methods of estimating pair counts that apply to finite geometries are very sparse in the literature, with only two such works found to our best knowledge. Demina et al. (2018) developed a semi-analytic method to compute RR and DR in two of the three dimensions, but still using a random catalogue to account for angular correlations. Breton & de la Torre (2021) proposed a method to estimate the angular pair counts based on analytic integral expressions. This scheme, however, relies on conducting numerical integrations of terms including the angular selection function over the full sky, which is non-trivial for surveys in subregions of the sky or surveys with masks.

In this chapter, we derive analytic formulas of $\widehat{RR}(r)$ with simple closed-form expressions and analytic algorithms of $\widehat{DR}(r)$ with perfect accuracy and zero variance, applicable to mask-free surveys with regular geometries. [1] We apply these formulas and algorithms to a mock galaxy catalogue from the EAGLE simulation (McAlpine et al., 2016) and assess the accuracy and speed of the method compared to traditional methods that utilize random catalogues.

The remainder of this chapter is organized as follows. In Section 6.2 we derive analytic formulas of $\widehat{RR}(r)$ for four groups of survey geometries. In Section 6.3 we estimate the fractional corrections on $\widehat{RR}(r)$ caused by edge corrections. In Section 6.4 we present algorithms to compute $\widehat{DR}(r)$ analytically. We compare our analytic method with the traditional Monte Carlo method in Section 6.5, followed by summaries and discussions in Section 6.6.

[1] A code written in Python is published (doi:10.5281/zenodo.5201479), as developed on `https://github.com/chongchonghe/analytic-2pcf/tree/v1.0.0`.

6.2 Analytic Formulas of $\widehat{RR}$

We start with deriving formulas of the random-random pair counts $\widehat{RR}\ (r)$ of a mask-free survey with boundaries, taking into account all edge corrections. The survey geometries we consider here are rectangles, cuboids, circles, and spheres. For each case, we first compute the bulk random-random pair counts ignoring any edge effects. Then we do edge corrections, excluding the pairs where the second data point is outside of the survey region. This method of calculating $\widehat{RR}$ is equivalent to the Monte Carlo method with infinite number of random points. With all done analytically, this algorithm of computing $\widehat{RR}\ (r)$ has $O(1)$ scaling, i.e., it does not scale with the number of data points at all.

It is necessary to point out that the number of random-random pair counts from r to $r + dr$ is $\widehat{RR}\ (r)dr$. One would need to integrate $\widehat{RR}\ (r)$ over r from r_1 to r_2 in order to get a bined $\widehat{RR}\ (r)$.

6.2.1 Rectangles

In the first geometry, we consider a rectangular region with sides a and b. We compute $\widehat{RR}$ (r) in three steps where we take care of 1) the whole region ignoring boundaries, 2) corrections of the edges, and 3) corrections of the corners.

In step I, we consider all possible pairs where the first object is drawn inside the rectangle. The number of such pairs with separations between r and $r + dr$ is simply

$$\Theta_{\mathrm{I}}(r)\ dr = (ab)(2\pi r)n^2\ dr = 2\pi abrn^2\ dr, \tag{6.4}$$

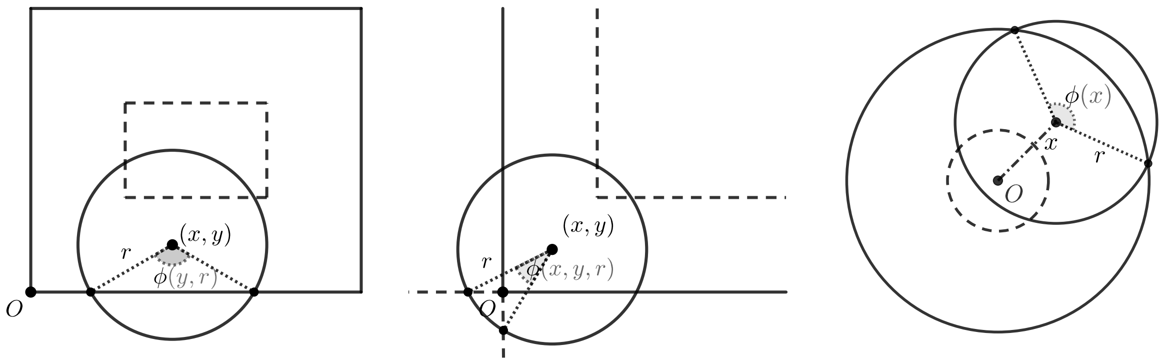

Figure 6.1: Diagrams showing edge corrections in the calculation of random-random and data-random pair counts. From left to right are corrections of the edges of a rectangle, the corners of a rectangle, and the edges of a circle. Cuboids and spheres are similar.

where n is the number density of objects. For simplicity, the dr is omitted on both sides of the formula for the rest of this article.

In step II, we exclude all the pairs where the second point is in either $x < 0$, or $x > a$, or $y < 0$, or $y > b$. The number of such pairs for $y < 0$ is

$$\Theta_{\mathrm{II,y<0}}(r) = \int_0^r dy\ \phi(y) arn^2 = 2ar^2n^2, \tag{6.5}$$

where

$$\phi(y) = 2\cos^{-1}(\frac{y}{r}) \tag{6.6}$$

is the angle of the arc at $y < 0$ (Fig. 6.1, left). Similarly,

$$\Theta_{\mathrm{II,y>b}}(r) = 2ar^2n^2, \tag{6.7}$$

$$\Theta_{\mathrm{II,x<0}}(r) = 2br^2n^2, \tag{6.8}$$

$$\Theta_{\mathrm{II,x>a}}(r) = 2br^2n^2. \tag{6.9}$$

The total number of pairs to exclude in this step is therefore

$$\Theta_{\mathrm{II}}(r) = \Theta_{\mathrm{II,x<0}}(r) + \Theta_{\mathrm{II,x>a}}(r) + \Theta_{\mathrm{II,y<0}}(r) + \Theta_{\mathrm{II,y>b}}(r) = 4(a+b)r^2n^2. \tag{6.10}$$

In step III, we add back the pairs that are excluded twice. These are the pairs where the second object is either $x < 0$ & $y < 0$, or $x > a$ & $y < 0$, or $x < 0$ & $y > b$, or $x > a$ & $y > b$. The number of pairs in these four cases is all identical and their total is given by

$$\Theta_{\mathrm{III}}(r) = 4 \int_0^r dx \int_0^{\sqrt{r^2-x^2}} dy\, \phi(x,y)r = 2r^3n^2, \tag{6.11}$$

where

$$\phi(x,y) = \frac{\pi}{2} - \sin^{-1}\frac{x}{r} - \sin^{-1}\frac{y}{r}, \tag{6.12}$$

is the angle of the arc at $x < 0$ & $y < 0$ (Fig. 6.1, center).

Finally, combining steps I, II, and III, the total number of valid random-random pairs for the rectangular field with sides a and b and object density n is given by

$$\Theta(r) = \Theta_{\mathrm{I}} - \Theta_{\mathrm{II}} + \Theta_{\mathrm{III}} \tag{6.13}$$

$$= \left[2\pi abr - 4(a+b)r^2 + 2r^3\right] n^2, \tag{6.14}$$

The normalized random-random pair count is therefore

$$\widehat{RR}_{\mathrm{rect}}\,(r) = \frac{\Theta(r)}{(abn)^2} = \frac{2\pi}{ab}r - \frac{4(a+b)}{a^2b^2}r^2 + \frac{2}{a^2b^2}r^3, \tag{6.15}$$

for $r \leq a \leq b$. The antiderivative is given below for an easy calculation of its integration over r.

$$\mathcal{F}[\widehat{RR}_{\text{rect}}\ (r)] = \frac{\pi}{ab}r^2 - \frac{4(a+b)}{3a^2b^2}r^3 + \frac{1}{2a^2b^2}r^4. \tag{6.16}$$

In a special case where $a = b$, Eq. (6.15) becomes

$$\widehat{RR}_{\text{square}}\ (r) = \frac{2\pi}{a^2}r - \frac{8}{a^3}r^2 + \frac{2}{a^4}r^3. \tag{6.17}$$

We further discuss the situation when $a < r \leq b$. In this case, Θ_{I} is unchanged. In the calculation of Θ_{II}, integrations over y is unchanged and yield $4ar^2n^2$. In the integration over x, however, the upper limit of the integral in Eq. (6.5) needs to be replaced by a. Summing up, it yields

$$\Theta_{\text{II}}(r) = \left[4ar^2 + 4br\left(r - \sqrt{r^2 - a^2} + a\cos^{-1}\frac{a}{r}\right)\right]n^2. \tag{6.18}$$

In Θ_{III}, similarly, the upper limit in the first integral needs to be changed to a in the integration over x, yielding

$$\Theta_{\text{III}}(r) = \left[1 + (2 - \frac{a}{r})\frac{a}{r}\right]r^3n^2. \tag{6.19}$$

Adding together and conducting normalization, we find

$$\widehat{RR}_{\text{rect}}\ (r) = \frac{2\pi}{ab}r - \frac{4a + 4b\left(1 - \sqrt{1 - (\frac{a}{r})^2} + \frac{a}{r}\cos^{-1}\frac{a}{r}\right)}{a^2b^2}r^2 + \frac{1 + \left(2 - \frac{a}{r}\right)\frac{a}{r}}{a^2b^2}r^3 \tag{6.20}$$

for $a < r \leq b$.

6.2.2 Cuboids

Now we consider a cuboid in 3D space with sides a, b, and c. We calculate $\widehat{RR}\,(r)$ in four steps where we take care of 1) the whole region ignoring edge effects, 2) corrections from the faces, 3) corrections from the edges, and 4) corrections from the corners.

In step I, consider all possible pairs where the first point is inside, ignoring any edge effects,

$$\Theta_{\mathrm{I}}(r) = (abc)(4\pi r^2)n^2 = 4\pi abcr^2n^2. \tag{6.21}$$

In step II, we exclude the pairs where the second point is outside one of the faces of the cuboid. There are a total of 6 cases, corresponding to the 6 faces of a cuboid. Two of them are related to the particle being outside of the x dimension, either $x < 0$ or $x > a$. The number of such pairs is

$$\Theta_{\mathrm{II},x}(r) = 2\int_0^a dx\,\Omega(x)bcr^2n^2 = 2\pi bcr^3n^2, \tag{6.22}$$

where

$$\Omega(x) = 2\pi\left(1 - \frac{x}{r}\right) \tag{6.23}$$

is the solid angle of the area outside of one face. Other terms related to y and z axis are obtained by simply replacing bc with ac or ab. Therefore,

$$\Theta_{\mathrm{II}} = \Theta_{\mathrm{II},x} + \Theta_{\mathrm{II},y} + \Theta_{\mathrm{II},z} = 2\pi(ab + ac + bc)r^3n^2. \tag{6.24}$$

In step III, we include back those pairs that are counted at least twice in step II. Those are the pairs where the second point is outside of the domain of two of the three axes. There are a total of 12 cases, corresponding to the 12 edges of a cuboid. The four cases related to x and y are identical. Here we focus on the case where $x < 0$ & $y < 0$,

$$\frac{1}{4}\Theta_{\mathrm{III},xy}(r) = \int_0^r dx \int_0^{\sqrt{r^2-x^2}} dy\, c\, \Omega(\frac{x}{r}, \frac{y}{r}) r^2 n^2 = \int_0^1 dx \int_0^{\sqrt{1-x^2}} dy\, \Omega(x,y)\, c\, r^4 n^2 \quad (6.25)$$

where $\Omega(x, y)$ is the solid angle of the area on a unit sphere $\mathrm{Sph}(x', y', z')$ with $x' > x$, $y' > y$ for positive x and y with $x^2 + y^2 < 1$.

It can be shown that the surface area of a constant latitude strip on a sphere between two longitudes is simply $R\Delta z \Delta l$, where Δz and Δl are the differences on the cylindrical height and on the longitudes, respectively. Using this fact, we can express the solid angle as

$$\Omega(x, y) = \int_y^{\sqrt{1-x^2}} dy'\; 2\cos^{-1}\frac{x}{\sqrt{1-y'^2}}. \quad (6.26)$$

plugging into Eq. (6.25) gives

$$\frac{\Theta_{\mathrm{III},xy}(r)}{4cr^4n^2} = \int_0^1 dx \int_0^{\sqrt{1-x^2}} dy \int_y^{\sqrt{1-x^2}} dy' 2\cos^{-1}\frac{x}{\sqrt{1-y'^2}} \quad (6.27)$$

$$= \int_0^1 dx \int_0^{\sqrt{1-x^2}} dy' \int_0^{y'} dy\; 2\cos^{-1}\frac{x}{\sqrt{1-y'^2}} \quad (6.28)$$

$$= \int_0^1 dx \int_0^{\sqrt{1-x^2}} dy'\; y' 2\cos^{-1}\frac{x}{\sqrt{1-y'^2}} \quad (6.29)$$

$$= \int_0^1 dy' \int_0^{\sqrt{1-y'^2}} dx\; y' 2\cos^{-1}\frac{x}{\sqrt{1-y'^2}} \quad (6.30)$$

$$= \int_0^1 dy'\; y' 2\sqrt{1-y'^2} \quad (6.31)$$

$$= \frac{2}{3}, \quad (6.32)$$

where we swapped the order of y and y' integration in step 1 and swapped the order of x and y' integration in step 3. Here we have found $\Theta_{\mathrm{III},xy}(r) = 8\, c\, r^4 n^2/3$. Similarly, other terms related to x and z or to y and z is simply obtained by replacing c with b or a. Therefore,

$$\Theta_{\mathrm{III}} = \frac{8}{3}(a+b+c)r^4 n^2. \tag{6.33}$$

In step IV, we exclude those that are overlapped in step III. Those are the pairs where the second point is outside of the domain in all three axes. There are a total of 8 identical cases, corresponding to the 8 corners of a cuboid. Here we focus on the case where $x < 0$ & $y < 0$ & $z < 0$.

$$\begin{aligned}
\frac{1}{8}\Theta_{\mathrm{IV}}(r) &= \int_0^r dx \int_0^{\sqrt{r^2-x^2}} dy \int_0^{\sqrt{r^2-x^2-y^2}} dz\, \Omega(\frac{x}{r}, \frac{y}{r}, \frac{z}{r})\, r^2 n^2 \\
&= \int_0^1 dx \int_0^{\sqrt{1-x^2}} dy \int_0^{\sqrt{1-x^2-y^2}} dz\, \Omega(x, y, z)\, r^5 n^2,
\end{aligned} \tag{6.34}$$

where $\Omega(x, y, z)$ is the area on a unit sphere Sph(x', y', z') with $x' > x$, $y' > y$, $z' > z$ for positive x, y, and z with $x^2 + y^2 + z^2 < 1$.

Following the same logic of Eq. (6.26), we have

$$\Omega(x, y, z) = \int_z^{\sqrt{1-x^2-y^2}} dz' \left(\cos^{-1} \frac{x}{\sqrt{1-z'^2}} - \sin^{-1} \frac{y}{\sqrt{1-z'^2}} \right) \tag{6.35}$$

Plugging into Eq. (6.34) and we get

$$\frac{\Theta_{\mathrm{IV}}(r)}{8r^5n^2} = \int_0^1 dx \int_0^{\sqrt{1-x^2}} dy \int_0^{\sqrt{1-x^2-y^2}} dz \int_z^{\sqrt{1-x^2-y^2}} dz' \left(\cos^{-1}\frac{x}{\sqrt{1-z'^2}} - \sin^{-1}\frac{y}{\sqrt{1-z'^2}}\right) \tag{6.36}$$

$$= \int_0^1 dx \int_0^{\sqrt{1-x^2}} dy \int_0^{\sqrt{1-x^2-y^2}} dz' \int_0^{z'} dz \left(\cos^{-1}\frac{x}{\sqrt{1-z'^2}} - \sin^{-1}\frac{y}{\sqrt{1-z'^2}}\right), \tag{6.37}$$

where we have swapped the order of z and z' integration. Perform the integration on z and rename z' to z for notational simplicity

$$\frac{\Theta_{\mathrm{IV}}(r)}{8r^5n^2} = \int_0^1 dx \int_0^{\sqrt{1-x^2}} dy \int_0^{\sqrt{1-x^2-y^2}} dz\, z \left(\cos^{-1}\frac{x}{\sqrt{1-z^2}} - \sin^{-1}\frac{y}{\sqrt{1-z^2}}\right). \tag{6.38}$$

Noticing that x, y, z are integrated over an octant, we swap the order to put z on the outside

$$\frac{\Theta_{\mathrm{IV}}(r)}{8r^5n^2} = \int_0^1 dz \int_0^{\sqrt{1-z^2}} dx \int_0^{\sqrt{1-x^2-z^2}} dy\, z \left(\cos^{-1}\frac{x}{\sqrt{1-z^2}} - \sin^{-1}\frac{y}{\sqrt{1-z^2}}\right). \tag{6.39}$$

Perform variable change $u = x/\sqrt{1-z^2}$, $v = y/\sqrt{1-z^2}$, and move forward

$$\frac{\Theta_{\mathrm{IV}}(r)}{8r^5n^2} = \int_0^1 dz \int_0^1 du \int_0^{\sqrt{1-u^2}} dv\; z(1-z^2)(\cos^{-1}u - \sin^{-1}v) \tag{6.40}$$

$$= \int_0^1 dz\; z(1-z^2) \int_0^1 du \int_0^{\sqrt{1-u^2}} dv(\cos^{-1}u - \sin^{-1}v) \tag{6.41}$$

$$= \int_0^1 dz\; z(1-z^2) \int_0^1 du\; (1-u) \tag{6.42}$$

$$= \int_0^1 dz\; z(1-z^2)\, \frac{1}{2} \tag{6.43}$$

$$= \frac{1}{8}. \tag{6.44}$$

Therefore,

$$\Theta_{\mathrm{IV}}(r) = r^5n^2. \tag{6.45}$$

Finally, combining steps I, II, III, and IV, the total number of valid random-random pairs for the cuboidal region with sides a, b, and c and object density n is given by

$$\Theta(r) = \Theta_{\mathrm{I}} - \Theta_{\mathrm{II}} + \Theta_{\mathrm{III}} - \Theta_{\mathrm{IV}} = \left[4\pi abcr^2 - 2\pi(ab+ac+bc)r^3 + \frac{8}{3}(a+b+c)r^4 - r^5\right] n^2. \tag{6.46}$$

The normalized random-random pair count is therefore

$$\widehat{RR}_{\mathrm{cuboid}}\,(r) = \frac{\Theta(r)}{(abcn)^2} = \frac{4\pi}{abc}r^2 - \frac{2\pi(ab+ac+bc)}{a^2b^2c^2}r^3 + \frac{8}{3}\frac{a+b+c}{a^2b^2c^2}r^4 - \frac{1}{a^2b^2c^2}r^5, \tag{6.47}$$

for $r \leq \min(a,b,c)$. The antiderivative is given below for an easy calculation of its integration over r.

$$\mathcal{F}[\widehat{RR}_{\text{cuboid}}\,(r)] = \frac{4\pi}{3abc}r^3 - \frac{\pi(ab+ac+bc)}{2a^2b^2c^2}r^4 + \frac{8}{15}\frac{a+b+c}{a^2b^2c^2}r^5 - \frac{1}{6a^2b^2c^2}r^6. \tag{6.48}$$

In a special case where $a = b = c$, Eq. (6.47) becomes

$$\widehat{RR}_{\text{cuboid}}\,(r) = \frac{4\pi}{a^3}r^2 - \frac{6\pi}{a^4}r^3 + \frac{8}{a^5}r^4 - \frac{1}{a^6}r^5. \tag{6.49}$$

6.2.3 Circles

Now we consider a circle in 2D space. Without loss of generality, we assume the radius of the circle is unity. The calculation of $\widehat{RR}\,(r)$ is done in two steps where we take care of the whole region ignoring boundaries and then make corrections from the edge.

In step I, consider all possible pairs where the first point is inside the circle and ignore edge effects. The number of pairs separated by r is given by

$$\Theta_{\text{I}}(r) = \pi 1^2\; 2\pi r\; n^2 = 2\pi^2 r n^2. \tag{6.50}$$

In step II, we exclude the pairs where the second point is outside of the circle. The number of such pairs is given by the following integral

$$\Theta_{\text{II}}(r) = \int_{1-r}^{1} dx\; 2\pi x \phi(x) r n^2, \tag{6.51}$$

where

$$\phi(x) = 2\cos^{-1}\frac{1-x^2-r^2}{2xr} \tag{6.52}$$

is the angle of the arc outside of the circle (Fig. 6.1, right). Substituting it into Eq. (6.51) gives

$$\Theta_{\mathrm{II}}(r) = \left(\pi r^2\sqrt{4-r^2} + 4\pi r\sin^{-1}\frac{r}{2}\right)n^2 \tag{6.53}$$

Combining steps I and II, the total number of valid random-random pairs for a unitary circular region with object density n is given by

$$\Theta(r) = \Theta_{\mathrm{I}}(r) - \Theta_{\mathrm{II}}(r) = \left(2\pi^2 r - \pi r^2\sqrt{4-r^2} - 4\pi r\sin^{-1}\frac{r}{2}\right)n^2, \tag{6.54}$$

and the normalized random-random pair count,

$$\widehat{RR}_{\mathrm{circ}}(r) = \frac{\Theta(r)}{(\pi\cdot 1^2\cdot n)^2} = 2r - \frac{1}{\pi}r^2\sqrt{4-r^2} - \frac{4}{\pi}r\sin^{-1}\frac{r}{2}, \tag{6.55}$$

for $r \le 1$. The antiderivative is given below for an easy calculation of its integration over r.

$$\mathcal{F}[\widehat{RR}_{\mathrm{circ}}(r)] = r^2 - \frac{1}{4\pi}\sqrt{4-r^2}\left(r^2+2\right)r + \frac{2}{\pi}\left(1-r^2\right)\sin^{-1}\frac{r}{2}. \tag{6.56}$$

6.2.4 Spheres

In the final one of the four geometries, we consider a unit sphere. We calculate $\widehat{RR}(r)$ in two steps where we take care of the whole region ignoring boundaries and then make corrections from its edge.

In step I, we consider all possible pairs where the first point is inside the circle and ignore edge effects. The number of pairs separated by r is given by

$$\Theta_{\mathrm{I}}(r) = \frac{4\pi}{3} 1^3 4\pi r^2 n^2 = \frac{16\pi^2}{3} r^2 n^2. \tag{6.57}$$

In step II, we exclude the pairs where the second point is outside of the unit sphere. The number of such pairs is

$$\Theta_{\mathrm{II}}(r) = \int_{1-r}^{1} dx\; 4\pi x^2 \Omega(x) r^2 n^2 = \left(4\pi^2 r^3 - \frac{\pi^2}{3} r^5\right) n^2, \tag{6.58}$$

where

$$\Omega(x) = \left(1 + \frac{x^2 + r^2 - 1}{2xr}\right) 2\pi \tag{6.59}$$

is the solid angle of the area on a sphere of radius r that is outside of the unit sphere.

Combining step I and step II, the total number of valid random-random pairs for the unitary spherical region with object density n is given by

$$\Theta(r) = \Theta_{\mathrm{I}} - \Theta_{\mathrm{II}} = \left(\frac{16\pi^2}{3} r^2 - 4\pi^2 r^3 + \frac{\pi^3}{3} r^5\right) n^2, \tag{6.60}$$

and the normalized random-random pair count,

$$\widehat{RR}_{\mathrm{sph}}\,(r) = \frac{\Theta(r)}{\left(\frac{4\pi}{3} n\right)^2} = 3r^2 - \frac{9}{4} r^3 + \frac{3}{16} r^5, \tag{6.61}$$

Table 6.1: Percentage errors $\epsilon(\hat{r})$ of the calculated $\widehat{RR}\,(\hat{r})$ when certain edge corrections are not included. It is shown that all corrections in the rectangular, circular, and spherical cases must be considered in order to limit the relative error to sub-percent. For the cuboidal case, however, the corner correction causes at most sub-percent changes (highlighted) to the calculated $\widehat{RR}$ at all radii.

Field geometry	**Corrections included**	$\epsilon(0.001)$	$\epsilon(0.01)$	$\epsilon(0.1)$	$\epsilon(0.2)$	$\epsilon(0.4)$
Rectangle	None	0.13	1.3	14	32	85
	Edge	-3.2e-05	-0.0032	-0.36	-1.7	-9.4
	Edge + Corner	0	0	0	0	0
Cuboid	None	0.15	1.5	17	38	100
	Face	-6.4e-05	-0.0065	-0.73	-3.4	-19
	Face + edge	**8e-09**	**8.1e-06**	**0.0093**	**0.088**	**1.0**
	Face + edge + corner	0	0	0	0	0
Circle	None	0.064	0.64	6.8	15	34
	Edge	0	0	0	0	0
Sphere	None	0.075	0.76	8.1	18	42
	Edge	0	0	0	0	0

for $r \le 1$. The antiderivative is given below for an easy calculation of its integration over r.

$$\mathcal{F}[\widehat{RR}_{\text{sph}}\,(r)] = r^3 - \frac{9}{16}r^4 + \frac{1}{32}r^6. \tag{6.62}$$

6.3 Accounting for Edge Corrections in $\widehat{RR}$

The formulas of $\widehat{RR}\,(r)$ derived in this work, Eqs. (6.15), (6.47), (6.55), and (6.61), have included all edge corrections and are precise. However, the calculation of $\widehat{DR}\,(r)$ is more complex because iteration over all data points is required. Given the complexity of the edge-correction formulas, it would be beneficial if some of the terms could be ignored without sacrificing accuracy.

To account for the contributions from various edge effects, we break the formulas of $\widehat{RR}$, Eqs. (6.15), (6.47), (6.55), and (6.61), into various terms based on the powers of r and rewrite them as follow:

$$\widehat{RR}_{\rm rect}\,(r) = \frac{2\pi}{ab} r \left(1 - \frac{2(a+b)}{\pi ab} r + \frac{1}{\pi ab} r^2\right), \tag{6.63}$$

$$\widehat{RR}_{\rm cuboid}\,(r) = \frac{4\pi}{abc} r^2 \left(1 - \frac{ab+ac+bc}{2abc} r + \frac{2}{3\pi}\frac{a+b+c}{abc} r^2 - \frac{1}{4\pi abc} r^3\right), \tag{6.64}$$

$$\widehat{RR}_{\rm circ}\,(r) = 2r \left(1 - \frac{2}{\pi} r + \frac{1}{12\pi} r^3 + \frac{1}{320\pi} r^5 + O(r^7)\right), \tag{6.65}$$

$$\widehat{RR}_{\rm sph}\,(r) = 3r^2 \left(1 - \frac{3}{4} r + \frac{1}{16} r^3\right). \tag{6.66}$$

The 0th, 1st and 2nd-order terms of $\widehat{RR}_{\rm rect}$ correspond to the inside, the edges, and the corners of the rectangle. The 0th, 1st, 2nd, and 3rd-order terms of $\widehat{RR}_{\rm cuboid}$ are the inside, the faces, the edges, and the corners of the cuboid. The 0th-order term of $\widehat{RR}_{\rm circ}$ or $\widehat{RR}_{\rm sph}$ is the inside of the circle or sphere and the other terms are edge correction.

$\widehat{RR}$ are calculated up to various degrees of edge corrections and are compared to its precise values. The fractional errors at a list of radii are listed in Table 6.1. Of all the geometries, unitary sides or radius is assumed. We conclude that in all but the cuboidal case, all the edge-correction terms are necessary in order to limit the errors of $\widehat{RR}\,(r)$ to within 1% at all r. In the cuboidal case, the error caused by ignoring the corner correction is sub-percent even at large r. This latter fact helps to significantly simplify the computation of $\widehat{DR}_{\rm rect}$ in the following section.

6.4 Computing $\widehat{DR}$ Analytically in $O(N_{\rm g})$ Time

The computation of $\widehat{DR}$ requires iterations over all data particles. For a data point away from the edges of the survey area, the number of data-random pairs shared by this data point is simply $2n\pi r dr$ in 2D case or $4n\pi r^2 dr$ for 3D case, where n is the mean number density of the random catalogue. When a data point is close to the edges, corrections are necessary to exclude pairs where the random point is outside.

In the previous section, we have derived various edge-correction terms for the four geometries. In this section, we use those terms to calculate the contribution of each data point to the data-random pair counts with full edge corrections. We work out extra steps of integrating over r for an easy calculation of the edge corrections without numerical integration. The subsequent algorithms to compute the edge-corrected $\widehat{DR}(r)$ in $O(N_\mathrm{g})$ time is presented in Appendix D.1.

6.4.1 Rectangles

For a data point D that is close to any of the edges of a rectangle, a circle around D with radius r has a part outside of the region when $r > y$, where y is the distance from D to the edge. The angle of this arc, $\phi(y)$, is given by Eq. (6.6). The integration of the length of the arc, $\phi(r)r$, over r is therefore

$$\mathcal{F}(r; y) = \int \phi(y) r \, dr = \int 2\cos^{-1}\left(\frac{y}{r}\right) r \, dr = r^2 \cos^{-1}\frac{y}{r} - y\sqrt{r^2 - y^2}. \tag{6.67}$$

When D is close to a corner, i.e., $\sqrt{x^2+y^2} < r$, where x and y are the distances to the two sides, the part of the arc outside of both extended sides are excluded twice in the previous step (see Fig. 6.1, *Center*), therefore we need to include them back. The angle of this arc, $\phi(x, y)$, is given by Eq. (6.12). The integration of the length of the arc, $\phi(r)r$, over r is therefore

$$\mathcal{F}(r; x, y) = \int \phi(x, y) r dr = \frac{1}{4}\left[\pi r^2 - 2x\sqrt{r^2 - x^2} - 2y\sqrt{r^2 - y^2} - 2r^2\left(\sin^{-1}\frac{x}{r} + \sin^{-1}\frac{y}{r}\right)\right] + C \tag{6.68}$$

where $C = xy$ is chosen such that $\mathcal{F}(r; x, y)$ approaches 0 when $r \to \sqrt{x^2 + y^2}$.

Based on Eq. (6.67) and Eq. (6.68), we write an algorithm to compute the data-random pair counts analytically by doing iterations over all data points where the contribution from each data point is calculated 1) as $2\pi r\, dr$ if not touching the edges, or 2) using Eq. (6.67) and Eq. (6.68) it touches at least one of the edges. This algorithm has a time complexity of $O(N_{\rm g})$, where $N_{\rm g}$ is the number of galaxies or particles. The pseudocode is presented in Appendix D.1.

6.4.2 Cuboids

The calculation of Data-Random pair counts in a cuboidal region is similar to that in a rectangular region, with the angle ϕ replaced by a solid angle Ω, plus an extra step to take care of the corners of the cuboid.

For a data point D that is close to any of the faces of a cuboid, the part on a sphere centered at D with radius r that is outside of the cuboid is given by Eq. (6.23), where x is the distance to the edge. The integration of the area of this part, $\Omega(x)r^2$, over r is therefore

$$\mathcal{F}(r; x) = \int \Omega(x) r^2 dr = \int 2\pi(r^2 - xr) dr = 2\pi \left(\frac{r^3}{3} - \frac{xr^2}{2} \right). \tag{6.69}$$

When D is close to one of the edges of the cuboid such that $\sqrt{x^2 + y^2} < r$, where x and y are the distances to two adjacent faces, the part of the sphere outside of both faces are excluded twice in the previous step, therefore we need to include them back. The solid angle of this surface, when assuming $r = 1$, is given by Eq. (6.26), which equals

$$\Omega(x, y) = \left(\frac{1}{2} - x - y \right) \pi + 2x \tan^{-1} \frac{y}{t} + 2y \tan^{-1} \frac{x}{t} + \tan^{-1} \frac{t^2 - x^2 y^2}{2xyt}, \tag{6.70}$$

where $t \equiv \sqrt{1 - x^2 - y^2}$. Replacing x with x/r and y with y/r, we get $\Omega(r; x, y)$. The integration of the area of the surface, $\Omega(r; x, y)r^2$, over r is therefore

$$\begin{aligned}
\mathcal{F}(r; x, y) &= \int \Omega(r; x, y) r^2 dr \\
&= \int \left[\pi\left(\frac{r^2}{2} - rx - ry\right) + 2ry\tan^{-1}\left(\frac{x}{h}\right) + 2rx\tan^{-1}\left(\frac{y}{h}\right) + r^2\tan^{-1}\frac{r^2h^2 - x^2y^2}{2xyrh}\right] dr \\
&= r^2\left(y\tan^{-1}\left(\frac{x}{h}\right) + x\tan^{-1}\left(\frac{y}{h}\right)\right) + \frac{1}{6}\pi r^2(r - 3(x + y)) \\
&\quad + x^3\cot^{-1}\left(\frac{y}{h}\right) + y^3\cot^{-1}\left(\frac{x}{h}\right) + 2xyh \\
&\quad + \frac{x^3}{3}\left[\tan^{-1}\left(\frac{rx + x^2 + y^2}{hy}\right) + \tan^{-1}\left(\frac{-rx + x^2 + y^2}{hy}\right)\right] \\
&\quad + \frac{y^3}{3}\left[\tan^{-1}\left(\frac{ry + x^2 + y^2}{hx}\right) + \tan^{-1}\left(\frac{-ry + x^2 + y^2}{hx}\right)\right] \\
&\quad - \frac{r^3}{3}\tan^{-1}\left(\frac{x^2y^2 - r^2h^2}{2xyrh}\right) \\
&\quad - \frac{4}{3}yxh + C
\end{aligned} \tag{6.71}$$

where $h \equiv \sqrt{r^2 - x^2 - y^2}$ and $C = -\frac{\pi}{3}(x^3 + y^3)$ is chosen such that $\lim_{r \to \sqrt{x^2+y^2}} \mathcal{F}(r; x, y) = 0$, or $\lim_{h \to 0^+} \mathcal{F}(r; x, y) = 0$.

To compute $\widehat{DR}\,(r)$ with perfect accuracy, one would need to take into account the effects of the corners, which is when a sphere around D is outside of three adjacent faces simultaneously. They are included back twice in the previous step and need to be subtracted again. However, this effect is ignored in this work because the computation is too complicated and its contribution is at most sub-percent (Table 6.1).

An algorithm to compute $\widehat{DR}\,(r)$ analytically is presented in Appendix D.1.

6.4.3 Circles

When a data point D is close to the edge of a unitary circular survey region, a circle around D with radius r has a segment outside of the region when $r > 1 - x$, where x is this point's distance to the regional center. The angle of this arc is given by Eq. (6.52). The integration of the length of the arc, $\phi(r)r$, over r is therefore

$$\mathcal{F}(r;x) = \int \phi(x) r dr = \frac{\eta}{2} + r^2 \cos^{-1}\left(\frac{1-r^2-x^2}{2xr}\right) + \sin^{-1}\left(\frac{1-r^2+x^2}{2x}\right) + C, \quad (6.72)$$

where $\eta \equiv \sqrt{(-r+x+1)(r-x+1)(r+x-1)(r+x+1)}$ and $C = -\pi/2$ is chosen such that $\lim_{r\to(1-x)^+} \mathcal{F}(r) = 0$.

An algorithm to compute $\widehat{DR}\,(r)$ analytically is presented in Appendix D.1.

6.4.4 Spheres

When a data point D is close to the edge of a unitary spherical region, a circle around D with radius r has a segment outside of the region when $r > 1-x$, where x is this point's distance to the center of the region. The solid angle of this segment is given by Eq. (6.59). The integration of the surface area of this segment, $\Omega(r)r^2$, over r is therefore

$$\mathcal{F}(r;x) = \int \Omega(x) r^2 dr = \frac{\pi r^2\left(-6+3r^2+8rx+6x^2\right)}{12x}. \quad (6.73)$$

An algorithm to compute $\widehat{DR}\,(r)$ analytically in $O(n)$ time is given in Appendix D.1.

6.5 Comparisons with the Monte Carlo Method

In this section, we compare the accuracy and speed of the analytic method from this work with the Monte Carlo method used in most literature.

The test data set we use is a mock galaxy catalogue inside a $100\ \mathrm{cMpc}$ cube from the `RefL0100N1504_Subhalo` simulation of the EAGLE database (McAlpine et al., 2016). The positions of the galaxies are normalized to a unitary box for simplicity. For the 2D geometries, the third dimension of the positions is removed. For the circular or spherical cases, the box is shifted, normalized, and trimmed to a unit sphere centered at the origin.

We compare the $\xi(r)$ computed using our analytic method with that using a brute-force Monte Carlo code[2] (Fig. 6.2), using both the Natural estimator (left column) and the Landy-Szalay estimator (right column), applying to the four geometries we have discussed. For a quick runtime, we choose 1000 galaxies from the galaxy catalogue and adopt a low random-to-data ratio 16 to make the computation manageable on a laptop. A total of 40 random catalogues are generated to estimate the mean and standard deviation of $\widehat{RR}\ (r)$ and $\widehat{DR}\ (r)$ in 25 separation bins, evenly distributed in logarithmic scale. They are then passed to $\xi(r)$ to estimate its mean (red dots) and standard deviation (errorbars). Our analytic calculation is, by construction, the asymptotic limit of the Monte Carlo calculation as $N_{\mathrm{r}} \to \infty$, hence zero variance.

We observe that the Monte Carlo estimations of $\xi(r)$ have means strictly following the analytic results [3]. The perfect agreement with the Monte Carlo estimations demonstrates the validity of the analytic formulas of $\widehat{RR}$ and the analytic algorithms of $\widehat{DR}$ proposed in this work.

[2] The code we are using is `scipy.spatial.cKDTree`, which is supposed to embrace a tree-based algorithm and have better performance than brute force. However, what we observe is that both its performance and accuracy under default setting are very close to brute force with a scaling close to $O(N^2)$.

[3] The only exception is $\xi_{\mathrm{cuboid}}(r)$ at $r \geq 0.4$. This is caused by the exclusion of corner corrections (Section 6.4.2).

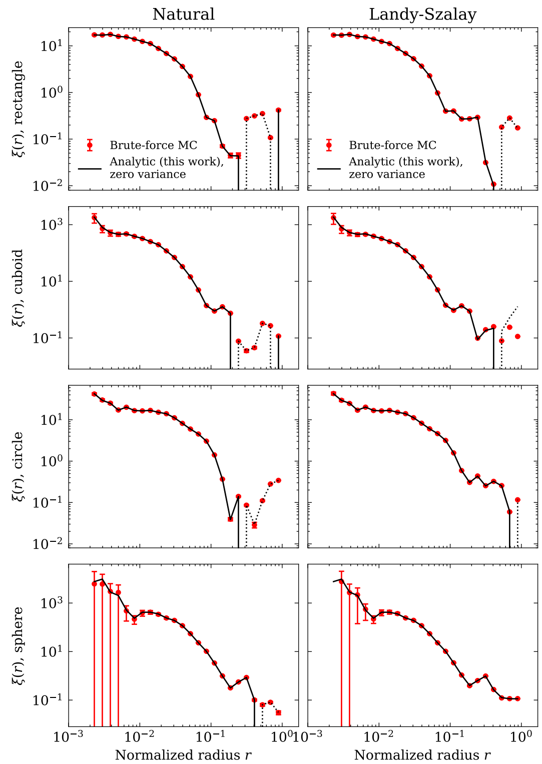

Figure 6.2: Comparing the two-point correlation functions $\xi(r)$ of a mock galaxy population calculated from the analytic method from this work (solid black curve) with that from brute-force Monte Carlo method (red dots and error bars). The former is shown to be the asymptotic limit of the latter as the size of the random catalogue goes to infinity, evident from the fact that the means (red dots) of the brute-force Monte Carlo estimations strictly follow the analytic predictions. The natural estimator, $\xi_0 = \widehat{DD} \ / \ \widehat{RR} - 1$, and the Landy-Szalay estimator, $\xi_{\rm LS} = \widehat{DD} \ / \ \widehat{RR} - 2 \ \widehat{DR} \ / \ \widehat{RR} + 1$, are applied in the left and right panel, respectively. The error bars are the standard deviations estimated from 40 random catalogues. Negative ξ is donated as dotted lines. While the Monte Carlo estimations exhibit significant scattering at small r, the analytic method has zero variance at all scales.

While the brute-force Monte Carlo estimations exhibit significant scattering at small scales, the analytic method has zero variance at all scales.

In practice, the brute-force Monte Carlo method is usually used for accurate computation of the TPCF of a small galaxy catalogue. For large galaxy catagloues, people tend to faster tree-based algorithms with some sacrifice in accuracy. We compare the time it takes to compute $\widehat{RR} \ (r)$ and $\widehat{DR} \ (r)$ using different methods (Fig. 6.3). The brute force Monte Carlo code

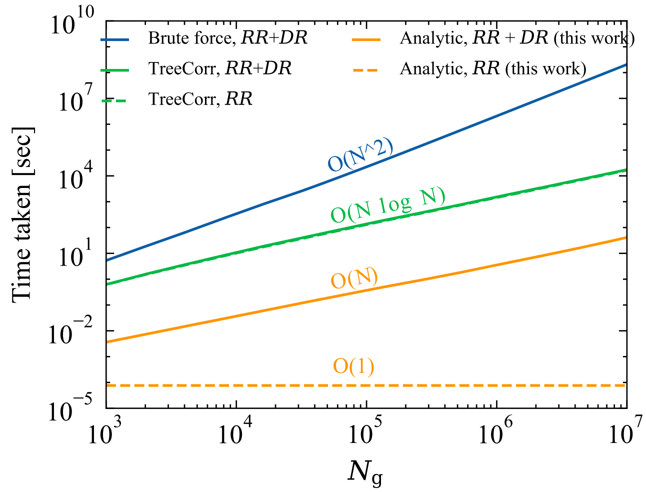

Figure 6.3: Comparing the speed of the analytic approach from this work to that of the traditional Monte Carlo method. The performance of our analytic method is 3 to 6 orders of magnitude higher than the brute force method and 2.5 orders of magnitude higher than a fast tree-based algorithm for sizes of galaxy catalogues explored.

is running with a random catalogue 50 times bigger than the data catalogue, a typical practice in the community. TreeCorr (Jarvis et al., 2004) is used as a representative of tree-based code. Our method does not use random catalogues since all terms are calculated analytically. Despite running with Python, all the programs do the actual computation either with C/C++ or using Numba to achieve comparable speed to C. Our analytic method computes $RR + DR$ at a speed 3 to 6 orders of magnitude faster than brute-force Monte Carlo method and 2.5 orders of magnitude faster than tree-based code[4] for galaxy catalogues with sizes up to 10 million. At $N_{\rm g} = 10^7$, while it takes the brute force Monte Carlo code a projected time of 100,000 hours and the tree-based code 6 hours, our analytic method gets it done in under 1 minute on a single core. Particularly, the calculation of $\widehat{RR}$ through our analytic method takes only 10^{-4} second, independent of the size of the galaxy catalogue.

[4]The benchmarking of TreeCorr is performed under the default setting (`bin_slop=1`). For a better accuracy, say `bin_slop=0.1`, the computation time of TreeCorr is supposed to be $\sim$ 30 times longer (Siewert et al. 2020).

6.6 Summary and Discussion

We have proposed a new analytic method to compute the galaxy TPCF in an extremely efficient and accurate way, applicable to mask-free surveys with regular geometries. We have derived simple closed-form formulas of the normalized random-random pair counts $\widehat{RR}(r)$ for mask-free surveys with the following geometries: rectangles with sides a and b (Eqs. (6.15) and (6.20)), cuboids with sides a, b, and c (Eq. (6.47)), a unit circle (Eq. (6.55)), and a unit sphere (Eq. (6.61)). With all edge corrections fully considered, these formulas calculate $\widehat{RR}(r)$ with perfect accuracy and zero variance in $O(1)$ time. We have also presented a set of pseudocode to compute the data-random pair counts $\widehat{DR}(r)$ analytically and precisely with zero variance in $O(N_{\rm g})$ time, applicable to the above-mentioned geometries. These algorithms are presented in Appendix D.1 with a link to the Python code. $\widehat{RR}(r)$ and $\widehat{DR}(r)$ together can be used to calculate $\xi(r)$ using any estimator.

We have applied our method to a mock galaxy catalogue from the EAGLE simulation (McAlpine et al., 2016) and compared the calculated $\xi(r)$ with that from the brute-force Monte Carlo method (Fig. 6.2). Perfect agreement is found. We have also compared the speed of our method with that of the brute-force Monte Carlo method, which has $O(N^2)$ scaling, and the tree-based method, which has $O(N \log N)$ scaling. Our analytic method is 3 to 6 orders of magnitude faster than the brute force Monte Carlo method and 2.5 orders of magnitude faster than the tree-based code. Our proposed method is favored over the traditional numerical method whenever applicable.

Our method can be used to replace the brute-force Monte Carlo method as the benchmark of evaluating the accuracy of existing or new code. It could also be particularly useful in the study of non-linear correlation functions and power spectra of galaxies, dark matters, and haloes with exceptional accuracy and efficiency. While most cosmological simulations are done with periodic boundary conditions where the correlation is trivially analytic, researchers may find its applications in particular cases: the study of local clustering of a subregion with high precision, or the study of isolated systems.

For a realistic survey with masks, weight patterns, and/or irregular shapes, the applicability of our approach is very limited, although in special circumstances some applications can be found. Our method can be used to account for masks with regular shapes on top of a mask-free background. Clustering in subregions of a large survey can be explored with ease and with high precision. Although, in both cases, the correlation between the mask or weighted area and the background has to be computed numerically.

Our proposed analytic method is also directly applicable to galactic angular TPCFs when the survey area is close to Euclidean (flat).

Chapter 7: Conclusion and Future Work

7.1 Conclusion

My thesis has focused on understanding the physics of star formation from giant molecular clouds and its role in shaping the galaxies and the Universe using multiscale radiation-magneto-hydrodynamics simulations. Along the path, I explored star formation efficiency laws regulated by photoionization feedback, the escape of ionizing photons from molecular clouds and its implications on the sources of cosmic reionization, star and galaxy clustering, and formation of large circumstellar disks in massive prestellar cores, and proposed a solution to the 'magnetic braking catastrophe' for disk formation.

In Chapter 2, I explored the physics and laws of star cluster formation from molecular clouds. Using RAMSES-RT, I simulated the collapse of GMCs spanning a large parameter space in mass (10^3 - 3×10^5 $\mathrm{M}_\odot$), density (10^2-10^4 cm^{-3}), and metallicity (0.025 - 1 $Z_\odot$), while resolving the formation of individual stars. *This remains one of the largest sets of resolved simulations of SF with stellar feedback.* I found a physically motivated scaling relation for SF timescale and efficiency regulated by photoionization feedback. I established a simple law of star formation efficiency where the GMC forms stars at a rate that depends on the density of the cloud ($\epsilon_{\rm ff} \propto \rho^{1-2}$) throughout a timescale of several sound-crossing time of the cloud, proportional to the cloud size. The simulated stars have mass distributions in excellent agreement with the mass-normalized empirical IMF in both the characteristic power-law slope and normalization if shifted to the left by 40%. The implication is a physical model where a sink particle converts $\sim 40\%$ of its mass to a single star and the rest to smaller stars, a mechanism inferred from the mapping between the observed core mass functions and stellar IMFs. I have shown convincing evidence that star formation in GMCs can be understood as a purely stochastic process: instantaneous star formation follows a universal mass probability distribution similar to the empirical IMF. An apparent behavior of this stochastic process is that low-mass stars form first followed by both low- and high-mass stars, providing the first definitive answer to an open question – do low-mass or high-mass stars form first?

In Chapter 3, I published the *first* study of the escape of LyC photons from GMCs into the intercloud medium that takes into account contributions from spatially resolved stars. I showed that the LyC escape fraction increases with the cloud density. I explained this by showing that high-density GMCs form stars so fast that the cloud is dispersed and fully ionized $\lesssim 2$ Myr after the formation of O/B stars, allowing a significant fraction of their LyC photons to escape, whereas the most massive stars in low-density clouds live most of their lives deeply embedded in neutral gas. I, therefore, concluded that the stellar component of the sources of LyC photons responsible for cosmic reionization must have been very compact star clusters, or globular cluster progenitors, forming in more compact environments than the Milky Way's.

In Chapter 4, I followed up with a series of extremely high-resolution simulations of prestellar core formation and fragmentation using a novel zoom-in AMR technique. With this approach, I was able to push the state of the art of prestellar core simulations by accurately following the accretion and tidal forces on protostellar environments, rather than assuming idealized initial and boundary conditions as in most literature. I showed that stars more massive than 30

$\mathrm{M}_\odot$ form from the filamentary collapse of cores and grow to masses several times bigger than the initial core mass owing to fast accretion from larger scales. This result provides compelling evidence for the 'competitive accretion' scenario of high-mass SF, a problem that is still under debate. The fragments eventually become embedded in large, thick, quasi-steady accretion disks/toroids that are Toomre stable and supported by magnetic and turbulent pressure, explaining puzzling features in recent ALMA observations of high-mass star-forming regions.

In Chapter 5, I explored the magnetic braking problem in disk formation. Protostellar disk formation is a critical step between the collapse of prestellar cores and the formation of stars and planets. However, magnetic fields can in principle transport away angular momentum during the core collapse through magnetic braking and hence suppress disk formation, a phenomenon known as the magnetic braking 'catastrophe'. I showed that the magnetic field in large prestellar cores is extremely turbulent and incoherent, reducing the effect of magnetic braking by roughly one order of magnitude compared to the perfectly aligned and coherent case. This effect leads to the formation of large Keplerian disks even in magnetically critical cores, averting the catastrophe.

In Chapter 6, I studied star clustering by quantifying the clumpiness of the stars using the two-point correlation function $\xi(r)$. The computation of $\xi(r)$ is usually a time-consuming task when the number of particles is large due to the $O(N^2)$ scaling. I develop a novel analytic method of computing $\xi(r)$ which is both more accurate and more efficient than the traditional brute-force or tree-based numerical method, achieving a boost of 2 to 6 orders of magnitude in speed in certain applications. This method can expedite the calculation of galaxy and halo $\xi(r)$ in large-scale cosmological simulations.

7.2 Future Work

The work presented in this thesis marks the beginning rather than the endpoint of a long journey. In this section, I outline a few future projects that build on the research presented in previous chapters.

7.2.1 Resolving the Complete IMF of a Star Cluster

Stars in the local Universe form from GMCs with masses between 10^4 and 10^6 $\mathrm{M}_{\odot}$ (McKee & Ostriker, 2007). So far no radiation-MHD simulation has managed to follow the evolution of a cloud with this size and resolve the formation of individual high- and low-mass stars. I plan to combine a series of high-resolution simulations of star cluster formation from GMCs (Chapter 2, He et al. 2019) that resolves individual intermediate- to high-mass stars with ultra-high-resolution zoom-in simulations (Chapters 4 and 5, He & Ricotti 2022) that resolve the collapse of low-mass prestellar cores.

For this purpose, I will continue to use the RAMSES-RT code and adapt the novel zoom-in AMR technique presented in Chapter 4 (He & Ricotti, 2022). I propose to extend the parameter space of both the GMC simulation set and the prestellar core simulation set (Figure 7.1). I will also add updated physics, including protostellar jets from low-mass stars, radiation pressure, and more realistic cooling. Consistently simulating the formation of prestellar cores in GMCs and their subsequent collapse in realistic environments may bring unique opportunities for the study of some of the most important questions in star formation: How do gravity, turbulence, and magnetic fields interplay at various scales? What sets the SFE of a cloud or a core? What does the similarity between core mass function and stellar IMF imply? What can we learn about the

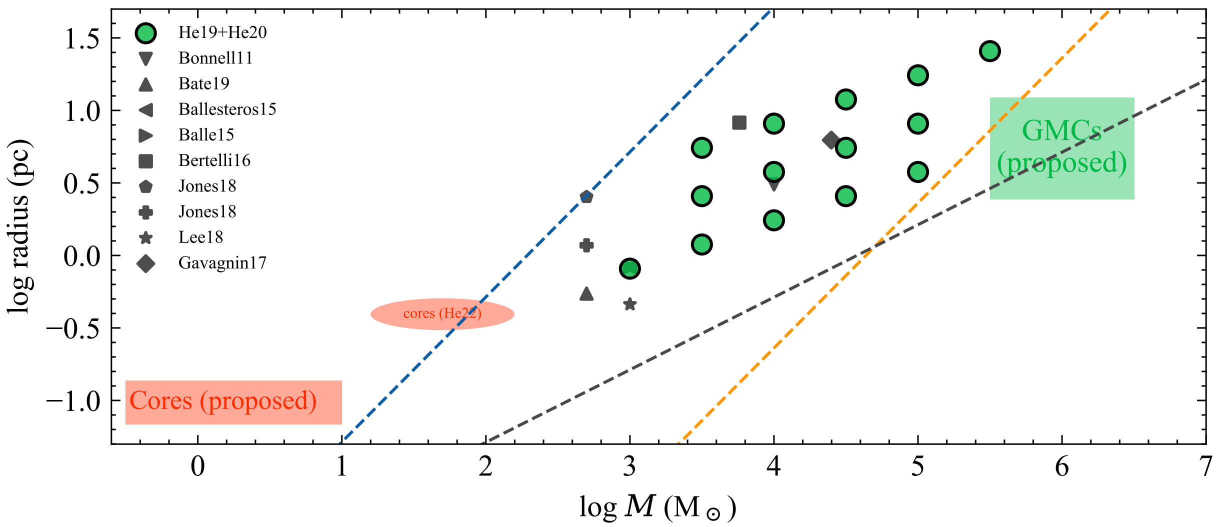

Figure 7.1: Demonstration of the set of proposed simulations in the context of my past work (circles) and the literature (other shapes in gray). The relevant physics are marked in dashed lines with blue representing protostellar outflow ($v_{\rm esc} = 1$ km/s), orange photoionization feedback ($v_{\rm esc} = 15$ km/s), black radiation pressure ($\Sigma = 3000\ {\rm M}_\odot\ {\rm pc}^{-2}$). The relevant physics is important in the parameter space above the line.

binary formation and stellar dynamics from the observed binary period/eccentricity distribution? This project will also provide a set of realistic initial conditions for the simulation of star cluster dynamics discussed in the following section.

7.2.2 Dynamics of Massive Compact Star Clusters and SMBH Growth

The origin of supermassive black holes (SMBHs) that exist at the center of most galaxies remains an open question. The recent detection of 1.5 billion solar mass quasars at $z = 7.5$ put a strong constraint to the early SMBH growth, which requires a seed BH of $\gtrsim 10^4\ {\rm M}_\odot$ just 100 Myr after the Big Bang (Yang et al., 2020; Wang et al., 2021), considering that the SMBH growth model shows an order of magnitude growth every 100 Myr. High-redshift nuclear star clusters (NSCs) are very promising candidates for the formation of intermediate-mass black holes (IMBHs) at a very early time. Analytic work, as well as simulations, demonstrate that, under the right conditions, runaway stellar collisions in a dense star cluster can produce a very massive star that may collapse to form an IMBH that could be the seeds of SMBHs (Spitzer, 1969; Portegies Zwart et al., 2004; Katz et al., 2015). Pushing the formation of SMBH seed of 10^5 $M_\odot$ to 200 Myr after the Big Bang would allow growing the observed quasars. *I plan to conduct the first self-consistent simulations of the resolved formation of massive, dense star clusters and their dynamic evolution*. My goal is to advance our understanding of the properties and dynamics of high-redshift NSCs and investigate their potential role in the production of SMBH seeds.

Simulations of NSC dynamics in the literature rely on simplified initial conditions using statistical properties of observed star clusters, missing a very important and dramatic phase of star cluster evolution (Goodwin & Whitworth, 2004). For instance, a random sample of stars with a Plummer sphere density profile is often generated as the initial condition. My thesis work (Chapters 2, 4, and 6), however, indicates that star clusters forming in turbulent molecular clouds have a fractal structure with significant hierarchical sub-clumping. This suggests that the distribution of stars in realistic young compact star clusters is significantly different from the simplified initial conditions used in most literature. In a review article, Latif & Ferrara (2016) called out that self-consistently simulating the formation and evolution of NSCs is necessary for a better understanding of this BH formation channel.

Based on the results of the work planned in Section 7.2.1, I will use a semi-analytic approximation to sample more realistic star clusters by breaking sink particles (cores) into stars following a mass distribution and dynamical state inferred from zoom-in simulations of prestellar cores described in Chapter 4 and Chapter 5. I will then simulate the dynamical evolution of such hierarchical compact young star clusters using a direct N-body code (e.g. NBODY6++, Aarseth 2003) and study possible channels of IMBH formation and growth. With this *novel* and promising approach which combines resolved simulations of the formation of massive, dense star clusters and their dynamic evolution, I aim to understand the dynamics of dense nuclear star clusters at high redshift and put constraints on the possibility of SMBH seed formation from run-away stellar collisions. The seed BH may potentially reach 10^4 $M_\odot$ in a star cluster of a few $\times 10^6$ $M_\odot$, extrapolating the results of Katz et al. (2015). The substructure and clumpiness of the realistic initial conditions that I will create could potentially allow more rapid core collapse and lead to higher seed BH mass (Goodwin & Whitworth, 2004; Allison et al., 2010).

7.2.3 GPU-accelerated Computing Methods for Astrophysics in the Era of Exascale Computing

Exascale computers – supercomputers that can perform 10^{18} floating point operations per second (exaFLOPS) – debuted in 2022. The first exascale computer on record, the Frontier supercomputer at the Oak Ridge National Laboratory in Tennessee, USA, clocked in at 1.1 exaFLOPS in May 2022. Supercomputers offer unprecedented opportunities for modeling complex astrophysical processes.

The new exascale computing systems raise the question of how to design an efficient, heterogeneous computing approach with optimal use of central processing units (CPUs) and graphical processing units (GPUs) for dedicated tasks in astrophysical simulations. These new approaches will generate enormous amounts of data, whose management and efficient exploitation in advanced AI models will pose major challenges.

This project aims to develop GPU-accelerated computing methods for astrophysics that can drive supercomputers to peak performance in the era of exascale computing. GPU-accelerated computing is a technique that uses GPUs to perform computations that are traditionally done by CPUs. GPUs have a parallel architecture that allows them to process large amounts of data simultaneously, making them ideal for applications that require high performance and scalability.

The specific objectives of this research project are:

- To design and implement GPU-accelerated algorithms for solving MHD and radiative transfer equations on adaptive meshes.
- To evaluate the performance and accuracy of the GPU-accelerated algorithms against existing CPU-based methods, and to identify the challenges and opportunities for further improvement.
- To optimize the algorithms for exascale computing platforms by reducing load balancing and communication and increasing scalability and energy efficiency.
- To apply the GPU-accelerated algorithms to simulate and analyze complex astrophysical phenomena of interest, such as predicting star formation activities in galactic environments, unveiling the winds of star-forming galaxies, and resolving protoplanetary disk formation from giant molecular clouds.

Appendix A: Appendices for Chapter 2

A.1 Clump finder criteria

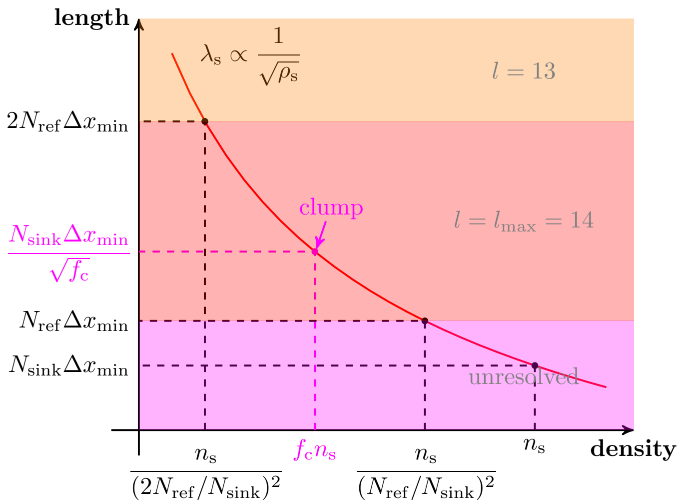

Figure A.1: Explanation of the sink formation criteria in Equation (A.1). The x-axis is the density of a given cell and the y-axis is the corresponding Jeans length. Refer to the text for the meaning of the labels. We impose that the clump finder acts at the highest refinement level but before the clump becomes unresolved.

In this appendix we justify out choice for the value of $N_{\rm sink} = 5$ in Section 2.2.2. We find that $N_{\rm sink}$ should be constrained by the relationship:

$$N_{\rm ref}\sqrt{f_c} < N_{\rm sink} < 2N_{\rm ref}\sqrt{f_c}, \tag{A.1}$$

where $N_{\rm ref}$ is number of Jeans lengths for the refinement criteria, and $f_c = 1/10$ is the ratio of clump-finder threshold density to the sink threshold density. In our case, for $f_c = 0.1$ and $N_{\rm ref} = 10$, we have $3 < N_{\rm sink} < 6$. Therefore in all our simulations we set $N_{\rm sink} = 5$ to satisfy Equation (A.1). The constraint in Equation (A.1) can be understood by inspecting the sketch in Figure A.1, showing the Jeans length as a function of the gas density in a cell at different refinement levels (horizontal bands). As the gas density increases the Jeans length decreases and the level of refinement increases up to the maximum level in the simulation (*e.g.*, $n_{\rm refine} = 14$). The clump finder has a lower density threshold than the sink formation threshold in order to identify structures that should form sinks. In order to ensure that these clumps are maximally resolved, we set all clumps to be at the highest refinement level. This gives the constraint $\frac{1}{(2N_{\rm ref}/N_{\rm sink})^2} < f_{\rm c} < \frac{1}{(N_{\rm ref}/N_{\rm sink})^2}$, and therefore Equation (A.1) follows.

A.2 Emission from clusters

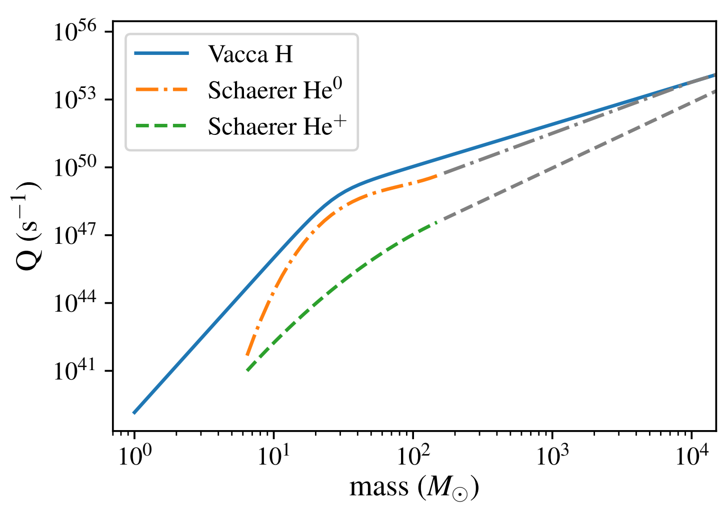

Figure A.2: Ionising photon emission rate as a function of stellar mass. The colored lines are $Q_{\rm H}$ from Vacca fit and $Q_{\rm He^0}$, $Q_{\rm He^+}$ from Schaerer fit. The gray lines are their extrapolations.

In this appendix, we estimate the approximate helium-ionising photon emission rate from

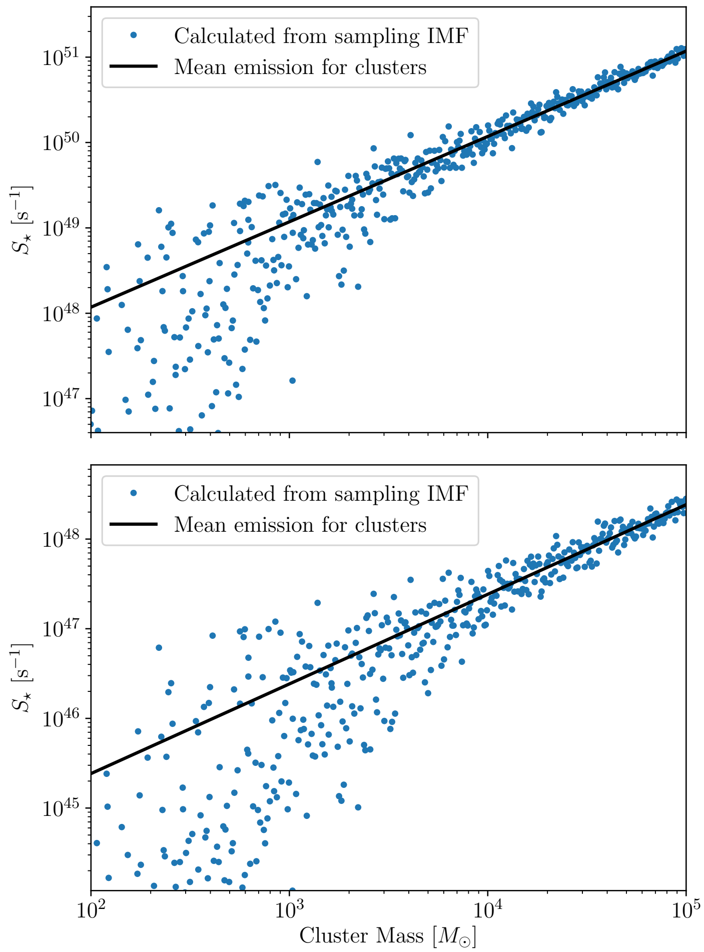

Figure A.3: He^0 (top) and He^+(bottom) ionising photon emission rate as a function of the star cluster mass. The black solid lines are given by $S_* = kM_*$, where M_* is mass of the star cluster and k is 1.178×10^{46} s$^{-1}M_\odot^{-1}$ and 2.422×10^{43} s$^{-1}M_\odot^{-1}$ for He^0 and He^+, respectively.

stellar clusters of a range of masses. The ionising photon emission rate from individual stars is plotted in Figure A.2. We do a Monte Carlo sampling of clusters of stars with a Kroupa IMF and calculate the He^0 and He^+ ionising photon emission rates using Schaerer (2002) fit for each star. We assume a upper and lower limits of the star masses of $0.08M_\odot$ and $100M_\odot$. These results are

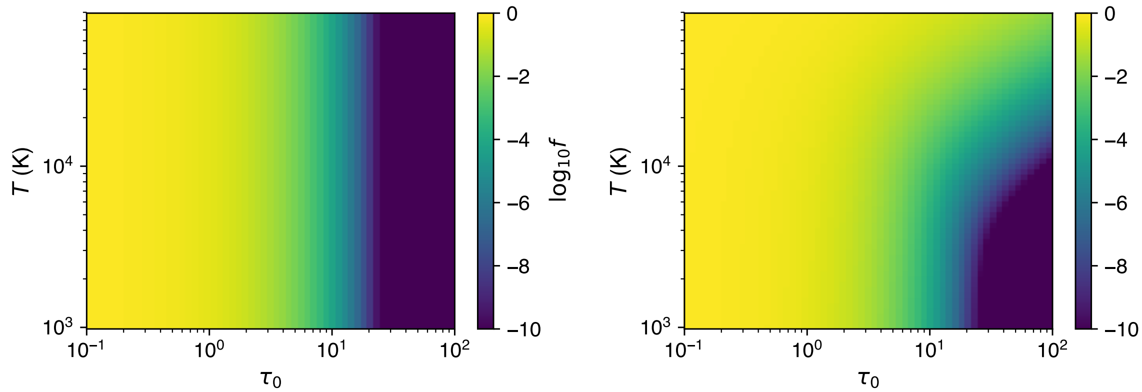

Figure B.1: Color plots of $f(\tau_0, T)$ where $\tau_0 \equiv N_{HI}\sigma_0/m_p$. Top: Eq. (3.2) assuming $\tau_\nu = \tau_0$; Right: Eq. (3.3). At high temperatures, the escape fraction calculated from Eq. (3.3) is much higher than $\exp(-N\sigma_0)$ when $N\sigma_0 > 2$. This modulation makes the calculated escape fraction higher than estimated from $\exp(-N\sigma_0)$.

plotted in Figure A.3, along with a linear fit assuming a perfect sampling of the stellar population.

Appendix B: Appendices for Chapter 3

B.1 Converting column density to escape fraction

A comparison between Eq. (3.3) and Eq. (3.2) is shown in Figure B.1. The x axis is $\tau_0 \equiv N_{HI}\sigma_0/m_p$ and y axis is the surface temperature of a star. On the top panel is $f(\tau_0, T) = \exp(-\tau_0)$. On the bottom panel is $f(\tau_0, T) = f_{esc}(N_{HI}, T)$, following Eq. (3.3). Clearly Eq. (3.3) drops much slower with τ than Eq. (3.2) does at high temperatures. In order to compute Eq. (3.3) effectively, we do an interpolation of it and apply it in our code.

In the calculation of escape fraction, some classical mass-luminosity (Bressan et al., 1993) and mass-radius (Demircan & Kahraman, 1991) relations are used.

Appendix C: Appendices for Chapter 5

C.1 Mass-to-flux ratio of a non-singular isothermal sphere

The density profile of a non-singular isothermal core in hydrostatic equilibrium is given by

$$\rho(r) = \frac{\rho_0}{1 + (\frac{r}{r_c})^2}. \tag{C.1}$$

Defining the dimensionless radius $\xi \equiv r/r_c$, we can show that the mass of the gas within ξ is $M(\xi) = 4\pi\rho_0 r_c^3(\xi - \arctan\xi)$. Assuming a parallel magnetic field threading the midplane of the sphere with the magnetic strength proportional to $\rho^{1/2}$ and equal to B_0 a the centre, then we have

$$\Phi_B = \int_0^{\xi_1} 2\pi r_c \xi \frac{B_0}{\sqrt{1+\xi^2}} r_c d\xi = 2\pi B_0 r_c^2 \left(\sqrt{1+\xi_1^2} - 1\right). \tag{C.2}$$

The magnetic critical mass is given by Equation (5.2).

The gravitational binding energy of a core with radius ξ_1 is given by this integral

$$\begin{aligned} W &= -\int_0^{\xi_1} GM(\xi) 4\pi r \rho(r) r_c d\xi \\ &= -(4\pi)^2 G\rho_0^2 r_c^5 \int_0^{\xi_1} \frac{\xi(\xi - \arctan\xi)}{1+\xi^2} d\xi. \end{aligned} \tag{C.3}$$

The total magnetic energy inside radius ξ_1 is

$$e_B = \int_0^{\xi_1} 2\pi r_c^2 \xi d\xi 2r_c \sqrt{\xi_1^2 - \xi^2} \frac{1}{8\pi} \frac{B_0^2}{1+\xi^2}$$
$$= \frac{1}{2} B_0^2 r_c^3 \int_0^{\xi_1} \frac{\xi \sqrt{\xi_1^2 + \xi^2}}{1+\xi^2} d\xi. \tag{C.4}$$

We plot $\mu_1 = M/M_\Phi$ and $\mu_2 = \sqrt{|W|/e_B}$ for an isothermal core with $\rho_0 = 10^9 m_p\ \mathrm{cm}^{-3}$, $r_c = 1000$ AU, and $B_0 = 0.01$ Gauss in the top panel of Figure C.1. In the bottom panel, we show the value of the equivalent geometrical factor $c_\Phi = \sqrt{G}M/(\Phi_B \mu_2)$ in Equation (5.2), required to have $\mu_2 = \mu_1$.

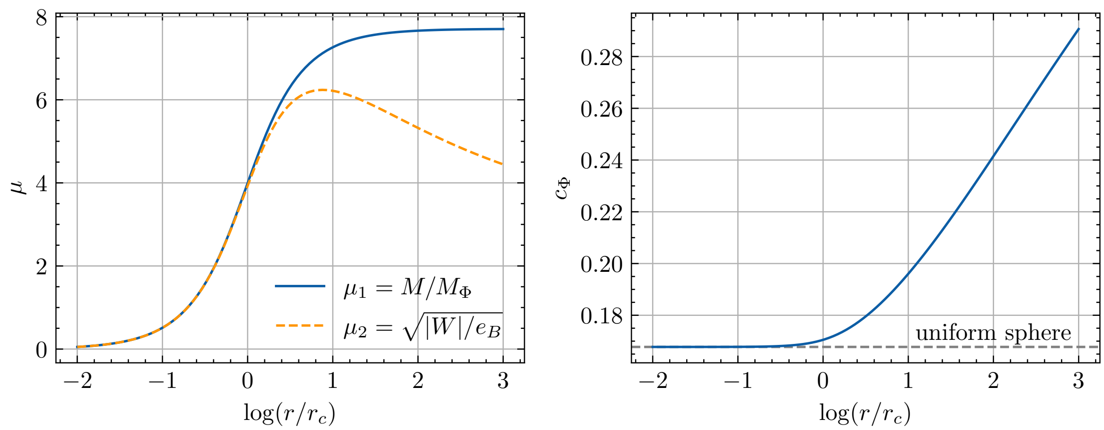

Figure C.1: Comparing two definitions of the relative importance of the gravitational and magnetic forces in a non-singular isothermal sphere as a function of its radius: the relative mass-to-flux ratio $\mu_1 = M/M_\Phi$ and the square root of the binding to magnetic energy $\mu_2 = \sqrt{|W|/e_B}$. In the former case, the geometrical factor c_Φ in Eq. (5.2) equals $1/\sqrt{2}$. The value of c_Φ required for the two definitions of μ to be equivalent to each other (*i.e.*, $\mu_1 = \mu_2$) is shown in the bottom panel, showing that c_Φ increases as the core becomes more centrally concentrated.

C.2 Resolution study

In this section we explore the numerical convergence of the results by comparing μ`3M7` with μ`3Ma7-hires` which differs only in resolution, with the latter being 4 times higher in linear resolution. We show edge-on projections of the disks from these two simulations in Figure C.2. We observe no significant difference in the morphology of the disks among them, ruling out resolution effect on large disk formation.

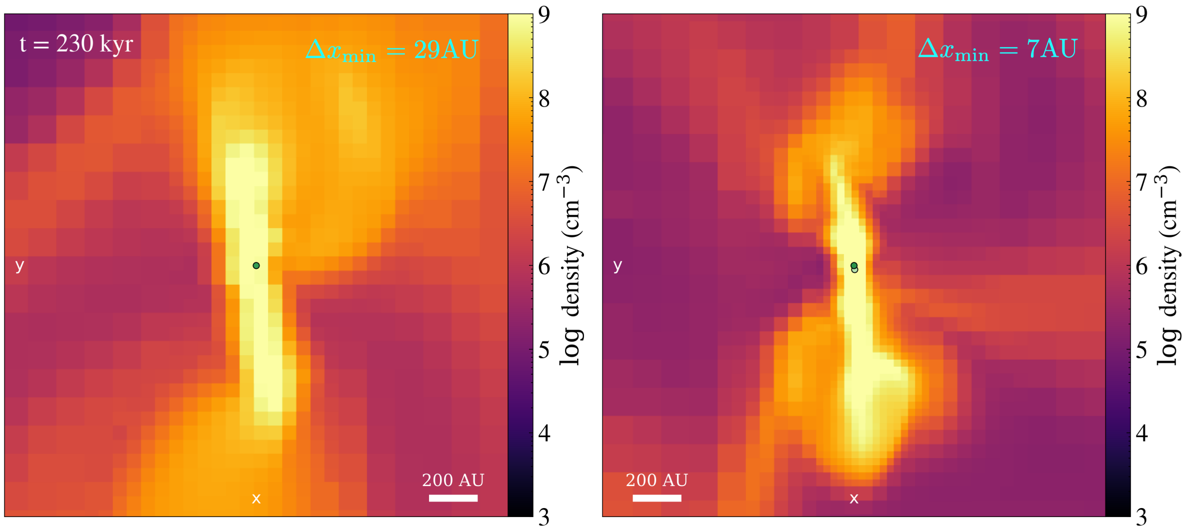

Figure C.2: A comparison of disk structure between two simulations with different resolutions. The figure shows an edge-on view of the disks from two simulations with the same initial conditions but varying resolution. The left panel is run μ3M7 with $l = 18$ and $\Delta x_{\rm min} = 29$AU, and the right panel is run μ3M7-hires with $l = 20$ and $\Delta x_{\rm min} = 7$AU. The disk structure is similar in both runs, indicating numerical convergence of the resolution.

Appendix D: Appendices for Chapter 6

D.1 Algorithms to Compute $\widehat{DR}$ Analytically in $O(N_{\rm g})$ Time

In this appendix, we present pseudocode to calculate $\widehat{DR}\ (r)$ precisely in $O(N_{\rm g})$ time, applicable to survey areas with rectangular (Fig. D.1), cuboidal (Fig. D.2), circular (Fig. D.3), or spherical (Fig. D.4) shapes. The explanations of the algorithms are discussed in Section 6.4. A

Figure D.1: An algorithm for precise calculations of $\widehat{DR}\,(r)$ in $O(N_{\mathrm{g}})$ time, applying to rectangular regions.

```
a, b: dimensions of the rectangular region.
N: the total number of data points.
rlist: array of boundaries defining the real space radial bins in which pairs are counted.
rsteps: a list of discrete differences along rlist.
for i ∈ 1 : (len(rlist) − 1) do
    drpair ← 0
    rthis ← rlist[i]
    rnext ← rlist[i + 1]
    r ← rnext
    for par ∈ data set do

        drpair ← drpair + pi ∗ (rnext^2 − rthis^2)   ▷ All the pairs, assuming a periodic boundary condition.

        x, y: coordinates of par
        if x < r then
            xgapl ← x
        else
            xgapl ← −1
        if x > a − r then
            xgapr ← a − x
        else
            xgapr ← −1
        if y < r then
            ygapl ← y
        else
            ygapl ← −1
        if y > b − r then
            ygapr ← b − y
        else
            ygapr ← −1
                                                      ▷ Exclude the edges
        for igap ∈ [xgapl, xgapr, ygapl, ygapr] do
            if igap > 0 then
                if igap > rthis then
                    F1 ← 0
                else
                    F1 ← int_rec_edge(rthis, igap)     ▷ Eq. (6.67)
                F2 ← int_rec_edge(rnext, igap)
                drpair ← drpair − (F2 − F1)
                                                      ▷ Include the corners back
        for (xgap, ygap) ∈ [(xgapl, ygapl), (xgapl, ygapr), (xgapr, ygapl), (xgapr, ygapr)] do
            if xgap > 0 & ygap > 0 & xgap^2 + ygap^2 < r^2 then
                if xgap^2 + ygap^2 ≥ rthis^2 then
                    F1 ← 0
                else
                    F1 ← int_rec_corner(rthis, xgap, ygap)     ▷ Eq. (6.68)
                F2 ← int_rec_corner(rnext, xgap, ygap)
                drpair ← drpair + F2 − F1

        DR^[i] ← drpair/(N ∗ a ∗ b)
```

Figure D.2: An algorithm for precise calculations of $\widehat{DR}\,(r)$ in $O(N_{\mathrm{g}})$ time, applying to cuboidal regions.

```
a, b, c: dimensions of the cuboidal region.
N: total number of data points.
rlist: array of boundaries defining the real space radial bins in which pairs are counted.
rsteps: a list of discrete differences along rlist.
for i ∈ 1 : (len(rlist) − 1) do
    drpair ← 0
    rthis ← rlist[i]
    rnext ← rlist[i + 1]
    r ← rnext
    for par ∈ data set do
        drpair ← drpair + 4/3 ∗ π ∗ (rnext^3 − rthis^3)
        x, y, z: coordinates of par
        if x < r then                    ▷ Calculate the gaps between the particle and the edges
            xgapl ← x
        else
            xgapl ← −1
        if x > a − r then
            xgapr ← a − x
        else
            xgapr ← −1
        if y < r then
            ygapl ← y
        else
            ygapl ← −1
        if y > b − r then
            ygapr ← b − y
        else
            ygapr ← −1
        if z < r then
            zgapl ← z
        else
            zgapl ← −1
        if z > c − r then
            zgapr ← c − z
        else
            zgapr ← −1
        for igap ∈ [xgapl, xgapr, ygapl, ygapr, zgapl, zgapr] do          ▷ Exclude the faces
            if igap > 0 then
                if igap > rthis then
                    F1 ← intface(igap, igap)                           ▷ Eq. (6.69)
                else
                    F1 ← intface(rthis, igap)
                F2 ← intface(rnext, igap)
                drpair ← drpair − (F2 − F1)
        xgaps ← (xgapl, xgapr)                                     ▷ Include back the edges
        ygaps ← (ygapl, ygapr)
        zgaps ← (zgapl, zgapr)
        for (igaps, jgaps) ∈ [(xgaps, ygaps), (xgaps, zgaps), (ygaps, zgaps)] do
            for gapi ∈ igaps do
                for gapj ∈ jgaps do            ▷ 3 × 2 × 2 = 12 is the number of edges in a cuboid.
                    if gapi > 0 & gapj > 0 & gapi^2 + gapj^2 < r^2 then
                        if gapi^2 + gapj^2 ≥ rthis^2 then
                            F1 ← 0
                        else
                            F1 ← intedge(rthis, gapi, gapj)              ▷ Eq. (6.71)
                        F2 ← intedge(rnext, gapi, gapj)
                        drpair ← drpair + F2 − F1
    DR^[i] ← drpair/(N ∗ a ∗ b ∗ c)          ▷ Calculate the normalized data-random pair counts
```

Figure D.3: An algorithm for precise calculations of $\widehat{DR}\,(r)$ in $O(N_{\mathrm{g}})$ time, applying to circular regions.

```
N: the total number of data points.
rlist: array of boundaries defining the real space radial bins in which pairs are counted.
rsteps: a list of discrete differences along rlist.
for i ∈ 1 : (len(rlist) − 1) do
    drpair ← 0
    rthis ← rlist[i]
    rnext ← rlist[i + 1]
    r ← rnext
    for par ∈ data set do

        drpair ← drpair + π ∗ (rnext^2 − rthis^2)

        x, y: coordinates of par
        d ← sqrt(x^2 + y^2)
        gap ← 1 − d
        if r > gap then
            if rthis ≤ gap then
                F1 ← 0.
            else
                F1 ← int_unit_circle_edge(rnext, d)                ▷ Eq. (6.72)
            F2 ← int_unit_circle_edge(rnext, d)
            drpair ← drpair − (F2 − F1)

    DR^[i] ← drpair/(N ∗ π)
```

Figure D.4: An algorithm for precise calculations of $\widehat{DR}\,(r)$ in $O(N_{\mathrm{g}})$ time, applying to spherical regions.

```
N: the total number of data points.
rlist: array of boundaries defining the real space radial bins in which pairs are counted.
rsteps: a list of discrete differences along rlist.
for i ∈ 1 : (len(rlist) − 1) do
    drpair ← 0
    rthis ← rlist[i]
    rnext ← rlist[i + 1]
    r ← rnext
    for par ∈ data set do
        drpair ← drpair + (4/3)π ∗ (rnext^3 − rthis^3)
        x, y, z: coordinates of par
        d ← sqrt(x^2 + y^2 + z^3)
        gap ← 1 − d
        if r > gap then
            if rthis ≤ gap then
                F1 ← int_unit_sphere_edge(gap, d)                ▷ Eq. (6.73)
            else
                F1 ← int_unit_sphere_edge(rthis, d)
            F2 ← int_unit_sphere_edge(rnext, d)
            drpair ← drpair − (F2 − F1)

    DR^[i] ← drpair/(N ∗ (4/3)π)
```

Python code based on these algorithms is published as doi:10.5281/zenodo.5201479, as developed on https://github.com/chongchonghe/analytic-2pcf/tree/v1.0.0.

Bibliography

Aarseth S. J., 2003, Gravitational N-Body Simulations

Agertz O., et al., 2007, MNRAS, 380, 963

Allen A., Li Z.-Y., Shu F. H., 2003, The Astrophysical Journal, 599, 363

Allison R. J., Goodwin S. P., Parker R. J., Portegies Zwart S. F., de Grijs R., 2010, MNRAS, 407, 1098

Alves J., Lombardi M., Lada C. J., 2007, A&A, 462, L17

André Oliva G., Kuiper R., 2020, arXiv e-prints, p. arXiv:2008.13653

Andrews S. M., Wilner D. J., Hughes A. M., Qi C., Dullemond C. P., 2009, ApJ, 700, 1502

Arce H. G., Shepherd D., 2007, Annual Review of Astronomy and Astrophysics, 45, 245

Audit E., Hennebelle P., 2005, A&A, 433, 1

Ballesteros-Paredes J., Gazol A., Kim J., Klessen R. S., Jappsen A.-K., Tejero E., 2006, The Astrophysical Journal, 637, 384

Ballesteros-Paredes J., Hartmann L. W., Pérez-Goytia N., Kuznetsova A., 2015, MNRAS, 452, 566

Bally J., 2016, Annual Review of Astronomy and Astrophysics, 54, 63

Bate M. R., 2009a, MNRAS, 392, 1363

Bate M. R., 2009b, Monthly Notices of the Royal Astronomical Society, 392, 590

Bate M. R., 2012, MNRAS, 419, 3115

Bate M. R., 2014, MNRAS, 442, 285

Bate M. R., 2019, Monthly Notices of the Royal Astronomical Society, 484, 2341

Bate M. R., Bonnell I. A., 2005, Monthly Notices of the Royal Astronomical Society, 356, 1201

Bate M. R., Burkert A., 1997, MNRAS, 288, 1060

Bate M. R., Bonnell I. A., Bromm V., 2003, MNRAS, 339, 577

Belloche A., 2013, in Hennebelle P., Charbonnel C., eds, EAS Publications Series Vol. 62, EAS Publications Series. pp 25–66 (arXiv:1305.0627)

Belokurov V., et al., 2007, ApJ, 654, 897

Beltrán M. T., de Wit W. J., 2016, A&A Rev., 24, 6

Beltrán M. T., Cesaroni R., Neri R., Codella C., Furuya R. S., Testi L., Olmi L., 2004, ApJ, 601, L187

Beltrán M. T., Cesaroni R., Neri R., Codella C., Furuya R. S., Testi L., Olmi L., 2005, A&A, 435, 901

Beltrán M. T., Cesaroni R., Codella C., Testi L., Furuya R. S., Olmi L., 2006, Nature, 443, 427

Beltrán M. T., Cesaroni R., Neri R., Codella C., 2011, A&A, 525, A151

Beltrán M. T., et al., 2014, A&A, 571, A52

Bertelli Motta C., Clark P. C., Glover S. C. O., Klessen R. S., Pasquali A., 2016, MNRAS, 462, 4171

Beuther H., Walsh A. J., Thorwirth S., Zhang Q., Hunter T. R., Megeath S. T., Menten K. M., 2008, A&A, 481, 169

Bleuler A., Teyssier R., 2014, MNRAS, 445, 4015

Bolatto A. D., et al., 2011, The Astrophysical Journal, 741, 12

Bonnell I. A., Bate M. R., Clarke C. J., Pringle J. E., 2001, MNRAS, 323, 785

Bonnell I. A., Bate M. R., Vine S. G., 2003, MNRAS, 343, 413

Bonnell I. A., Vine S. G., Bate M. R., 2004, MNRAS, 349, 735

Bonnell I. A., Clarke C., Bate M., 2006, Monthly Notices of the Royal Astronomical Society, 368, 1296

Bonnell I. A., Smith R. J., Clark P. C., Bate M. R., 2011, MNRAS, 410, 2339

Bontemps S., Andre P., Terebey S., Cabrit S., 1996, Astronomy and Astrophysics, 311, 858

Bourke T. L., Myers P. C., Robinson G., Hyland A. R., 2001, ApJ, 554, 916

Bowman J. D., Rogers A. E. E., Monsalve R. A., Mozdzen T. J., Mahesh N., 2018, Nature, 555, 67

Boylan-Kolchin M., 2018, MNRAS, 479, 332

Bressan A., Fagotto F., Bertelli G., Chiosi C., 1993, A&AS, 100, 647

Breton M.-A., de la Torre S., 2021, A&A, 646, A40

Bridge C. R., et al., 2010, ApJ, 720, 465

Casassus S., et al., 2015, ApJ, 811, 92

Caselli P., Benson P. J., Myers P. C., Tafalla M., 2002, ApJ, 572, 238

Cesaroni R., Neri R., Olmi L., Testi L., Walmsley C. M., Hofner P., 2005, A&A, 434, 1039

Cesaroni R., Galli D., Lodato G., Walmsley C. M., Zhang Q., 2007, in Reipurth B., Jewitt D., Keil K., eds, Protostars and Planets V. p. 197 (arXiv:astro-ph/0603093)

Cesaroni R., Galli D., Neri R., Walmsley C. M., 2014, A&A, 566, A73

Chabrier G., 2005, in Corbelli E., Palla F., Zinnecker H., eds, The Initial Mass Function 50 Years Later. Springer Netherlands, Dordrecht, pp 41–50

Cheng Y., et al., 2022, arXiv e-prints, p. arXiv:2205.15108

Chon S., Hosokawa T., 2019, MNRAS, 488, 2658

Churchwell E., 2002, ARA&A, 40, 27

Clark P. C., Glover S. C. O., 2014, Monthly Notices of the Royal Astronomical Society, Volume 444, Issue 3, p.2396-2414, 444, 2396

Clark P. C., Bonnell I. A., Klessen R. S., 2008, Monthly Notices of the Royal Astronomical Society, 386, 3

Codella C., et al., 2014, A&A, 568, L5

Coe D., Bradley L., Zitrin A., 2015, ApJ, 800, 84

Colin P., Vazquez-Semadeni E., Gomez G. C., 2013, Monthly Notices of the Royal Astronomical Society, 435, 1701

Crocker R. M., Krumholz M. R., Thompson T. A., Baumgardt H., Mackey D., 2018, MNRAS, 481, 4895

Crutcher R. M., 1999, ApJ, 520, 706

Crutcher R. M., 2012, ARA&A, 50, 29

Crutcher R. M., Wandelt B., Heiles C., Falgarone E., Troland T. H., 2010, ApJ, 725, 466

Cunningham A. J., Krumholz M. R., McKee C. F., Klein R. I., 2018, Monthly Notices of the Royal Astronomical Society, 476, 771

Dale J. E., Bonnell I. A., Clarke C. J., Bate M. R., 2005, MNRAS, 358, 291

Dale J. E., Ercolano B., Bonnell I. A., 2012, Monthly Notices of the Royal Astronomical Society, 424, 377

Dale J. E., Ngoumou J., Ercolano B., Bonnell I. A., 2014, MNRAS, 442, 694

Dale J. E., Haworth T. J., Bressert E., 2015, Monthly Notices of the Royal Astronomical Society, 450, 1199

Davies B., Hoare M. G., Lumsden S. L., Hosokawa T., Oudmaijer R. D., Urquhart J. S., Mottram J. C., Stead J., 2011, MNRAS, 416, 972

Demina R., Cheong S., BenZvi S., Hindrichs O., 2018, MNRAS, 480, 49

Demircan O., Kahraman G., 1991, Ap&SS, 181, 313

Doran E. I., et al., 2013, A&A, 558, A134

Draine B. T., 2011, Physics of the Interstellar and Intergalactic Medium

Eisenstein D. J., et al., 2005, ApJ, 633, 560

Ellis R. S., et al., 2013, ApJ, 763, L7

Elmegreen B. G., 2000, ApJ, 530, 277

Elmegreen B. G., Scalo J., 2004, ARA&A, 42, 211

Espaillat C., Furlan E., D'Alessio P., Sargent B., Nagel E., Calvet N., Watson D. M., Muzerolle J., 2011, ApJ, 728, 49

Ferland G. J., 2003, Annual Review of Astronomy and Astrophysics, 41, 517

Fielding D. B., McKee C. F., Socrates A., Cunningham A. J., Klein R. I., 2015, MNRAS, 450, 3306

Figer D. F., 2005, Nature, 434, 192

Fontani F., et al., 2016, Astronomy and Astrophysics, 593, L14

Fontani F., Commerçon B., Giannetti A., Beltrán M. T., Sánchez-Monge , Testi L., Brand J., Tan J. C., 2018, Astronomy & Astrophysics, 615, A94

Fromang S., Hennebelle P., Teyssier R., 2006, A&A, 457, 371

Fukushima H., Yajima H., Sugimura K., Hosokawa T., Omukai K., Matsumoto T., 2020, MNRAS, 497, 3830

Fuller G. A., Williams S. J., Sridharan T. K., 2005, A&A, 442, 949

Fumagalli M., da Silva R. L., Krumholz M. R., 2011, ApJ, 741, L26

Galli D., Shu F. H., 1993, ApJ, 417, 243

Galli D., Lizano S., Shu F. H., Allen A., 2006, ApJ, 647, 374

Gammie C. F., Lin Y.-T., Stone J. M., Ostriker E. C., 2003, The Astrophysical Journal, 592, 203

Gaudel M., et al., 2020, A&A, 637, A92

Gavagnin E., Bleuler A., Rosdahl J., Teyssier R., 2017, MNRAS, 472, 4155

Geen S., Hennebelle P., Tremblin P., Rosdahl J., 2016, MNRAS, 463, 3129

Geen S., Soler J. D., Hennebelle P., 2017, MNRAS, 471, 4844

Geen S., Watson S. K., Rosdahl J., Bieri R., Klessen R. S., Hennebelle P., 2018, Monthly Notices of the Royal Astronomical Society, 481, 2548

Geen S., Bieri R., Rosdahl J., de Koter A., 2021, MNRAS, 501, 1352

Ginsburg A., Bally J., Goddi C., Plambeck R., Wright M., 2018, ApJ, 860, 119

Girichidis P., Federrath C., Banerjee R., Klessen R. S., 2011, MNRAS, 413, 2741

Glover S. C. O., Federrath C., Mac Low M. M., Klessen R. S., 2010, Monthly Notices of the Royal Astronomical Society, 404, 2

Gnedin N. Y., Kravtsov A. V., Chen H.-W., 2008, ApJ, 672, 765

Gnedin N. Y., Tassis K., Kravtsov A. V., 2009, The Astrophysical Journal, 697, 55

Gong M., Ostriker E. C., 2015, ApJ, 806, 31

Goodman A. A., Benson P. J., Fuller G. A., Myers P. C., 1993, ApJ, 406, 528

Goodwin S. P., Whitworth A. P., 2004, A&A, 413, 929

Goodwin S. P., Whitworth A. P., Ward-Thompson D., 2004a, A&A, 414, 633

Goodwin S. P., Whitworth A. P., Ward-Thompson D., 2004b, A&A, 423, 169

Goodwin S. P., Kroupa P., Goodman A., Burkert A., 2007, in Reipurth B., Jewitt D., Keil K., eds, Protostars and Planets V. p. 133 (arXiv:astro-ph/0603233)

Górski K. M., Hivon E., Banday A. J., Wandelt B. D., Hansen F. K., Reinecke M., Bartelmann M., 2005, ApJ, 622, 759

Gray W. J., McKee C. F., Klein R. I., 2018, MNRAS, 473, 2124

Gritschneder M., Naab T., Walch S., Burkert A., Heitsch F., 2009, The Astrophysical Journal, 694, L26

Grudić M. Y., Hopkins P. F., Quataert E., Murray N., 2018, preprint, (arXiv:1804.04137)

Grudić M. Y., Guszejnov D., Hopkins P. F., Offner S. S. R., Faucher-Giguère C.-A., 2021, MNRAS, 506, 2199

Guszejnov D., Hopkins P. F., 2016, Monthly Notices of the Royal Astronomical Society, 459, 9

Gutermuth R. A., Pipher J. L., Megeath S. T., Myers P. C., Allen L. E., Allen T. S., 2011, The Astrophysical Journal, 739, 84

Guzmán A. E., Sanhueza P., Zapata L., Garay G., Rodríguez L. F., 2020, ApJ, 904, 77

Hansen C. E., Klein R. I., McKee C. F., Fisher R. T., 2012, ApJ, 747, 22

Hartley B., Ricotti M., 2016, MNRAS, 462, 1164

Haworth T. J., Harries T. J., Acreman D. M., Bisbas T. G., 2015, MNRAS, 453, 2277

He C.-C., 2021, ApJ, 921, 59

He C.-C., Ricotti M., 2022, arXiv e-prints, p. arXiv:2210.11629

He C.-C., Ricotti M., Geen S., 2019, MNRAS, 489, 1880

He C.-C., Ricotti M., Geen S., 2020, MNRAS, 492, 4858

Heiderman A., Evans II N. J., Allen L. E., Huard T., Heyer M., 2010, The Astrophysical Journal, 723, 1019

Heitsch F., Ballesteros-Paredes J., Hartmann L., 2009, ApJ, 704, 1735

Hennebelle P., Chabrier G., 2008, ApJ, 684, 395

Hennebelle P., Chabrier G., 2011, ApJ, 743, L29

Hennebelle P., Fromang S., 2008, A&A, 477, 9

Hony S., et al., 2015, Monthly Notices of the Royal Astronomical Society, 448, 1847

Hopkins P. F., 2012a, MNRAS, 423, 2037

Hopkins P. F., 2012b, Monthly Notices of the Royal Astronomical Society, 423, 2016

Howard C. S., Pudritz R. E., Harris W. E., 2016, MNRAS, 461, 2953

Howard C. S., Pudritz R. E., Harris W. E., 2017, MNRAS, 470, 3346

Howard C. S., Pudritz R. E., Harris W. E., 2018a, Nature Astronomy, 2, 725

Howard C. S., Pudritz R. E., Harris W. E., Klessen R. S., 2018b, MNRAS, 475, 3121

Hunter J. D., 2007, Computing in Science & Engineering, 9, 90

Ilee J. D., Cyganowski C. J., Brogan C. L., Hunter T. R., Forgan D. H., Haworth T. J., Clarke C. J., Harries T. J., 2018, ApJ, 869, L24

Inoue A. K., 2002, ApJ, 570, 688

Ishiki S., Okamoto T., Inoue A. K., 2018, MNRAS, 474, 1935

Izotov Y. I., Worseck G., Schaerer D., Guseva N. G., Thuan T. X., Fricke Verhamme A., Orlitová I., 2018, MNRAS, 478, 4851

Jarvis M., Bernstein G., Jain B., 2004, MNRAS, 352, 338

Jaura O., Glover S. C. O., Wollenberg K. M. J., Klessen R. S., Geen S., Haemmerlé L., 2022, MNRAS, 512, 116

Johnston K. G., et al., 2015, ApJ, 813, L19

Johnston K. G., et al., 2020, A&A, 634, L11

Jones M. O., Bate M. R., 2018, MNRAS, 478, 2650

Joos M., Hennebelle P., Ciardi A., 2012, Astronomy & Astrophysics, 543, A128

Joos M., Hennebelle P., Ciardi A., Fromang S., 2013, A&A, 554, A17

Katz H., 2022, MNRAS, 512, 348

Katz H., Ricotti M., 2013, MNRAS, 432, 3250

Katz H., Ricotti M., 2014, MNRAS, 444, 2377

Katz H., Sijacki D., Haehnelt M. G., 2015, MNRAS, 451, 2352

Kauffmann J., Pillai T., Goldsmith P. F., 2013, ApJ, 779, 185

Keihänen E., et al., 2019, A&A, 631, A73

Kennicutt Jr. R. C., 1998, ApJ, 498, 541

Kerscher M., Szapudi I., Szalay A. S., 2000, ApJ, 535, L13

Khaire V., Srianand R., Choudhury T. R., Gaikwad P., 2016, MNRAS, 457, 4051

Kim J.-G., Kim W.-T., Ostriker E. C., Skinner M. A., 2017, ApJ, 851, 93

Kim J.-G., Kim W.-T., Ostriker E. C., 2018, ApJ, 859, 68

Kim J.-G., Ostriker E. C., Filippova N., 2021, ApJ, 911, 128

Kimm T., Blaizot J., Garel T., Michel-Dansac L., Katz H., Rosdahl J., Verhamme A., Haehnelt M., 2019, MNRAS, 486, 2215

Klessen R. S., 2001, ApJ, 556, 837

Klessen R. S., Hennebelle P., 2010, A&A, 520, A17

Klessen R. S., Clark P. C., Bonnell I. A., 2008, Monthly Notices of the Royal Astronomical Society, 386, 3

Koyama H., Inutsuka S.-i., 2004, The Astrophysical Journal, 602, L25

Kratter K., Lodato G., 2016, ARA&A, 54, 271

Kraus S., et al., 2010, Nature, 466, 339

Kroupa P., 2002, Science, 295, 82

Kroupa P., Weidner C., 2003, ApJ, 598, 1076

Krumholz M. R., 2013, Monthly Notices of the Royal Astronomical Society, 436, 2747

Krumholz M. R., 2014, Phys. Rep., 539, 49

Krumholz M. R., Matzner C. D., 2009, ApJ, 703, 1352

Krumholz M. R., McKee C. F., 2005, ApJ, 630, 250

Krumholz M. R., Klein R. I., McKee C. F., 2007, The Astrophysical Journal, 656, 959

Krumholz M. R., Klein R. I., McKee C. F., Offner S. S. R., Cunningham A. J., 2009, Science, 323, 754

Krumholz M. R., Klein R. I., McKee C. F., 2011, ApJ, 740, 74

Krumholz M. R., Dekel A., McKee C. F., 2012, ApJ, 745, 69

Krumholz M. R., Myers A. T., Klein R. I., McKee C. F., 2016, Monthly Notices of the Royal Astronomical Society, 460, 3272

Krumholz M. R., McKee C. F., Bland Hawthorn J., 2019, ARA&A, 57, 227

Kuffmeier M., Haugbølle T., Nordlund Å., 2017, ApJ, 846, 7

Kuffmeier M., Calcutt H., Kristensen L. E., 2019, Astronomy and Astrophysics, 628, A112

Kuhlen M., Krumholz M. R., Madau P., Smith B. D., Wise J., 2012, The Astrophysical Journal, 749, 36

Kuiper R., Klahr H., Beuther H., Henning T., 2010, ApJ, 722, 1556

Kuiper R., Turner N. J., Yorke H. W., 2016, ApJ, 832, 40

Lada C. J., Lombardi M., Alves J. F., 2010, The Astrophysical Journal, 724, 687

Landy S. D., Szalay A. S., 1993, ApJ, 412, 64

Larson R. B., 1969, MNRAS, 145, 271

Larson R. B., 1981, MNRAS, 194, 809

Latif M. A., Ferrara A., 2016, PASA, 33, e051

Law C.-Y., et al., 2022, arXiv e-prints, p. arXiv:2201.01411

Lee Y.-N., Hennebelle P., 2018a, A&A, 611, A88

Lee Y.-N., Hennebelle P., 2018b, A&A, 611, A89

Lee E. J., Miville-Deschênes M.-A., Murray N. W., 2016, ApJ, 833, 229

Lee C.-F., Li Z.-Y., Ho P. T. P., Hirano N., Zhang Q., Shang H., 2017, Science Advances, 3, e1602935

Leroy A. K., Walter F., Brinks E., Bigiel F., de Blok W. J. G., Madore B., Thornley M. D., 2008, The Astronomical Journal, 136, 2782

Lewis B. T., Bate M. R., 2018, MNRAS, 477, 4241

Li H.-b., Fang M., Henning T., Kainulainen J., 2013, MNRAS, 436, 3707

Li Z. Y., Banerjee R., Pudritz R. E., Jørgensen J. K., Shang H., Krasnopolsky R., Maury A., 2014, in Beuther H., Klessen R. S., Dullemond C. P., Henning T., eds, Protostars and Planets VI. pp 173–194 (arXiv:1401.2219), doi:10.2458/azu˙uapress˙9780816531240-ch008

Ma X., Kasen D., Hopkins P. F., Faucher-Giguère C.-A., Quataert E., Kereš D., Murray N., 2015, MNRAS, 453, 960

Mac Low M.-M., Klessen R. S., 2004, Reviews of Modern Physics, 76, 125

Machida M. N., Omukai K., Matsumoto T., Inutsuka S.-i., 2008, ApJ, 677, 813

Majewski S. R., et al., 2007, ApJ, 670, L9

Marino S., Perez S., Casassus S., 2015, ApJ, 798, L44

Martin N. F., et al., 2009, ApJ, 705, 758

Masson J., Chabrier G., Hennebelle P., Vaytet N., Commerçon B., 2016, Astronomy & Astrophysics, 587

Masunaga H., Inutsuka S.-i., 2000, ApJ, 531, 350

Masunaga H., Miyama S. M., Inutsuka S.-i., 1998, ApJ, 495, 346

Matsukoba R., Tanaka K. E. I., Omukai K., Vorobyov E. I., Hosokawa T., 2022, arXiv e-prints, p. arXiv:2206.03497

Matzner C. D., McKee C. F., 2000, ApJ, 545, 364

McAlpine S., et al., 2016, Astronomy and Computing, 15, 72

McKee C. F., Ostriker E. C., 2007, ARA&A, 45, 565

McKee C. F., Tan J. C., 2003, ApJ, 585, 850

Mellon R. R., Li Z.-Y., 2008, ApJ, 681, 1356

Mestel L., Spitzer L., 1956, Monthly Notices of the Royal Astronomical Society, 116, 503

Mocz P., Burkhart B., Hernquist L., McKee C. F., Springel V., 2017, ApJ, 838, 40

Moore A. W., et al., 2001, in Banday A. J., Zaroubi S., Bartelmann M., eds, Mining the Sky. p. 71 (arXiv:astro-ph/0012333), doi:10.1007/10849171_5

Moseley E. R., Teyssier R., Draine B. T., 2023, Monthly Notices of the Royal Astronomical Society, 518, 2825

Motte F., Andre P., Neri R., 1998, A&A, 336, 150

Mottram J. C., et al., 2011, ApJ, 730, L33

Murillo N. M., Lai S.-P., Bruderer S., Harsono D., van Dishoeck E. F., 2013, A&A, 560, A103

Muzerolle J., et al., 2009, ApJ, 704, L15

Myers A. T., Krumholz M. R., Klein R. I., McKee C. F., 2011, ApJ, 735, 49

Myers A. T., McKee C. F., Cunningham A. J., Klein R. I., Krumholz M. R., 2013, The Astrophysical Journal, 766

Nestor D. B., Shapley A. E., Kornei K. A., Steidel C. C., Siana B., 2013, ApJ, 765, 47

O'dell C. R., Wen Z., 1992, ApJ, 387, 229

Oesch P. A., et al., 2016, The Astrophysical Journal, 819, 129

Offner S. S. R., Chaban J., 2017, ApJ, 847, 104

Offner S. S. R., Klein R. I., McKee C. F., 2008, The Astrophysical Journal, 686, 1174

Olguin F. A., Sanhueza P., Ginsburg A., Chen H.-R. V., Zhang Q., Li S., Lu X., Sakai T., 2022, The Astrophysical Journal, 929, 68

Ouchi M., et al., 2009, ApJ, 706, 1136

Padoan P., Nordlund A., 2002, The Astrophysical Journal, 576, 870

Padoan P., Nordlund A., Jones B. J. T., 1997, MNRAS, 288, 145

Padoan P., Juvela M., Goodman A. A., Nordlund A., 2001, The Astrophysical Journal, 553, 227

Padoan P., Nordlund A., Kritsuk A. G., Norman M. L., Li P. S., 2007, The Astrophysical Journal, 661, 972

Padoan P., Pan L., Juvela M., Haugbølle T., Nordlund Å., 2020, ApJ, 900, 82

Park J., Ricotti M., Sugimura K., 2021a, MNRAS, 508, 6176

Park J., Ricotti M., Sugimura K., 2021b, MNRAS, 508, 6193

Park K., Chiaki G., Wise J. H., 2022, ApJ, 936, 116

Patel N. A., et al., 2005, Nature, 437, 109

Peebles P. J. E., 1980, The large-scale structure of the universe

Pei Y. C., 1992, ApJ, 395, 130

Peters T., Banerjee R., Klessen R. S., Low M.-M. M., Galván-Madrid R., Keto E. R., 2010, The Astrophysical Journal, 711, 1017

Portegies Zwart S. F., Baumgardt H., Hut P., Makino J., McMillan S. L. W., 2004, Nature, 428, 724

Razoumov A. O., Sommer-Larsen J., 2010, ApJ, 710, 1239

Ricotti M., 2002, MNRAS, 336, L33

Ricotti M., 2016, MNRAS, 462, 601

Ricotti M., Shull J. M., 2000, ApJ, 542, 548

Ricotti M., Parry O. H., Gnedin N. Y., 2016, ApJ, 831, 204

Robertson B., Goldreich P., 2012, ApJ, 750, L31

Robertson B. E., Kravtsov A. V., 2008, The Astrophysical Journal, 680, 1083

Robertson B. E., Ellis R. S., Furlanetto S. R., Dunlop J. S., 2015, ApJ, 802, L19

Rosdahl J., Teyssier R., 2015, MNRAS, 449, 4380

Rosdahl J., Blaizot J., Aubert D., Stranex T., Teyssier R., 2013, MNRAS, 436, 2188

Rosdahl J., et al., 2018, MNRAS, 479, 994

Rosen A. L., Krumholz M. R., McKee C. F., Klein R. I., 2016, MNRAS, 463, 2553

Rosenfeld K. A., et al., 2012, ApJ, 757, 129

Rosolowsky E., 2005, Publications of the Astronomical Society of the Pacific, 117, 1403

Salpeter E. E., 1955, ApJ, 121, 161

Sánchez-Monge Á., Palau A., Estalella R., Kurtz S., Zhang Q., Di Francesco J., Shepherd D., 2010, ApJ, 721, L107

Santos-Lima R., de Gouveia Dal Pino E. M., Lazarian A., 2012, ApJ, 747, 21

Schaerer D., 2002, A&A, 382, 28

Schaerer D., Charbonnel C., 2011, MNRAS, 413, 2297

Schaller G., Schaerer D., Meynet G., Maeder A., 1992, Astronomy and Astrophysics Supplement Series, 96, 269

Schmidt M., 1959, ApJ, 129, 243

Seifried D., Banerjee R., Pudritz R. E., Klessen R. S., 2013, MNRAS, 432, 3320

Seifried D., et al., 2017, MNRAS, 472, 4797

Shapley A. E., Steidel C. C., Strom A. L., Bogosavljević M., Reddy N. A., Siana B., Mostardi R. E., Rudie G. C., 2016, ApJ, 826, L24

Sharma M., Theuns T., Frenk C., Bower R., Crain R., Schaller M., Schaye J., 2016, MNRAS, 458, L94

Siewert T. M., et al., 2020, A&A, 643, A100

Smith R. J., Clark P. C., Bonnell I. A., 2009, MNRAS, 396, 830

Spitzer Jr. L., 1969, ApJ, 158, L139

Stacy A., Greif T. H., Bromm V., 2010, MNRAS, 403, 45

Sugimura K., Ricotti M., 2020, MNRAS, 495, 2966

Sutherland R. S., Dopita M. A., 1993, The Astrophysical Journal Supplement Series, 88, 253

Takahashi S., Saigo K., Ho P. T. P., Tomida K., 2012, ApJ, 752, 10

Tan J. C., Beltrán M. T., Caselli P., Fontani F., Fuente A., Krumholz M. R., McKee C. F., Stolte A., 2014, in Beuther H., Klessen R. S., Dullemond C. P., Henning T., eds, Protostars and Planets VI. p. 149 (`arXiv:1402.0919`)

Teyssier R., 2002, A&A, 385, 337

Tobin J. J., Hartmann L., Chiang H.-F., Wilner D. J., Looney L. W., Loinard L., Calvet N., D'Alessio P., 2012, Nature, 492, 83

Troland T. H., Heiles C., 1986, ApJ, 301, 339

Truelove J. K., Klein R. I., McKee C. F., Holliman II J. H., Howell L. H., Greenough J. A., 1997, ApJ, 489, L179

Turk M. J., Smith B. D., Oishi J. S., Skory S., Skillman S. W., Abel T., Norman M. L., 2011, The Astrophysical Journal Supplement Series, 192, 9

Vacca W. D., Garmany C. D., Shull J. M., 1996, ApJ, 460, 914

Vanzella E., et al., 2012, ApJ, 751, 70

Vanzella E., et al., 2016, ApJ, 825, 41

Vanzella E., et al., 2018, MNRAS, 476, L15

Vaytet N., Commerçon B., Masson J., González M., Chabrier G., 2018, Astronomy & Astrophysics,, 615

Vazquez-Semadeni E., Ballesteros-Paredes J., Rodriguez L. F., 1997, The Astrophysical Journal, 474, 292

Vázquez-Semadeni E., Zamora-Avilés M., Galván-Madrid R., Forbrich J., 2018, Monthly Notices of the Royal Astronomical Society, 479, 3254

Verliat A., Hennebelle P., Maury A. J., Gaudel M., 2020, A&A, 635, A130

Walch S. K., Whitworth A. P., Bisbas T., Wünsch R., Hubber D., 2012, Monthly Notices of the Royal Astronomical Society, 427, 625

Walsh S. M., Jerjen H., Willman B., 2007, ApJ, 662, L83

Wang K. S., van der Tak F. F. S., Hogerheijde M. R., 2012, A&A, 543, A22

Wang Y.-H., Leigh N. W. C., Liu B., Perna R., 2021, MNRAS, 505, 1053

Weingartner J. C., Draine B. T., 2001, ApJ, 548, 296

Williams G. M., et al., 2022, MNRAS, 509, 748

Willman B., et al., 2005, ApJ, 626, L85

Willott C. J., et al., 2010, AJ, 140, 546

Wise J. H., Cen R., 2009, ApJ, 693, 984

Wise J. H., Demchenko V. G., Halicek M. T., Norman M. L., Turk M. J., Abel T., Smith B. D., 2014, MNRAS, 442, 2560

Xu H., Ahn K., Wise J. H., Norman M. L., O'Shea B. W., 2014, ApJ, 791, 110

Xu H., Wise J. H., Norman M. L., Ahn K., O'Shea B. W., 2016, ApJ, 833, 84

Yajima H., Choi J.-H., Nagamine K., 2011, MNRAS, 412, 411

Yang J., et al., 2020, ApJ, 897, L14

Yen H.-W., et al., 2022, Increasing mass-to-flux ratio from the dense core to the protostellar envelope around the Class 0 protostar HH 211

Yorke H. W., 1986, ARA&A, 24, 49

Zapata L. A., Ho P. T. P., Rodríguez L. F., Schilke P., Kurtz S., 2007, A&A, 471, L59

Zapata L. A., Palau A., Ho P. T. P., Schilke P., Garrod R. T., Rodríguez L. F., Menten K., 2008, A&A, 479, L25

Zhang L. L., Pen U.-L., 2005, New A, 10, 569

Zonca A., Singer L., Lenz D., Reinecke M., Rosset C., Hivon E., Gorski K., 2019, Journal of Open Source Software, 4, 1298

Zucker D., et al., 2006a, ApJ, 643, L103

Zucker D. B., et al., 2006b, ApJ, 650, L41

de Wit W. J., Hoare M. G., Oudmaijer R. D., Nürnberger D. E. A., Wheelwright H. E., Lumsden S. L., 2011, A&A, 526, L5

van Kempen T. A., Longmore S. N., Johnstone D., Pillai T., Fuente A., 2012, ApJ, 751, 137

van der Tak F. F. S., Shipman R. F., Jacq T., Herpin F., Braine J., Wyrowski F., 2019, A&A, 625, A103

van der Walt S., Colbert S. C., Varoquaux G., 2011, Computing in Science and Engineering, 13, 22